Production of Engineered Cardiac Tissue from Encapsulated hiPSCs for Scale-up Studies and Drug-Testing

by

Ferdous Bebe Finklea

A dissertation submitted to the Graduate Faculty of
Auburn University
in partial fulfillment of the
requirements for the Degree of
Doctor of Philosophy

Auburn, Alabama
May 1, 2021

Keywords: hiPSC encapsulation, engineered cardiac tissue, microspheroid, photocrosslinking, drug-testing, biomanufacturing

Approved by

Elizabeth A. Lipke, Chair, Mary and John H. Sanders Professor of Chemical Engineering
Rajesh H. Amin, Associate Professor of Drug Discovery and Development
Selen Cremaschi, B. Redd Professor of Chemical Engineering
Thomas R. Hanley, Professor of Chemical Engineering
Christopher J. Easley, C. Harry Knowles Professor of Chemistry

Abstract

Cardiovascular disease is the leading cause of death worldwide, causing a global health and financial burden. The first chapter of this dissertation highlights the needs for scalable, clinically relevant production of human pluripotent stem cell-derived cardiac tissue and provides an introduction to cardiac tissue engineering. The first project (Chapter 2) presents a rapid, scalable, and single-cell handling approach for the production of 3D functional cardiac tissue microspheres directly differentiated from encapsulated hiPSCs. Encapsulation occurred using a custom microfluidic system, which provides tight control over size and shape of the microspheres both between and within batches. The microspheres supported efficient cardiac differentiation, and the resulting CMs had appropriate temporal changes in gene expression and response to pharmacological and electrical stimuli. This microsphere direct differentiation platform using microfluidic encapsulation of hiPSCs was expanded in Chapter 3 to demonstrate ECT microsphere production with a variety of sizes and in chemically defined conditions. Chapter 4 highlights the flexibility of the microfluidic encapsulation system to produce ECT microspheroids with varying sizes and axial ratios (AR) with initial diameters ranging from 400–1000 μm with ARs from 1–9, and the impact of these parameters along with initial cell and PEG-fibrinogen concentrations on cardiac differentiation outcomes was assessed. Furthermore, initial scale-up studies were performed showing that microspheroids can be cultured and differentiated in shaker flasks, producing over 40 million cells per batch with consistent cardiac differentiation efficiencies. Photocrosslinking of PEG-fibrinogen for

ECT production using the photoinitiator, LAP, which is commonly used in bioprinting, is demonstrated in Chapter 5. Two light sources were used for photocrosslinking of LAP, which was compared with the established Eosin Y crosslinking system. There were no differences in cardiac differentiation efficiency or cell numbers from the resulting ECTs photocrosslinked with the three light sources. Photocrosslinking with LAP allowed for non-destructive monitoring of action potentials using a genetically encoded voltage indicator cell line. Finally, the thalidomide induced changes to cardiac tissue formation, differentiation, and function were investigated in Chapter 6, showing that drug-induced changes during cardiac differentiation from hiPSCs could be detected. Overall, the results here demonstrate advancements in production of ECTs directly differentiated from encapsulated hiPSCs towards scalable, clinically relevant production with potential for use in high-throughput drug screening, bioprinting, and regenerative medicine.

Acknowledgments

This compilation of my research in graduate school would not have been possible without the support of various people of whom I would like to thank. First and foremost, I would like to thank my research advisor, Dr. Elizabeth Lipke, for her guidance and mentorship throughout graduate school. I would like to thank the previous and current graduate students in the Lipke Lab including Morgan Ellis, Dr. Petra Kerscher, Dr. Wen (Aaron) Seeto, Dr. Yuan Tian, Mohammadjafar Hashemi, Nicole Habbit, Iman Hassani, Benjamin Anbiah, and Mayra Paez, for assistance with training, helping with experiments, and for providing valuable feedback, support, and friendship throughout the last five years. I had the privilege of working with some talented undergraduates who provided much assistance and insight into my research projects, particularly Bryana Harris, Gabi Bradley, Emma Hicks, Michaela Bush, and Hanna Hammons. I would like to thank my committee members, Dr. Rajesh Amin, Dr. Selen Cremaschi, Dr. Thomas Hanley, and outside reader Dr. Easley, for their time serving on my dissertation committee. I would also like to further thank Dr. Cremaschi and her graduate students, Bianca Williams and Samira Mohammadi, for their collaborative work on the microspheroid project, particularly with the modeling approaches. Furthermore, I would like to thank Dr. Robert Zweigerdt in Hannover, Germany for the opportunity to work in his lab and learn a variety of techniques and procedures including aggregate differentiation and cardiomyocyte production in stirred-tank bioreactors. I would also like to thank all of his graduate students for their kindness and assistance, particularly Caroline Halloin, Weibke Triebert, and Felix Manstein. Thank

you to Dr. Lauren Black and his graduate student Bre Duffy for providing the proteomics analysis and scientific input for the thalidomide project. I would like to thank Dr. Michael Greene for his time in teaching me RT-qPCR and for allowing me to work in his lab. I am thankful for Allison Church Bird for her assistance and input in my flow cytometry experiments as well as for the chemical engineering support staff, especially Brian Schwieker and Georgetta Dennis. Finally, none of this would have been possible without the constant support of my friends and family. I would especially like to acknowledge and thank my parents, Majid and Kathy Torabinejad, and my husband, Zachary Finklea, for their unconditional love, support, and encouragement.

Table of Contents

List of Tables

List of Figures

List of Abbreviations

αSA	Alpha sarcomeric actinin
3D-dECT	3D-developing engineered cardiac tissue
APD	Action potential duration
AR	Axial ratio
ASD	Atrial septal defect
BSA	Bovine serum albumin
CAD	Coronary artery disease
CDM3	Chemically defined differentiation media
CHD	Congenital heart defect
CM	Cardiomyocyte
CTD	Calcium transient duration
cTnT	Cardiac troponin T
CV	Coefficient of variance
CVD	Cardiovascular disease
Cx43	Connexin 43
DMSO	Dimethyl sulfoxide
EB	Embryoid body
ECM	Extracellular matrix
ECT	Engineered cardiac tissue
ESC	Embryonic stem cell

FBS	Fetal bovine serum
GelMA	Gelatin methacryloyl
GEVI	Genetically encoded voltage indicator
GMP	Good manufacturing practices
hESC	Human embryonic stem cell
hiPSC	Human induced pluripotent stem cell
hiPSC-CM	Human induced pluripotent stem cell derived cardiomyocyte
hPSC	Human pluripotent stem cell
hPSC-CM	Human pluripotent stem cell derived cardiomyocyte
LAP	Lithium phenyl-2,4,6-trimethylbenzoylphosphinate
LC-MS	Liquid chromatography-mass spectrometry
MEA	Multielectrode array
miRNAs	microRNAs
MQM	Mitochondrial quantification using MATLAB
MSC	Mesenchymal stem cell
NVP	N-vinyl-2-pyrrolidone
PBS	Phosphate buffered saline
PBS-T	Phosphate buffered saline with Triton-X
PDMS	Polydimethylsiloxane
PEG	Poly(ethylene glycol)
PEGDA	Poly(ethylene glycol) diacrylate
PSC	Pluripotent stem cell
PSC-CM	Pluripotent stem cell derived cardiomyocyte

RT	Room temperature
RT-qPCR	Quantitative reverse transcription polymerase chain reaction
S	Surface area
SDS	Sodium dodecyl sulfate
SEM	Scanning electron microscopy
TCEP	Tris (2-carboxyethyl) phosphine hydrochloride
TEOA	Triethanolamine
UV	Ultraviolet
V	Volume
VSD	Ventricular septal defect

Chapter 1: Introduction to Cardiac Tissue Engineering

Cardiovascular Disease

Cardiovascular disease (CVD) is the leading cause of death in the world. Globally from 2007–2017, 21% of all deaths were caused by CVD (Virani et al. 2020), which encompasses any disease or disorder that involves the heart or blood vessels, including arrhythmias, congenital heart defects, and coronary artery disease (CAD). Arrhythmias are irregular beating patterns in the heart that can entail the heart beating too slow (bradycardia), too fast (tachycardia), or irregularly. Congenital heart defects are structural problems in the heart or blood vessels that occur during development; these are the most common type of birth defects that affect over 40,000 infants each year in the United States (Mozaffarian et al. 2016). CAD is the most prevalent type of CVD and occurs because of the build-up of plaque, consisting of cholesterol, fatty substances, cellular waste, calcium, and fibrin, along the inner walls of the arteries. This build-up leads to a decrease in the blood flow, which can eventually lead to a myocardial infarction, or heart attack, and/or stroke. Approximately 965,000 Americans have a myocardial infarction each year, accounting for 46% of all CVD-related deaths (Mozaffarian et al. 2016).

Current treatments for CVD consist of medications and surgery; however, these options only treat the side effects and cannot restore function due to the inability of the heart to regenerate after damage is caused. A combination of medications, a pacemaker, or cardiac defibrillation is used for the treatment of arrhythmias; pacemakers can malfunction and be damaged or interfered. Following a heart attack caused by CAD, treatments include medications, a coronary angioplasty, or a coronary artery bypass. There are limitations and

challenges to these treatments. Medications only treat the symptoms and decrease the risk of further problems, and surgeries can be unsuccessful and come with an increased risk of infection. In severe cases, a heart transplant can be performed to restore and improve function. However, there are not enough transplants available for the number of people waiting on the transplant list, and even with a heart transplant, patients must remain immunosuppressed, leading to an increased risk for other diseases, including certain types of cancers and kidney disease. Furthermore, the life expectancy following a heart transplant is only 18–20 years (Politi et al. 2004). Due to the inability for current treatments to restore function and structure to damaged myocardium, new methods for treating CVD are needed.

Human Heart Development and Cardiomyocyte Function

Heart development is a complex process relying on precise cell signaling and mechanical cues. During embryogenesis, germ line specification occurs during gastrulation, and the heart originates from the lateral plate mesoderm containing two cardiac populations, the first and second heart fields. The first heart field forms the primitive heart tube, and the heart is formed from the primitive heart tube and slowly differentiating second heart field cells between embryonic days 22 and 56 in humans (Marchiano, Bertero, and Murry 2019). Cells in the left ventricle originate in the first heart field, while the second heart field contributes to the left and right atria, right ventricle, and outflow tract. The heart is a four chambered organ responsible for pumping blood throughout the body and consists of a variety of cell types, primarily cardiac muscle cells, or cardiomyocytes (CMs), as well as fibroblasts and endothelial cells. Deoxygenated blood from the body is pumped into the right atrium from the superior vena cava. From there, the blood is pumped into the right

ventricle where it travels in the pulmonary arteries to the lungs for oxygenation. The oxygenated blood flows back into the left atrium and then to the left ventricle in the pulmonary veins. The oxygenated blood leaves the heart through the aorta where it then travels through the veins throughout the body. The heart pumps blood at an average of 60–100 beats per minute, resulting in over 30 million beats in a year.

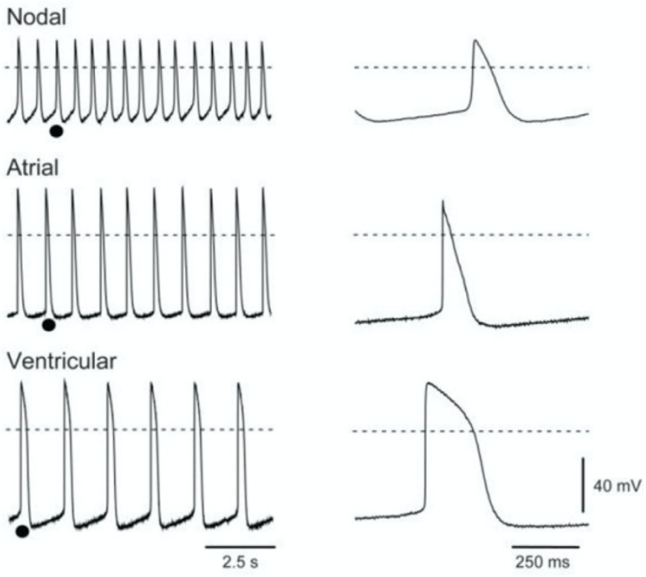

Figure 1.1 Cardiac action potentials for the major types of CMs: ventricular, atrial, and nodal.

The cardiac action potential is the change in voltage of the CMs due to the influx of sodium, potassium, and calcium ions in and out of the cell. Action potentials are initiated in the sinoatrial node, composed of nodal cells. Ventricular action potentials are characterized by the long plateau phase. Figure reprinted with permission from (Mummery et al. 2012).

Successful function of the heart requires synchronous function as a whole organ, including the different classes of cardiomyocytes and the resulting cell types. There are three major classes of cardiomyocytes in the heart: nodal, atrial, and ventricular. The

electrical impulses, called action potentials, originate in the sinoatrial node, travel throughout the heart, resulting in physical contraction of the heart to pump blood; the cells capable of generating these action potentials are called nodal or pacemaker CMs. Ventricular and atrial type cardiomyocytes differ by their location in the heart as well as having different functions, morphology, and electrophysiological and contractile properties (S.Y. Ng, Wong, and Tsang 2010). Figure 1.1 shows the difference in action potentials between nodal, atrial, and ventricular cardiomyocytes. Action potential propagation is initiated by sodium ions entering the CMs, causing a rapid increase in membrane potential and initiating the opening of potassium channels, allowing for a rapid decrease in potassium ions out of the cell. Calcium ions flow into the CMs, initiating cardiac excitation-contraction coupling, the process between the electrical signals and the physical contraction of the CMs. Compared to atrial CMs, ventricular CMs have a lower resting membrane potential, -85 mV and -90 mV, respectively, as wells as having a longer plateau following the upstroke and transient repolarization. After the plateau, rapid repolarization is the driving force for returning the membrane potential to its resting state. The build-up of plaque in the arteries causes impaired blood flow and can cause a myocardial infarction, resulting in the loss of millions of these contractile CMs. During a myocardial infarction, primarily ventricular CMs are lost; therefore, methods for generating ventricular are needed for successful cardiac regeneration.

Cardiac Tissue Engineering

Tissue engineering holds immense promise for treating CVD; the goal of tissue engineering is to create an engineered product from cells and/or biomaterials that can be used for

regenerative medicine, using the cells and tissues as the therapeutic to restore function and structure to the diseased or damaged heart (D.A. Dunn, Hodge, and Lipke 2014). Furthermore, tissue engineering can be employed to establish disease models and drug-testing platforms as well as for studying cardiac development (Figure 1.2). In order for these products to be successfully translated for clinical applications, complexity of production will need to be minimized while still recapitulating the key aspects of tissue formation and function.

Previous animal studies have shown that stem cell-derived cardiomyocytes can improve function to damaged myocardium, or heart tissue (Chong et al. 2014; Carpenter et al. 2012; Chow et al. 2017; Wang et al. 2016; L. Gao et al. 2018). There is great excitement for the utilization of these tissue engineered products for therapeutic use, and initial studies in a human clinical trial using cardiovascular progenitor cells has been completed (Menasche et al. 2018). Beyond cell therapy, engineered cardiac tissue can be used for studying development and for high-throughput pharmaceutical candidate screening (Mordwinkin, Burridge, and Wu 2013; H.F. Lu et al. 2017). Of the pharmaceuticals withdrawn from the market between 1953 and 2013, 14% were recalled due to their undesirable side effects to the heart due to insufficient preclinical testing (Onakpoya, Heneghan, and Aronson 2016). Current models for assessing the effects of candidate pharmaceuticals on the human heart are primarily focused on cardiac toxicity and generation of arrhythmias using model (non-CM) cell lines and small animal testing. The current small animal model for the human heart is mice; however, the human and rodent hearts have different physiology and characteristics (Rajamohan et al. 2016), and rodent models have failed at predicting cardiac toxicity in the past, as with the drug

thalidomide (Vargesson 2015; Ito, Ando, and Handa 2011). Incorporating human-derived CMs, such as engineered cardiac tissues (ECTs), provides significant advances for enhanced recapitulation of the *in vivo* environment for drug-testing.

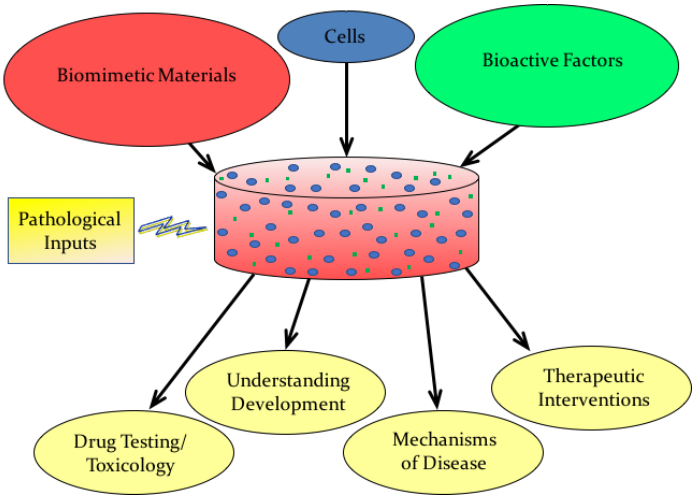

Figure 1.2 Tissue engineering can be used for drug testing, regenerative medicine, and studying development and disease.

The goal of tissue engineering is to create a product that combines cells, biomimetic materials, and bioactive factors that can be used for mimicking the *in vivo* environment for *in vitro* studies. Figure reprinted with permission from (A.J. Hodge et al. 2013).

Cell Sources for Cardiac Regeneration

CMs isolated from adult tissue are nearly impossible to culture long-term *in vitro* due to their low turnover rate and highly specialized function (Feric and Radisic 2016b). Therefore, another cell source must be considered when designing engineered cardiac tissue (ECT) products. Stem cell-based models can be used for cell therapy and for creating human cardiomyocytes due to their ability to mimic the human developmental process as well as their ability to proliferate indefinitely (Thomson and Marshall 1998). There are

several different types of stem cells including: mesenchymal stem cells, embryonic stem cells (Thomson et al. 1998), and induced pluripotent stem cells (Wilson and Wu 2015). Mesenchymal stem cells (MSCs) are adult stem cells that can only be differentiated into certain cell types such as osteoblasts, chondrocytes, myocytes, and adipocytes (Ullah, Subbarao, and Rho 2015). These cells have limited capability to be differentiated into cardiomyocytes (Mathur et al. 2016); however, MSCs have been shown to improve cardiac function following a myocardial infarction, likely due to paracrine signaling (Sun and Nunes 2015; Mirotsou et al. 2011). Pluripotent stem cells (PSCs) consist of both embryonic stem cells (ESCs) and human induced pluripotent stem cells (hiPSCs). ESCs are obtained from an embryo and have the most differentiation potential, but there are ethical issues associated with the process of obtaining them. HiPSCs are stem cells that can be obtained by lentiviral reprogramming of adult somatic cells using a combination of transcription factors (Takahashi and Yamanaka 2006; Sommer et al. 2010). HiPSCs have immense potential for cell therapy and drug-testing due to their ability to differentiate into almost any cell type, maintained pluripotency after prolonged culture, and the limited ethical concerns. One advantage that hiPSCs have over ESCs is the possibility of an autologous treatment, or patient-specific cells. Autologous treatments may cause less of an immune reaction, potentially increasing the likelihood for successful cell delivery and engraftment.

Protocols for differentiating CMs from hiPSCs involve the activation and subsequent inhibition of the Wnt signaling pathway using either growth factors or small molecules (Mummery et al. 2012). Traditional methods for generating pluripotent stem cell-derived cardiomyocytes (PSC-CMs) without a biomaterial include two-dimensional (2D) cell sheets and embryoid bodies. Initial cardiomyocyte differentiation studies used

embryoid bodies (EBs), small clumps of pluripotent stem cells grown in suspension culture (Boheler 2002; Kehat et al. 2001). The size and shape of EBs can be difficult to control leading to inherent variability in aggregate size, resulting in cardiac differentiation variability between cell lines and batches from the same cell line (Osafune et al. 2008). EBs can be formed by printing, seeding into specialized microwell plates, shaker flasks, stirred-flask bioreactors, or by patterning (Henning Kempf, Andree, and Zweigerdt 2016). For 2D cell sheets, PSCs are seeded on a material such as Matrigel and then differentiated into CMs (Laflamme et al. 2007). 2D sheets can be used to obtain CMs up to 98% purity (Lian et al. 2012; Burridge et al. 2014), likely due to uniform diffusion of small molecules and growth factors without a concentration gradient. However, 2D monolayers fail to adequately mimic the *in vivo* three-dimensional (3D) microenvironment, has limited scalability, and CMs obtained from this method need further processing to become mature, functional cardiomyocytes. Traditional methods for the formation of ECTs involve assembling dissociated pluripotent stem cell-derived CMs (PSC-CMs) with a biomaterial; this process can result in cell loss and disruption of important cell-cell junctions. However, previous work in the Lipke group established a direct differentiation platform in which the PSCs were combined with biomaterial and then differentiated in a 3D microenvironment for formation of ECTs (P. Kerscher, Turnbull, et al. 2016; Petra Kerscher, Kaczmarek, et al. 2016).

Biomaterials in Cardiac Tissue Engineering

Due to the variability, low viability, and engraftment of human pluripotent stem cell-derived cardiomyocytes (hPSC-CMs), biomaterials can be used to aid in cell delivery

and direct differentiation by providing physiological and biological cues to cells. The cellular microenvironment can be tightly controlled using biomaterials, providing a similar microenvironment each time. Biomaterials are beneficial in tissue engineering due to the ability to tune their mechanical, chemical, and biological properties as well as promote cell adhesion and engraftment in the body. For scalable production, biomaterials help provide protection from shear stress to cells during scalable culture systems and during and after implantation in the body (D.A. Dunn, Hodge, and Lipke 2014).

There are three types of biomaterials: natural, synthetic, and hybrid. A natural biomaterial is a polymer derived from a living organism. Natural biomaterials are biocompatible with a low host response, enzymatically degradable, and contain ligands that support cell growth and adhesions (Bajaj et al. 2014). However, the synthesis of these materials can be costly, their properties cannot be adjusted, and these materials come with a risk of microbial contamination. The most common natural materials used in cardiac tissue engineering include collagen and gelatin which are derived from commonly found proteins in the extracellular matrix (ECM) of the heart (Huyer et al. 2015). Other natural biomaterials used include: fibrin (Wendel et al. 2014), hyaluronic acid (Yoon et al. 2009), alginate (Landa et al. 2008), Matrigel (Laflamme et al. 2007), chitosan (W.N. Lu et al. 2009), and decellularized ECM (Singelyn and Christman 2010). Synthetic biomaterials are polymers that can be synthesized in the lab. These materials are desirable to use due to their reproducibility, cost-effective synthesis, and ability for tuning the material properties. The mechanical properties, topography, structure, and chemistry can be altered to obtain the desired properties. However, these materials are not as biocompatible as natural biomaterials and have no cell adhesion sites as well as possibly cytotoxic degradation

products. Common natural polymers include poly(ethylene glycol) (PEG), poly(acrylamide), poly(2-hydroxy ethyl methacrylate) (PHEMA), poly(ε-caprolactone), polyurethane, polylactic acid, and polyglycolic acid (Reis et al. 2016; Domenech et al. 2016; Z. Li and Guan 2011). More recently, biomaterials that combine a natural and a synthetic element, hybrid biomaterials, have been used for cardiac tissue engineering (Giusti et al. 1994; Ellis and Lipke 2018). These materials combine the advantages of natural and synthetic biomaterials with the goal of creating a reproducible, biocompatible, cost-effective material that promotes cell adhesion and growth with tunable mechanical properties. This project used PEG-fibrinogen— a hybrid biomaterial with natural component, fibrinogen, covalently crosslinked to synthetic polymer, poly(ethylene glycol) diacrylate (PEGDA) (Almany and Seliktar 2005). PEG-fibrinogen is photocrosslinkable, exhibits high biocompatibility, and has cell attachment and degradation sites provided by the fibrinogen component (Figure 1.3).

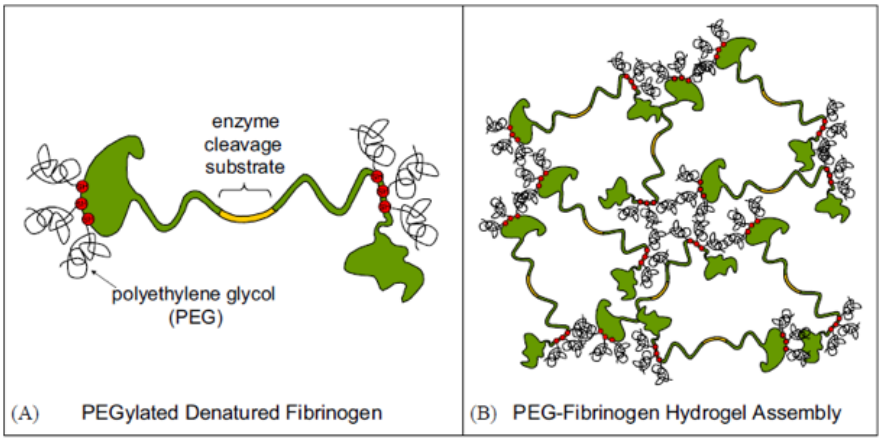

Figure 1.3 PEG-fibrinogen supports direct formation of cardiac tissue.

PEG-fibrinogen is a hybrid biomaterial composed of fibrinogen covalently bound to PEG. This biomaterial can be photocrosslinked to form a 3D polymer network. Figure reprinted with permission from (Almany and Seliktar 2005).

Engineered Cardiac Tissue Formation and Delivery

Different matrix fabrication methods have been investigated for production of functional ECT including: electrospinning, phase separation, 2-photon polymerization, decellularization, bioprinting, and hydrogel formation (Mathur et al. 2016; Boffito, Sartori, and Ciardelli 2014; Hinderer, Brauchle, and Schenke-Layland 2015). Electrospinning, thermally induced phase separation, 2-photon polymerization, and decellularization involve fabrication of the scaffolds and then seeding of the CMs and other cell types. Electrospun matrices can be uncontrollable, and the resulting pore size is not sufficiently large enough for cell migration (Badrossamay et al. 2014; G. Zhao et al. 2015), which is needed to produce a completely cellular tissue and to promote action potential propagation. Thermally induced phase separation fabrication techniques have restricted control of scaffold architecture and are often difficult to reproduce. Decellularization requires complex washing steps, sacrificial tissue, and may have immunogenicity issues. All of these techniques traditionally require differentiation of CMs, often in cell sheets or embryoid bodies, and then incorporation with the fabricated matrix such as with a cardiac patch (Shadrin et al. 2017; L. Gao et al. 2018); this CM dissociation step disrupts important cell-cell junctions and typically results in a loss of cells. Other methods such as bioprinting and hydrogel formation are being investigated for the formation of engineered cardiac tissue that incorporates a cell source during production; however, bioprinting involves complex instrumentation, often has long preparation processes that can be damaging to cells and is limited by the viscosity of materials and cells (Lee et al. 2016; Kupfer et al. 2020). The work presented here produced ECTs directly differentiated from hiPSCs

encapsulated in a photocrosslinkable biomaterial, overcoming the need for multiple cell handling steps and CM dissociation for tissue formation.

The desired ECT geometry is dependent on the resulting application. For example, in high-throughput screening, distribution is important, making a spheroidal tissue geometry beneficial. For therapeutic use, the delivery method plays an important role in determining appropriate fabrication technique to obtain the desired cell composition, size, and shape. Delivery of ECT can be done through open heart surgery or using an injectable suspension (Radisic and Christman 2013; C.P. Jackman et al. 2015). Open heart surgery requires fracturing the breastbone for the surgeon to access the heart and perform surgery; this is one of the most invasive surgeries and comes with the risk of infection, blood clots, and pneumonia as well as a substantial recovery time. A cardiac patch requires open heart surgery and can be attached without sutures or surgical glues (Miki et al. 2012). An injectable suspension has the possibility of being delivered via catheter so that surgery is not required. One limitation of this method is lower cell retention and engraftment in the heart; research has shown cell retention and engraftment is improved in direct injection of cardiac microtissues to the myocardium compared to delivery through intracoronary or intravenous injections or using an epicardial tissue patch (Don and Murry 2013; Gerbin et al. 2015).

Cardiomyocyte Maturity

One challenge for generating functional cardiac tissue differentiated from hPSCs is the maturity of the resulting CMs. CMs undergo many structural and functional changes during cardiac development from the fetal to adult cardiomyocyte phenotype. Compared to adult

cardiomyocytes, hPSC-derived CMs (hPSC-CMs) exhibit more fetal like properties (Scuderi and Butcher 2017; Feric and Radisic 2016a; Karbassi et al. 2020). Adult CMs are rod shaped with organized sarcomeres and are approximately 25% binucleated (Olivetti et al. 1996). Comparatively, hPSC-CMs are round or triangular shaped, mononucleated, and have disorganized sarcomere alignment, similar to fetal CMs. CMs derived from PSCs have proliferation capabilities, while adult CMs do not (Yang, Pabon, and Murry 2014). The presence of transverse tubules, also called T-tubules, is an important structure for adult CMs, and are not regularly seen in hPSC-CMs, although our research group has previously seen the presence of T-tubules in 3D-ECT differentiated from encapsulated hiPSCs (P. Kerscher, Turnbull, et al. 2016). Compared to adult CMs, hPSC-CMs have decreased conduction velocity, upstroke velocity, excitation-contraction coupling, and a higher resting membrane potential, indicating a more fetal-like phenotype (Sun and Nunes 2017). Adult CMs primarily use fatty acid metabolism for energy generation while fetal-like CMs, such as hPSC-CMs, depend on glycolysis (Lopaschuk and Jaswal 2010).

There is ongoing research in promoting maturity of hPSC-CMs using methods such as mechanical stimulation, electrical stimulation, incorporation of other cell types, as well as delivery of microRNAs (miRNAs), chemicals, and ECM components. Mechanical and electrical stimulation is used to replicate the *in vivo* stresses that occur during formation that are critical for heart development (Sun and Nunes 2017). These mechanical stresses induced *in vitro* such as cyclic stretch have been shown to improve expression of gap junctions, ion channels, and sarcomeric proteins as well as improved calcium handling (Mihic et al. 2014). Electrical stimulation has been shown to improve conduction velocity, cardiomyocyte size, and calcium handling (Nunes et al. 2013). Due to their regulatory role

during heart development, the overexpression of miRNAs has been used to promote maturation towards adult-like CMs (White, Pang, and Yang 2016). Delivery of ECM components and other chemicals such as thyroid hormone 3 has been used to induce maturation of engineered cardiac tissues; thyroid hormone 3 has been shown to induce more adult-like CM size, sarcomeric length, contractile force, calcium handling kinetics, and metabolism (Yang et al. 2014). Incorporation of other cell types such as cardiac fibroblasts, endothelial cells, and smooth muscle cells has been shown to increase the functionality and maturation of CMs due to the ability of these cell types to remodel the ECM and exert paracrine effects for the remodeling and maturation of CMs (Ou et al. 2011; Liau et al. 2011; Tulloch et al. 2011; Giacomelli et al. 2020).

Biomanufacturing of Engineered Cardiac Tissues

Multiple functional and safety parameters must be considered for engineered cardiac tissue production, including resulting CM phenotype and maturity, electrical coupling and electrophysiology, biocompatibility, delivery method, and scalability of tissue engineered product. It has been estimated that billions of CMs will be needed to restore function and structure to the damaged myocardium (R. Zweigerdt 2009); therefore, the production and subsequent CM maturation must be scalable. Furthermore, for clinical translation, the ECT must also be able to be manufactured in a clinical-grade setting using good manufacturing practices, such as xeno-free production of CMs. Typically, cell culture formulations use animal-derived serum and/or other animal components, and chemically defined products without human or animal components, xeno-free, are needed for clinical translation. Previous work has shown successful cardiac differentiation in chemically defined

conditions (Burridge et al. 2014; Halloin et al. 2019). Production of CMs will need to utilize bioreactor culture in order to produce a clinically relevant number of cells. Bioreactors have been well established in the production of bacterial cells and antibodies (Chu and Robinson 2001), resulting in a foundational understanding of the critical parameters and potential challenges in process scale-up. Large-scale production of CMs has been previously reported using the formation of self-aggregated EBs (Halloin et al. 2019; H. Kempf et al. 2015; Chen et al. 2015; Fonoudi et al. 2015) and microcarriers (Laco et al. 2020) in stirred-tank bioreactors. Homogenous mixing occurs in a stirred-tank bioreactor, allowing for even distribution of oxygen and nutrients. Furthermore, these bioreactor systems can be coupled with instrumentation for continuous monitoring of culture conditions such as pH, dissolved oxygen, and cell metabolism (dos Santos et al. 2013). However, other types of bioreactors are being employed in cell and tissue production, such as perfusion, wave, and packed-bed bioreactors (Portner et al. 2005). Beyond scalable tissue production, biomanufacturing design considerations include tissue packaging, storage and preservation, and appropriate transfer of cell and therapy products from the manufacturing facility to the location of use (Roh, Nerem, and Roy 2016).

Chapter 2: Engineered Cardiac Tissue Microsphere Production through Direct Differentiation of Hydrogel-encapsulated Human Pluripotent Stem Cells

Introduction

Cardiovascular disease is the leading cause of death worldwide due to the limited ability of damaged myocardium to efficiently regenerate (Del Alamo et al. 2016; Y. Zhang, Mignone, and MacLellan 2015). It has been estimated that billions of cardiac muscle cells, cardiomyocytes (CMs), will be needed for cell therapy to be effective in treating myocardial disease (Stevens and Murry 2018). Because of the inability to culture and expand adult CMs, pluripotent stem cell-derived cardiomyocytes (PSC-CMs) are a critical cell source for prevention and treatment of human cardiovascular disease (Gwathmey, Tsaioun, and Hajjar 2009). Human induced pluripotent stem cells (hiPSCs) provide an option for production of specialized cells, such as cardiomyocytes (CMs), that are difficult to obtain from native tissue and cannot be cultured long-term *in vitro* (Rajamohan et al. 2013; Takahashi et al. 2007). Therefore, further advancements in the scalable production of SC-CMs are needed to revolutionize their application in regenerative medicine, including treatment of heart failure patients, preclinical drug-testing, and studying disease mechanisms while overcoming interspecies and donor variation.

Currently 2D hiPSC monolayers are widely utilized for CM differentiation (Burridge et al. 2014; Lian et al. 2013b); however, this approach requires large surface areas, inherently limiting its scalability. Multiple emerging strategies employ suspension culture and differentiation of hiPSCs for scalable production of CMs, as recently reviewed by Kempf et al. (Henning Kempf, Andree, and Zweigerdt 2016). In particular, bioreactor-

based formation of self-aggregated hiPSC embryoid bodies (EBs) is advantageous because of the single step approach, scalability, and elimination of the need for microcarrier removal (Fonoudi et al. 2015; H. Kempf et al. 2014; Halloin et al. 2019). Although these strategies possess great potential, efficiency of cardiac differentiation between pluripotent stem cell lines and even between batches of the same line can be highly variable (Rajala, Pekkanen-Mattila, and Aalto-Setala 2011; Kehat et al. 2001; Burridge et al. 2007; Osafune et al. 2008). Furthermore, the size and shape of EBs can be difficult to control and the self-aggregation process is shear rate dependent and lacks control over the resulting cell density and cellular microenvironment. Incorporating hiPSCs within a photocrosslinkable biomaterial can be used to enhance initial spheroid uniformity, provide a homogeneous cellular microenvironment, guide stem cell differentiation, and provide localized physiological and biochemical cues to cells. Biomaterials have tunable mechanical, chemical, and biological properties as well as the ability to provide protection from shear stress, justifying their use in CM production from hiPSCs.

To meet the needs for bioreactor-based hiPSC derived CM (hiPSC-CM) production, encapsulation materials must be degradable, while still providing the consistency, ease and speed of handling necessary for commercial scale-up. Natural biomaterials, including Matrigel (Laflamme et al. 2007), collagen, gelatin (Huyer et al. 2015), alginate (Landa et al. 2008), and fibrin (Wendel et al. 2014) have long been used for formation of engineered cardiac tissue post-hiPSC differentiation, but have inherent limitations for use in rapid cell encapsulation and bioreactor culture. Incorporating a synthetic component to create a hybrid biomaterial overcomes these challenges, providing a reproducible, rapidly photocrosslinkable, and tunable microenvironment (D.A. Dunn,

Hodge, and Lipke 2014). Previously, the hybrid biomaterials — poly(ethylene glycol)-fibrinogen (PEG-fibrinogen) and gelatin methacryloyl (GelMA) — have proven successful in the encapsulation and direct differentiation of hiPSCs to form 3D cardiac tissues (P. Kerscher, Turnbull, et al. 2016; Petra Kerscher, Kaczmarek, et al. 2016). These materials provide essential structural and biological components necessary for the production of 3D cardiac tissues from hiPSCs (Almany and Seliktar 2005) while enabling rapid photocrosslinking, which is necessary for scale-up and automatable process development.

Generation of 3D engineered cardiac tissues for use in regenerative medicine and drug-testing applications typically involves dissociation of CMs into single cells for further processing and assembly (Jenkins and Farid 2015). This requirement for CM dissociation creates challenges for cardiac tissue production and clinical translation due to the loss of cells and disruption of cell-cell junctions caused by the multiple cell-handling steps and the need for complex instrumentation and protocols. Rather than assembling tissues using pre-differentiated CMs, stem cell encapsulation and subsequent direct differentiation within supporting biomaterial scaffolds provides an alternative approach for reproducible and scalable production of functional human cardiac tissue and can eliminate multiple cell-handling steps that otherwise limit the potential for process automation and production scale-up.

Previously, our group produced 3D cardiac tissues through hiPSC encapsulation and direct differentiation in PEG-fibrinogen (P. Kerscher, Turnbull, et al. 2016) and GelMA (Petra Kerscher, Kaczmarek, et al. 2016) microislands. Whereas there are multiple advantages to this platform over 2D monolayer differentiation, including observation of T-tubule formation (P. Kerscher, Turnbull, et al. 2016) and the use of a clinically relevant

material (Trattnig et al. 2015), the microisland tissue geometry is not the optimal shape for use in suspension bioreactor culture, high-throughput drug screening, or injectable cell therapy. Therefore, to translate our approach to meet these needs, we a microfluidic system to rapidly encapsulate hiPSCs in hydrogel microspheres was established using a modified microfluidic water-in-oil emulsion technique.

Building on work initiated by Petra Kerscher and Wen Seeto, together with Yuan Tian, here these results producing functional cardiac tissue microspheres through direct differentiation of encapsulated hiPSCs within a PEG-fibrinogen hydrogel in a single unit operation are described. Our custom microfluidic system can produce approximately 45 hiPSC microspheres per minute with a cell density of 25 million cells/mL, an approximate diameter of 900 μm, and tight control over roundness. Encapsulated hiPSCs remained viable in a PEG-fibrinogen hydrogel and continued to proliferate and grow to form larger and denser microspheres. Microspheres consistently showed initial areas of contraction on day 8 of differentiation, with high cardiac differentiation efficiency and reproducibility by day 10. Engineered cardiac microspheres showed appropriate functional responses to pharmaceutical stimuli isoproterenol and propranolol. Furthermore, microsphere CMs responded to outside pacing frequencies up to 6.0 Hz. Microspheres developed cell-cell junctions and displayed aligned myofibrils (day 60) and were maintained in culture long-term (over 3 years). These results demonstrate our ability to reproducibly fabricate hiPSC-laden microspheres in an automatable and scalable manner with high CM yield and functionality, necessary for future applications in cell-therapy.

Materials and Methods

HiPSC expansion and maintenance

IMR-90 Clone 1 and 19-9-11 cell lines were obtained from WiCell. The hiPSC line SCVI55 was obtained from Joseph C. Wu MD, PhD at the Stanford Cardiovascular Institute, and the cell line, Un-Arc 16 Facs II (Shinnawi et al. 2015), was graciously provided by Dr. Lior Gepstein at Technion — Israel Institute of Technology. HiPSCs were cultured on hESC qualified Matrigel (Corning) using mTeSR-1 medium (Stem Cell Technologies) or E8 and passaged into cell clusters using Versene (Invitrogen). E8 media consisted of ascorbic acid (64 mg/L, Sigma), sodium selenite (14 μg/L, Sigma), sodium bicarbonate (543 mg/L, Sigma), insulin (20 mg/L, Sigma), transferrin (10.7 mg/L, Sigma), basic fibroblast growth factor (100 μg/L, Peprotech), and transforming growth factor-beta (2 μg/L, Peprotech) in DMEM/F12 (Gibco). For 24 h after passaging, hiPSCs were maintained in mTeSR-1 (IMR90, 19-9-11, UA16F2) or E8 (SCVI55) medium supplemented with rock inhibitor (5–10 μM, RI, Y-27632, Stem Cell Technologies).

PEG-fibrinogen synthesis

All chemicals were purchased from Sigma-Aldrich unless specified otherwise. Poly(ethylene glycol)-diacrylate (PEGDA) was formed by acrylating PEG (10 kDa) as described previously (DeLong, Moon, and West 2005). PEG-fibrinogen was prepared as previously described (Dikovsky, Bianco-Peled, and Seliktar 2006). Briefly, bovine fibrinogen (300 mg) was dissolved in PBS with 8 M urea and tris (2-carboxyethyl) phosphine hydrochloride (TCEP-HCl, 22.53 mg) was added to the fibrinogen solution (7 mg/mL). Next, PEGDA (1.9392 g) was reacted with fibrinogen (4:1 molar ratio) for 3 h,

precipitated in acetone, and dissolved in PBS with 8 M urea. The reacted PEG-fibrinogen was dialyzed against PBS at 4 ºC for 24 h. To characterize the PEGylated product, fibrinogen content was measured using Pierce BCA assay (Thermo Scientific).

PDMS microfluidic device fabrication

The frame for fabricating the microfluidic device was made by 3D printing an acrylonitrile butadiene styrene bracket and then attaching a glass bottom and metal spacers to form the channels in the mold. The glass bottom was treated with Rain-X® for removal of the PDMS mold from the frame following curing of the PDMS. PDMS was synthesized using a Sylgard 184 silicone elastomer kit (Dow Corning) and poured into the frame, degassed, and cured at 60 °C for 2 h.

HiPSC microspheres production and cardiac differentiation

PEG-fibrinogen precursor solution was prepared by combining PEG-fibrinogen with triethanolamine (1.5 v/v%, TEOA), N-vinyl pyrrolidone (0.39 v/v%, NVP), and Eosin Y (0.1 mM, Fisher Scientific) photoinitiator (in PBS). HiPSCs were resuspended in PEG-fibrinogen precursor solution at 25 million cells/mL. The PEG-fibrinogen-cell mixture was added to one inlet of the custom-built microfluidic device. In parallel, mineral oil was added to the other inlet of the microfluidic device which, when combined with the PEG-fibrinogen-cell mixture, causes the formation of spherical droplets (Figure 2.1A). Flowrates for the PEG-fibrinogen-cell mixture and mineral oil were set at 1 mL/h and 10 mL/h, respectively. A light source (Prior) was used for photocrosslinking the liquid PEG-fibrinogen-cell mixture to form cell-laden microspheres. Microspheres were

collected by washing down with mTeSR-1 medium, removed from the oil phase and spent media, and cultured in mTeSR-1 medium + RI (5–10 μM) for 24 h (day -3). Microspheres were then cultured for an additional 48 h in mTeSR-1 medium with daily media changes (days -2 and -1).

Three days after microsphere production (day 0), cardiac differentiation (Lian et al. 2013b) was initiated by changing medium from mTeSR-1 to RPMI/B27 minus insulin (4 mL, RPMI/B27-I, Thermo Fisher) supplemented with CHIR (10–12 μM, Stem Cell Technologies) per well. On day 1 (24 h after CHIR addition), medium was changed to RPMI/B27-I (4 mL). 48 h after that (day 3), 2 mL old media was combined with 2 mL fresh RPMI/B27-I supplemented with IWP2 (5 μM, Stem Cell Technologies). On day 5, media was replaced with RPMI/B27-I (4 mL) and on day 7, RPMI/B27-I was changed to RPMI/B27 medium (Thermo Fisher). RPMI/B27 medium was replaced every three to four days following differentiation.

Self-aggregated EB formation and cardiac differentiation

To form the self-aggregated EBs (day -3), hiPSCs were dissociated using Versene and collected in a single-cell suspension. One million cells were added to 4 mL of mTeSR + RI (5 μM) in a 6-well plate and placed on a shaker plate (Infors) at 70 rpm in a 5% CO_2 incubator. EBs formed overnight, and daily media changes occurred prior to initiation of cardiac differentiation on day 0. Cardiac differentiation followed the same protocol as the microspheres.

DNA quantification

The DNA was quantified using a DNA Quantification Assay (Sigma-Aldrich) according to the manufacturer's instructions utilizing bisbenzimide H 33258 (Hoechst 33258). Individual microspheres were dissociated in Collagenase-B (1 mg/mL in PBS) for 10 minutes at 37 °C and resuspended in bisbenzimide H 33258 solution (1 μg/mL) for measurement on a plate reader (BIO-TEK Synergy HT). The data is reported as the mean ± standard deviation of 5 individual batches with a minimum of 2 microspheres per batch at each timepoint.

Microsphere diameter, roundness, and early growth quantification

Daily phase contrast images of microspheres were taken from the time of encapsulation (day -3) until initiation of cardiac differentiation (day 0). Microsphere diameter and size of eight individual batches were determined 24 h after encapsulation. Autofluorescence of the photoinitiator Eosin Y in PEG-fibrinogen microspheres was captured using long acquisition times with the FITC filter on a fluorescence microscope at low magnification. Images were analyzed using ImageJ with standard plugins.

Microsphere growth prior to the initiation of spontaneous contraction was determined by analyzing phase contrast images on days -3, 0, 3, and 7 of differentiation by manual outlining of microspheres using ImageJ (n = 10).

HiPSC viability and immunofluorescence staining

24 h after encapsulation, hiPSC viability within PEG-fibrinogen microspheres was assessed using a LIVE/DEAD® viability kit (Invitrogen) and images were taken using a

fluorescent microscope (Nikon). Alexa Fluor 568-Phalloidin (Invitrogen) was used as described by the manufacturer's protocol to visualize actin filaments in encapsulated cells. Whole, dissociated, or sectioned cell-laden microspheres were immunostained with Ki67 (Abcam), α-sarcomeric actinin (αSA, Sigma Aldrich), cardiac troponin T (cTnT, Invitrogen), and connexin 43 (Cx43, Sigma Aldrich). Microspheres were first rinsed with PBS and fixed in paraformaldehyde (4%, Electron Microscopy Sciences) or ice-cold acetone/ethanol (50/50) (Cx43) for 20 min at room temperature (RT) or -20 °C, respectively. Samples were rinsed with PBS and blocked with FBS (3%) overnight at 4 °C or 1 h at RT. Then, the cardiac microsphere samples were incubated in primary antibodies overnight at 4 °C or 1 h at RT followed by the addition of Alexa Fluor 488 and Alexa Fluor 568 secondary antibodies. Nuclei were counterstained with 4',6-diamidino-2-phenylindole (DAPI, Molecular Probes) or Bisbenzimide Hoechst 3342 (MilliporeSigma). All samples were visualized using a Nikon A1R laser-scanning confocal microscope.

Cryosectioning

Microspheres were frozen and sectioned using a Microtome Cryostat HM 505E for immunostaining. The microspheres were embedded within Optimal Tissue Cutting Compound (TissueTek) in a square dish and frozen in methylbutane (EMD) that was kept cold using liquid nitrogen for 15–20 s. The frozen blocks were stored at -80 °C until sectioned. The cryostat was used to cut the blocks into 100–200 μm sections which were added to positively charged slides. The sections were then used for immunostaining and confocal imaging.

XTT assay

To verify hiPSC proliferation within PEG-fibrinogen hydrogels after encapsulation, cell activity on days -2 and -1 were determined using XTT assay (Biotium). One microsphere was placed in each well of a 96-well plate. Media was combined with XTT working solution and the well plate was incubated for 18 h at 37 °C; following incubation, the absorbance was measured using a Microplate Reader (Biotek).

Microsphere cardiomyocyte dissociation

Microspheres were washed with PBS followed by the incubation in dissociation solution containing collagenase type 2 (1 mg/mL, Worthington) at 37 °C for 2 h or Collagenase B (Sigma-Aldrich) for 10 min. The dissociation solution contained NaCl (120 mM), KCl (5.4 mM), $MgSO_4$ (5 mM), Na-pyruvate (5 mM), glucose (20 mM), taurine (20 mM), and HEPES (10 mM, pH 6.9) supplemented with $CaCl_2$ (30 μM) and rock inhibitor (5 μM). Microspheres were centrifuged, resuspended in trypsin EDTA (0.25%, Corning) and incubated at 37 °C for 5 min. Trypsin was neutralized using RPMI20 (FBS (20%) in RPMI1640 medium); cells were resuspended in RPMI20 with rock inhibitor (5 μM). Dissociated cells were plated on fibronectin coated (25 μg/mL, ThermoFisher) substrates (PDMS-coated glass coverslips or MEA) and incubated for three days.

Scanning electron microscopy

For SEM, microspheres were rinsed with PBS and fixed in paraformaldehyde (4%) and glutaraldehyde (2%) in PBS for 15 min. The microspheres were rinsed with PBS and then

osmium tetraoxide (2%) was added for 1.5 h. After further PBS rinses, the microspheres were flash frozen using liquid nitrogen and then lyophilized. Dried microspheres were mounted on aluminum stubs, sputter-coated with gold (Pelco SC-6 sputter coater) and imaged using JEOL JSM-7000F scanning electron microscope.

Parallel plate mechanical testing

Day -2, 5, 8, and 17 microspheres were compressed using a micron-scale mechanical testing system (Microsquisher, CellScale) (Kinney et al. 2014) to determine their mechanical properties using a Tungsten cantilever beam (modulus = 411 GPa, diameter = 203.2 μm). All microsphere samples were analyzed in PBS at 37 ºC. Young's modulus was calculated at 10% deformation using the previously published method (K. Kim, Cheng, et al. 2010). The force at 10% deformation was determined from a linear regression of force versus displacement (n = 8 microspheres per condition).

cDNA synthesis and RT-qPCR

RNA was isolated using a Nucleospin RNA XS kit (Machery-Nagel) from hiPSC microspheres as well as engineered cardiac microspheres on day 10, 20, and 30. Tissues were frozen in liquid nitrogen and stored at -80 °C until time for analysis. The cells were thawed and lysed by vortexing. The lysate was filtered to remove large cell particles and debris. The RNA was bound to the RNA XS column and the DNA was digested using a DNase. After a series of washes, the pure RNA was eluted and collected. The concentration of the RNA was determined using a NanoDrop 1000 UV-Spectrophotometer (ThermoFisher).

A SuperScript III Platinum One-Step RT-qPCR kit (Invitrogen) was used for qPCR analysis with 25 ng of RNA sample. A Bio-Rad CFX96 thermal cycler was used to run the samples at 50 °C for 15 min for cDNA synthesis followed by a 95 °C incubation for 3 mins. The genes of interest were amplified using 45 cycles 95 °C for 15 s followed by 55 °C for 30 s. Detection of amplification was done using Taqman probes along with forward and reverse primers (**Table 1**). Three biological replicates were analyzed in duplicate for each time point. The fold change in gene expression was determined from the $2^{-(\Delta Ct)}$ method in which ΔCt is the difference between the Ct from the sample and Day 10 Ct (or hiPSCs for Oct4). Statistical analysis was performed on the Ct values using a one-way ANOVA with Tukey's test for post-hoc analysis for samples with equal variance, and Games-Howell test for samples with unequal variances. A value of $p < 0.05$ was used for statistical significance.

Gene	Forward Primer	Reverse Primer	Probe
Oct4	CCT GGG GGT TCT ATT TGG GA	CCA CCC ACT TCT GCA GCA A	/56-FAM/ CAA ACG ACC/ZEN/ATC TGC CGC TTT GAG/3IABkFQ/
MLC2v	GGG CGG AGT GTG GAA TTC TT	CCC GGC TCT CTT CTT TGC TT	/56-FAM/AGT GCT GGG/ ZEN/TCC TTT CCA CCA T/3IABkFQ/
αMHC	ACC AAC CTG TCC AAG TTC CG	TTG CTT GGC ACC AAT GTC AC	/56- FAM/AGC ATG AGC/ZEN/TGG ATG AGG CAG AG/3IABkFQ/
βMHC	CAC AGC CAT GGG AGA TTC GG	CAG GCA CGA AGA CAT CCT TCT	/56-FAM/CCT ACC TGC/ZEN/GCA AGT CAG AGA AGG/3IABkFQ/
Cx43	TGA GCA GTC TGC CTT TCG TT	CCA GAA GCG CAC ATG AGA GA	/56-FAM/ ACA CTC AGC/ZEN/AAC CTG GTT GTG AAA/3IABkFQ/

Table 2.1 Primer sequences for RT-qPCR.

Flow cytometry

After tissue dissociation, a cell pellet was collected through centrifugation. After washing with PBS, the cells were labeled with Zombie Dye (Biotium) for 30 min at 4 °C. Cells were then washed with Blocking Buffer (bovine serum albumin (1%, BSA, Sigma), fetal bovine serum (10%, FBS, Atlanta Biologics) in PBS), and then fixed with Foxp3 Transcription Factor Staining Buffer Set (eBioscience) overnight at 4 °C. The cells were then filtered using a 70 μm cell strainer (Scienceware Flowmi) and permeabilized with FACS buffer (BSA (1%), FBS (10%) in 1x Permeabilization Buffer (eBioscience)) at RT for 30 mins. The primary antibodies (cTnT (1:400, Invitrogen), MF20 (1:200, DSHB), TE-7 (1:100, Sigma), MYL11 (1:100, Sigma), PDGFRα (20 μL/1x10^6 cells, BD), Ki67 (1:200, Abcam), and/or P4HB (1:200, Abcam)) were then incubated with the cells for 1 *h* at RT or 4°C overnight. After incubation in the primary antibody, washing occurred with Permeabilization Buffer. The secondary antibodies (1:300, AlexaFluor 488 goat anti-rabbit IgG and AlexaFluor 647 goat anti-mouse IgG (ThermoFisher)) were added for 30 mins at RT. The cells were then washed with Permeabilization Buffer and resuspended in Blocking Buffer for analysis. An Accuri C6 or Beckman Coulter CytoFlex LX was used for sample analysis. At least 10,000 cells were recorded for analysis. Isotype controls (Anti-Mouse IgG1 and Anti-Rabbit IgG (ThermoFisher)) were used to ensure there was not any non-specific binding.

Masson's Trichrome Staining

Microspheres were fixed in Bouin's fixative for 1 h, washed with water three times for 10 min each, 70% ethanol two times for 10 min each, 80% ethanol for 10 min, 95% ethanol

for 10 min, 100% ethanol two times for 5 min, and 3 times with XS-3 (StatLab); all washing steps were done with agitation. Microspheres were paraffin embedded, sectioned at a thickness of 5 μm, and heated in a 58°C oven for 10 min. Masson's trichrome staining (Poly Scientific R&D) was performed according to the manufacturer's instructions. Microsphere sections were imaged using a ScanScope CS (Leica).

Multielectrode array

Day 20 and 50 dissociated microsphere CMs were seeded onto a fibronectin coated S2 type MEA200/30-Ti-gr (Multichannel Systems) and cultured for at least 24 h. Adhering microsphere CMs were perfused with Tyrode's solution, composed of $CaCl_2$ (1.8 mM), glucose (5 mM), HEPES (5 mM), $MgCl_2$ (1 mM), KCl (5.4 mM), NaCl (135 mM), and NaH_2PO_4 (0.33 mM) at pH 7.4 and 37 ºC. Once stabilized, field potentials of spontaneous contractions were recorded at a sampling frequency of 10 kHz. Drug response of day 20 microsphere CMs was tested by adding the β-adrenergic agonist isoproterenol (1 μM) and antagonist propranolol (1 μM). Day 50 microsphere CMs were exogenously paced from 0.5–6.0 Hz.

Optical mapping of calcium transients

A high-speed camera (Andor iXon+ 860 EMCCD) was used to take calcium recordings of at least 1600 pixels of plated engineered cardiac tissue microspheres using our previously established optical mapping system (A. J. Hodge, Zhong, and Lipke 2016). The cardiomyocytes were stained with Rhod-2 AM dye (5 μM, Invitrogen) with Pluronic F-127 (0.02%) in Tyrode's Solution for 30–120 min with blebbistatin (10 μM, EMD).

Tyrode's solution was prepared by combining calcium chloride (1.8 mM) and glucose (5.0 mM) with HEPES (5.0 mM), magnesium chloride (1.0 mM), potassium chloride (5.4 mM), sodium chloride (135 mM), and sodium phosphate (0.33 mM) and adjusting the pH to 7.4 with sodium hydroxide. Warm Tyrode's Solution was perfused through the optical mapping chamber before adding the sample. The plated engineered cardiac tissue microspheres were added to the chamber and recordings were taken with and without electrical pacing. A custom MATLAB script was used for analysis in which the change in fluorescence was used to calculate the calcium transient duration (CTD) at each location in a recording.

Statistical Analysis

Unless otherwise noted, statistical analysis was performed using Minitab statistical software where results are presented as mean ± standard deviation. One-way ANOVA was performed with Tukey's test for post-hoc analysis for samples with equal variance, and the Games-Howell test was performed for samples with unequal variances. A value of $p < 0.05$ was used for statistical significance.

Results

Rapid, one-step microfluidic encapsulation system produced uniform hiPSC microspheres

A microfluidic cell-encapsulation system was developed to rapidly produce uniform spherical hydrogels using a modified microfluidic water-in-oil emulsion technique. The central component of the system is a device made of polydimethylsiloxane (PDMS), which

has two inlets, an outlet, and a modified T-junction (Figure 2.1A). Within this system, a suspension of hiPSCs in aqueous PEG-fibrinogen precursor solution — the discrete phase — was pumped through the top inlet of the PDMS microfluidic device. In parallel, mineral oil — the continuous phase — was pumped through the bottom inlet of the device; the two inlet streams come together at the device T-junction. Microspheres were formed through emulsification and traveled through the perpendicular outlet channel where they were photocrosslinked. Crosslinking occurred rapidly, with a light exposure time of 1.6 seconds per microsphere, and crosslinked microspheres were collected from the end of the outlet channel using a continuous downward flow of cell culture media, removed from the oil phase and washing media, and transferred to a well-plate.

Encapsulation of hiPSCs occurred on day -3 of cardiac differentiation. Following encapsulation, hiPSCs (25×10^6 cells/mL PEG-fibrinogen) maintained high viability (Figure 2.1B), and as a result of the high cell density, hiPSCs were tightly packed throughout the microsphere, displaying a round morphology with some cells being exposed beyond the PEG-fibrinogen hydrogel boundary (Figure 2.1F). Approximately 45 hiPSC microspheres were produced per minute with tight control over size and roundness (Figure 2.1C-E). Each microsphere contained approximately 9500 hiPSCs; this equates to an encapsulation rate of 420,000 cells/min. Therefore, a clinically relevant number of cells, 8 million, as used in our previous large animal wound healing study (Seeto et al. 2017) can be encapsulated using this system in less than 20 minutes, and enough spheres to fill a 384-well plate for high-throughput screening assays can be produced in less than 10 minutes with one microfluidic device.

Batch	Ave. Diameter	CV (diameter)	Roundness	CV (roundness)	n=
1	850 ± 32 μm	3.76	0.979 ± 0.01	1.02	46
2	883 ± 55 μm	6.23	0.966 ± 0.03	3.11	32
3	952 ± 93 μm	9.77	0.933 ± 0.04	4.29	58
4	936 ± 46 μm	4.91	0.940 ± 0.02	2.13	65
5	921 ± 34 μm	3.69	0.973 ± 0.01	1.03	72
6	936 ± 46 μm	4.91	0.947 ± 0.02	2.11	91
7	854 ± 36 μm	4.22	0.967 ± 0.02	2.07	66
8	900 ± 46 μm	5.11	0.944 ± 0.03	3.18	55

Table 2.2 Size and shape of microsphere batches.

The average ± standard deviation is presented for microsphere diameter and roundness for 8 batches along with the coefficient of variance (CV) and sample size (n).

This microfluidic system reproducibly produced uniform microspheres with highly consistent size and shape not only within a batch, but also between batches. For 8 batches, the average diameter of the microspheres ranged from 850–952 μm and the average roundness was above 0.933 with low variance within a batch (diameter coefficient of variance (CV) < 10%, roundness CV < 5%, n ≥ 32 microspheres per batch, Table 2.2). Furthermore, variance between batches was also low; on the day of encapsulation (day -3, Figure 2.1C), average initial microsphere diameter was 908 ± 40 μm (CV = 4.4%, Figure

2.1D) and roundness was 0.956 ± 0.02 (CV = 2.1%, Figure 2.1E, n = 8 independent batches).

HiPSC microspheres continued to proliferate and grow prior to initiation of cardiac differentiation. Following encapsulation (day -3), cells first grew within the original hydrogel boundaries, maintaining the initial microsphere diameter. Encapsulated hiPSCs were evenly distributed within the PEG-fibrinogen hydrogels with high cell density throughout the microspheres as shown by immunofluorescent labeling of the nuclei in cryosections (Figure 2.1G). HiPSCs were cultured in their pluripotent state for three days before cardiac differentiation was initiated on day 0 (Figure 2.1). Previously, it was demonstrated that three days was sufficient for hiPSCs to adapt to their new 3D hydrogel microenvironment and initiate cell growth within the hydrogel, forming a continuous tissue over time (P. Kerscher, Turnbull, et al. 2016; Petra Kerscher, Kaczmarek, et al. 2016). HiPSC microspheres behaved similarly, occupying the majority of the spherical volume by day 0 (Figure 2.1F).

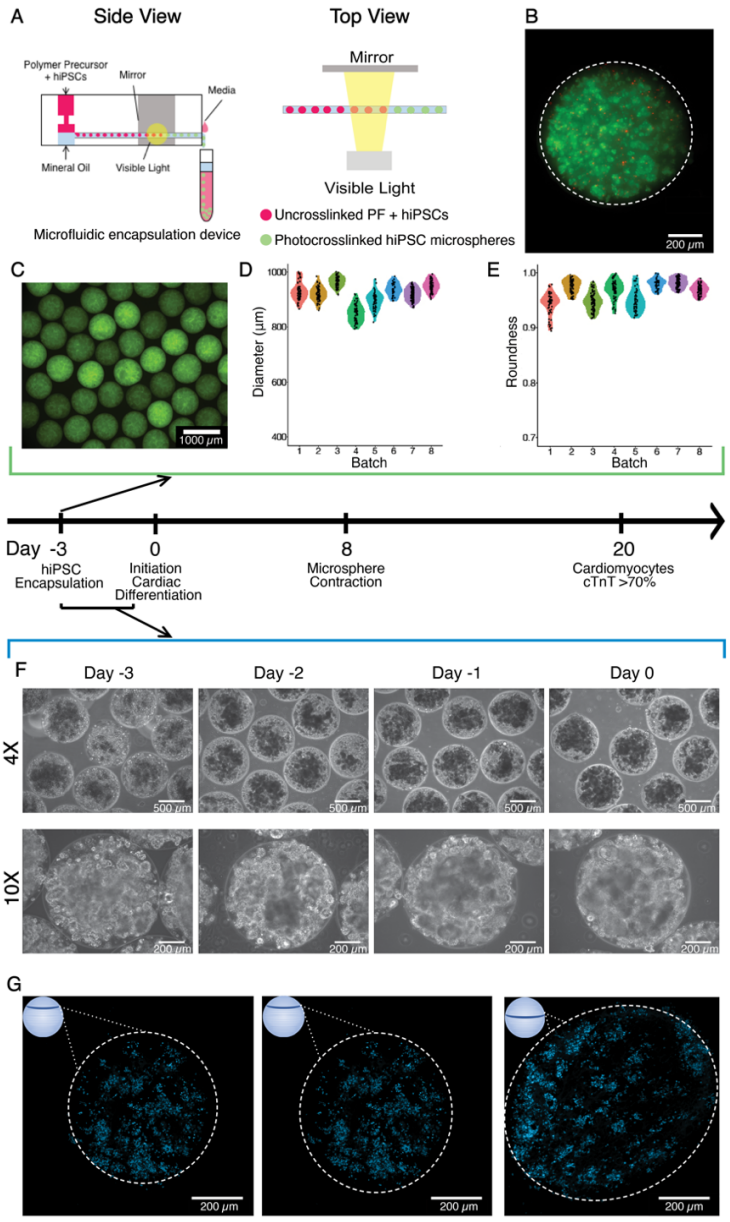

Figure 2.1 Rapid, highly reproducible hiPSC-encapsulation process to produce uniform cardiac tissue microspheres.

(A) HiPSCs suspended in aqueous hydrogel precursor solution (25 million cells mL^{-1}, discrete phase) were infused through a custom PDMS mold opposite an oil phase (continuous phase) to produce uniform cell-laden microspheres. Microspheres formed at the junction of the PDMS device and then traveled through the outlet channel where

photocrosslinking occurred for 1.6 seconds, resulting in a cell encapsulation rate of 420,000 cells per minute. (B) Encapsulated hiPSCs maintained high cell viability as visualized using a Live/Dead Assay with live cells shown in green and dead cells in red. Dashed white line indicates microsphere perimeter. (C) Microspheres were highly uniform as visualized at 24 h post-production using long acquisition times to detect the Eosin Y autofluorescence. (D–E) Microsphere diameter and circularity were consistent both within a batch and between batches as shown in the violin plots. Each color represents an individual batch while each measured microsphere is represented by a black dot. Microspheres were (D) 908 ± 40 μm in diameter and (E) were highly circular (0.956 ± 0.02) (n = 8 individual batches, 485 spheres analyzed). (F) HiPSCs were successfully encapsulated in microspheres and maintained in suspension culture prior to cardiac differentiation initiation, as visualized here in daily phase contrast images. (G) Cryosections from day 0 show uniform distribution of cells throughout the hydrogel based on number of Hoechst-labeled (blue) nuclei per cross sectional area. Inset schematic shows slice location based on measured diameter.

Encapsulated hiPSCs grew to form continuous cell-laden microspheres

After initiation of cardiac differentiation (day 0), the cells continued to grow within and then beyond the initial microsphere boundaries to produce denser and larger tissues with decreasing roundness (Figure 2.2A). For two different lines of encapsulated hiPSCs, IMR90 and 19-9-11, XTT assay results confirmed higher metabolic activity on day -1 than on day -2 (n = 5 microspheres, Figure 2.2B), which combined with visual phase contrast data (Figure 2.2A) and Ki67 staining (Figure 2.2C), confirms an increase in the number of

viable and proliferative cells. By differentiation day 3, microsphere diameter had increased by a factor of 1.27 ± 0.22 when compared to day 0 and had further increased to 1.7 ± 0.11 times by day 7 (n = 10, Figure 2.2D). The total number of cells increased throughout differentiation with a significantly higher number of cells by day 7. The number of cells per encapsulated hiPSC on day -3 was 0.96 ± 0.55, 1.43 ± 0.70, and 2.8 ± 0.54 on days 0, 3, and 7 (n = 5 individual batches). Additionally, the ratio of DNA on days 3 and 10 with respect to day 0 was 1.32 ± 0.49 and 1.40 ± 0.41, respectively (n = 5 individual batches).

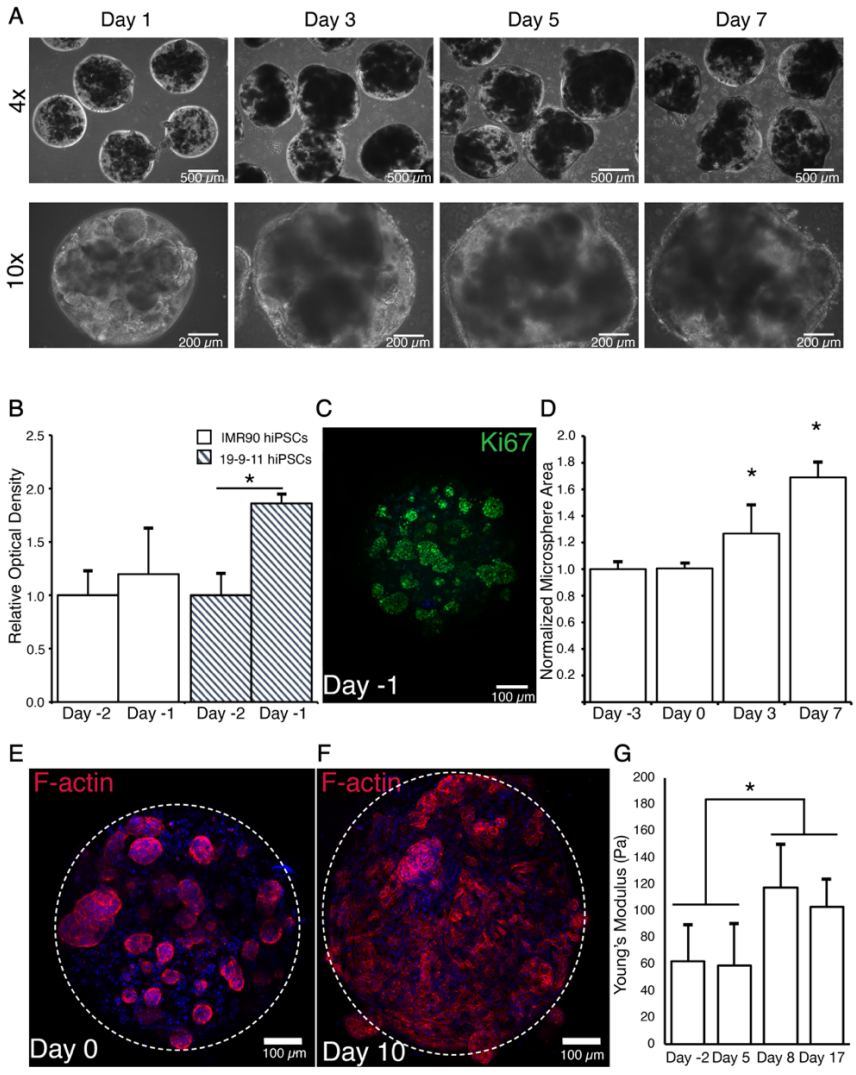

Figure 2.2 Cell-laden PEG-fibrinogen microspheres grew to form uniform tissues.

(A) During differentiation, the cells within the microspheres continued to proliferate and remodel their provided PEG-fibrinogen microenvironment as seen in phase contrast images throughout the time course of cardiac differentiation. (B) Prior to cardiac differentiation, cell proliferation for two hiPSC lines was verified by XTT assay, which showed an increase in optical density between day -2 and day -1 ($n = 5$ microspheres per condition, $*p < 0.05$), indicating continued proliferation and growth of the cells. (C) The hiPSCs maintain their proliferative phenotype following cell encapsulation as shown by positive expression of Ki67 (green) on day -1. (D) From the onset of cardiac differentiation (day 0), microsphere size increased by a factor of 1.27 by day 3 and 1.7 by day 7 ($n = 10$, $*p < 0.05$). (E) Prior to initiation of cardiac differentiation, hiPSCs grew as rounded colonies within the microspheres as visualized on day 0 (3 days post-encapsulation) through labeling of F-actin filaments (red). Dashed white line indicates microsphere perimeter. (F) Following cardiac differentiation, cells are more elongated, indicative of cardiomyocyte phenotype. (G) The PEG-fibrinogen provides an initially soft microenvironment (< 250 Pa), and a significant increase in stiffness occurs during cardiac differentiation ($n = 8$ microspheres per condition, $*p < 0.05$).

Encapsulated hiPSCs differentiated into engineered cardiac tissue microspheres

HiPSC-laden microspheres were successfully differentiated into spontaneously contracting engineered cardiac tissue. Suspension cultured microspheres initiated spontaneous contractions by day 8 of differentiation, with approximately 78% of microspheres contracting by day 10 (n = 90 microspheres). Differentiation efficiency on day 10 was consistently high between batches with approximately 75% total CMs (75.1 ± 6.7 %

cTnT+, 75.2 ± 7.1 % MF20+, n = 16 individual batches, Figure 2.3A); this corresponds to efficiency previously achieved with our differentiation protocol (P. Kerscher, Turnbull, et al. 2016) and hiPSC lines using 2D sheet differentiation (Lian et al. 2012) and is significantly higher than self-aggregated EBs using the same protocol (20.8 ± 19.3 % cTnT+). Further examination showed 3.3 ± 2.9% of the cells were positive for fibroblast marker, TE-7, 7.36 ± 5.75% were positive for cardiac fibroblast marker, PDGFRα, and 10.3 ± 2.7% were positive for smooth muscle marker, MYL11 (Figure 2.3B); this indicates that the non-CM cell population was comprised mostly of fibroblasts and smooth muscle cells, similar to previously published work using this differentiation protocol (Shadrin et al. 2017). Following differentiation, 5.8 ± 1.2 million CMs were obtained per batch yielding 2.0 ± 0.34 CMs per encapsulated hiPSC on day -3; although comparable cell numbers were obtained per batch in the EBs on day 10 (6.3 ± 1.4 million cells), only 1.4 ± 1.3 million of those cells were CMs, due in part to the large variability in differentiation efficiency. EB differentiation yielded 1.4 ± 1.3 CMs per hiPSC with larger variability than in the engineered cardiac tissue microspheres. The cell population was maintained through at least day 20, with 71.6 ± 8.4% CMs, 7.1 ± 1.7% proliferative CMs (cTnT+/Ki67+), and 8.41 ± 6.5% of the cells positive for P4HB, a fibroblast marker (n = 3 individual batches). Cell density increased during cardiac differentiation from day 0 (initiation of differentiation, Figure 2.1G) through day 12 (Figure 2.3C). CM distribution and morphology in both whole microspheres and sections was observed through immunostaining for cardiac markers, cardiac troponin T (cTnT) and α-sarcomeric actinin (αSA), and functional protein Cx43 (Figure 2.3C, I–K). Sarcomere alignment and

organization increased with progressing culture time, and engineered cardiac microspheres expressed gap junction protein, Cx43 (Figure 2.3I–K).

Microspheres displayed appropriate temporal expression of initially pluripotent and then later cardiac genes, which was quantified using RT-qPCR (primer sequences can be found in Table 2.1). During cardiac differentiation, an expected decrease occurred in the expression of pluripotency gene, OCT4 (Figure 2.3D). Expression of MLC2v, a ventricular CM gene, and βMHC, a cardiac gene, significantly increased from day 10 to day 30 (Figure 2.3E, G). These results, along with an increase in the ratio of βMHC/αMHC expression from day 10 to day 30, are consistent with expression patterns during CM development and maturation. Expression of αMHC increased from day 10 to day 20 and then decreased from day 20 to 30 (Figure 2.3F). Additionally, days 10, 20, and 30 cardiac microspheres had similar expression of functional gap junction protein Cx43 (Figure 2.3H).

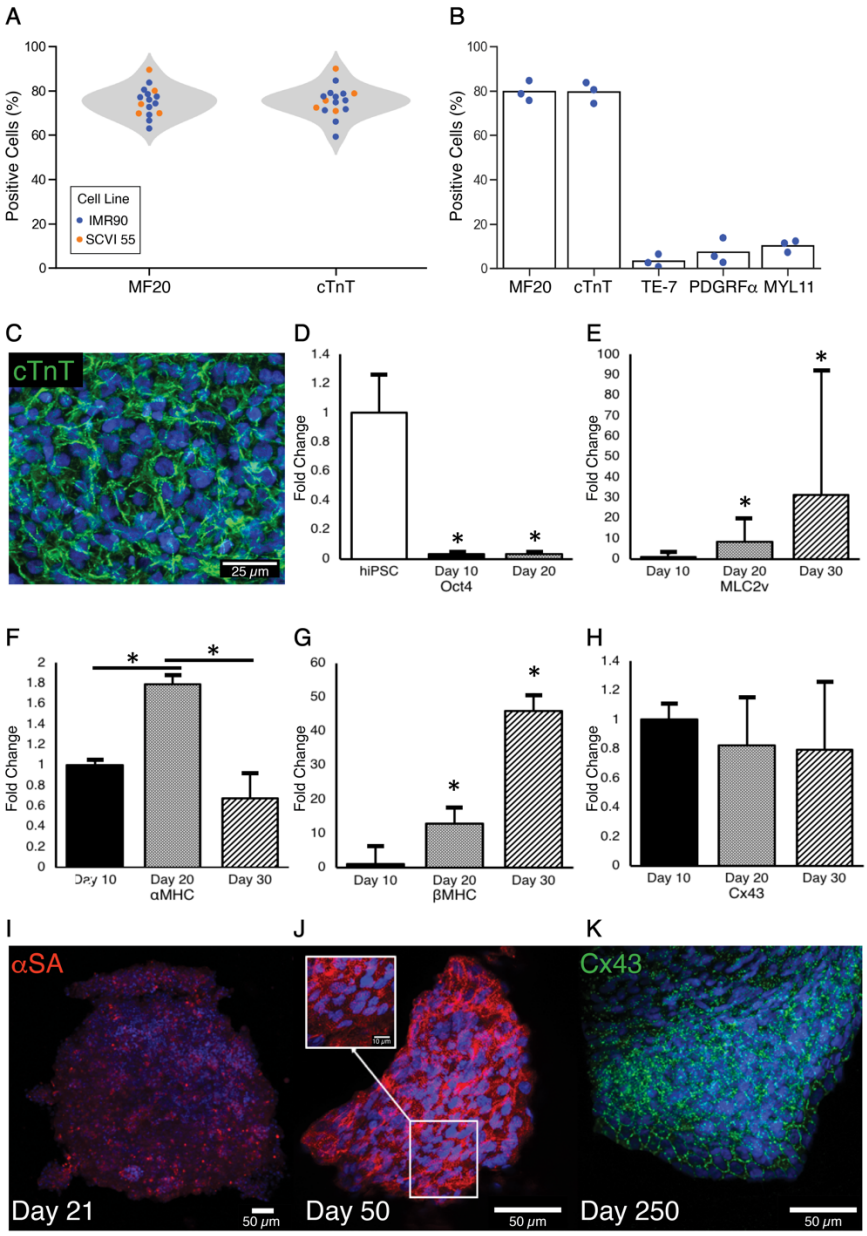

Figure 2.3 3D cardiac microsphere differentiation enabled high CM yield and reproducibility between batches with appropriate gene expression.

(A) For two different cell lines, IMR90 and SCVI55, 75.2 ± 7.1% and 75.1 ± 6.7% were positive for cardiac markers, MF20 and cTnT, respectively, on day 10 (n = 16 individual batches). Each dot represents an individual batch. (B) Additional cells were primarily fibroblasts and smooth muscle cells, with 3.3 ± 2.9% positive for fibroblast marker, TE-7,

7.36 ± 5.75% positive for cardiac fibroblast marker, PDGFRα, and 10.3 ± 2.7% positive for smooth muscle marker, MYL11. (C) CM morphology and distribution on the surface of a microsphere visualized by positive expression of cTnT (green) and Hoechst (blue) on day 12. (D–H) The resulting engineered cardiac microspheres exhibited appropriate temporal changes in gene expression, including a decrease in pluripotency gene, Oct4, as well as appropriate changes in cardiac genes MLC2v, αMHC, and βMHC. The expression of functional protein Cx43 remained constant between day 10 and day 30. (n = 3 biological replicates in duplicate, *$p < 0.05$) (I–J) From day 21 to day 50, the sarcomeres become more aligned, a feature of maturing CMs, shown by positive expression of αSA (red) and Hoechst (blue) within cryosections. (K) Cardiac tissue microspheres express the gap junction protein Cx43 (green, day 250) with nuclei labeled (blue).

Engineered cardiac microspheres showed dynamic remodeling of their PEG-fibrinogen microenvironment

With progressing culture time, encapsulated cells completely remodeled their PEG-fibrinogen microenvironment and differentiated into maturing cardiac tissues. Examining sequential cryosections from microspheres in culture for over a year, cardiomyocytes were present throughout the entire cardiac tissue microsphere, based on positive αSA expression; representative sections from the middle of the microsphere are shown in Figure 2.4A–C. ECT microspheres secreted extracellular matrix (ECM), including an increase in collagen deposition from day 28 (Figure 2.4D) to day 98 (Figure 2.4E) throughout the microsphere and around the edge as visualized by Masson's trichrome staining on cardiac microsphere sections (Figure 2.4D–E). Some sections of the cardiac microspheres

contained cells with highly organized structure and alignment, reminiscent of native cardiac tissue structure (Figure 2.4F). Scanning electron microscopy (SEM) of microspheres showed a smooth cell-based surface (Figure 2.4G), demonstrating cellular remodeling of the matrix during cardiac differentiation. At higher magnification, tightlyconnected cells and ECM deposition were observed on the microsphere surface (Figure 2.4H). Day 120 microspheres showed aligned cells (Figure 2.4H) on the microsphere surface, with neighboring cells forming cell-cell junctions (Figure 2.4I). Additionally, day 60 microspheres appeared to have aligned myofibril arrangement (Figure 2.4J), similar to SEM images of native human heart tissue (Figure 2.4K) (Saunders and Amoroso 2010). Understanding CM functionality and maturity on both a tissue and single-cell level is often desired. Engineered cardiac microspheres can be dissociated into single CMs, with CMs spontaneously contracting after dissociation. CMs attached to unpatterned PDMS surfaces with elongated cell morphology, which is normal for maturing CMs (P. Kerscher, Turnbull, et al. 2016). Dissociated, plated CMs displayed defined sarcomere structures with internal alignment and length of 1.85 μm (Figure 2.4L) which falls between the range for fetal (1.8 μm) and adult (2.0–2.2 μm) CMs, and is greater than typical hPSC-CMs (1.6–1.7 μm); an organized sarcomere arrangement improves the mechanical contractile output and is indicative of cardiomyocyte maturation (Feric and Radisic 2016a).

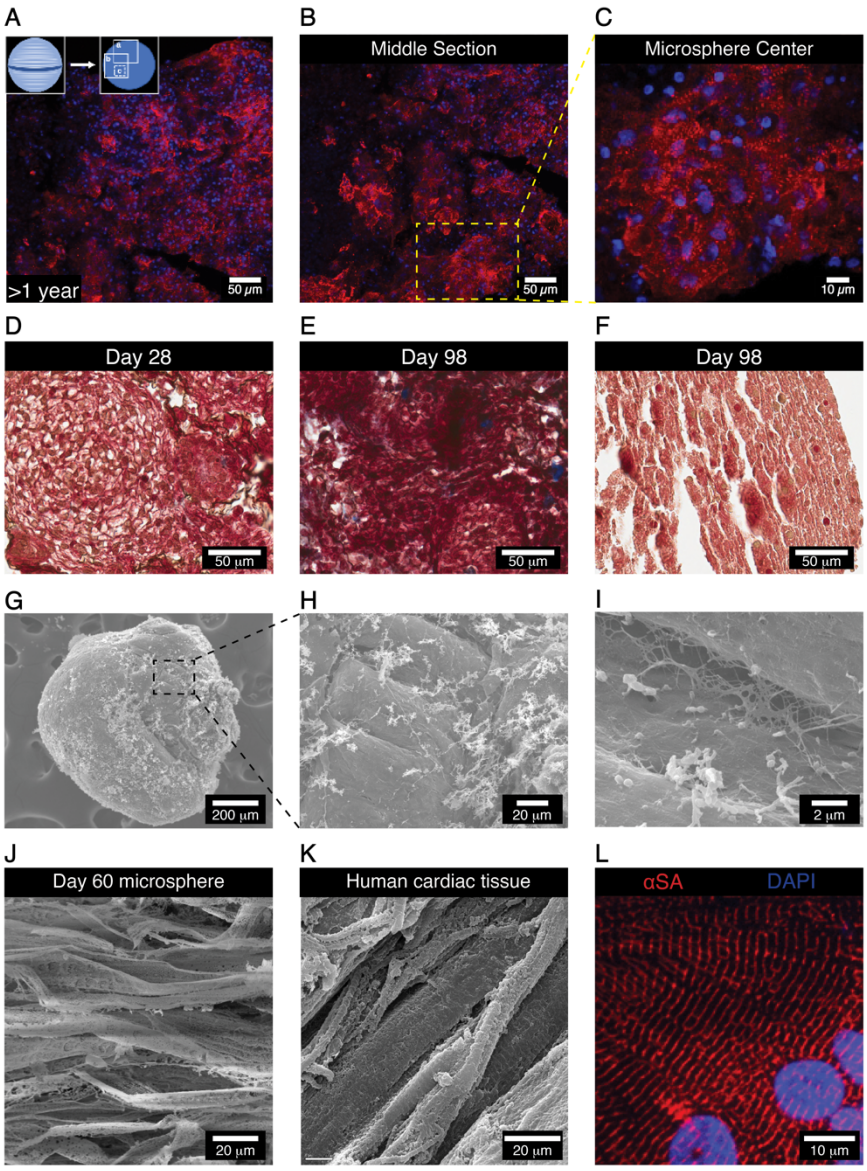

Figure 2.4 Engineered cardiac tissue microspheres displayed features of maturing cells.

Cardiac tissue microspheres were maintained long-term in culture. (A–C) A representative cryosection from the middle of the microsphere showing that cardiac differentiation occurred throughout the entire engineered cardiac microsphere volume (cardiac marker αSA (red), nuclei Hoechst (blue)). (D–F) As visualized by Masson's trichrome staining, CMs remodeled their microenvironment and deposited ECM; an increasing amount of

collagen (blue) was detected during culture time with minimal collagen detected on (D) day 28 with increasing collagen deposition by (E) day 98. (F) ECT microsphere sections on day 98 contained areas of cell alignment and organization similar to native cardiac tissue. Scanning electron microscopy (SEM) images show (G) the cells remodeled their PEG-fibrinogen microenvironment to form dense cardiac tissue microspheres with (H) aligned cells along the edge and ECM deposition on the microsphere surface. (I) At higher magnification, junctions between two adjoining cells could be visualized. (J) Myofibril structure was observed on the edge of day 60 microspheres, similar to (K) human cardiac tissue samples (Saunders and Amoroso 2010) (Figure reprinted with permission). (L) Dissociated CMs show highly aligned sarcomeres (red) indicating progression of CM maturation, as visualized by positive αSA expression.

Microsphere CMs responded to drug treatment and electrical stimuli

For the successful translation of engineered cardiac tissues towards regenerative medicine and drug-screening applications, the appropriate response to pharmacological and electrical stimuli is essential. Response to these stimuli indicates functionality and maturity of the resulting CMs. Using a multielectrode array (MEA) (Figure 2.5A–C), we evaluated the response of our day 20 engineered cardiac microspheres to pharmacologic stimuli including the β-adrenergic agonist, isoproterenol, and the β-adrenergic antagonist, propranolol. Isoproterenol increases the frequency of contraction, while the subsequent addition of propranolol slowed down the rate of contraction (Figure 2.5B). In addition to drug-testing, we also investigated the response of engineered cardiac microspheres to electrical pacing. Day 50 microsphere CMs exhibited 1:1 capture up to 6.0 Hz when paced

on the MEA (Figure 2.5C). Ion exchange of calcium, sodium, and potassium through the CMs is responsible for the contractile motion of these cells; a key difference between fetal and adult CMs is the rate at which ions are transported throughout the CMs. The calcium transients through plated engineered cardiac tissue microspheres were visualized using an optical mapping platform in which a calcium dye, Rhod-2, was employed to quantify the calcium transient duration (CTD). The CTD at 50% and 80% repolarization for these engineered cardiac tissue microspheres was 450 ms and 680 ms for samples paced at 1 Hz (n = 2 recordings) and 380 ms and 500 ms at 1.5 Hz, respectively (n = 3 recordings, Figure 2.5D). Contraction analysis was performed using a custom MATLAB script (Huebsch et al. 2015) in which videos were converted into a set of tiff files for macroblock tracing to detect the frequency of contraction as well as the contraction and relaxation velocities. Microspheres contracted at a frequency of 16.6 ± 5.9, 13.8 ± 2.3, and 25.6 ±1 0.8 beats per minute on days 20, 30, and 60 respectively ($n \geq 11$, Figure 2.5E). The contraction and relaxation velocities were 110 ± 49, 161 ± 69, and 175 ± 112 μm s^{-1} on days 20, 30, and 60 with relaxation velocities of 70 ± 36, 106 ± 42, and 146 ± 88 μm s^{-1}, respectively ($n \geq 11$, Figure 2.5F); a representative trace can be seen in Figure 2.5G. Appropriate response to drug treatment and electrical pacing, both on the MEA and in an optical mapping platform, along with increasing contraction and relaxation velocities indicate functionality of the resulting CMs within the engineered cardiac tissue microspheres.

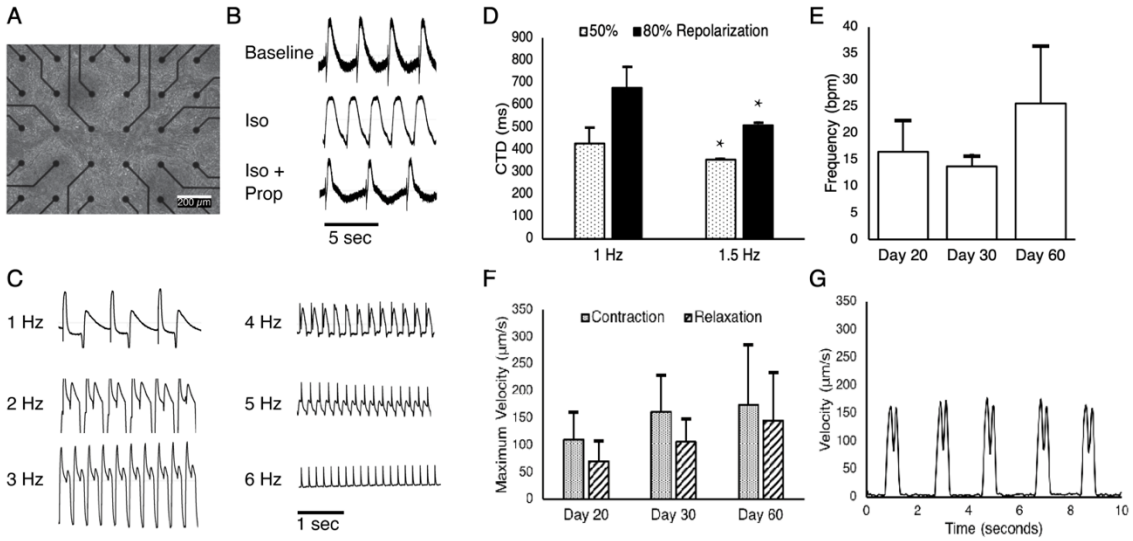

Figure 2.5 Microsphere CMs responded to pharmacological and electrical stimuli indicating functionality.

(A–C) Microspheres were dissociated and plated on the MEA. (B) Day 20 CMs responded to β-adrenergic agonist, isoproterenol (Iso), increasing the contraction rate. The subsequent addition of propranolol (Prop), a β-adrenergic antagonist, reversed the initial increase in contraction rate caused by isoproterenol. (C) In addition to appropriate response to drug treatment, day 50 microsphere CMs showed 1:1 capture in response to exogenous pacing frequencies up to 6.0 Hz. (D) Optical mapping was used to visualize calcium transients in plated cardiac microspheres tissues (day 74); recordings showed an expected decrease in calcium transient duration (CTD) with increased frequency of electrical pacing (n = minimum 3200 locations, *$p < 0.05$). The CTD was 430 ms and 350 ms for 50% repolarization and 680 ms and 500 ms at 80% repolarization for 1 Hz and 1.5 Hz pacing, respectively. (E) Analysis of engineered cardiac microsphere tissues showed a contraction rate of 16.6 ± 5.9, 13.8 ± 2.3, and 25.6 ± 10.8 beats per minute on days 20, 30, and 60, respectively (n = minimum 11 per condition). (F) Cardiac microsphere contraction

velocities were 110 ± 49, 161 ± 69, and 175 ± 112 μm/s on days 20, 30, and 60 with relaxation velocities of 70 ± 36, 106 ± 42, and 146 ± 88 μm/s, respectively; a representative trace is shown in (G) (n = minimum 11 samples per condition).

Discussion

High-throughput production of 3D cardiac tissues is necessary for applications in drug-testing and clinical translation of regenerative therapies. Engineered cardiac tissue production must be reproducible, cost-effective, and scalable to become a viable treatment option for cardiovascular disease. Building on spherical CM production using self-aggregated EBs, here the ability to produce spheroidal tissues for hiPSC differentiation while simultaneously controlling the cellular microenvironment and tissue geometry through the incorporation of a cellular responsive biomaterial, PEG-fibrinogen is shown. A custom microfluidic system has been implemented to rapidly encapsulate approximately 420,000 cells per minute, forming highly uniform hiPSC microspheres for direct differentiation into functional engineered cardiac tissue microspheres.

Following encapsulation using this microfluidic system, hiPSCs were evenly distributed throughout the PEG-fibrinogen microspheres and maintained high viability; cell density within the constructs began to increase shortly after encapsulation based on visual observation and metabolic activity analysis. Cell proliferation was observed throughout the time course of cardiac differentiation with cells initially filling the original hydrogel construct and then continuing beyond, resulting in tissue growth and a decrease in roundness of the tissues. Spontaneous contractions consistently started by day 8 of differentiation, and engineered cardiac tissue microspheres were composed of over 75%

CMs on day 20, achieving similar efficiency to small molecule 2D monolayer differentiations using the same hiPSC lines and differentiation protocol (Lian et al. 2013b). Contraction and relaxation velocities increased over time and microsphere CMs responded appropriately to pharmacologic stimuli, including β-agonist, isoproterenol, and β-antagonist, propranolol. Furthermore, engineered cardiac microspheres exhibited 1:1 capture for external pacing up to 6.0 Hz. During culture, proliferating and differentiating cells remodeled their provided PEG-fibrinogen microenvironment while depositing their own ECM proteins. Results demonstrate hiPSC differentiation, cardiac tissue formation, and electromechanical function of microsphere CMs, making this a promising cardiac tissue model for cell-therapy and drug-testing.

Production of spherical cardiac tissue structures has been studied for years, starting with self-aggregated EBs (Kehat et al. 2001), the initial stem cell differentiation approach to form spontaneously contracting CMs. Successful EB cardiac differentiation relies on EB size and intercellular interactions; however, due to inherent variability in these processes, low CM differentiation efficiency and poor reproducibility can result (Bratt-Leal, Carpenedo, and McDevitt 2009). To improve control, microwell plates (Pettinato, Wen, and Zhang 2014; Branco et al. 2019), centrifugation (E.S. Ng et al. 2005; Ungrin et al. 2008), hanging droplet formation (Beauchamp et al. 2015), and vortexing (Pradhan et al. 2017) have been used for production of more uniform cell-laden spheroids. However, these modified methods can be tedious, relatively low-throughput, and/or have a high potential for variability and low reproducibility between laboratories. Recent work in large-scale production of CMs has demonstrated that the formation of pluripotent stem cell aggregates from a single-cell suspension can be controlled by bioreactor culture system operating

parameters (H. Kempf et al. 2014). This has proven successful for large-scale production of CMs, although optimization is still needed to obtain consistency in terms of CM yield and differentiation efficiency. In all cases, post-differentiation processing, consisting of CM dissociation and encapsulation within a biomaterial scaffold, is typically required to obtain a functional 3D engineered tissue.

By directly differentiating the hiPSCs within the PEG-fibrinogen matrix, the need for this post-differentiation processing can be overcome using a single cell-handling step for the formation of engineered tissues cardiac microsphere. PEG-fibrinogen is a hybrid biomaterial that is currently undergoing clinical trials for the repair of cartilage tissue (Trattnig et al. 2015). The use of biomaterials in cell and tissue production offers an additional tool to overcome challenges inherent to self-aggregated hiPSC EB formation and cardiac differentiation and maturation. Biomaterials can be employed not only to provide a controlled 3D supporting microenvironment (Jing, Parikh, and Tzanakakis 2010), such as for a cardiac patch (Shadrin et al. 2017; Madden et al. 2010), but also to protect encapsulated cells from shear in bioreactor culture or during injection (D.A. Dunn, Hodge, and Lipke 2014; Seeto et al. 2017; Tulloch et al. 2011; Reis et al. 2016; Habib et al. 2011). Biomaterials can be used to manipulate multiple aspects of the cellular microenvironment including: guiding cell-cell and cell-material interactions through inclusion of cell adhesion and degradation sites, controlling cell density and engineered tissue size and shape, and recapitulating mechanical and biological cues present in the *in vivo* systems of interest (Shao, Sang, and Fu 2015; Guyette et al. 2016; Bratt-Leal et al. 2011). Previous studies show biomaterials can promote consistency and drive CM phenotypical and functional maturation using nitric oxide (A. J. Hodge, Zhong, and Lipke

2016), electrically conductive materials (Spearman et al. 2015; Shin et al. 2013; Paul et al. 2014), patterning and topography (D.H. Kim, Lipke, et al. 2010; Sugiura et al. 2016), and mechanical and electrical stimulation (Nunes et al. 2013; Ronaldson-Bouchard et al. 2018). We take advantage of material cues to provide uniformity to the initial stem cell microenvironment, support CM differentiation, and push CM maturity.

Recapitulating embryonic and fetal cardiac properties has been previously shown to be effective in driving cardiac tissue formation and maturation, particularly with regard to electrical stimulation (Nunes et al. 2013). Prior studies have shown that 2D substrates with similar stiffness to the native adult heart (10 kPa) are beneficial to enhancing CM function and maturation following cardiac differentiation (Young and Engler 2011; Hazeltine et al. 2014). Developing cardiac tissues are much softer; the stiffness of chick embryo hearts increases 9-fold, from 900 Pa to 8.2 kPa, between 36 to 408 hours post-fertilization (Young and Engler 2011). However, prior to germ layer specification during gastrulation, embryos are much softer than either the adult heart or developing cardiac tissues with elastic moduli reported as low as 5 Pa for frog embryonic tissue (Davidson and Keller 2007); therefore, we hypothesize that a softer microenvironment, similar to that of an embryo, is critical for success of cardiac differentiation of hiPSCs within a biomaterial scaffold. Our results here demonstrating successful differentiation of CMs from hiPSCs within a PEG-fibrinogen matrix, as well as in our previous study within GelMA (Petra Kerscher, Kaczmarek, et al. 2016), support further investigation of this relationship; in both cases, constructs with a low initial elastic modulus (less than 250 Pa) supported efficient cardiac tissue formation.

For engineered cardiac tissues to be useful for downstream applications such as regenerative medicine or drug screening, they must reasonably mimic the adult cardiac electrophysiology. Engineered cardiac tissues have potential to make an immediate impact on the improving preclinical testing of new drug candidates; current methods of preclinical testing rely on *in vitro* assays using oversimplified immortalized cell lines and *in vivo* small animal testing platforms. These do not reliably mimic human electrophysiology or accurately predict cardiotoxicity of newly developed drugs on the adult heart, resulting in large numbers of Phase I clinical trial failures and post-approval drug withdrawals from the market (Ferri et al. 2013). The ability to recapitulate adult cardiac electrophysiology and accurately predict cardiotoxicity *in vitro* would provide measurable cost and time saving benefits to the pharmaceutical industry (Fermini, Coyne, and Coyne 2018). In this study, the engineered cardiac tissue microspheres appropriately responded to exogeneous pacing up to 6 Hz and drug testing with β-adrenergic agonist, isoproterenol, and the β-adrenergic antagonist, propranolol. Furthermore, optical mapping showed an expected decrease in CTD with increased frequency of electrical pacing. The engineered cardiac microspheres maintained their spontaneous contractile phenotype in culture with velocity of contraction trending upward over time. These results show appropriate response to external stimuli, displaying features of maturing CMs and potential for use in *in vivo* studies for regenerative medicine and drug-testing. Our tissues do not fully recapitulate the mature adult CM phenotype; however, they fall within the range of other hiPSC-CM platforms (Burridge et al. 2011; Feric and Radisic 2016a; Pioner et al. 2019), and further maturation may be achieved using external mechanical or electrical stimulation.

Once large quantities of CMs are produced for cell therapy, the engineered cardiac tissue must be successfully delivered and engraft to the infarcted myocardium, which has proven challenging; research has shown that direct injection of cardiac microtissues to the myocardium results in better CM retention and engraftment than delivery through intracoronary or intravenous injections or using an epicardial tissue patch (Don and Murry 2013; Gerbin et al. 2015). Pre-clinical studies infusing or transplanting hPSC-CMs (Carpenter et al. 2012; Chong et al. 2014; Lundy et al. 2014) into the heart have shown cell-therapy can increase cardiac function; although mechanisms for these observed improvements are not yet fully understood, electrical coupling and engraftment, as well as paracrine signaling, are thought to be involved (Laflamme et al. 2007; Mirotsou et al. 2011; Hodgkinson et al. 2016). PSC-derived cardiac progenitor cells (Blin et al. 2010) or hPSC-CMs (Chong et al. 2014) have successfully been used alone and in combination with fibrin (Bellamy et al. 2015) or collagen (Joanne et al. 2016) for small animal models and non-human primate trials. A human clinical trial using hPSC-derived cardiovascular progenitors has been initiated (Menasche et al. 2018); Dr. Menasche provides a detailed review on previous and ongoing cell therapy trials (Menasche 2018). The microfluidic cell encapsulation system employed here has been previously used to encapsulate cells for injectable cell delivery in large animal pre-clinical wound healing studies (Seeto et al. 2017). The engineered cardiac tissue microspheres produced using the microfluidic encapsulation system and differentiation method established in this study hold promise for use in injectable cardiac cell therapy. Current studies are ongoing to increase efficiency of cardiac differentiation and clinical relevance through adaption of xeno-free cell production methods (Burridge et al. 2014).

Uniform and precise 3D cell-material constructs can now be produced by emerging technologies including bioprinting (El-Kirat-Chatel et al. 2015; Kang et al. 2016; Ouyang et al. 2015; Y. Ma, Ji, et al. 2015) and microfluidic systems (Seeto et al. 2017; Chan, Zhang, and Leong 2016; X. Zhao et al. 2016; Jiang et al. 2017). The custom microfluidic system presented here can be used for scalable microsphere production that provides a reproducible 3D microenvironment while leveraging an EB-like differentiation approach. Currently in the field of tissue engineering, hydrogel-based microsphere size is limited to 100–200 μm (Chan, Zhang, and Leong 2016; X. Zhao et al. 2016) due to standard soft-lithography fabrication techniques (Rossow, Lienemann, and Mooney 2017); microspheres with larger diameters are often more difficult to produce with high uniformity and roundness. Stability constraints typically limit microfluidic systems to single cell encapsulation, and do not support encapsulation of small cell clusters, such as the post-dissociation hiPSCs employed here (Seeto et al. 2019). Testing has shown hiPSCs are sensitive to suspension in oil; therefore, the limiting light and oil exposure time were key factors during system design. In-line photocrosslinking and washing were critical for system success and maintaining cell viability, as compared to batch photocrosslinking (Chang et al. 2020b). Recently published work from our group showed successful hiPSC encapsulation and differentiation within PEG-fibrinogen and GelMA hydrogels to produce 3D-dhECT microislands (P. Kerscher, Turnbull, et al. 2016; Petra Kerscher, Kaczmarek, et al. 2016). In these studies, a 1 mm wide ring of dense cardiac tissue consistently formed around the edge of the microislands. Based on this finding, the desired initial microsphere diameter was chosen to be approximately 1 mm, and thus the resulting sphere diameter using our microfluidic system was 908 μm (n = 485 microspheres, 8 individual batches);

however, this microfluidic system enables modulation of size and shape, as well as initial cell seeding density. The tight control demonstrated here over size and shape of microsphere tissues both within a batch and between batches is critical for cell production and downstream applications.

In this study, a custom microfluidic system to rapidly encapsulate hiPSCs within a clinically relevant biomaterial, PEG-fibrinogen, was utilized to produce uniform microspheres in size and shape with high cell viability and maintained proliferative and pluripotent phenotype. Remodeling their PEG-fibrinogen microenvironment, these hiPSC microspheres were subsequently differentiated into functional engineered cardiac tissue microspheres with high CM yield that responded appropriately to outside electrical and pharmacological stimuli and could be maintained in culture long-term with maintenance of spontaneous contraction (over 3 years). The microspheres were cultured in static suspension conditions; however, a bioreactor or similar dynamic culture system could be used to improve mass transfer and scale-up production (H. Kempf et al. 2014). This microfluidic system has the potential to be leveraged in combination with a bioreactor system for scalable hiPSC differentiation by parallelization of PDMS devices for increased production in order to obtain commercially relevant numbers of engineered cardiac tissues for clinical translation and high-throughput drug testing applications.

Chapter 3: Towards Clinically Relevant Production of Engineered Cardiac Tissue Microspheres

Introduction

Following a myocardial infarct, as many as 1 billion cardiomyocytes (CMs) can die as a result of necrosis caused by impaired blood flow; these CMs cannot regenerate, resulting in scar tissue formation and loss of function following damage. There are currently no clinically available treatments for restoring CM function following disease or damage, leading to increased risk for further complications and other severe cardiac events. However, regenerative medicine, particularly through the use of cell therapy and engineered cardiac tissue (ECT) products differentiated from pluripotent stem cells (PSCs), has shown promise for the regeneration of function in the myocardium (Shiba et al. 2016). However, it has been estimated that billions of cells will be needed for each treatment to restore function in the myocardium, resulting in the need for large scale production of CMs (Robert Zweigerdt et al. 2011). In order for cell therapy to be a clinically approved treatment option, the production of cardiac tissue must be scalable, cost-effective, and able to be manufactured in a good manufacturing practices (GMP) setting. A key component in GMP production of cell and tissue products for regulatory approval requires that the culture of the cells occur in "xeno-free" conditions, employing chemically defined products without animal or human components.

Traditional methods for production of pluripotent stem cell-derived cardiomyocytes (PSC-CMs) utilize two-dimensional cell monolayers or self-aggregated embryoid bodies, both of which typically require further downstream processing for ECT

formation and to optimize functionality and maturation of cardiomyocytes. Monolayer technologies do not permit a feasible, cost-effective solution for scalable production of engineered tissues; therefore, bioreactors must be leveraged for large-scale production of CMs and cardiac tissues. Bioreactors are well-established for bacterial production and other cells in the production of products such as proteins and antibodies (Chu and Robinson 2001). Multiple types of bioreactors are currently being investigated for the production of cell and tissue products, including stirred-tank, perfusion, wave, and packed-bed bioreactors (Portner et al. 2005). Stirred tanks, or spinner flasks, are the most common type of bioreactor due to their ability for homogeneous mixing and distribution of nutrients and oxygen, and a spherical geometry for cell and tissue products is most conducive for utilization in these bioreactor systems. Current studies for the expansion of hiPSCs and cardiac differentiation in large-scale involve the formation of self-aggregated EBs in stirred-tank bioreactors (H. Kempf et al. 2014; H. Kempf et al. 2015; Chen et al. 2015; Fonoudi et al. 2015).

Formation of spheroidal tissues can be done either by self-aggregation, as hanging droplets (Beauchamp et al. 2015), vortexing (Chang et al. 2020a), through the aid of microcarriers (Ting et al. 2014; Laco et al. 2020), well plates (Branco et al. 2019), or incorporation within a biomaterial (Jing, Parikh, and Tzanakakis 2010). Self-aggregated EBs are formed by introducing a single cell suspension in either a stirred tank or shaker environment, and the shear stress of the spinning results in aggregate formation. Previously, Chen et al. investigated the differentiation of CMs in 125, 500, and 1000-mL spinner flasks and found a set of critical parameters including cell aggregate size, agitation rate, CHIR concentration, and IWP induction timing; however, the efficiency of

cardiomyocyte differentiation was found to be largely dependent on volume of reactor (Chen et al. 2015). The size and shape of the resulting EBs are hard to control, and it has been shown that the EB size can affect cardiac differentiation, with CM contents ranging from 26–90% in a bioreactor (H. Kempf et al. 2014). Microcarriers offer slightly more control over the size and shape of the microspheres but can still have a large degree of heterogeneity due to aggregation of the PSCs as well as attachment to the microcarriers. Furthermore, the microcarriers may have to be removed prior to clinical use (Kaitlin K. Dunn and Palecek 2018). Here, a direct differentiation platform was utilized, which includes encapsulation of the hiPSCs within a hybrid biomaterial, which provides cell adhesion sites and is enzymatically degradable, leveraging the ability for tight control of size and shape of tissue production.

Previously, our group established a platform for production of ECT microspheres directly differentiated from human induced pluripotent stem cells (hiPSCs), and this study demonstrates that this direct differentiation platform can be used to produce ECT microspheres in chemically defined conditions, both for hiPSC culture and cardiac differentiation. A custom-built microfluidic system was used to rapidly encapsulate hiPSCs in PEG-fibrinogen with tight control over initial microsphere size and shape. Efficient cardiac differentiation was achieved through continuous Wnt signaling with spontaneous contractions occurring by day 10; the resulting cardiomyocytes (CMs) responded appropriately to external pacing, indicating functionality. Furthermore, it is shown that hiPSC encapsulation in PEG-fibrinogen microspheres can produce a larger number of CMs per input hiPSC compared to the standard self-aggregated embryoid bodies (EBs). Taken

together, these results indicate that this platform has potential for scalable production of ECTs for clinical applications.

Materials and Methods

HiPSC expansion and maintenance

The hiPSC cell line, Un-Arc 16 Facs II (Shinnawi et al. 2015), was used for this study and graciously provided by Dr. Lior Gepstein at Technion — Israel Institute of Technology. HiPSCs were cultured on Geltrex (Gibco) with E8 media. E8 media was made with DMEM/F12 (Gibco) supplemented with ascorbic acid (64 mg/L, Sigma), sodium selenite (14 μg/L, Sigma), sodium bicarbonate (543 mg/L, Sigma), insulin (20 mg/L, Sigma), transferrin (10.7 mg/L, Sigma), basic fibroblast growth factor (100 μg/L, Peprotech), and transforming growth factor-beta (2 μg/L, Peprotech). The hiPSCs were passaged into single cells with Accutase (Innovative Cell Technologies). For one day after passaging, hiPSCs were maintained in E8 supplemented with rock inhibitor (5–10 μM, Y-27632, Stem Cell Technologies).

PEG-fibrinogen synthesis

All chemicals were purchased from Sigma-Aldrich unless specified otherwise. PEG-fibrinogen was prepared as previously described (Dikovsky, Bianco-Peled, and Seliktar 2006; P. Kerscher, Turnbull, et al. 2016). Briefly, bovine fibrinogen (300 mg) was dissolved in PBS with 8 M urea, and tris (2-carboxyethyl) phosphine hydrochloride (TCEP-HCl, 22.53 mg) was added to the fibrinogen solution (7 mg/mL). Next, PEGDA (1.9392 g) was reacted with fibrinogen (4:1 molar ratio) for 3 h, precipitated in acetone,

and dissolved in PBS with 8 M urea. The reacted PEG-fibrinogen was dialyzed against PBS at 4 ºC for 24 h. To characterize the PEGylated product, fibrinogen content was measured using Pierce BCA assay (Thermo Scientific).

HiPSC encapsulation using microfluidic system

PEG-fibrinogen precursor solution was prepared by combining PEG-fibrinogen with triethanolamine (1.5 v/v%, TEOA), N-vinyl pyrrolidone (0.39 v/v%, NVP), RI (12.5 μM) and Eosin Y (0.1 mM, Fisher Scientific) photoinitiator (in PBS). HiPSCs were resuspended in PEG-fibrinogen precursor solution at 30–60 million cells/mL. The PEG-fibrinogen-cell mixture was added to one inlet of a custom-built microfluidic device. In parallel, mineral oil was added to the other inlet of the microfluidic device which, when combined with the PEG-fibrinogen-cell mixture, causes the formation of spherical droplets. Flowrates for the PEG-fibrinogen-cell mixture and mineral oil were adjusted as previously described to maintain consistent crosslinking times and spherical geometry (Tian and Lipke 2020). A light source (Prior) was used for photocrosslinking the liquid PEG-fibrinogen-cell mixture to form cell-laden microspheres. Microspheres were collected by washing down with E8 media supplemented with 10 μM RI, removed from the oil phase and spent media and were cultured in E8 media + rock inhibitor (10 μM) for 24 h (day -3). Microspheres were then cultured for an additional 2 days in E8 media with daily media changes (days -2 and -1).

Diameter, axial ratio, and early growth quantification of microspheres and EBs

Phase contrast images of microspheres were taken from the time of encapsulation (day -3) through cardiac differentiation (day 10) using an Andor Luca S camera attached to a Nikon

Eclipse Ti microscope. Microsphere diameter and size of thirteen individual batches were determined after encapsulation and prior to initiation of cardiac differentiation. The autofluorescence of the photoinitiator Eosin Y in PEG-fibrinogen microspheres was captured using long acquisition times with the FITC filter on the Nikon Eclipse Ti fluorescence microscope at low magnification. EB size and shape were determined from daily phase contrast images. Standard plugins in ImageJ were used for quantification.

HiPSC viability and immunofluorescence staining

On day -2, the viability of the hiPSCs in PEG-fibrinogen microspheres was assessed using a LIVE/DEAD® viability kit (Invitrogen), and images were taken using a fluorescent microscope (Nikon). Dissociated CMs were immunostained α-sarcomeric actinin (αSA, Sigma Aldrich). For immunostaining, engineered cardiac tissue microspheres and EBs were dissociated using 1mg/mL Collagenase-b (Roche) and 0.05 mg/mL DNase in PBS for 10–30 minutes at 37 °C and were plated on Matrigel (Corning) coated coverslips for 2-4 days. The cells were rinsed with PBS and fixed in paraformaldehyde (4%, Electron Microscopy Sciences) for 20 min at room temperature (RT). Samples were rinsed with PBS and blocked with fetal bovine serum (FBS) (3%) overnight at 4 °C or 30 min at RT. Then, the dissociated CMs were incubated in the primary antibody (αSA) overnight at 4 °C or 1 h at RT followed by the addition of Alexa Fluor 488 or Alexa Fluor 568 secondary antibody. Nuclei were counterstained with Bisbenzimide Hoechst 3342 (MilliporeSigma). Samples were visualized using a Nikon A1R laser-scanning confocal microscope.

Cardiac Differentiation

Chemically defined cardiac differentiation media (CDM3) contained RPMI 1640 (Gibco) supplemented with 500 μg/mL recombinant human albumin (ScienCell) and 213 μg/mL ascorbic acid. To initiate cardiac differentiation on day 0, CHIR99021 (5–7.5 μM, STEMCELL Technologies), was added to the media; exactly 24 h later, the media was exchanged for CDM3 supplemented with 5 μM IWP2 (STEMCELL Technologies). Fresh CDM3 was added on days 3, 5, 7, and 10; following day 10, the ECTs were cultured with CDM3 or RPMI/B27 (Gibco) for selected batches, and the media was exchanged every 3–4 days.

Flow cytometry

On day 10, the engineered cardiac tissue microspheres and EBs were dissociated by incubation at 37 °C for 10–15 minutes with Collagenase-b (1 mg/mL, Roche) and DNase (0.05 mg/mL, Worthington) in PBS. After tissue dissociation, a cell pellet was collected through centrifugation. After washing with PBS, the cells were labeled with Zombie Dye (Biotium) for 30 min at 4 °C. Cells were then washed with Blocking Buffer (bovine serum albumin (1%, BSA, Sigma), fetal bovine serum (10%, FBS, Atlanta Biologics) in PBS), and then fixed with Foxp3 Transcription Factor Staining Buffer Set (eBioscience) overnight at 4 °C. The cells were filtered using a 40 μm cell strainer (Scienceware Flowmi) and permeabilized with FACS buffer (BSA (1%), FBS (10%) in 1x Permeabilization Buffer (eBioscience)) at RT for 30 mins. The primary antibodies (1:200, cTnT (Invitrogen) and MF20 (DSHB)) were then incubated with the cells for 1 h at RT. After incubation in the primary antibody, washing occurred with Permeabilization Buffer. The secondary

antibodies (1:300, AlexaFluor 647 goat anti-mouse IgG (ThermoFisher)) were added for 30 mins at RT. The cells were then washed with Permeabilization Buffer and resuspended in Blocking Buffer for analysis. A Beckman Coulter CytoFlex LX was used for sample analysis. At least 10,000 live cells were recorded for analysis. Anti-Mouse IgG1 isotype control (ThermoFisher) was used to ensure there was not any non-specific binding.

Contraction Analysis

Contraction analysis was done using motion tracking software in which macroblocks were tracked between frames to determine the beat rate in beats per minute (BPM), time interval in seconds, maximum contraction velocity in μm/s, and maximum relaxation velocity in μm/s. Videos of contractions, 10 s in length, were taken using an Andor Luca S camera attached to the microscope, converted to a series of tiff files, and imported into the Motion GUI in the open source MATLAB code (Huebsch et al. 2015).

Optical Mapping

Optical mapping recordings were taken using a high-speed camera (Andor iXon+ 860 EMCCD) attached to a fluorescent microscope (Nikon Eclipse Ti) with a Prior Lumen 200 light source. Voltage recordings of CMs were captured using the established optical mapping system in our lab. The hiPSC cell line used in this study has a green fluorescent voltage reporter that decreases in fluorescent intensity during membrane depolarization that can be visualized immediately prior to tissue contraction. The videos of voltage transients were taken using the FITC filter in either Tyrode's solution or media. Tyrode's solution was prepared by combining 1.8 mM calcium chloride and 5.0 mM glucose with

5.0 mM HEPES, 1.0 mM magnesium chloride, 5.4 mM potassium chloride, 135 mM sodium chloride, and 0.33 mM sodium phosphate; the pH was adjusted to 7.4 with sodium hydroxide. The samples were heated to 37 °C by perfusion of warm Tyrode's solution through the optical mapping system or through the use of a stage-top incubator (In Vivo Scientific) for non-destructive recordings in media or Tyrode's solution. When electrically paced, pacing starting at 0.5 Hz and continually increased by 0.5 Hz until 1:1 capture was no longer observed. Recordings were analyzed using a custom MATLAB script in which the change in fluorescence were used to calculate the action potential duration (APD) and conduction velocity.

Self-aggregated EB Formation and Differentiation

To form the EBs, a single cell suspension of hiPSCs in E8 with rock inhibitor (10 μM) was added to a shaker flask or a well plate containing E8 with rock inhibitor (10 μM). The shaker flask or well plate was placed on a shaker plate (Infors) at 70 rpm in a 5% CO_2 incubator to allow for self-aggregation. Prior to initiation of cardiac differentiation, daily media changes occurred in which one-half of the spent E8 was exchanged for fresh E8. On day 0, cardiac differentiation was initiated. For the shaker flask/plate platform, the cells were collected, counted, and distributed in 6-well plates for cardiac differentiation. To initiate differentiation in the shaker flask and well plate only platforms, the media was removed, and day 0 differentiation media was added. Cardiac differentiation followed the same protocol as the microspheres with 5 μM CHIR addition on day 0 and 5 μM IWP2 addition on day 1.

Statistical Analysis

Unless otherwise noted, statistical analysis was performed using Minitab statistical software where results are presented as mean ± standard deviation. One-way ANOVA was performed with Tukey's test for post-hoc analysis for samples with equal variance, and the Games-Howell test was performed for samples with unequal variances. A value of $p < 0.05$ was used for statistical significance.

Results and Discussion

To produce the engineered cardiac tissue microspheroids, hiPSCs were encapsulated in a clinically relevant material, PEG-fibrinogen, and photocrosslinked using a custom microfluidic system developed in our lab (Seeto et al. 2019) in which spheroid formation occurred through a modified water-in-oil emulsion technique (Figure 3.1B). Dissociated hiPSCs were combined with the polymer precursor solution in liquid form at high cell concentrations (30–60 million cells/mL) and were infused through a custom PDMS device opposite of mineral oil. The microspheres formed at the junction and traveled down the outlet channel for photocrosslinking. This microfluidic system was successfully used to encapsulate hiPSCs dissociated in both clusters and single cells. PEG-fibrinogen is currently undergoing clinical trials in Europe and in the United States for cartilage repair, making it a suitable choice in the transition to clinically relevant production of ECT microspheres (Trattnig et al. 2015). This microfluidic system has tight control over size and shape both within a batch and between batches, and through modulation of system parameters such as flow fraction and narrowing ratio, we can produce microspheres at a variety of sizes (Tian and Lipke 2020). Here, we show that we

can produce microspheres ranging from 400 to 800 μm in diameter (Figure 3.1C). The coefficient of variance (CV) within a batch was < 10% for all the batches (n = 13 batches, ≥ 82 microspheres per batch). Furthermore, the axial ratio (AR), ratio of axial diameter to radial diameter, was consistently 1.0 with an average of 1.04 ± 0.02 with a CV = 1.54% between batches; furthermore, the CV was < 5% for each batch (n = 13 batches, ≥ 82 microspheres per batch). Encapsulated hiPSCs maintained high cell viability (Figure 3.1H) and appropriate phenotype. The rounded morphology, indicative of hiPSC colony formation, can be visualized through labeling with Phalloidin (Figure 3.1J). The hiPSCs continued to proliferate and grow in the hydrogel microenvironment, visualized through labeling with proliferative marker, Ki67 (Figure 3.1K), and through daily phase contrast images (Figure 3.1F–G, Figure 3.2A) for three days prior to initiation of cardiac differentiation.

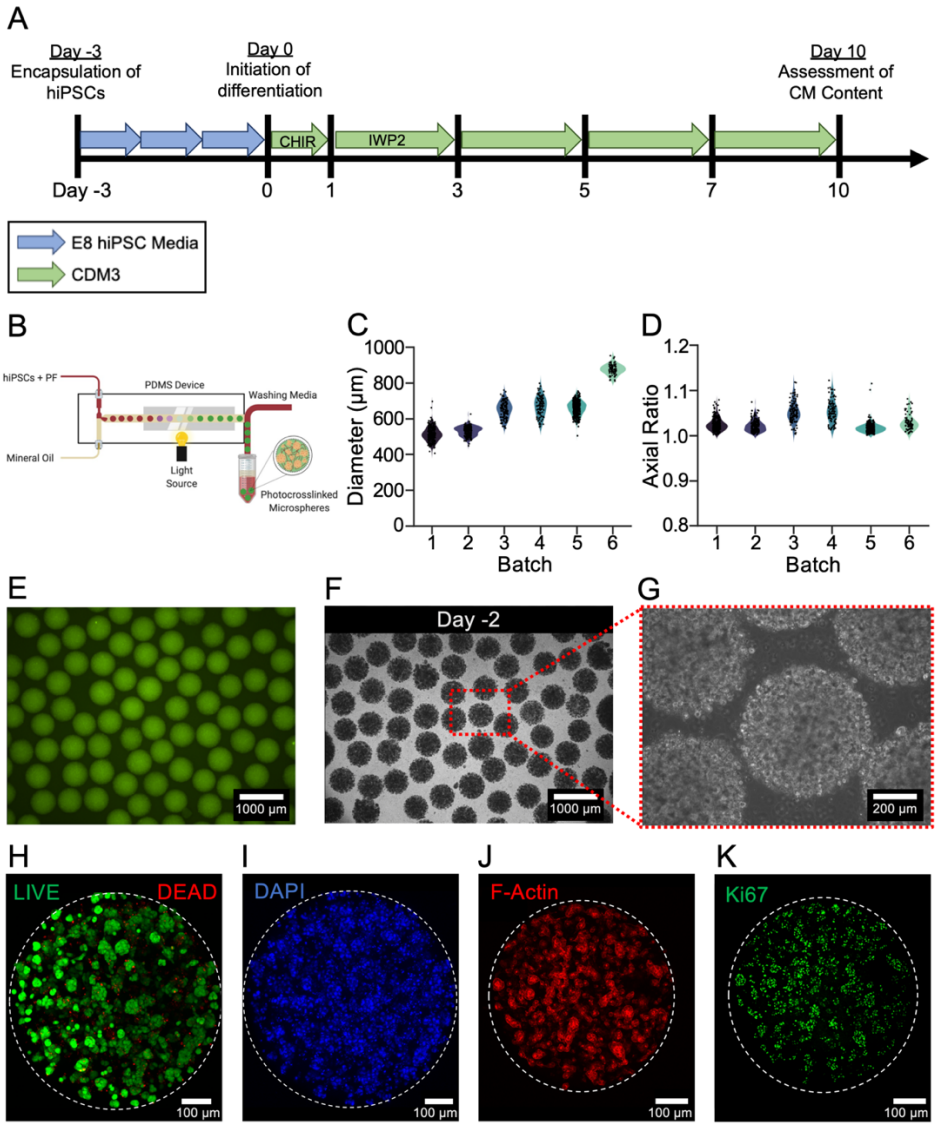

Figure 3.1 Production of engineered cardiac tissue microspheres in chemically defined conditions.

(A) For production of engineered cardiac tissue (ECT) microspheres, hiPSCs were encapsulated on day -3 with daily E8 media changes until day 0 when cardiac differentiation was initiated by the addition of CHIR in CDM3. On day 1, the media was exchanged and CDM3 supplemented with IWP2 was added to the microspheres for 48 h. The media was exchanged with fresh CDM3 on days 3, 5, and 7. On day 10, the CM content was determined using flow cytometry. (B) A custom-built microfluidic system was used

for hiPSC encapsulation in PEG-fibrinogen. Microspheres were formed at the junction of a PDMS device, the central component of the microfluidic system, through a water-in-oil emulsion and photocrosslinked using high intensity visible light. Microspheres were collected at the outlet for further experiments. (C) This microfluidic system can be used to produce microspheres with initial diameters of 400–800 μm (n = 31 batches). (D-G) The microspheres had an axial ratio of 1.04 ± 0.02 (n = 31 batches); furthermore, hiPSCs were encapsulated at a high cell density (30–60 million cells/mL precursor solution) and were highly uniform within a batch. (H–I) Following encapsulation, the hiPSCs maintained high cell viability and maintained the appropriate phenotype including (J) rounded colony formation and (K) expression of proliferative marker, Ki67. Figure created with biorender.com.

Advances in cardiac differentiation protocols have found that subsequent activation and inhibition of the Wnt signaling pathway through the use of small molecules can be used for highly efficient cardiac differentiation with a high degree of reproducibility (Lian et al. 2012). In this protocol, the Wnt pathway is activated by the presence of CHIR for 24 hours; after 24 hours (day 1), the CHIR is removed. 48 hours after the removal of CHIR (day 3), a Wnt inhibitor, IWP2, IWR1, or C-Wnt59, is added for 48 h (Lian et al. 2013b). This method involves the use of RPMI/B27 differentiation media, which is composed of RPMI media supplemented with L-glutamine that is combined with a B27 supplement. However, the B27 supplement is not chemically defined and is produced using 21 components, some of which are animal-derived. Burridge et al. systematically assessed the B27 components and found two critical components for cell viability and CM

differentiation: albumin and ascorbic acid (Burridge et al. 2014). Through the use of recombinant protein production, a fully defined differentiation protocol was developed using chemically defined differentiation media with three components (CDM3): RPMI 1640, ascorbic acid, and recombinant human albumin; in this protocol, the authors found that 48 h of CHIR supplementation immediately followed by 48 h of Wnt inhibition led to the highest percentage of CMs. Building on these protocols, Halloin et al. found that continuous Wnt control with early Wnt inhibition (day 1) was critical for the success of some hiPSC lines in CDM3 to differentiate to the cardiac lineage (Halloin et al. 2019). These results have been further expanded with the B27 differentiation showing that maintaining the Wnt pathway activation through a low dose of CHIR during the 48 h between the removal of the initial dose of CHIR and the addition of the Wnt inhibitor led to a more robust protocol in which both percentage and yield of CMs was increased for hiPSC lines derived from various origins (M. Zhao et al. 2019).

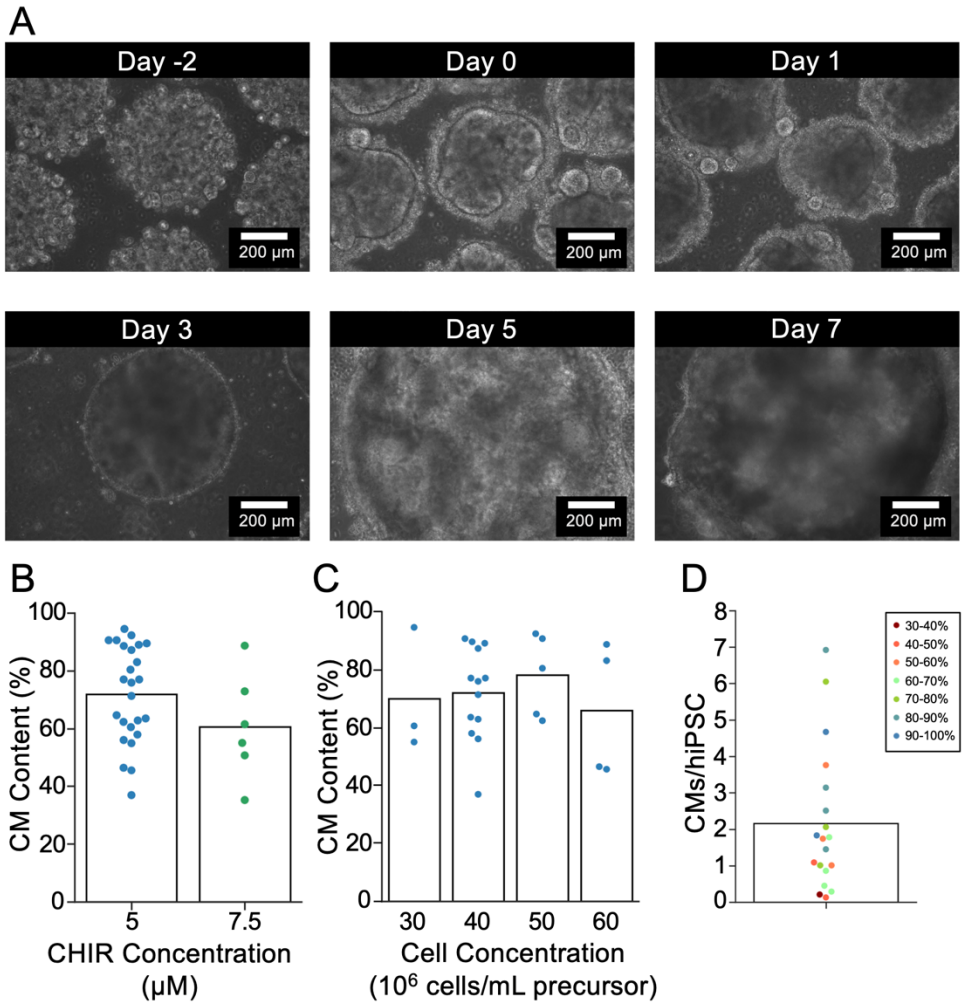

Figure 3.2. Engineered cardiac tissues with high CM content can be achieved with CDM3 differentiation.

(A) Throughout differentiation, the hiPSC colonies continued to increase in size and formed a dense, continuous tissue by day 7. (B) To initiate cardiac differentiation, a CHIR concentration of 5 or 7.5 µM was used, and the resulting CM content was 71.9 ± 16.8 and 60.7 ± 18.5% for 5 and 7.5 µM, respectively (n = 25, 6 batches). (C) A high cell density was critical for success of differentiation leading to a CM content of 70.0 ± 21.4, 71.9 ± 16.0, 78.0 ± 14.1, and 65.9 ± 23.1% CMs from ECT microspheres encapsulated at an initial cell density of 30, 40, 50, and 60 million cells/mL differentiated with 5 µM CHIR (n = 3,

13, 5, 4 batches, respectively). (D) After cardiac differentiation, the resulting number of CMs per input hiPSC was 2.23 ± 1.98, which was highly variable and influenced by CM content (the color of each data point is representative of CM content); however, as many as 6.9 CMs per hiPSC could be obtained (n = 19 batches).

Three days post-encapsulation, cardiac differentiation was initiated (day 0) using chemically defined media and the continuous Wnt control protocol established by Halloin et al. (Halloin et al. 2019). To initiate cardiac differentiation, a Wnt activator, CHIR, was supplemented in CDM3 at concentrations of 5 and 7.5 μM. Exactly 24 hours later (day 1), the media was exchanged and supplemented with 5 μM IWP2, a Wnt inhibitor, and microspheres were maintained in this media for 48 h. Cardiac specification continued to occur as the media was exchanged with fresh CDM3 on days 3, 5, and 7. On day 10, the efficiency of differentiation, or CM content (% CMs), was quantified using flow cytometry (Figure 3.1A). Cardiac differentiation successfully occurred using this chemically defined differentiation protocol with CM contents of 71.9 ± 16.8% and 60.7 ± 18.5% at 5 and 7.5 μM CHIR concentrations, respectively. Furthermore, a high initial cell density was critical for success in this differentiation platform. Initial cell densities from 30–60 million cells/mL could be used in this platform, resulting in CM contents of 70.0 ± 21.4, 71.9 ± 16.0, 78.0 ± 14.1, and 65.9 ± 23.1% for 30, 40, 50, and 60 million cells/mL, respectively for microspheres differentiated with 5 μM CHIR (Figure 3.1C, n = 3, 13, 5, 4 batches). Differentiation occurred similarly across these conditions with no statistically significant differences in CM content at these CHIR and initial cell concentrations. Using the CDM3 protocol, we can effectively get higher CM contents than we could using the RPMI/B27

differentiation protocol, as high as 95% CMs. However, there is a larger variability in the percentage, with some batches as low as 37%. For biomanufacturing and clinical translation, not only is the CM content important, but also the number of CMs, or yield. Using this differentiation platform, as many as 6.9 CMs per input hiPSC can be obtained; however, this result is highly variable with an average of 2.23 ± 1.98 CMs per hiPSC for 18 batches differentiated with 5 μM CHIR (Figure 3.1D). As expected, this is influenced by CM content on day 10 and cell loss prior to initiation of cardiac differentiation as well as throughout differentiation. Microspheres could not be maintained in CDM3 media long-term post-differentiation; therefore, the media was changed to RPMI/B27 with insulin on day 10 for long-term culture. This direct differentiation platform of ECTs could be utilized for efficient cardiac differentiation in chemically defined conditions; however, further classification of non-CM cell types along with increasing reproducibility between batches, particularly with regard to CM content and number of CMs per hiPSC will be needed for downstream applications.

ECT microspheres successfully differentiated into spontaneously contracting tissues using a chemically defined differentiation protocol with continuous Wnt pathway control. The onset of contraction started between day 7 and day 10. On day 10, the spontaneous contraction frequency was 46.6 ± 13.9 beats per minute (BPM) with a time interval of 0.267 ± 0.082 s (Figure 3.3A–B). The maximum contraction and relaxation velocities were 157 ± 42.3 and 120 ± 42.7 μm/s, respectively (Fig 3.3C–D, n = 5 batches). The resulting CMs from dissociated ECT microspheres showed the presence of well-defined sarcomeres forming with increased expression of gap junction protein, connexin 43 (Cx43), over time (Fig 3.3J–L). A genetically encoded voltage indicator (GEVI) was

used for optical mapping of the action potential (Fig 3.3E–F). Day 28 dissociated CMs in a monolayer could be electrically paced with 1:1 capture from 0.5 to 1.5 Hz. The spontaneous action potential at 50% and 80% repolarization was 349 ± 106 and 487 ± 113 ms, respectively, with a conduction velocity of 1.43 ± 0.19 cm/s (Figure 3.3G–I, n = 8 recordings). When electrically paced, the action potential duration (APD) at 50% repolarization decreased to 311 ± 16.0, 304 ± 6.8, and 283 ms and the APD at 80% repolarization decreased to 467 ± 15.6, 463 ± 5.1, and 430 ms for 0.5, 1.0, and 1.5 Hz electrical pacing, respectively (Fig 3.3G–H). Furthermore, the conduction velocity was 1.31 ± 0.08, 1.21 ± 0.06, and 0.86 cm/s for 0.5, 1.0, and 1.5 Hz paced samples (Fig 3.3I). Appropriate functional properties, including spontaneous contraction and response to electrical pacing, indicate appropriate functionality of the ECT microspheres; however, further assessment of functional properties will be needed to ensure the appropriate maturity for downstream applications.

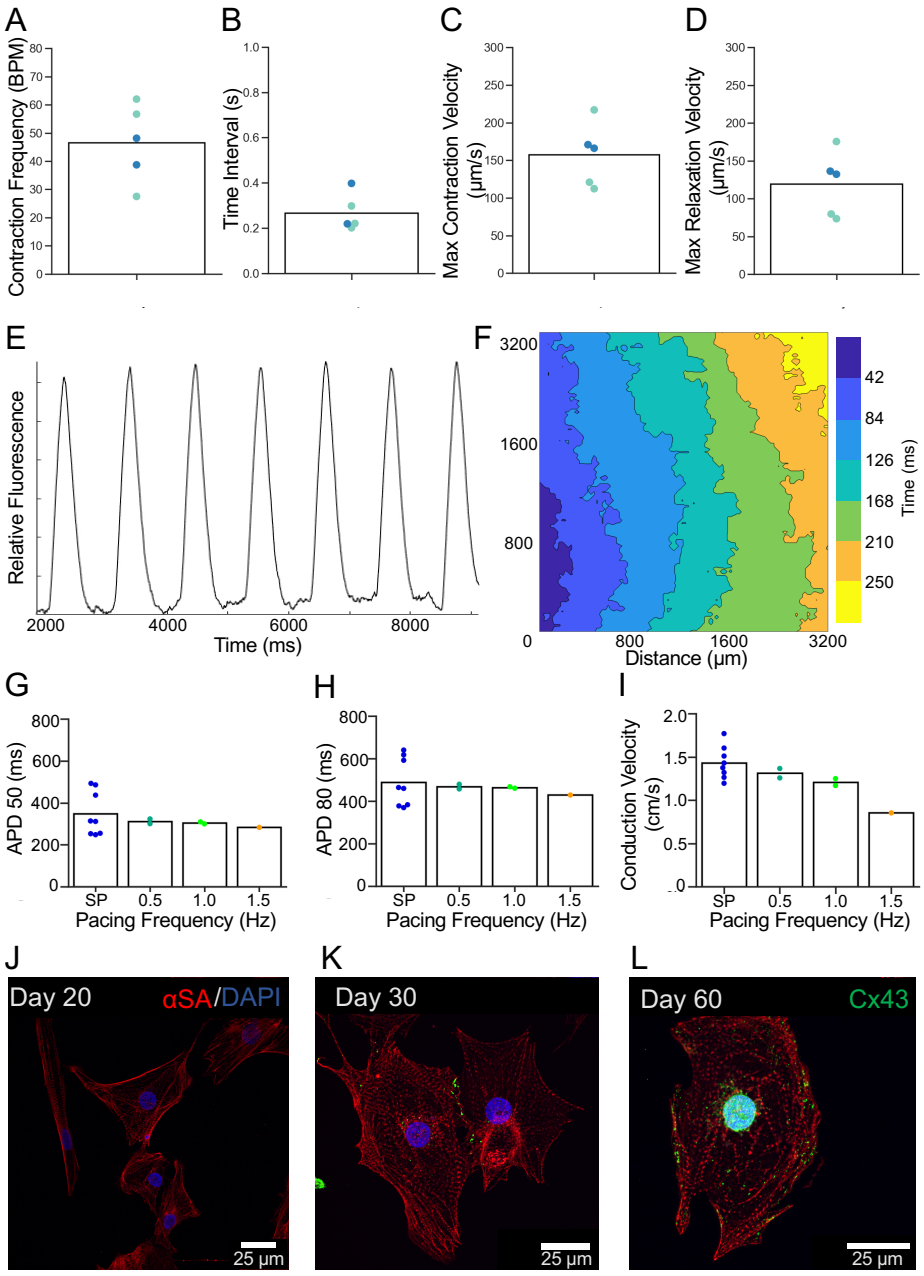

Figure 3.3 ECT microspheres spontaneously contract with appropriate changes in functionality.

(A–D) ECT microspheres started to spontaneously contract between days 7–10, and on day 10 the frequency of contraction was 46.6 ± 13.9 beats per minute (BPM) with a time interval of 0.267 ± 0.082 seconds. The (C) maximum contraction and (D) relaxation

velocities were 157 ± 42.3 and 120 ± 42.7 μm/s, respectively (n = 5 batches). (E–F) A custom MATLAB code was used for analysis of the high-frame rate fluorescent recordings. (G–I) Dissociated CMs from ECT microspheres with a genetically encoded voltage indicator (GEVI) responded appropriately to electrical pacing with 1:1 capture up to 1.5 Hz. (G) The APD at 50% repolarization was 349 ± 106, 311 ± 16.0, 304 ± 6.8, and 283 ms and (H) 487 ± 113, 467 ± 15.6, 463 ± 5.1, and 430 ms for 80% repolarization for spontaneous (SP), 0.5, 1.0 and 1.5 Hz pacing, respectively (n = 8, 2, 2, 1 recordings). (I) The conduction velocity was 1.43 ± 0.19, 1.31 ± 0.08, 1.21 ± 0.06, and 0.86 cm/s for SP, 0.5, 1.0, and 1.5 Hz paced samples (n = 8, 2, 2, 1 recordings). (J–L) Resulting CMs has the presence of well-defined sarcomeres (αSA, red), with organization and the Cx43 (green) expression increasing over time.

This microsphere direct differentiation platform was compared to self-aggregated EB differentiation, the current state-of-the-art for biomanufacturing of CMs. Formation of EBs occurs from seeding a single cell suspension in a stirred-tank bioreactor or shaker flask, resulting in limited control of resulting size and shape. Three different differentiation platforms for EB seeding and differentiation were employed: seeding and differentiation in a shaker flask (F), seeding and differentiation in a well plate (P), and seeding in a shaker flask and differentiation in a well plate (F/P). Shaker flasks are regularly used for scale-up studies prior to stirred-tank bioreactor experiments and provide a similar scale to the batches of ECT microspheres reported here. In the shaker flask platform (F), 3 million hiPSCs were seeded, and the number of cells on day 0 was used for differentiation without adjusting the cell density, cells per volume of media. The well plate platform (P) was

similar in that the number of cells on day 0 was used for differentiation without any adjustments prior to initiation of differentiation with CDM3 supplemented with CHIR. For the F/P platform, 3 million cells were seeded in the shaker flask, and on day 0, the cells were collected, a sample was counted, and the remaining EBs were distributed to provide a known cell density on day 0. The EBs had an average diameter of 194 ± 20.0, 200 ± 3.80, 264 ± 40.2, 247 ± 37.1, 232 ± 45.2, and 246 ± 71.5 μm with AR of 1.15 ± 0.04, 1.15 ± 0.07, 1.35 ± 0.06, 1.29 ± 0.07, 1.33 ± 0.05, and 1.36 ± 0.03 on days 0, 1, 3, 5, 7, and 10, respectively (Figure 3.4A, E–F, n = 3 batches, minimum of 22 EBs per batch). The CV for diameter on day 0 for the three batches of EBs was 26.1, 16.1, and 11.2%, which is higher than the CV for the microspheres on day -2, which was less than 10% for all 31 batches; furthermore, the CV for EB AR was higher than the microspheres at 23.8, 9.17, and 7.53% on day 0 compared to the microspheres with < 5% CV on day -2. The EBs were successfully differentiated using the same protocol with resulting CM content of 72.0 ± 21.0, 62.4 ± 25.0, and 49.3 ± 19.4% for F, P, and F/P platforms, respectively (Figure 3.4G, n = 3, 4, 8 batches). Interestingly, the F/P platform had the lowest efficiency of differentiation, although this platform had the most control on day 0 with regard to cell density. This may occur as a result of an increased cell density on day 0 (0.2–0.5 million cells/mL) compared to the flask, and that other uncontrolled parameters, such as integrin and cadherin expression, may be instrumental for successful cardiac differentiations. Some organization of the sarcomeres could be visualized by day 20 from αSA labeling of dissociated hiPSC-CM EBs (Figure 3.4B–D). The average number of CMs per input hiPSC was 0.65 ± 0.34, 1.82 ± 2.10, and 0.24 ± 0.43 for F, P, and F/P, respectively, which is lower than that the ECT microspheres with an average of 2.23 +/- 1.98 (Figure 3.4H, n = 3, 4, 8

batches, respectively). Additionally, the highest CM per input hiPSC obtained for the EBs was 4.7, which is considerably lower than the highest value of 6.9 for the ECT microspheres.

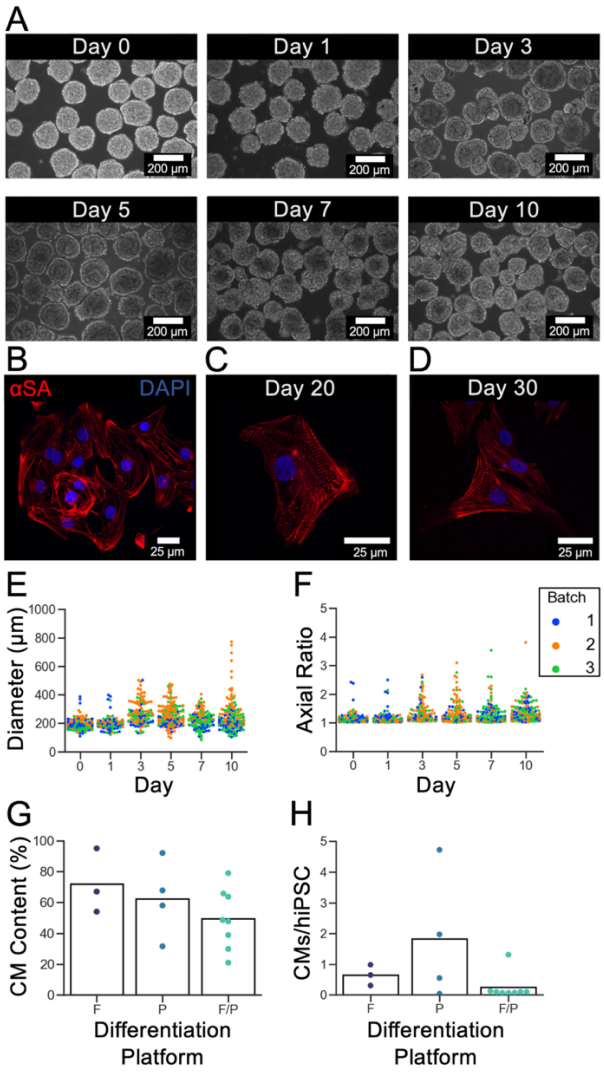

Figure 3.4 Self-aggregated EB formation and differentiation.

Self-aggregated EBs were formed by seeding a single cell suspension in a shaker flask (F) or well plate (P) on a shaker plate. Cardiac differentiation was initiated employing these two platforms as well as EB seeding and formation in a flask followed by cardiac differentiation in a well plate (F/P). (A) Successful self-aggregated EB formation occurred

and changes in morphology can be seen in phase contrast images. (B–D) EBs could be dissociated for visualization of sarcomere organization within individual CMs on (B–C) day 20 and (D) day 30 with αSA (red). Self-aggregated EBs had diameters of (E) 194 ± 20.0, 200 ± 3.80, 264 ± 40.2, 247 ± 37.1, 232 ± 45.2, and 246 ± 71.5 μm with (F) axial ratios of 1.15 ± 0.04, 1.15 ± 0.07, 1.35 ± 0.06, 1.29 ± 0.07, 1.33 ± 0.05, and 1.36 ± 0.03 on days 0, 1, 3, 5, 7, and 10 (n = 3 batches of at least 22 EBs per timepoint). (G) The CM content of the EBs on day 10 was 72.0 ± 21.0, 62.4 ± 25.0, and 49.3 ± 19.4% for F, P, and F/P platforms, respectively (n = 3, 4, 8 batches). (H) The number of CMs obtained after differentiation (day 10) per input hiPSC was 0.65 ± 0.34, 1.82 ± 2.10, and 0.24 ± 0.43 for F, P, and F/P, respectively (n = 3, 4, 8 batches)

Here, successful encapsulation of hiPSCs in PEG-fibrinogen microspheres and subsequent cardiac differentiation in chemically defined conditions is demonstrated. ECT microspheres could be efficiently differentiated using CDM3 with continuous Wnt control with CM contents as high as 95%; furthermore, an average of 2.2 CMs was obtained per input hiPSC, which is higher than for self-aggregated EBs. These ECT microspheres show appropriate changes in cell phenotype throughout differentiation, and spontaneous contractions could be visualized by day 10. The resulting CMs had the appropriate response to electrical pacing and formation of well-defined sarcomeres. Chemically defined conditions for cell culture and differentiation are critical for clinical translation of cell-based therapies for cardiovascular disease; additionally, the protocols described here provide substantial cost savings. The self-made E8 used here provides a 62% decrease in price compared to mTeSR, which was previously used for production of ECT

microspheres; similarly, the CDM3 is less than one-fourth the price of the RPMI/B27 media. This direct differentiation platform for the production of ECTs in chemically defined, low-cost conditions shows potential for use in downstream applications such as high-throughput drug testing and regenerative medicine.

Chapter 4: Scalable Production of Engineered Cardiac Tissue Microspheroids with Varying Size and Shape

Introduction

Engineered cardiac tissue (ECT) that accurately mimics the *in vivo* microenvironment is needed for regenerative medicine and for drug-testing applications. It is well-known that cells behave differently in 2D than 3D due to differences in cell-cell and cell-matrix interactions; furthermore, certain cell types can lose their phenotype in 2D and exhibit higher functionality in 3D (Fennema et al. 2013). Therefore, for production of the most native-like tissue, a 3D-ECT platform is necessary. A spheroidal platform is advantageous for the creation of 3D-ECTs from pluripotent stem cells (PSCs) because it mimics the stem cell niche (Scadden 2006), is scalable and injectable. Spheroids can be used for suspension culture which is vital for the scale-up processes needed for biomanufacturing. Finally, a spheroidal tissue model can be used for direct injection for the treatment of cardiovascular disease, which provides a less-invasive method of cell delivery over other options such as a cardiac patch.

Current methods for generating spheroidal tissues include hanging droplet formation, self-aggregation via spinner flask or bioreactor, microwell plates, liquid overlay technique, vortexing, and microfluidics. For the formation of hanging droplets, a cell suspension is pipetted in small amounts and the cells aggregate towards the bottom in the drop to form a spheroid (Tung et al. 2011; Beauchamp et al. 2015). This method can be tedious with a relatively low-throughput, produce variable sizes, and issues can result with evaporation and subsequent osmolarity changes in media. The shear stress from stirring in

spinner flasks or bioreactors causes aggregate formation and has been used for the formation of hPSC aggregates (Abecasis et al. 2017; Chen et al. 2015; H. Kempf et al. 2015). EBs can also be formed using gravitational forces in microwell plates (Pettinato, Wen, and Zhang 2014), centrifugation, (E.S. Ng et al. 2005) and vortexing (Jiang et al. 2017; Pradhan et al. 2017). Liquid overlay technique involves formation of spheroids by seeding cells on a non-adherent surface causing cell aggregation (Yuhas et al. 1977). Microfluidic devices have also been used for the formation of spheroidal embryoid bodies of mouse ESCs within a channel (Torisawa et al. 2007). These methods discussed involve the formation of spheroids without the addition of biomaterials. Microfluidic fabrication techniques can be used for the formation of spheroids that incorporate biomaterials which can provide protection to the cells as well as direct differentiation and provide mechanical and biological cues.

Microfluidics involves the study and manipulation of fluids at the micron or nanometer scale and is widely used in the biomedical field (Sackmann, Fulton, and Beebe 2014). A subcategory of microfluidics, droplet microfluidics, can be used for the encapsulation of cells within a biomaterial, and has been used previously for the encapsulation of yeast cells in alginate (Choi et al. 2007), breast cancer tumor cells in alginate (Yu, Chen, and Cheung 2010), human lung adenocarcinoma epithelial cells in PEGDA and PEG norbornene (Jiang et al. 2017), and human mesenchymal stem cells in gelatin norbornene (F. Li et al. 2017). This technique uses immiscible fluids, such as an aqueous solution and oil, to form uniform droplets (Anna, Bontoux, and Stone 2003). These emulsions are characterized by their low Reynolds number in which the fluid flow is in the laminar flow regime (Teh et al. 2008). Droplet formation occurs at a junction and is

governed by the dimensionless capillary number (Ca) and fluid flow rates (Choi et al. 2007). Formation of the fabrication devices typically uses glass capillary devices or soft-lithography fabrication techniques (Rossow, Lienemann, and Mooney 2017) which can be expensive and require specialized equipment.

Previously, our group developed a novel, cost-effective microfluidic system for rapid fabrication of highly uniform cell-laden microspheres using droplet microfluidics (Seeto et al. 2019). This platform is highly flexible and can be used to encapsulate a variety of cell types, including cancer cells, equine endothelial colony forming cells, and human induced pluripotent stem cells (hiPSCs), in photocrosslinkable biomaterials. Following hiPSC encapsulation in the microfluidic system, direct cardiac differentiation to produce ECT microspheres was performed (Chapter 2) using RPMI/B27 differentiation as well as in chemically defined conditions (Chapter 3). Recent work from our group has shown that this microfluidic system can be used to produce microspheroid hydrogels with varying sizes and axial ratios (ARs) by changing the capillary number through modulation of the narrowing ratio and flow fraction (Tian and Lipke 2020).

One of the current limitations for successful translation and implementation of ECTs utilizing PSC-CMs in the field of cardiac tissue engineering is the maturity of the resulting CMs, particularly with ECTs that are spheroidal in geometry. Typically, PSC-CMs have an immature phenotype compared to adult CMs, with key differences in phenotype and morphology, metabolism, and functional properties (Feric and Radisic 2016a; Karbassi et al. 2020). Adult CMs are anisotropic and rod-like in shape with a surface area of approximately 10,000 to 15,000 μm^2; whereas PSC-CMs are much smaller (900–1300 μm^2) with a variety of shapes ranging from circular to triangular to rectangular (Feric

and Radisic 2016a). Adult CMs have a high degree of organization of their internal components with aligned sarcomeres, the basic contractile unit of the CM, as the hallmark feature. These sarcomeres have an average length of 2.2 μm^2, whereas the sarcomere length of PSC-CMs is approximately 1.6 μm (Yang, Pabon, and Murry 2014). Typically, PSC-CMs lack T-tubules; however, previous work from our group (P. Kerscher, Turnbull, et al. 2016) as well as from Dr. Vunjak-Novakovic's (Ronaldson-Bouchard et al. 2018) show evidence of the formation of these invaginations in the CM membrane located at the adjacent sarcomeres. There are major differences in metabolic activity and mitochondria biology; adult CMs rely on fatty acid oxidation for energy utilization, whereas fetal CMs and PSC-CMs typically rely on glycolysis (Karbassi et al. 2020). Furthermore, because of differences in calcium handling, the functionality of the PSC-CMs is lower than adult CMs in terms of conduction velocity and contractile force. Advances in CM maturity following differentiation may be needed for the use of ECTs in clinical applications for sufficient electrical coupling and to prevent arrhythmias.

There have been significant efforts to enhance maturity of PSC-CMs through mechanical and electrical stimulation (Ronaldson-Bouchard et al. 2018), co-culture with other cell types (K. K. Dunn et al. 2019; Giacomelli et al. 2020; Pasquier et al. 2017), utilization of maturation media (Feyen et al. 2020), inhibition of mTOR signaling (Garbern et al. 2020), and delivery of miRNAs and hormones (White, Pang, and Yang 2016; C. Jackman, Li, and Bursac 2018; Yang et al. 2014). Previous work has shown that the geometry of ECTs can promote CM maturity, particularly when there is enhanced cell and tissue alignment (Ding et al. 2020; Hirt et al. 2014; Khan et al. 2015; X. Ma et al. 2018; Nunes et al. 2013; D. Zhang et al. 2013). Building on this work showing geometrical

differences with ECT maturity, specifically tissue alignment, the objective of this study was to produce ECT microspheroids with a variety of sizes and ARs, particularly those with high ARs (> 2) through microfluidic encapsulation of hiPSCs in PEG-fibrinogen for direct cardiac differentiation. Furthermore, an initial set of experiments was constructed to assess the impact of these parameters as well as PEG-fibrinogen concentration and initial cell concentration on resulting ECT differentiation and maturity (Figure 4.1B). Here, successful encapsulation of hiPSCs in microspheroids ranging from 400–1000 μm in diameter with initial AR from 1–9 is demonstrated. Following encapsulation, hiPSCs maintained high cell viability and continued to proliferate and grow throughout cardiac differentiation, forming a dense, continuous tissue. Cardiac differentiation occurred using a chemically defined differentiation protocol, and the resulting CM content was quantified on day 10. High CM contents and yield could be obtained, as high as 98% and as many as 6.9 CMs per hiPSC; however, there was large variability between batches. Feature selection and data-driven modeling was performed to predict CM content on day 10. Initial scale-up studies were performed using the microspheroids with a high AR (> 3), indicating that this platform has potential for use in bioreactor production of ECT.

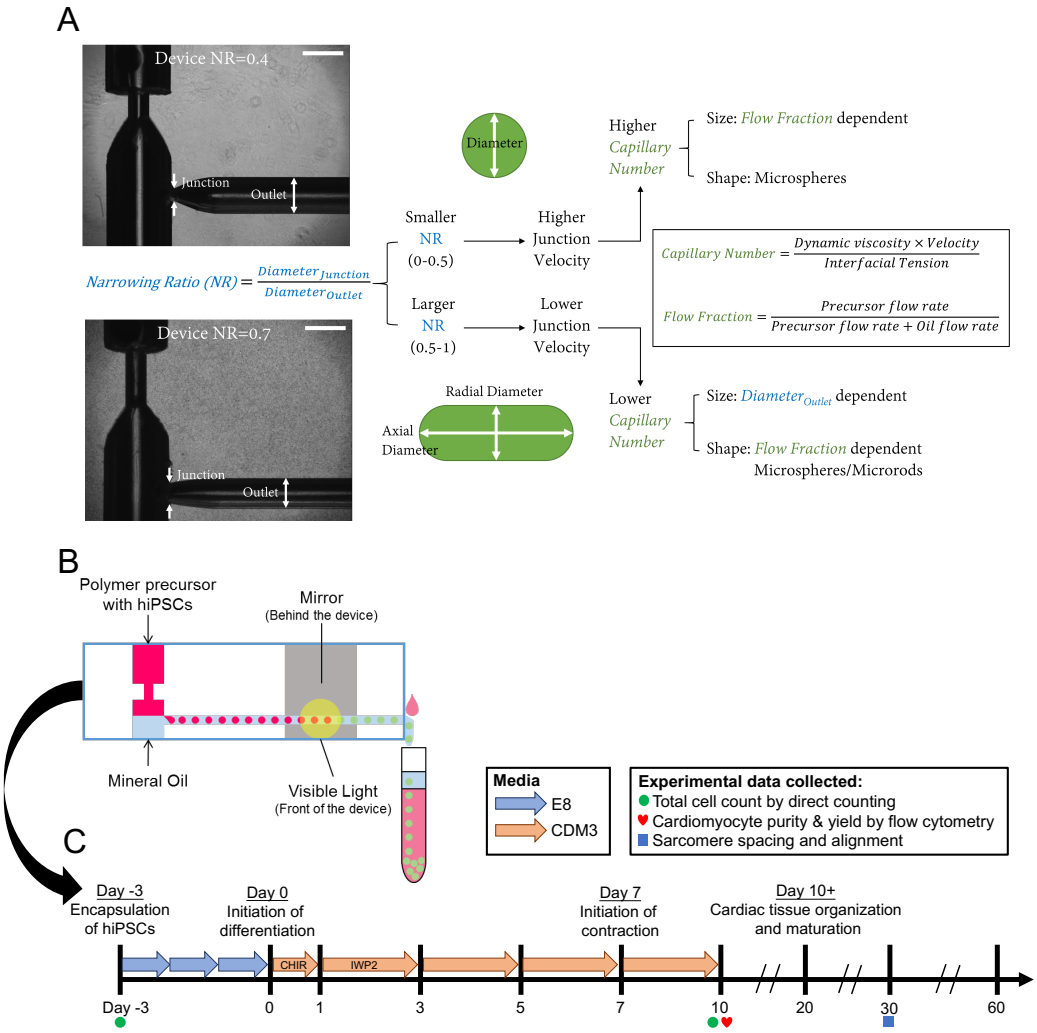

Figure 4.1 Production of ECT with varying sizes and ARs in chemically defined conditions.

(A) The diameter and axial ratio (AR) of microspheroids produced using a custom-built microfluidic system can be controlled. Previous work has shown that adjusting the narrowing ratio (NR) of the T-junction causes changes to the junction velocity, affecting the capillary number. At high capillary numbers, microspheres are produced, and the size of the microspheres can be changed by flow fraction. At lower capillary numbers, the resulting radial diameter is limited by the outlet diameter, and the AR can be modulated by changing the flow fraction. Figure reprinted with permission from (Tian and Lipke 2020).

Copyright 2020 American Chemical Society. (B) This microfluidic system was used to encapsulate hiPSCs in PEG-fibrinogen to produce microspheroids with varying sizes and ARs. (C) Encapsulation occurs on day -3, and cardiac differentiation is initiated on day 0 using a chemically defined differentiation protocol. To assess ECT differentiation, assessment of cell numbers and CM content occurred, and sarcomere staining was performed on day 30.

Materials and Methods

hiPSC culture

The genetically encoded voltage indicator cell line, Un-Arc 16 Facs II (Shinnawi et al. 2015), was used for this study and graciously provided by Dr. Lior Gepstein at Technion — Israel Institute of Technology. HiPSCs were cultured on Geltrex (Gibco) with E8 media. E8 media was made with DMEM/F12 (Gibco) supplemented with ascorbic acid (64 mg/L, Sigma), sodium selenite (14 μg/L, Sigma), sodium bicarbonate (543 mg/L, Sigma), insulin (20 mg/L, Sigma), transferrin (10.7 mg/L, Sigma), basic fibroblast growth factor (100 μg/L, Peprotech), and transforming growth factor-beta (2 μg/L, Peprotech). The hiPSCs were passaged into single cells with Accutase (Innovative Cell Technologies). For one day after passaging, hiPSCs were maintained in E8 supplemented with rock inhibitor (5–10 μM, RI, Y-27632, Stem Cell Technologies).

HiPSC encapsulation using the microfluidic system

PEG-fibrinogen precursor solution was prepared by combining PEG-fibrinogen with triethanolamine (1.5 v/v%, TEOA), N-vinyl pyrrolidone (0.39 v/v%, NVP), rock inhibitor

(12.5 μM), and Eosin Y (0.1 mM, Fisher Scientific) photoinitiator (in PBS). HiPSCs were resuspended in PEG-fibrinogen precursor solution at 30–60 million cells/mL. The PEG-fibrinogen-cell mixture was added to one inlet of a custom-built microfluidic device. In parallel, mineral oil was added to the other inlet of the microfluidic device which, when combined with the PEG-fibrinogen-cell mixture, causes the formation of spherical droplets. Flowrates for the PEG-fibrinogen-cell mixture and mineral oil were adjusted as previously described to maintain consistent crosslinking times and for modulation of size and AR (Tian and Lipke 2020). A light source (Prior) was used for photocrosslinking the liquid PEG-fibrinogen-cell mixture to form cell-laden microspheroids. Microspheroids were collected by washing down with E8 media supplemented with 10 μM RI, removed from the oil phase and spent media, and were cultured in E8 media + RI (10 μM) for 24 h (day -3). Microspheroids were then cultured for an additional 2 days in E8 media with daily media changes (days -2 and -1).

Design of Experiments

The initial design of experiments was provided by Dr. Selen Cremaschi's research group; this initial test matrix was produced using maximum entropy and contained 11 experiments. This original test matrix was designed to investigate the ECT differentiation and maturity through modulation of initial hiPSC concentration, PEG-fibrinogen concentration, microspheroid diameter, and microspheroid AR. The initial design included ranges of 20–60 million cells/mL precursor solution for initial hiPSC concentration, PEG-fibrinogen concentrations of 8–12 mg/mL of fibrinogen, diameters between 450–1000, and AR from 1–5 (Figure 4.4A).

Diameter, axial ratio, and early growth quantification of microspheroids

Phase contrast images of microspheroids were taken from the time of encapsulation (day -3) through cardiac differentiation (day 10) using an Andor Luca S camera attached to a Nikon Eclipse Ti microscope. Microspheroid diameter and size of thirteen individual batches were determined after encapsulation and prior to initiation of cardiac differentiation. The autofluorescence of the photoinitiator Eosin Y in PEG-fibrinogen microspheroid was captured using long acquisition times with the FITC filter on the Nikon Eclipse Ti fluorescence microscope at low magnification. Aggregate size and shape were determined from daily phase contrast images. Standard plugins in ImageJ were used for quantification.

HiPSC viability and immunofluorescence staining

On day -2, the viability of the hiPSCs in PEG-fibrinogen microspheroids was assessed using a LIVE/DEAD® viability kit (Invitrogen), and images were taken using a fluorescent microscope (Nikon). Dissociated CMs were immunostained α-sarcomeric actinin (αSA, Sigma Aldrich). For immunostaining, engineered cardiac tissue microspheroids were dissociated with 1 mg/mL Collagenase-b (Roche) and 0.05 mg/mL DNase in PBS for 10–30 minutes at 37 °C and were plated on Matrigel (Corning) coated coverslips for 2–4 days. The cells were rinsed with PBS and fixed in paraformaldehyde (4%, Electron Microscopy Sciences) for 20 min at room temperature (RT). Samples were rinsed with PBS and blocked with FBS (3–10%) overnight at 4 °C or 30 min at RT. Then, the dissociated CMs were incubated in the primary antibody (αSA) overnight at 4 °C or 1 h at RT followed by the addition of Alexa Fluor 488 or Alexa Fluor 568 secondary antibody. Nuclei were

counterstained with Bisbenzimide Hoechst 3342 (MilliporeSigma). Samples were visualized using a Nikon A1R laser-scanning confocal microscope.

Cardiac Differentiation

Chemically defined cardiac differentiation media (CDM3) contained RPMI 1640 (Gibco) supplemented with 500 μg/mL recombinant human albumin (ScienCell) and 213 μg/mL ascorbic acid. To initiate cardiac differentiation on day 0, CHIR99021 (5–7.5 μM, STEMCELL Technologies), was added to the media and the microspheroids were placed on a shaker plate (Infors) at 70 rpm; exactly 24 h later, the media was exchanged for CDM3 supplemented with 5 μM IWP2 (STEMCELL Technologies). Fresh CDM3 was added on days 3, 5, 7, and 10; following day 10, the ECTs were cultured with CDM3 or RPMI/B27 (Gibco) for selected batches, and the media was exchanged every 3–4 days.

Flow cytometry

On day 10, the engineered cardiac tissue microspheroids and EBs were dissociated by incubation at 37 °C for 10–15 minutes with Collagenase-b (1 mg/mL, Roche) and DNase (0.05 mg/mL, Worthington) in PBS. After tissue dissociation, a cell pellet was collected through centrifugation. After washing with PBS, the cells were labeled with Zombie Dye (Biotium) for 30 min at 4 °C. Cells were then washed with Blocking Buffer (bovine serum albumin (1%, BSA, Sigma), fetal bovine serum (10%, FBS, Atlanta Biologics) in PBS), and then fixed with Foxp3 Transcription Factor Staining Buffer Set (eBioscience) overnight at 4 °C. The cells were filtered using a 40 μm cell strainer (Scienceware Flowmi) and permeabilized with FACS buffer (BSA (1%), FBS (10%) in 1x Permeabilization

Buffer (eBioscience)) at RT for 30 mins. The primary antibodies (1:200, cTnT (Invitrogen) and MF20 (DSHB)) were then incubated with the cells for 1 h at RT. After incubation in the primary antibody, washing occurred with Permeabilization Buffer. The secondary antibodies (1:300, AlexaFluor 647 goat anti-mouse IgG (ThermoFisher)) were added for 30 mins at RT. The cells were then washed with Permeabilization Buffer and resuspended in Blocking Buffer for analysis. A Beckman Coulter CytoFlex LX was used for sample analysis. At least 10,000 live cells were recorded for analysis. Anti-Mouse IgG1 isotype control (ThermoFisher) was used to ensure there was not any non-specific binding.

Contraction Analysis

Contraction analysis was done using motion tracking software in which macroblocks were tracked between frames to determine the beat rate in beats per minute (BPM), time interval in seconds, maximum contraction velocity in μm/s, and maximum relaxation velocity in μm/s. Videos of contractions, 10–20 s in length, were taken using an Andor Luca S camera attached to the microscope, converted to a series of tiff files, and imported into the Motion GUI in the open source MATLAB code (Huebsch et al. 2015).

Statistical Analysis

Unless otherwise noted, statistical analysis was performed using Minitab statistical software where results are presented as mean ± standard deviation. One-way ANOVA was performed with Tukey's test for post-hoc analysis for samples with equal variance, and the Games-Howell test was performed for samples with unequal variances. A value of $p < 0.05$ was used for statistical significance.

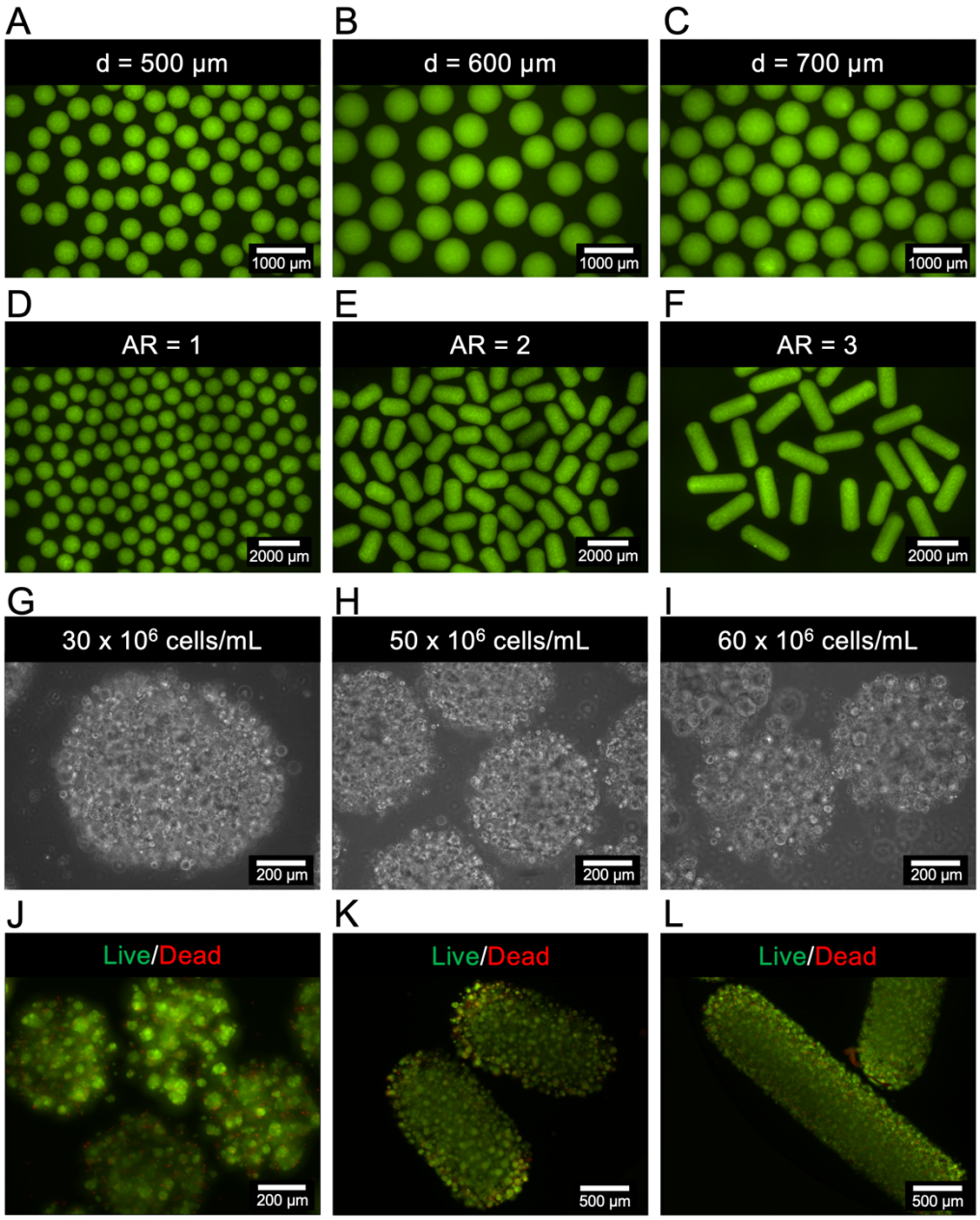

Figure 4.2 Production of uniform hiPSC-laden microspheroids with high cell density and high cell viability.

The custom microfluidic system can be used to produce hiPSC-laden microspheroids ranging from 450–1000 µm in diameter with axial ratios (ARs) from 1–9 that are highly uniform within a batch, with examples shown in (A–F). (G–I) This system can be used to encapsulate hiPSCs at a high cell density, ranging from 30 to 60 million hiPSCs per mL of

precursor solution. (J–L) Following encapsulation, the hiPSCs maintained high cell viability in PEG-fibrinogen microspheroids in all the geometries with live cells (green) growing in colonies throughout the microspheroids and dead cells (red) remaining as single cells.

Results and Discussion

Production of hiPSC-laden microspheroids with varying sizes and ARs

Production of engineered cardiac tissue microspheroids with a variety of sizes and axial ratios (AR) occurred through direct differentiation of encapsulated hiPSCs using a microfluidic system previously established by our group. The AR is the ratio of the axial diameter to the radial diameter. Previously, our group has shown that the modulation of size and AR is primarily dominated by changes to the capillary number (Figure 4.1A), which is the ratio of viscous drag forces (dynamic viscosity multiplied by the velocity) to the surface tension forces (interfacial surface tension) (Tian and Lipke 2020). In this system, Tian and Lipke showed that the junction velocity was important for determining the outcome of the capillary number; this feature is controlled by the narrowing ratio (NR), or the ratio of the diameter of the junction to the outlet channel diameter. Smaller NRs lead to an increase in junction velocity, causing an increase in capillary number. At high capillary numbers, the resulting shape is spherical (AR = 1), and the size of the microspheres can be changed through flow fraction, the ratio of the precursor flow rate to the total flow rate (oil + precursor) At larger NRs, the junction velocity is decreased, leading to a decrease in capillary number. At low capillary numbers, the size of the microspheroids is set by the outlet channel diameter and the AR can be controlled by flow

fraction. At these low NRs, when the flow fraction is increased, the resulting microspheroids become longer in length, leading to higher ARs. Tight control over size and shape within a batch has been maintained, and here were report the utilization of this microfluidic system for encapsulation of hiPSCs within PEG-fibrinogen hydrogels with diameters ranging from 420–1000 μm and ARs from 1–9. Furthermore, this system could be used for encapsulating hiPSCs at high cell density, at initial cell concentrations of 30–60 million cells per mL of precursor solution; example images for these varying conditions are shown in Figure 4.2

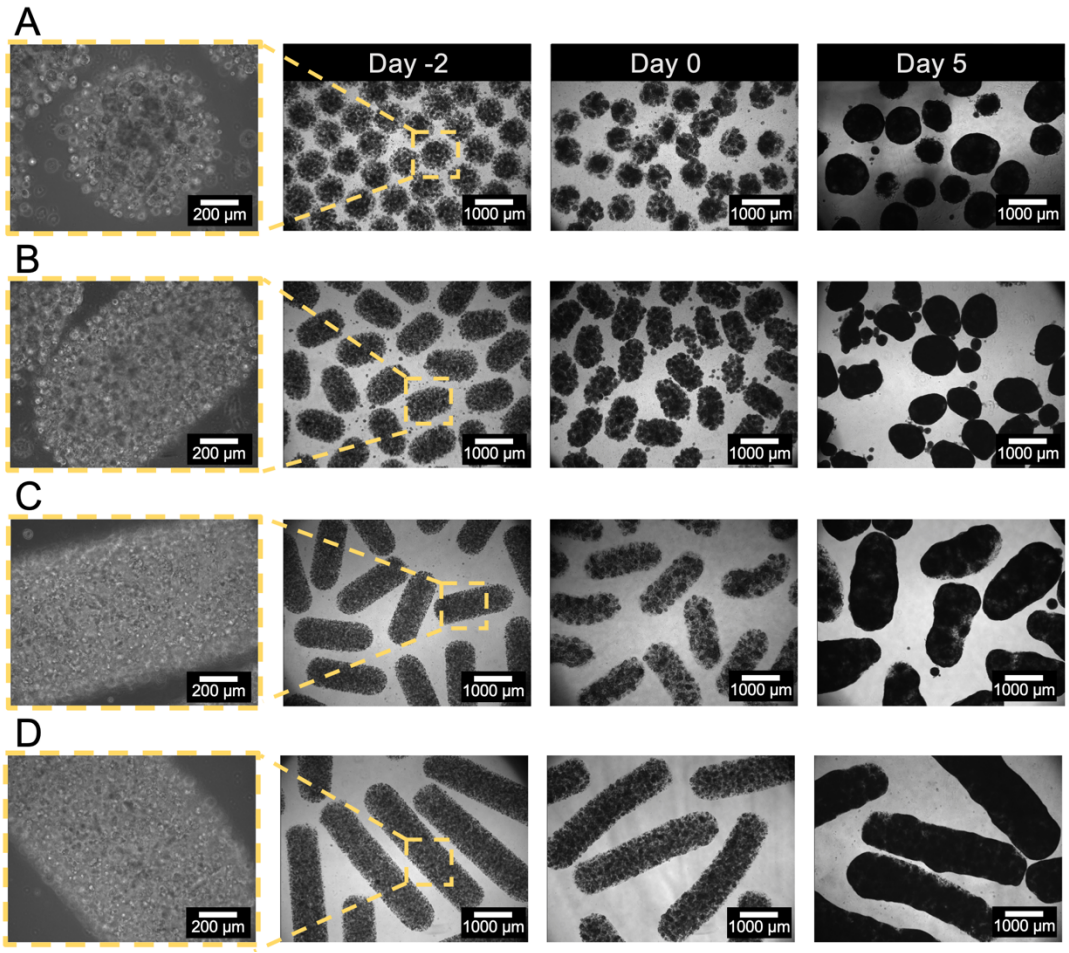

Figure 4.3 Encapsulated cells proliferate and grow within PEG-fibrinogen microspheroids throughout differentiation to form a continuous tissue.

On day -3, hiPSCs were encapsulated within a PEG-fibrinogen matrix. Following encapsulation, the hiPSCs continued to grow in their colonies, remodeling the provided matrix and forming a dense continuous tissue by day 5.

The central component of the microfluidic system is a PDMS device with a modified T-junction with two inlets connected to syringes with syringe pumps and an outlet channel (Figure 4.1B). In this study, seven different PDMS molds were used with NRs ranging from 0.37 to 0.79, based on the desired size and shape of the resulting cell-laden hydrogels. The precursor solution containing hiPSCs and polymer precursor solution were pumped in through the top inlet, and adjacently, mineral oil was pumped in through the bottom inlet. The flow rates for the precursor solution and mineral oil were adjusted based on the desired size and shape outcome, maintaining a constant total velocity in the microfluidic outlet channel to ensure consistent crosslinking times. The flow rates for the precursor solution and mineral oil were adjusted to ensure the velocity for each batch was maintained between 0.4 and 0.8 cm/s. Microspheroids formed at the junction and traveled down the outlet for rapid photocrosslinking. A syringe containing washing media was used at the outlet to wash down the microspheroids for collection and use in further experiments. Encapsulation occurred on day -3, and the hiPSC-laden microspheroids were cultured in E8 until the onset of cardiac differentiation on day 0. Following encapsulation, high viability was maintained in both the spherical geometry (Figure 4.2J) as well as in the microspheroids with higher ARs (Figure 4.2K–L).

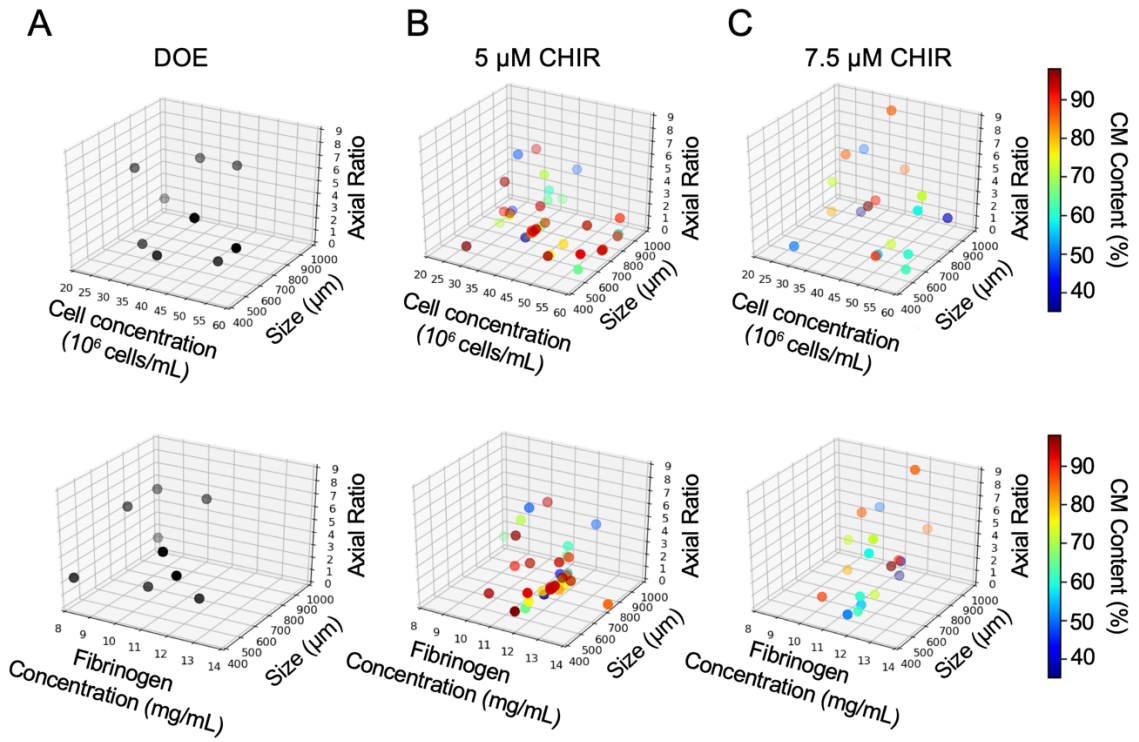

Figure 4.4 ECT microspheroids can be produced with a wide range of size, AR, cell concentration, and PEG-fibrinogen concentrations.

3D plots were generated to show the different conditions for each batch. CHIR concentrations of (A) 5 μM and (B) 7.5 μM were used for initiation of differentiation on day 0. Each dot represents an individual batch, and the color of the data point is based on CM content (color bar on right) (n = 46, 18 batches for 5 and 7.5 μM, respectively).

ECT Microspheroid Directed Cardiac Differentiation

Cardiac differentiation was initiated three days post-encapsulation and occurred through activation and inhibition of the Wnt signaling pathway using small molecules in chemically defined differentiation media (CDM3, Figure 4.1C). To initiate differentiation (day 0), the Wnt activator CHIR was added at 5 μM or 7.5 μM in CDM3. On day 1, the media was

exchanged for CDM3 containing Wnt inhibitor, IWP2, for 48 h. Cardiac specification and differentiation continued throughout differentiation, and the media was exchanged on days 3, 5, and 7 with fresh CDM3. Following hiPSC encapsulation and throughout cardiac differentiation, cells continued to proliferate and remodel the provided PEG-fibrinogen matrix; initially, hiPSCs can be seen in rounded cell colonies on day -2 and throughout differentiation, the formation of dense, dark tissue occurs by day 5 (Figure 4.3). ECT microspheroids began to spontaneously contract by day 10 of cardiac differentiation. Following cardiac differentiation, the resulting CM content, percent CMs, and yield, number of CMs per input hiPSCs, were quantified on day 10 using flow cytometry labeling of cardiac antibodies MF20 and cardiac troponin T (cTnT).

Design of Experiments

This microfluidic system is flexible with multiple adjustable input parameters; therefore, an initial design of experiments was constructed with the aid of computational collaborators to assess the impact of initial cell concentration, PEG-fibrinogen concentration, size, and AR on CM differentiation efficiency and maturity. An initial experimental campaign included 11 experiments with PEG-fibrinogen concentrations of 8–12 mg/mL of fibrinogen, initial hiPSC concentrations between 20–60 million cells/mL, initial radial diameters from 450–1000 μm (size), and ARs from 1–5 (Figure 4.4A). Initially, experiments from this test matrix were conducted as experimentally feasible, and then more batches were produced to increase data for building the models (Figure 4.4). In trying to complete this initial set of experiments, current limitations and future opportunities for expansion of this microfluidic system were realized. Using this current

system design and encapsulation and cardiac differentiation timeline, no successful differentiations occurred at initial cell concentrations less than 30 million cells/mL precursor solution. Increasing the time between encapsulation and initiation of differentiation, allowing hiPSCs to expand in the microspheres for longer, could promote cardiac differentiation and higher cell numbers, as seen previously with microcarriers employing a 5-day expansion period prior to initiation of cardiac differentiation (Laco et al. 2020). Furthermore, crosslinking was not successful below 10 mg/mL of PEG-fibrinogen; and changes to polymer synthesis and/or crosslinking of microspheroids utilizing a different light source may provide success of the system at those parameters. Although some limitations were realized, microspheroids could be produced at the sizes and ARs in the initial test matrix and even could be extended beyond the initial design of experiments, such as with AR.

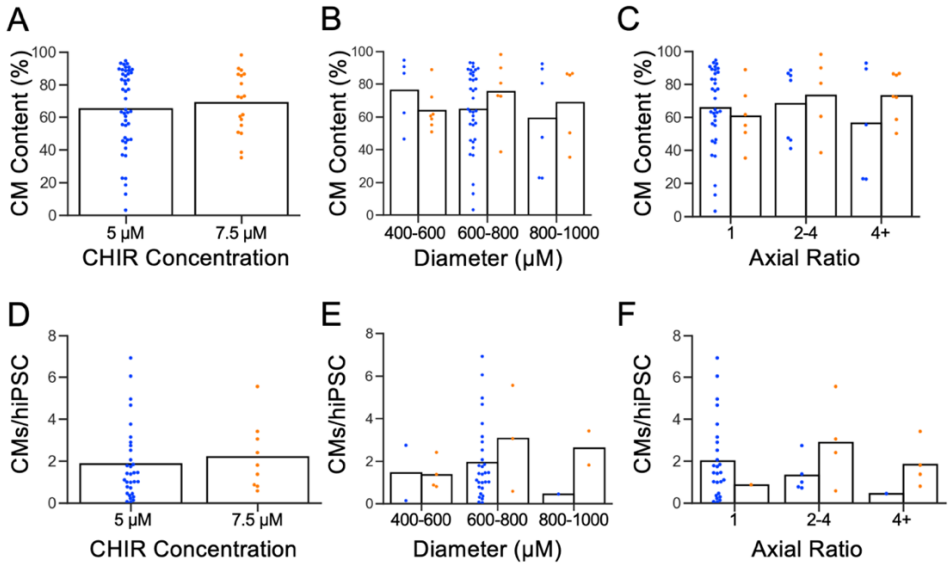

Figure 4.5 High variability in efficiency of cardiac differentiation and resulting number of cells among conditions.

(A) The CM content was 65.2 ± 24.7 and 69.0 ± 18.6 for microspheroids differentiated with 5 and 7.5 μM, respectively (n = 46, 18 batches). Microspheroids were divided into three groups for diameter and AR for assessment of CM content (B–C) and cell yield (E–F). (B) The CM content was for 76.1 ± 20.8 and 63.8 ± 12.8% (n = 5, 7 batches), 64.7 ± 24.0 and 75.4 ± 20.6% (n = 35, 6 batches), and 59.1 ± 32.4 and 68.7 ± 24.3% (n = 6, 5 batches) for microspheroids with initial diameters of 400–600, 600–800, and 800–1000 differentiated with 5 and 7.5 μM CHIR, respectively. (C) Microspheroids with initial ARs of 1, 2–4, and 4+ differentiated with 5 and 7.5 μM CHIR was 65.8 ± 24.3 and 60.7 ± 18.5% (n = 34, 6 batches), 68.1 ± 22.0 and 73.44 ± 24.0 (n = 7, 5 batches), and 56.5 ± 34.2 and 73.0 ± 14.4% (n = 5, 7 batches), respectively. (D) The number of CMs per input hiPSC was 1.85 ± 1.76 and 2.2 ± 1.61 for 5 and 7.5 μM CHIR, respectively (n = 32 batches, 9 batches). (E) For microspheroids at 5 and 7.5 μM, the average number of CMs/hiPSCs obtained was 1.43 ± 1.84 and 1.36 ± 0.74 (n = 2, 4 batches), 1.93 ± 1.79 and 3.06 ± 2.49 (n = 29, 3 batches), and 0.44 and 2.61 ± 1.13 (n = 1, 2 batches), for radial diameters of 400–600 μm, 600–800 μm, and 800–1000 μm, respectively. (F) The resulting yield, or number of CMs/hiPSC, was 2.00 ± 1.89 and 0.864 (n = 26, 1 batches), 1.32 ± 0.84 and 2.89 ± 2.06 (n = 5, 4 and 0.44 and 1.85 ± 1.12 (n = 1, 4 batches).

Successful cardiac differentiation in ECT microspheroids

Preliminary results showed that the CHIR concentration was geometry dependent, matching previously published results demonstrating the impact of CHIR concentration for efficient cardiac differentiations based on geometry (M. Zhao et al. 2019), cell line (Halloin

et al. 2019), and bulk cell density (H. Kempf et al. 2016), the number of cells per volume of cell culture media; therefore, cardiac differentiation occurred at CHIR concentrations of either 5 or 7.5 μM. For the 64 differentiations in this study, microspheroidal ECTs differentiated at 5 μM CHIR resulted in a CM content of 65.2 ± 24.7%, similarly 7.5 μM CHIR resulted in CM contents of 69.0 ± 18.6% (Figure 4.5A, n = 46, 18 batches). The resulting cell yield from ECT microspheroids differentiated at 5 and 7.5 μM CHIR was 1.85 ± 1.76 and 2.2 ± 1.61 (Figure 4.5D, n = 32, 9 batches). ECT microspheroids initially 400–600 μm in diameter had CM contents of 76.1 ± 20.8 and 63.8 ± 12.8% (Figure 4.5 B, n = 5, 7 batches) with resulting yield of 1.43 ± 1.84 and 1.36 ± 0.74 CMs per hiPSCs for 5 and 7.5 μM CHIR, respectively (Figure 4.5E, n = 2, 4 batches). Microspheroids with initial diameters of 600–800 μm and 800–1000 μm differentiated at 5 μM CHIR had CM contents of 64.7 ± 24.0 and 59.1 ± 32.4% (Figure 4.5B) with yields of 1.93 ± 1.79 and 0.44 CMs per hiPSC (Figure 4.5E, n = 29, 1 batches); for 7.5 μM CHIR, the resulting CM content was 63.8 ± 12.8 and 75.4 ± 20.6% for initial sizes between 600–800 μm and 800–1000 μm, respectively (Figure 4.5B, n = 6, 5 batches) with cell yields of 3.06 ± 2.49 and 2.61 ± 1.13 CMs per hiPSC (Figure 4.5E, n = 3, 2 batches). The CM content for microspheroids differentiated with 5 μM CHIR was 65.8 ± 24.3, 68.1 ± 22.0, and 56.5 ± 34.2% for axial ratios of 1, 2–4, and 4+, respectively (n = 34, 7, and 5 batches). For ARs of 1, 2–4, and 4+ with 7.5 μM CHIR differentiation, the CM content was 60.7 ± 18.5, 73.44 ± 24.0, and 73.0 ± 14.4% (n = 6, 5, 7 batches). Additionally, for AR of 1 differentiated with 5 and 7.5 μM CHIR, the resulting number of CMs/hiPSC was 2.00 ± 1.89 and 0.864 (n = 26, 1 batches); the number of CMs/hiPSC for ARs of 2–4 was 1.32 ± 0.84 and 2.89 ± 2.06 for 5 and 7.5 μM

CHIR, respectively (n = 5, 4 batches). For the longest AR (4+), the number of CMs/hiPSCs differentiated with 5 and 7.5 μM CHIR was 0.44 and 1.85 ± 1.12 (n = 1, 4 batches). There was large variability in the CM content and yield at each of the conditions, with CM contents ranging from 3 to 98% and yields from 0.04 to 6.9 CMs per encapsulated hiPSC. Although no statistical differences were found between the conditions for CM content or cell yield, there appears to be a trend that higher CHIR concentration yield higher CM contents for ECT microspheroids with larger diameters (600–1000 μm) and ARs (2+), while 5 μM CHIR is sufficient for smaller diameters (400–600) and microspheres (AR = 1).

Microspheroidal ECTs started to contract between days 7 and 10 of differentiation. On day 30, microspheroids with an initial AR 2+ spontaneously contracted at 32.2 ± 8.17 beats per min and had a time interval, the time between contraction and relaxation, of 0.32 ± 0.1 s. The maximum contraction and relaxation velocities were 172 ± 61.5 and 147 ± 70.8 μm/s (n = 3 batches). Microspheroids were maintained for 60 days in culture; initial experiments showed that CDM3 media was not sufficient for maintaining the contractile phenotype long-term and promoting CM maturation and function. Therefore, for some of the batches, media was changed to RPMI/B27 beginning on day 10. To investigate the CM phenotype and maturity, microspheroidal tissues were dissociated and labeled with antibody, α-sarcomeric actinin (αSA, Figure 4.6). The formation of well-defined sarcomeres can be seen in CMs at each AR; however, there is heterogeneity within a batch for sarcomere definition as well as the alignment and organization of the sarcomeres in the CMs. At an AR of 1 (Figure 4.6A–C), the CMs are larger in size compared to the ones with higher ARs and are more circular in geometry (Figure 4.6D–I); as the AR increases, the

cells become more elongated with increasing organization of the sarcomeres in the CMs. Following cardiac differentiation, there are features of maturing CMs, such as the formation of well-defined and organized sarcomeres, with more elongated cells present in ECT microspheroids with higher initial ARs.

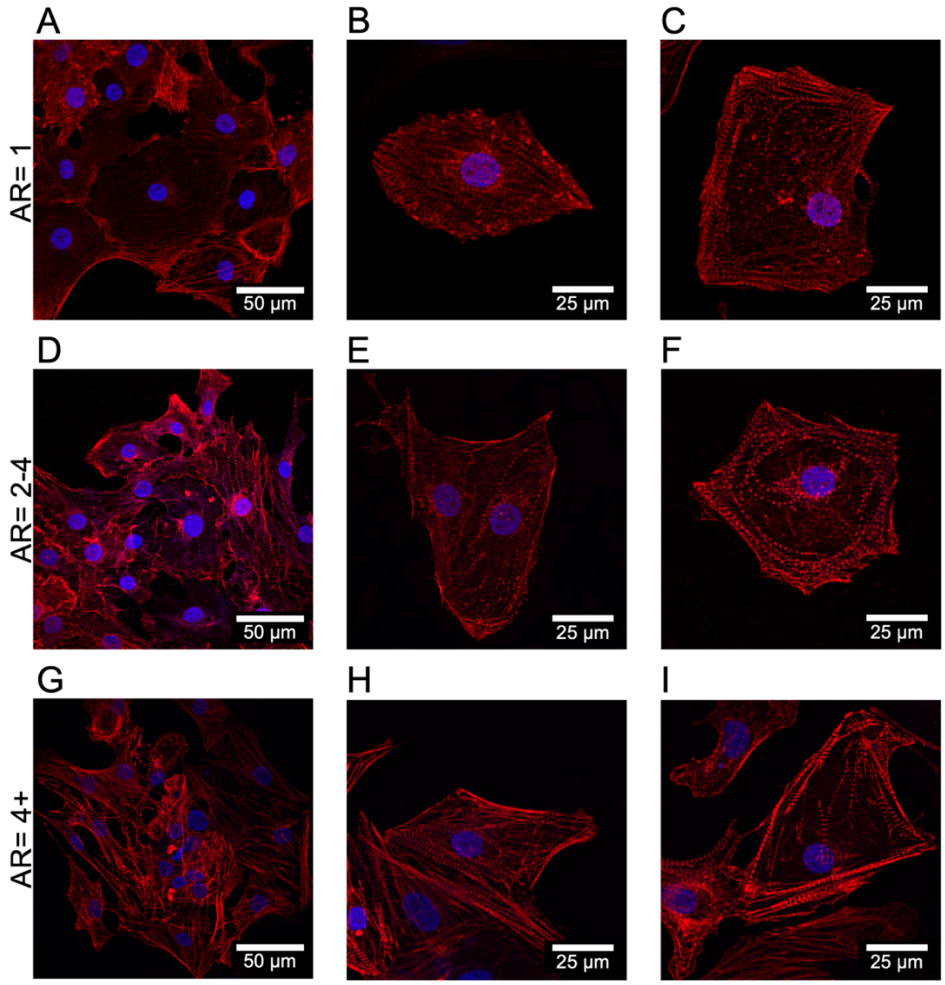

Figure 4.6 CMs from dissociated from ECT microspheroids show the presence of well-defined sarcomeres.

Day 30 microspheroids were dissociated and the sarcomeres were labeled with αSA (red) and the nuclei were stained with Hoechst 33342 (blue). The presence of well-defined

sarcomeres can be visualized in CMs at each of the axial ratios; however, there is quite a bit of intra-batch heterogeneity in sarcomere definition and organization at each axial ratio.

Data-driven modeling to predict CM content on day 10

Previously, existing bioreactor data of PSC-CM production in self-aggregated EBs throughout differentiation was used for constructing data-driven models to predict CM content on day 10 (Williams et al. 2020). These models were able to predict whether a CM differentiation would be "insufficient" by day 7 with a 90% accuracy and precision using random forests and Gaussian process modeling. Cardiac differentiation from PSCs is inherently complex, requiring tight control of the Wnt pathway through small molecule dosing, and relying on several downstream autocrine and paracrine signaling for successful differentiations. This work demonstrated that advantage of data-driven models to study combinations of features and assess their impact on resulting cardiac differentiation outcome.

Building on this work, feature selection and data-driven model development was performed to predict resulting CM content on day 10 for the ECT microspheroids. Initially, feature engineering was performed to obtain a set of potential inputs, or features, for predicting CM content. The linear correlation between the continuous features and the CM content was calculated (Figure 4.7). As expected, there were no strong linear correlations between any of the features and resulting efficiency of cardiac differentiation; however, there were strong correlations between some of the features. For the features that were strongly correlated (> 0.9 correlation), only one of the features was used; this resulted in a final feature set containing 12 features. The final features used for building the models

were the number of cells, passage post-freeze, differentiation media, CHIR concentration, cell concentration, PEG-fibrinogen concentration, microspheroid size, axial ratio, surface area (S) divided by volume (V) divided by CHIR concentration, CHIR/S, CHIR/S/V, and S/CHIR; principal component analysis was performed to reduce the dimensionality of the feature set. Using the principal components as the inputs, a classification model was trained using support vector machines to classify and predict CM content as sufficient (> 65%) or insufficient (< 65%). This model performed with a 68% accuracy, the proportion of batches correctly identified (Sokolova and Lapalme 2009), with Matthew's correlation coefficient of 0.31, a correlation statistic for binary classifications (Matthews 1975). These results indicate that there are most likely features significantly impacting cardiac differentiation outcomes that are not captured in the feature set, such as biological components previously shown to impact cardiac differentiation such as cell cycle (Laco et al. 2018), integrin expression (Santoro et al. 2019), and cell secreted factors (H. Kempf et al. 2016). Additionally, the initial experiment campaign was designed to assess ECT differentiation efficiency and CM maturity; studies to characterize the resulting CM maturity and functionality for use in model development are ongoing.

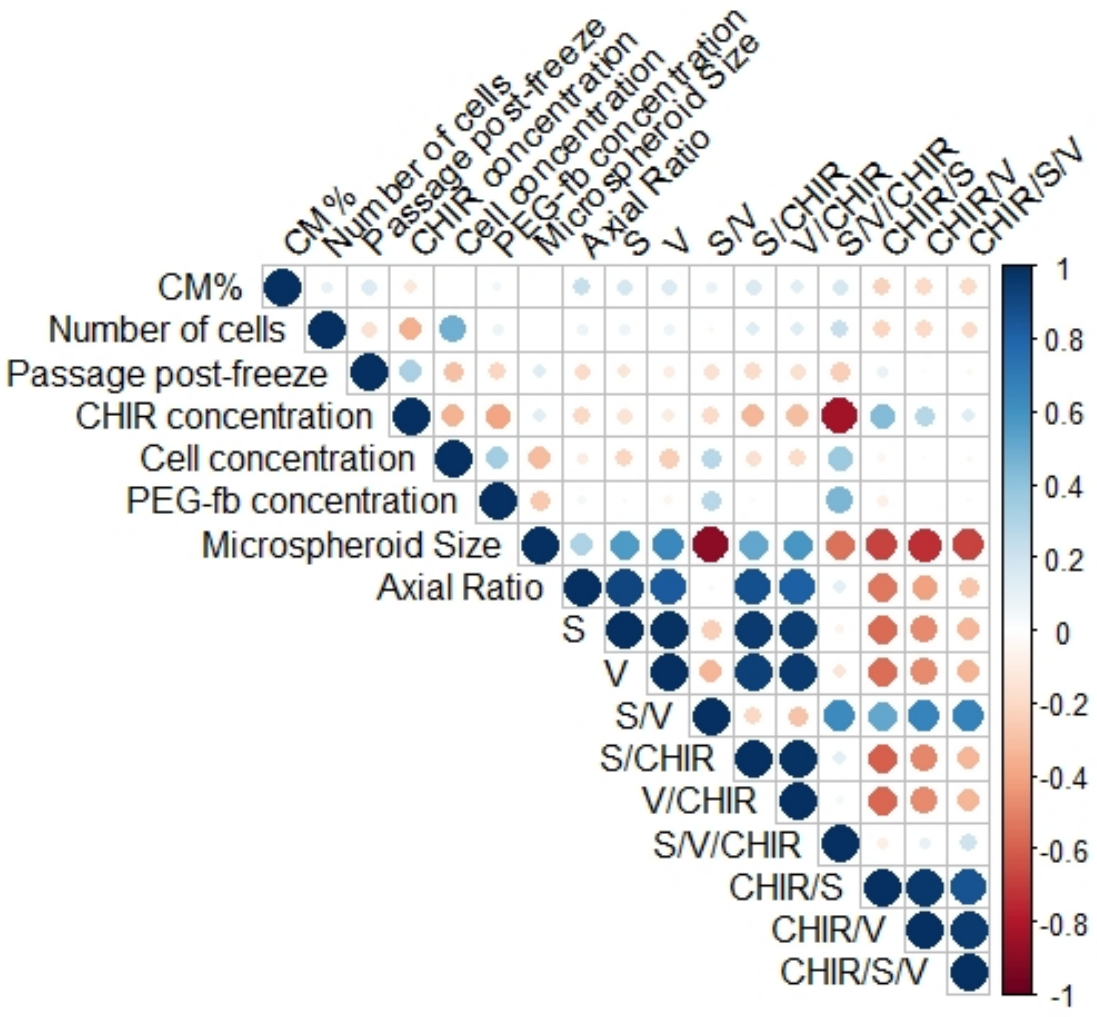

Figure 4.7 Linear correlation of ECT microspheroid production features.

Linear correlations between each of the continuous features and the resulting CM content were calculated and are shown in the plot. Both size and color of each point indicates the strength of correlation. Positive correlations are blue, and negative correlations are red.

Scalable production of ECT microspheroids

Producing clinically relevant cell numbers will require production of ECTs in large stirred-tank bioreactors. Shaker flasks are standard for initial scale-up studies; here, the production of microspheroidal ECTs from encapsulated hiPSCs is shown. For initial studies, a high

AR and diameter were selected to try to maximize CM yield, or the number of CMs per input hiPSCs. Microspheroids were produced with an initial diameter of 960 ± 11 μm and AR of 4 ± 0.7 (n = 3 batches). Microspheroids were highly uniform within a batch and between batches as shown in the violin plots for the diameter (Figure 4.8A) and AR (Figure 4.8B). Cardiac differentiation followed the same protocol as above; following encapsulation on day -3, the cell-laden microspheroids were transferred to a shaker plate and cultured for three days in stem cell media in static conditions. On day 0, cardiac differentiation was initiated, and the shaker flasks were transferred to a shaker plate at 70 rpm. On day -3, 8.7 ± 1.3 million cells were encapsulated and between day -3 and day 0, the cell number slightly increased to 10 ± 1.1 million cells. Similar to previous experiments in a well-plate, the hiPSCs continued to proliferate and remodel the hydrogel matrix, and the total cell number increased to 34 ± 15 million cells on day 5. On day 10, each batch consisted of 27 ± 4.3 million cells (Figure 4.8C). On day 10, the normalized cell number was 3.11 ± 0.61, normalized to the number of cells encapsulated on day -3; this corresponds to approximately 250,000 cells per microspheroid on day 10. ECT microspheroids efficiently differentiated in the shaker flasks with 75.7 ± 4.6% MF20+ and 74.7 ± 4.5% cTnT+ (Figure 4.8D, n = 3 batches). This corresponds to a cell yield of 2.37 ± 0.52 CMs per hiPSC. The other supporting cell types obtained during cardiac differentiation are known to play a role in CM function and maturation (Giacomelli et al. 2020), and the percent of fibroblasts was quantified by labeling with antibody TE-7. ECTs were composed of 9.4 ± 8.3% fibroblasts (Figure 4.8D); surprisingly, there was large variability in the number of resulting fibroblasts between batches following cardiac differentiation, especially with regard to the consistency of CM content in these studies.

Overall, these results indicate that microfluidic encapsulation of hiPSCs in PEG-fibrinogen microspheroids and direct cardiac differentiation is suitable for scalable production.

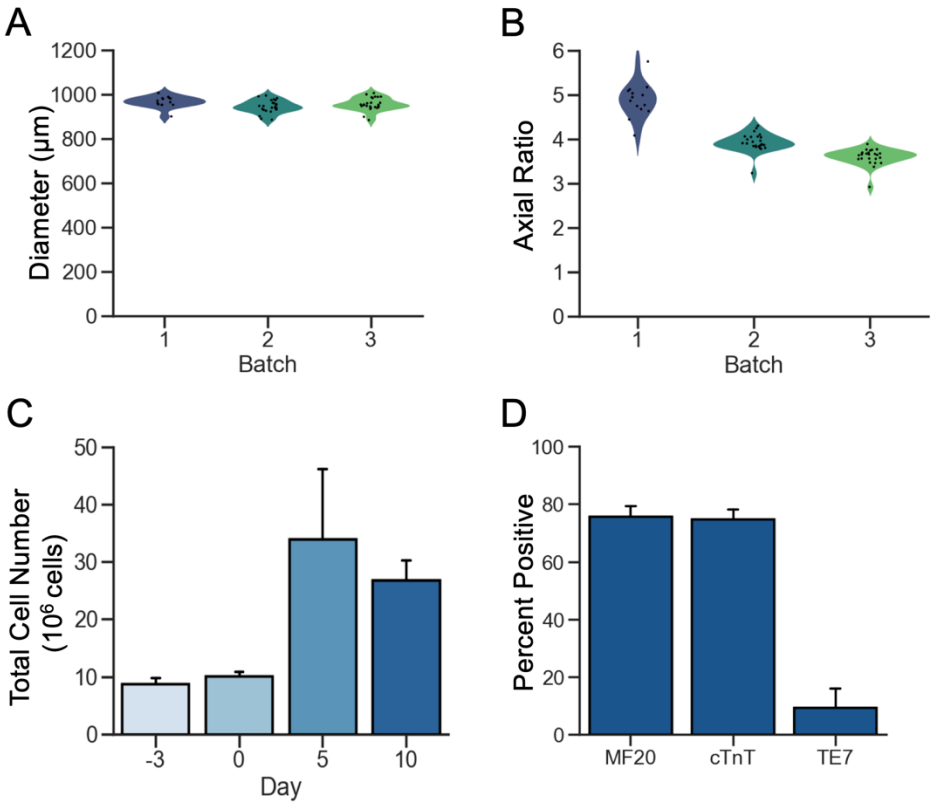

Figure 4.8 Scalable Production of ECT-Microspheroids.

Initial scale-up studies indicate the microspheroid platform can be used to produce a large number of CMs. A microfluidic system was used to encapsulate microspheroids with a (A) diameter of 960 ± 11 μm and (B) AR of 4 ± 0.7 (n = 3 batches). These batches were highly uniform within a batch and between batches as visualized in violin plots; each black dot represents a microspheroid. (C) On day -3, 8.7 ± 1.3 million cells were encapsulated, and the total cell numbers were 10 ± 1.1, 34 ± 15, and 27 ± 4.3 million cells on days 0, 5, and 10, respectively. (D) Cardiac differentiation occurred efficiently in the microspheroids differentiated in the shaker flask with 75.7 ± 4.6% MF20+ and 74.7 ± 4.5% cTnT+, with 9.4 ± 8.3% fibroblasts (TE7).

Conclusions

In this study, successful encapsulation of hiPSCs in microspheroids with varying sizes and shapes is demonstrated. A custom, flexible microfluidic system was used for encapsulation of the hiPSCs in microspheroids with high cell viability. Microspheroids were uniform within a batch, and hiPSC-laden microspheroids could be produced with diameters between 400–1000 μm with ARs of 1–9. Encapsulated hiPSCs were used for chemically defined direct cardiac differentiation, and the resulting CM content and yield were quantified on day 10 using flow cytometry. High CM contents and resulting cell yields could be obtained at each geometry, with CM contents as high as 98% CMs; however, there was a large amount of variability between batches, and the reason for this variability was not immediately clear from single-feature analysis. Feature selection was performed to obtain a set of 12 features that were used to build data-driven models that could predict CM content on day 10 with 68% accuracy. ECT microspheroids had defined sarcomeres by day 30 and indication of progressing cell elongation and sarcomere organization in microspheroids with higher ARs compared to microspheres (AR = 1). Future work to assess the resulting CM functionality and maturity is ongoing to elucidate any initial geometry, cell concentration, or PEG-fibrinogen concentration effects on CM maturity. Furthermore, proof-of-concept scale-up studies were performed showing that ECT microspheroids can be differentiated in shaker flasks, obtaining over 40 million cells per batch, and have the potential for use in stirred-tank bioreactors.

Chapter 5: LAP-Initiated Photocrosslinking of PEG-fibrinogen for ECT Formation from Encapsulated hiPSCs

Introduction

Cardiovascular disease (CVD) is the leading cause of death in the United States and globally today, accounting for approximately 800,000 deaths annually (Virani et al. 2020). The large financial and health burden caused by CVD is due in part to the inability of the myocardium to regenerate after disease or damage. Current treatments for CVD, other than a full heart transplant, only treat the resulting side-effects, decrease the risk of further problems, and are inadequate at restoring function. However, the use of pluripotent stem cell-derived cardiomyocytes (PSC-CMs) has shown promise in regenerative medicine to improve cardiac function following damage (Chong et al. 2014), for enhancing high-throughput drug-screening (Mordwinkin, Burridge, and Wu 2013; H.F. Lu et al. 2017; Mathur et al. 2015; Del Alamo et al. 2016), and for studying development and disease (Kodo et al. 2016; Smith et al. 2017). Because adult CMs cannot be cultured long term *in vitro*, stem cell differentiation is necessary, and human induced pluripotent stem cells (hiPSCs) have shown success in ECT applications because of their ability to be maintained long-term with maintained pluripotency and proliferation phenotypes, and the use of hiPSCs offers the possibility of an autologous treatment option. Typically, ECT is produced by combining dissociated PSC-CMs with a biomaterial following cardiac differentiation in either monolayers or embryoid bodies (EBs). Previously in our lab, a novel direct differentiation platform was established in which the PSCs are combined with a biomaterial and directly differentiated to form 3D-ECT in an ontomimetic approach (P. Kerscher, Turnbull, et al. 2016; Petra Kerscher, Kaczmarek, et al. 2016).

Biomaterials that can undergo rapid polymerization to form a crosslinked network are critical for successful production of engineered tissue products, particularly those utilizing challenging cell types, including hiPSCs. The two primary methods for crosslinking use modifications to physical properties or chemical structure. Physical crosslinking involves changing material properties by changing temperature, pH, electric field, or salt or ionic concentrations; whereas, chemical crosslinking occurs by changing the chemical structure of the material, typically by the addition of functional groups (Yu and Ding 2008). Photocrosslinking, one type of chemical crosslinking, is beneficial for use in tissue engineering due to the ability for crosslinking to occur rapidly and at mild conditions, such as physiological or ambient temperature and pH. During photocrosslinking, a photoinitiator, a compound with high absorption in the ultraviolet (UV) or visible light range, provides free radicals for polymerization. Key parameters for photoinitiators are their biocompatibility, solubility in aqueous solutions, stability, and cytotoxicity (Nguyen and West 2002). Free radical generation for photocrosslinking occurs through either photocleaving, where two radicals are produced following light absorption (Type I), or through the hydrogen abstraction of a coinitiator (Type II). Certain molecules with absorption in the light range with carbon–carbon, –chlorine, –oxygen, or –sulfur bonds can be cleaved for the formation of radicals when exposed to light (Nguyen and West 2002). During hydrogen abstraction, a ketyl radical is formed by the abstraction of hydrogen from a donor molecule. Commonly used Type I photoinitiators in tissue engineering are Irgacure 2959 (Mironi-Harpaz et al. 2012; Fedorovich et al. 2009) and lithium phenyl-2,4,6-trimethylbenzoylphosphinate (LAP) (Fairbanks et al. 2009; Brooks et al. 2018), and Eosin Y is the most commonly used Type II photoinitiator (Elbert and

Hubbell 2001; Shih and Lin 2013; Cruise et al. 1998). There has been much interest in 3D printing tissue structures, particularly through photocrosslinking with photoinitiators Irgacure 2959 and LAP (Pereira and Bártolo 2015).

PEG-fibrinogen is a hybrid biomaterial consisting of a natural component, fibrinogen, covalently crosslinked to a synthetic component, poly(ethylene glycol) diacrylate (PEGDA); PEG-fibrinogen can be rapidly photocrosslinked (less than 30 s), has tunable properties, and supports cardiac differentiation for production of 3D-ECT (Almany and Seliktar 2005). In our previous work for the formation of 3D-ECT, photocrosslinking of PEG-fibrinogen occurred through free-radical polymerization with Eosin Y. Although, Eosin Y is water soluble, biocompatible, and absorbs light in the visible range, it requires a coinitiator that can be mildly cytotoxic and has green autofluorescence that overlaps with commonly used fluorophores in cell imaging assays. Previously, an hiPSC line has been developed with a genetically encoded voltage indicator (GEVI) (Shinnawi et al. 2015); however, the autofluorescence of Eosin Y in the green channel overlaps with this GEVI. Therefore, this project investigates the ability to use a photocleavage (Type I) photoinitiator, LAP, for crosslinking of PEG-fibrinogen hydrogels for 3D-ECT production and non-destructive monitoring of cardiac electrophysiology. The ability to non-destructively monitor CM differentiation and function through incorporation of fluorescent reporter cell lines in 3D would provide substantial improvements for utilization of ECT in clinical applications.

Here, we present successful LAP-initiated photocrosslinking of PEG-fibrinogen for production of 3D-ECT directly differentiated from encapsulated hiPSCs. LAP is a cytocompatible photoinitiator with high water solubility that can be crosslinked with

ultraviolet (UV) or blue (405 nm) light (Fairbanks et al. 2009). Here, two light sources were used for crosslinking PEG-fibrinogen with LAP, including a UV lamp (365 nm) and handheld, low-cost blue light flashlight (390–410 nm); these hydrogels were compared to our previously established method using Eosin Y with visible light photocrosslinking. Successful crosslinking of PEG-fibrinogen with LAP occurred for both light sources, and the mechanical properties of acellular hydrogels and cellular hydrogels were determined using parallel plate compression. Encapsulated hiPSCs maintained high viability and appropriate phenotype. Following encapsulation on day -3, cardiac differentiation was initiated on day 0, and the growth of the tissues throughout cardiac differentiation was quantified. Efficient cardiac differentiation occurred in the PEG-fibrinogen constructs crosslinked with LAP, and cardiac tissue contraction could be visualized by day 8 of differentiation, with synchronous contractions occurring by day 20. Finally, crosslinking with LAP allowed for monitoring of the action potentials, and the ECTs displayed features of maturing CMs over time.

Materials and Methods

HiPSC cell culture

Stem cell lines IMR-90 (WiCell) and Un-Arc 16 Facs II (UA16F2) were used in this study. Cell line UA16F2 was kindly provided by Dr. Lior Gepstein at Technion — Israel Institute of Technology and contained a GEVI (Shinnawi et al. 2015). The hiPSCs were maintained in E8 or mTeSR (STEMCELL Technologies) media on a Matrigel (Corning) or Geltrex™ LDEV-Free Reduced Growth Factor Basement Membrane Matrix (Gibco) coated flask. E8 media consisted of ascorbic acid (64 mg/L, Sigma), sodium selenite (14 μg/L, Sigma),

sodium bicarbonate (543 mg/L, Sigma), insulin (20 mg/L, Sigma), transferrin (10.7 mg/L, Sigma), basic fibroblast growth factor (100 μg/L, Peprotech), and transforming growth factor-beta (2 μg/L, Peprotech) in DMEM/F12 (Gibco). When the cells reached 70-90% confluency, they were passaged with Accutase (Innovative Cell Technologies) or Versene (Gibco) and resuspended in cell culture media containing 10 μM Y-27632 (rock inhibitor, STEMCELL Technologies).

PEG-fibrinogen synthesis

All chemicals were purchased from Sigma-Aldrich unless otherwise specified. PEGDA and PEG-fibrinogen were prepared as described previously (DeLong, Moon, and West 2005; Dikovsky, Bianco-Peled, and Seliktar 2006). Briefly, to synthesize PEG-fibrinogen, denatured bovine fibrinogen (300 mg) was added to 8M urea (Lonza) in PBS (urea-PBS), and the pH was adjusted to 7.4. Tris(2-carboxyethyl) phosphine (22.53 mg, TCEP) was added to the solution, and the pH was adjusted to 8.0. PEGDA (1.94 g, 10 kDa) was completely dissolved in urea-PBS, and the PEGDA solution (280 mg/mL) was added to the fibrinogen solution (7 mg/mL) and allowed to react at room temperature (RT) for 3 hours. PEG-fibrinogen was precipitated using acetone (398 mL, BDH), collected, and then dissolved in urea-PBS. The product was dialyzed against sterile PBS for 24 hours at 4°C and stored long-term at -80°C. The protein content was determined using a Pierce BCA protein assay kit (ThermoScientific), and the PEGylation percentage was determined by lyophilization.

PEG-fibrinogen hydrogel encapsulation and cardiac differentiation

Polymer precursor solutions were prepared by combining PEG-fibrinogen with 1.5% (v/v) triethanolamine (TEOA, Acros), 0.39% (v/v) n-vinylpyrrolidone (NVP), 12.5 μM rock inhibitor, and 0.1 mM Eosin Y (EY, Fisher Scientific) or by combining PEG-fibrinogen with 2.5 mM LAP and 12.5 μM rock inhibitor. The hiPSCs were encapsulated using previously published methods (P. Kerscher, Turnbull, et al. 2016; Petra Kerscher, Kaczmarek, et al. 2016). Briefly, a polydimethylsiloxane (PDMS) mold with either circular or rectangular holes was attached to an acrylated glass coverslip. The hiPSCs were enzymatically detached and centrifuged to obtain a cell pellet; the cell pellet was combined with the PEG-fibrinogen precursor solution containing either 0.1 mM Eosin Y and coinitiators or 2.5 mM LAP. The precursor-hiPSC solution was pipetted into the holes of the PDMS mold and photocrosslinked. Two light sources were used for photocrosslinking with LAP: a UV Lamp (Cole-Parmer, 365 nm) and an LED visible light source (HOPDAY, 390–410 nm) for 30 s and 120 s, respectively.

Encapsulated cells were cultured for three days with daily media changes prior to initiation of cardiac differentiation on day 0. Cardiac differentiation occurred using previously published methods with RPMI/B27 (P. Kerscher, Turnbull, et al. 2016; Lian et al. 2013b) and chemically defined media (CDM3, (Halloin et al. 2019; Burridge et al. 2014). Cardiac differentiation was directed through temporal control of the Wnt signaling pathway, employing small molecules for subsequent activation and inhibition of the pathway. For the RPMI/B27 differentiation, cardiac differentiation was initiated on day 0 by adding RPMI/B27 w/o insulin (Gibco) supplemented with 12 μM CHIR99021 (StemCell Technologies) to the hydrogels. After 24 hours, the media was changed to

RPMI/B27 w/o insulin. On day 3 of differentiation, 2 mL of fresh RMPI/B27 w/o insulin was combined with 2 mL of old media and was supplemented with 5 μM IWP2 (StemCell Technologies) for 48 h. On day 5, the media was replaced and RPMI/B27 w/o insulin, and on day 7 the media was replaced with RPMI/B27. Following the completion of cardiac differentiation (day 7), the media was changed every 3–4 days with RPMI/B27.

CDM3 media contained RPMI 1640 (Gibco) supplemented with 500 μg/mL recombinant human albumin and 213 μg/mL ascorbic acid. To initiate cardiac differentiation on day 0, CHIR99021 (5–7.5 μM) was added to the media; exactly 24 h later, the media was exchanged for CDM3 supplemented with 5 μM IWP2. Fresh CDM3 was added on days 3, 5, 7, and 10; following day 10, the ECTs were cultured with RPMI/B27, and the media was exchanged every 3–4 days.

Viability assay

Cell viability was assessed using a Live/Dead Viability/Cytotoxicity Kit (Invitrogen). The samples were washed with PBS, and then calcein AM, ethidium homodimer, and Hoechst 33342 in PBS were added to the samples for 30 mins at RT. The samples were washed with PBS to remove any background and then were imaged using an Andor Luca S camera attached to a Nikon Eclipse Ti fluorescence microscope. The FITC and TRITC filters were used for imaging calcein AM labeled cells (live) and ethidium homodimer labeled cells (dead), respectively, and the DAPI filter was used for imaging the cell nuclei labeled with Hoechst 33342.

Tissue growth analysis

Phase contrast images were taken prior to, during, and after cardiac differentiation, and were imported into Image-J software and converted to a binary image for automated quantification of tissue area using standard Image-J plugins.

Mechanical Testing using a Microsquisher

Parallel plate compression was used to determine the Young's Modulus of the hydrogels using a micron-scale mechanical testing system, Microsquisher (CellScale). Measurements occurred in 37 °C PBS. The stress (σ) and strain (ε) were calculated from the measured force, tissue compression area, and height. Young's modulus was determined from the linear range of the stress versus strain curve.

Flow cytometry

Tissues were dissociated by incubating with 1 mg/mL Collagenase-b (Roche) and 0.05 mg/mL DNase (Worthington) for 10–15 minutes at 37 °C, and a cell pellet was collected through centrifugation. After washing with PBS, the cells were incubated with Zombie Dye (Biotium) for 30 min at 4 °C. Cells were then washed with Blocking Buffer (1% bovine serum albumin (BSA, Sigma), 10% fetal bovine serum (FBS, Atlanta Biologics) in PBS), and then fixed with Foxp3 Transcription Factor Staining Buffer Set (eBioscience) overnight at 4 °C. The cells were then filtered using a 40 μm cell strainer (Scienceware Flowmi) and permeabilized with FACS buffer (1% BSA, 10% FBS in 1x Permeabilization Buffer (eBioscience)) at RT for 30 mins. The primary antibodies (cTnT (1:400, Invitrogen), MF20 (1:200, DSHB), PDGFR-α (20 μL/1x10^6 cells, BD

Biosciences) and/or TE-7 (1:100)) were then incubated with the cells for 1 hour at RT or 4°C overnight. After incubation in the primary antibody, washing occurred with Permeabilization Buffer. The secondary antibodies (1:300, AlexaFluor 488 goat anti-rabbit IgG and AlexaFluor 647 goat anti-mouse IgG (ThermoFisher)) were added for 30 mins at RT. The cells were then washed with Permeabilization Buffer and resuspended in Blocking Buffer for analysis. A Beckman Coulter CytoFlex LX was used for sample analysis. At least 20,000 live cells were recorded for analysis. Isotype controls (Anti-Mouse IgG1 and Anti-Rabbit IgG (ThermoFisher)) were used to ensure there was not any non-specific binding.

Immunostaining

Tissues were either dissociated following the dissociation protocol above or immunostained whole. Following tissue dissociation, the cell solution was plated on fibronectin-coated glass coverslips. After culturing at least 48 h following dissociation, the dissociated cells or whole tissues were washed with PBS and fixed with 4% paraformaldehyde (Electron Microscopy Sciences) in PBS for 20 min at RT. The cells were then permeabilized with PBS-T (PBS + 1 % w/v bovine serum albumin (BSA) and 0.2% v/v TritonX-100) three times for 10 min each. Blocking buffer was added for either 30 mins at RT or overnight at 4°C. The primary antibodies, sarcomeric α-actinin (αSA), cardiac troponin T (cTnT), Ki67, Oct4, Connexin 43(Cx43), and/or Caveolin 3 (Cav3), were added to the cells for 1 h at RT or overnight at 4°C. Following incubation with the primary antibodies, the cells were washed with PBS-T minimally 4 times. The secondary antibodies, 488-rabbit, 568-mouse (1:300), along with Hoechst 33342 (0.02 mg/mL) were

added for 40 min at RT and then washed with PBS-T at least three times. A Nikon A1R laser-scanning confocal microscope was used for imaging.

Contraction Analysis

Contraction analysis was done using motion tracking software in which macroblocks were tracked between frames to determine the beat rate in beats per minute (BPM), time interval in seconds, maximum contraction velocity in μm/s, and maximum relaxation velocity in μm/s. Videos of contractions, 10 s in length, were taken using an Andor Luca S camera attached to the microscope, converted to a series of tiff files, and imported into the Motion GUI in the open source MATLAB code (Huebsch et al. 2015).

Optical mapping of calcium and voltage transients

Optical mapping recordings were taken using a high-speed camera (Andor iXon+ 860 EMCCD) attached to a fluorescent microscope (Nikon Eclipse Ti) with a Prior Lumen 200 light source. Calcium and/or voltage recordings of CMs were captured using the established optical mapping system in our lab. For calcium recordings, the cardiomyocytes were stained with 5 μM Rhod-2 AM dye (Invitrogen) and 10 μM blebbistatin (EMD) for 30–120 mins. The GEVI cell line has a green fluorescent voltage reporter that decreases in fluorescent intensity during membrane depolarization that can be visualized immediately prior to tissue contraction. The videos of calcium and/or voltage transients were taken using the FITC and TRITC filters, respectively, in either Tyrode's solution or media. Tyrode's solution was prepared by combining 1.8 mM calcium chloride and 5.0 mM glucose with 5.0 mM HEPES, 1.0 mM magnesium chloride, 5.4 mM potassium chloride, 135 mM

sodium chloride, and 0.33 mM sodium phosphate; the pH was adjusted to 7.4 with sodium hydroxide. The samples were heated to 37 °C by perfusion of warm Tyrode's solution through the optical mapping system or through the use of a stage-top incubator (In Vivo Scientific) for non-destructive recordings in media or Tyrode's solution. When electrically paced, pacing starting at 0.5 Hz and continually increased by 0.5 Hz until 1:1 capture was no longer observed. Recordings were analyzed using a custom MATLAB script in which the change in fluorescence were used to calculate the calcium transient duration (CTD), heterogeneity index (HI), and conduction velocity.

Statistical analysis

Unless otherwise indicated, results are presented as mean ± standard deviation. One-way ANOVA with post-hoc analysis using Tukey's test for samples with equal variance and the Games-Howell test for unequal variances was performed using Minitab. Statistical significance was determined when $p < 0.05$.

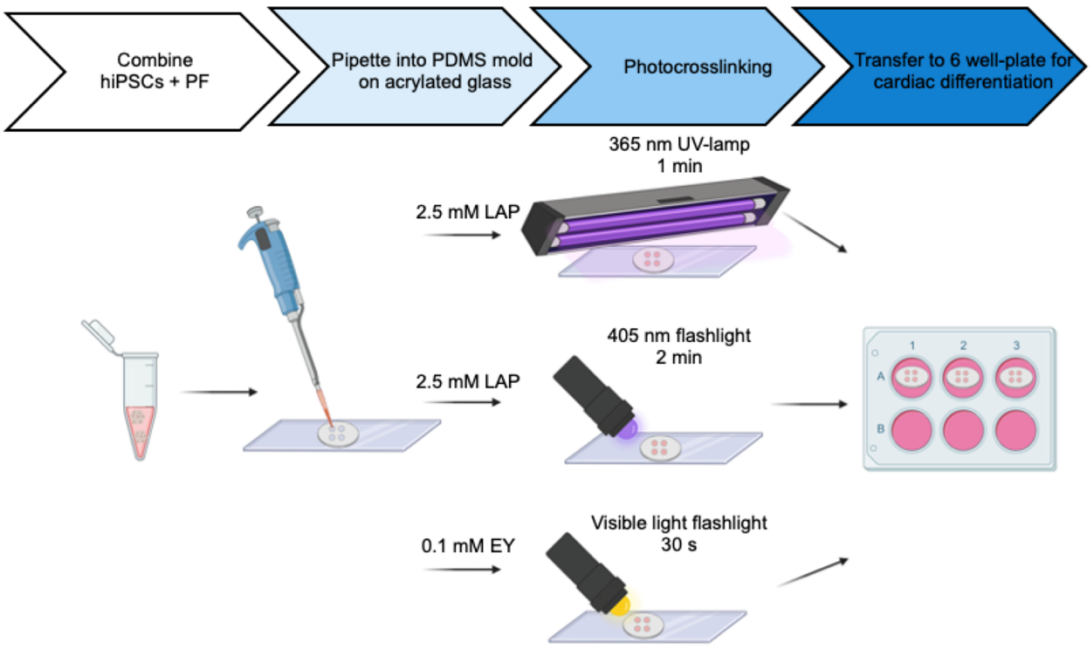

Figure 5.1 Formation of ECT through LAP-initiated photocrosslinking.

For encapsulation, a cell pellet of hiPSCs was combined with the polymer precursor solution, consisting of PEG-fibrinogen and the photoinitiator species. The hiPSC and polymer precursor solution was pipetted into a PDMS mold on acrylated glass, photocrosslinked, and transferred to a well plate for cardiac differentiation. Two different light sources, a UV lamp (365 nm, 3 mW/cm^2) and low-cost handheld blue light (405 nm, 28 mW/cm^2) were used for photocrosslinking LAP hydrogels (2.5 mM). Eosin Y (0.1 mM, 64 mW/cm^2) hydrogels were photocrosslinked using a handheld visible light source. Photocrosslinking occurred for 1 minute, 2 minutes, and 30 seconds for the UV lamp (LAP 365), blue light (LAP 405), and Eosin Y (EY), respectively. Figure created with Biorender.com

Results

Successful encapsulation of PEG-fibrinogen through LAP-initiated photocrosslinking

The photoinitiator, LAP, could be used for photocrosslinking of PEG-fibrinogen hydrogels and for encapsulation of hiPSCs for directed cardiac differentiation. Formation of the cell-laden hydrogels occurred as previously described (P. Kerscher, Turnbull, et al. 2016), in which the hiPSCs were combined with the polymer precursor solution, pipetted into the holes of a PDMS mold on acrylated glass, photocrosslinked, and transferred to a 6-well plate with hiPSC media (Figure 5.1). Two different light sources were used for crosslinking with the photoinitiator LAP for comparison to our previously published results using Eosin Y initiation for photocrosslinking with a visible light source. LAP has a maximum absorbance at 375 nm with absorbance from 340–400 nm (Fairbanks et al. 2009); therefore, a UV lamp (365 nm) and a handheld, low-cost blue light flashlight (390–410 nm) were used for photocrosslinking. The light intensities of the light sources used for photocrosslinking were 3, 28, and 64 mW/cm^2 for the UV lamp (LAP 365), blue light (LAP 405), and visible light sources (EY), respectively. Crosslinking of the hydrogels successfully occurred with a LAP concentration of 2.5 mM and Eosin Y concentration of 0.1 mM at crosslinking times of 1 min, 2 min, and 30 s for LAP 365, LAP 405, and Eosin Y, respectively. Acellular hydrogels were prepared to assess the mechanical properties, and the elastic moduli were 540 ± 158, 266 ± 36.9, and 521 ± 113 Pa for LAP 365, LAP 405, and Eosin Y, respectively, quantified using parallel-plate compression (Figure 5.4N, $n \geq 7$ hydrogels). Hydrogels crosslinked with LAP 405 were significantly softer than those crosslinked with LAP 365 and EY, with no significant difference between LAP 365 and

EY hydrogels ($p < 0.05$). Furthermore, the LAP hydrogels exhibited no autofluorescence following encapsulation, overcoming the primary limitation of Eosin Y, enabling long-term tracking with a genetically encoded voltage indicator.

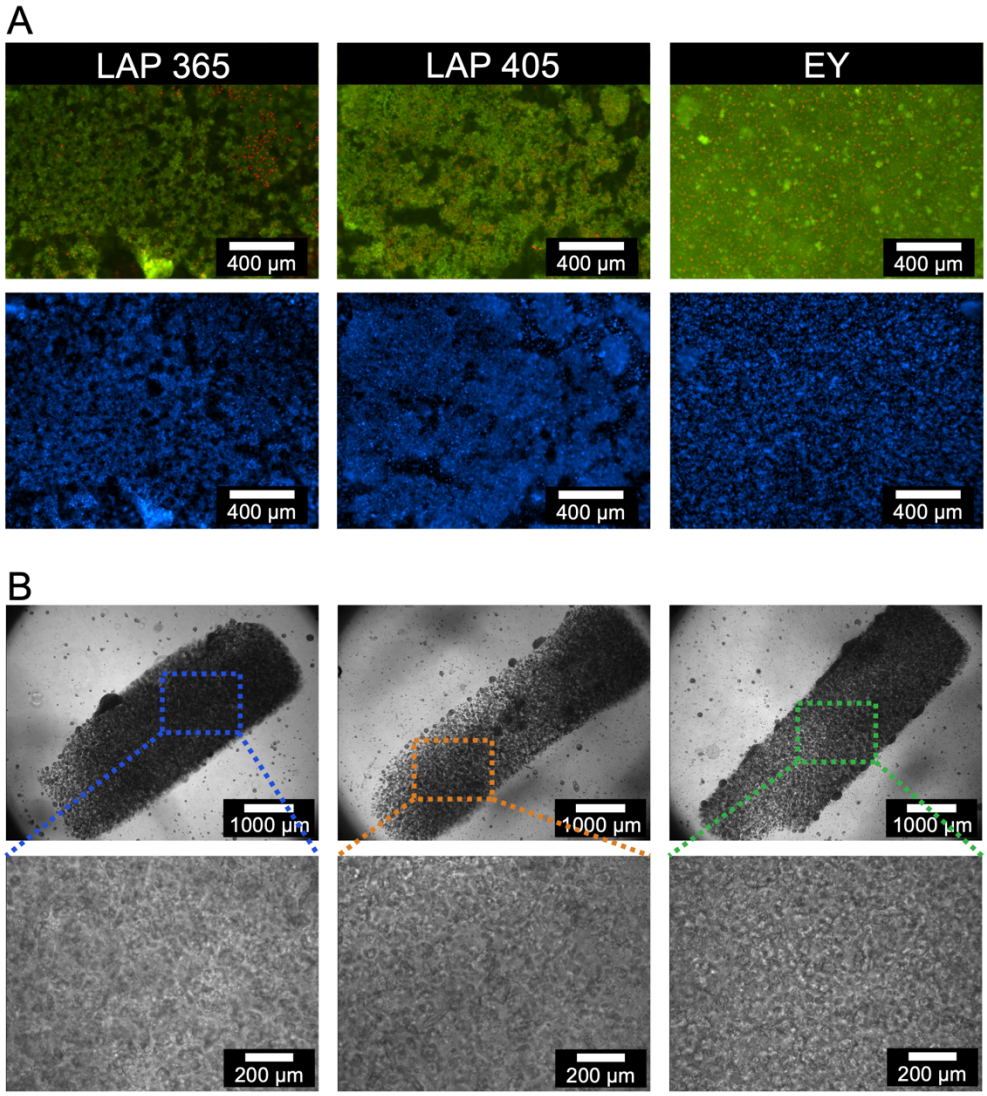

Figure 5.2 HiPSCs maintain high viability following photocrosslinking with UV, blue, and visible light.

(A) Following encapsulation of hiPSCs in PEG-fibrinogen with LAP and Eosin Y (EY) initiated photocrosslinking, cells maintain high cell viability with live cells in (green) and

dead cells in (red) with (B) appropriate morphology of hiPSCs in rounded colonies at a high cell density (> 50 million cells/mL).

Pluripotent stem cells maintain high viability and appropriate phenotype in LAP-photocrosslinked hydrogels

The hiPSCs were encapsulated in PEG-fibrinogen to form cell-laden hydrogels with both microisland and rectangular geometries. The microislands were disk shaped in geometry, with an initial diameter of 3.7 mm and height of 0.8 mm; the rectangular molds had an initial length of 6.4 mm, width of 2.1 mm, and were 0.85 mm in height. Encapsulation occurred on day -3, and the cells were cultured for 3 days prior to initiation of cardiac differentiation. Following encapsulation, the hiPSCs maintained high viability (Figure 5.2A), and cell-laden hydrogels crosslinked with LAP exhibited less background compared to Eosin Y when using a Live/Dead viability kit, demonstrating the decrease in autofluorescence. The hiPSCs were encapsulated at a high cell density (≥ 50 million cells/mL), a critical parameter for the success of this direct differentiation platform (Figure 5.2B). Rounded colonies of hiPSCs can be visualized on day -2, a characteristic of hiPSC viability and proliferation following encapsulation (Figure 5.2B). To confirm the hiPSCs maintained appropriate phenotype after LAP-initiated photocrosslinking with a UV lamp (365 nm) and a blue light (405 nm) prior to initiation of cardiac differentiation, cell-laden hydrogels were immunostained with Ki67, a proliferation marker, and Oct 4, a pluripotency marker, with nearly all of the hiPSCs within these LAP hydrogels expressing both Ki67 and Oct4 (Figure 5.3).

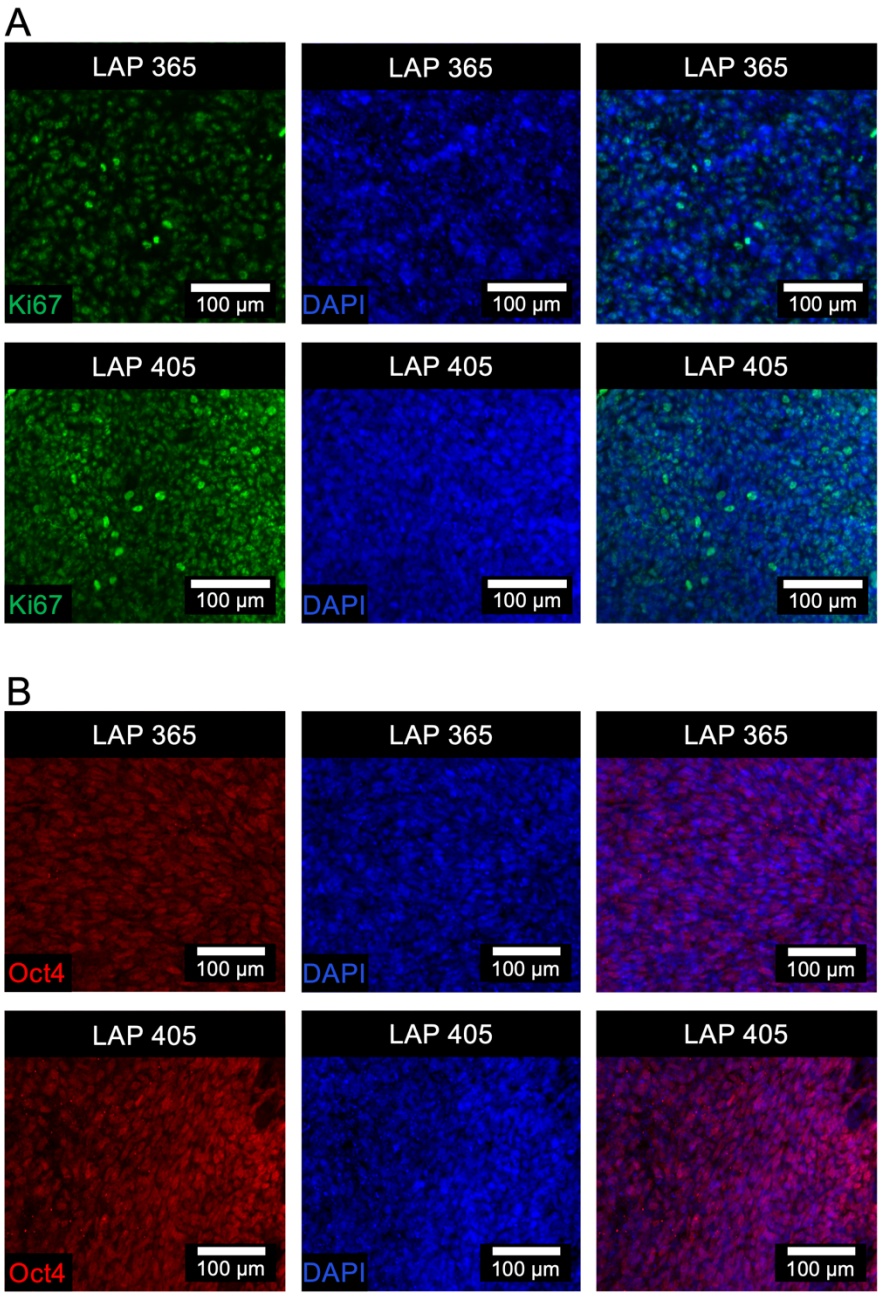

Figure 5.3 Following photocrosslinking of PEG-fibrinogen with LAP, hiPSCs appropriately express Ki67 and Oct4.

Prior to initiation of cardiac differentiation, hiPSCs encapsulated in PEG-fibrinogen photocrosslinked with LAP maintain appropriate (A) proliferative (Ki67, green) and (B) pluripotent (Oct4, red) phenotypes.

Cardiac differentiation of hiPSCs within LAP-photocrosslinked PEG-fibrinogen hydrogels

Cardiac differentiation was initiated on day 0 using previously published small molecule differentiation protocols invoking small molecule directed control of the Wnt pathway (Lian et al. 2013b; Burridge et al. 2014; Halloin et al. 2019). Cardiac specification occurred by subsequent activation and then inhibition of the Wnt pathway using CHIR, a Wnt activator, and IWP2, a Wnt inhibitor. Throughout cardiac differentiation, the cell colonies continued to increase in size, visualized through phase contrast images (Fig 4), forming a dense, continuous ECT by day 7 (Figure 5.4J–L). The overall change in tissue area increased from 1.00 on day 0 to 1.03 ± 0.03, 1.16 ± 0.17, and 1.34 ± 0.28 on days 1, 3, and 7 for LAP 365 (Figure 5.4M, n ≥ 31 tissues, normalized at each day to the day 0 area); furthermore, the tissue area increased from 1.00 on day 0 to 1.06 ± 0.05, 1.28 ± 0.16, and 1.41± 0.22 on days 1, 3, and 7 for the LAP 405 photocrosslinked tissues (Figure 5.4M, n ≥ 30 tissues, normalized at each day to the day 0 area). In comparison, the Eosin Y tissues decreased from 1.00 on day 0 to 0.99 ± 0.04 on day 1 and then increased to 1.13 ± 0.17 and 1.25 ± 0.23 on days 3 and 7, respectively (Fig 5.4M, n ≥ 23 tissues, normalized at each day to the day 0 area). Although EY tissues were significantly smaller than LAP 405 on day 3 and day 5, there was no significant difference in tissue area between any of the samples on day 7. Furthermore, there was a significant increase in tissue area from day 1 to day 7 for all conditions, indicating that tissue growth occurs similarly over the time course of cardiac differentiation.

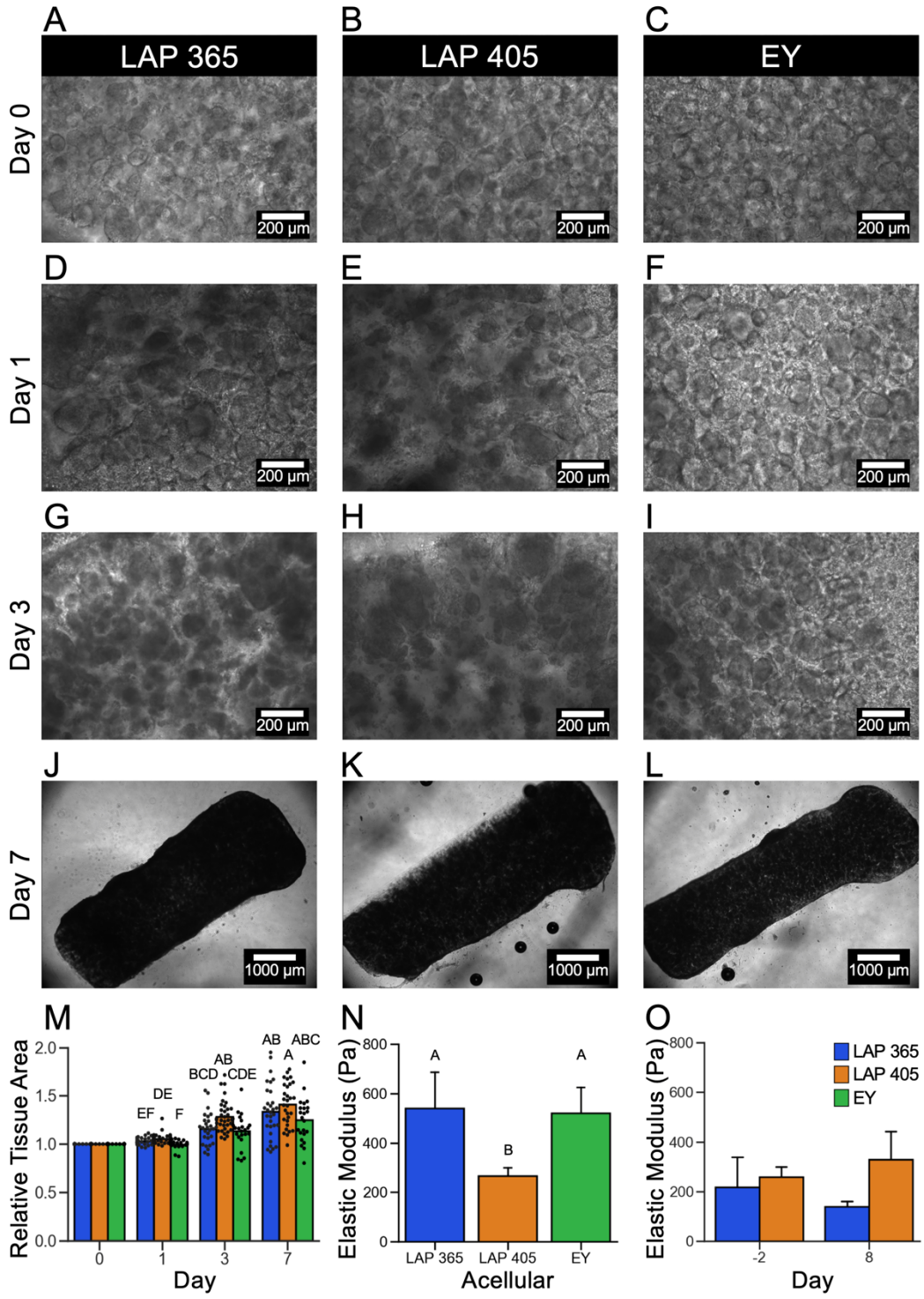

Figure 5.4 Dense continuous ECT formation following directed cardiac differentiation.

(A–L) Throughout cardiac differentiation, the cell colonies in LAP 365, LAP 405, and Eosin Y (EY) hydrogels continue to increase in size forming a dense, continuous tissue by day 7. (M) This increase in cell colony area is accompanied by an increase in overall tissue area. The tissue area for individual tissues throughout differentiation was quantified, and the relative area was calculated by normalizing tissue area at each time point to its area on day 0. The relative area of LAP 365 and LAP 405 tissues increased from 1.00 on day 0 to 1.03 ± 0.03 and 1.06 ± 0.05 on day 1, 1.16 ± 0.17 and 1.28 ± 0.16 on day 3, and 1.34 ± 0.28 and 1.41± 0.22 on days 1, 3, and 7, respectively. The EY tissues decreased from 1.00 on day 0 to 0.99 ± 0.04 on day 1 and then increased to 1.13 ± 0.17 and 1.25 ± 0.23 on days 3 and 7, respectively ($n \geq 23$ tissues). (N) The elastic modulus of LAP 405 acellular hydrogels was 266 ± 36.9 Pa, which is significantly lower than LAP 365 (540 ± 158 Pa), and EY (521 ± 113 Pa) ($n \geq 7$ hydrogels, $p < 0.05$). (O) On day -2, the elastic modulus of LAP 365 and LAP 405 cell-laden hydrogels was 218 ± 147 and 259 ± 49.4 Pa, and 140 ± 24.0 and 329 ± 131 Pa on day 8 ($n \geq 3$ hydrogels). A value of $p < 0.05$ was used for significance; samples that do not share a letter are significantly different.

On day 10, the percentage of CMs, or CM content, was determined through positive expression of MF20 and quantified with flow cytometry. There were no significant differences in the CM content or normalized cell number following differentiation for IMR90 hiPSCs, and the resulting CM content was 50.3 ± 11.4, 47.4 ± 6.97, and 49.1 ± 4.95% for LAP 365, LAP 405, and Eosin Y, respectively (Figure 5.5A, $n \geq 3$ batches). The normalized cell number, the number of cells on day 10 per number of starting hiPSCs, was 2.15 ± 0.69, 2.19 ± 1.82, and 1.03 ± 0.53 for LAP 365, LAP 405, and Eosin Y ECTs,

respectively (Figure 5.5B, n ≥ 3 batches). Furthermore, the CM content for UA16F2 hiPSCs was 39.8 ± 0.82 for ECTs photocrosslinked with LAP 365. The elastic modulus was quantified for the LAP 365 and LAP 405 tissues on day -2 and day 8; the LAP 365 tissues were 218 ± 147 Pa on day -2 and 140 ± 24 Pa on day 8; the elastic modulus of the LAP 405 tissues was 259 ± 49.4 on day -2 and 330 ± 131 on day 8 (Figure 5.4O, n ≥ 3 tissues). CMs could be visualized throughout the LAP hydrogels, visualized with positive expression of αSA (Figure 5.5C); to confirm cardiac differentiation and for visualization of individual CMs, ECTs were dissociated and labeled with cardiac marker, cTnT (Figure 5.5D). ECT formation and differentiation occur similarly for all three conditions; although not statistically significant, tissues photocrosslinked with LAP, both with the 365 and 405 nm light sources, had a higher trend of normalized cell numbers on day 10 compared to those photocrosslinked with the visible light source. This indicates that the exposure to the UV and blue light used for rapid crosslinking (1–2 min) does not cause any differences in hiPSC viability and proliferation and resulting cardiac tissue formation and differentiation in PEG-fibrinogen hydrogels compared to photocrosslinking with Eosin Y.

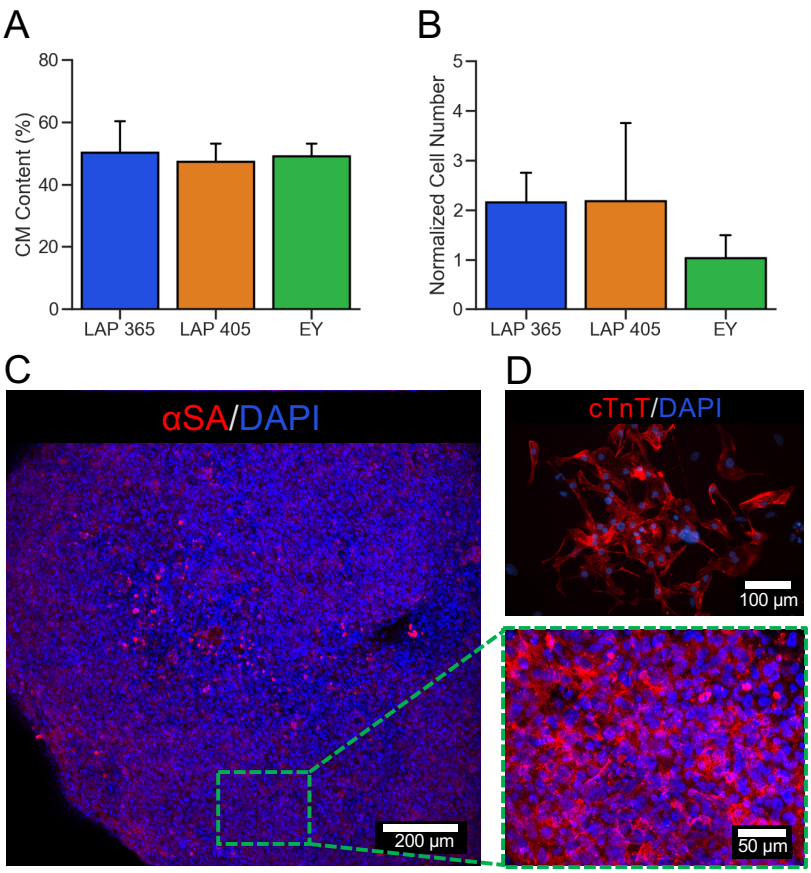

Figure 5.5 Successful cardiac differentiation in ECTs photocrosslinked with LAP.

(A) The CM content on day 10 was 50.3 ± 11.4, 47.4 ± 6.97, and 49.1 ± 4.95% for LAP 365, LAP 405, and EY, respectively. (B) The number of cells on day 10 normalized to the starting number of hiPSCs was 2.15 ± 0.69, 2.19 ± 1.82, and 1.03 ± 0.53 for LAP 365, LAP 405, and EY ECTs on day 10. (C) CM differentiation occurred throughout the tissues photocrosslinked with LAP 365, visualized by positive expression of αSA (red). (D) LAP 365 ECTs were dissociated for confirmation of cardiac differentiation and visualization of individual CMs through labeling with cTnT (red).

Synchronous contraction and functionality of resulting 3D-ECT

ECTs began to spontaneously contract between days 7–10 of cardiac differentiation, with synchronous, whole tissue contractions occurring by day 20. After initiation of spontaneous contraction, contractile analysis could be performed, and on day 11, the frequency of spontaneous contraction was 50.9 ± 11.5, 43.0 ± 4.33, and 56.1 ± 12.5 beats per minute (BPM) for LAP 365, LAP 405, and Eosin Y ECTs, respectively. The time between contraction and relaxation, or time interval, for LAP 365, LAP 405, and EY was 0.196 ± 0.011, 0.178 ± 0.023, and 0.168 ± 0.032, respectively. Furthermore, for LAP 365, LAP 405, and Eosin Y, the maximum contraction velocity was 42.1 ± 12.9, 30.3 ± 6.19, and 56.5 ± 10.9 μm/s and the maximum relaxation velocity was 23.6 ± 11.9, 12.2 ± 5.51, and 32.0 ± 5.40, respectively (n = 6, 6, 4 tissues for LAP 365, LAP 405, EY). On day 22, the frequency of spontaneous contraction was 32.5 ± 14.8, 34.4 ± 17.7, and 27.7 ± 12.3 beats per minute (BPM) for LAP 365, LAP 405, and Eosin Y ECTs. The maximum contraction and relaxation velocities were 153 ± 37.7 and 93.8 ± 30.5, 115 ± 17.7 and 64.0 ± 12.8, and 86.6 ± 54.5 and 46.6 ± 30.7 μm/s for LAP 365, LAP 405, and Eosin Y, respectively, quantified using an open-source MATLAB code (Huebsch et al. 2015). The time interval for the spontaneous contractions of the LAP 365, LAP 405, and Eosin Y ECTs was 0.334 ± 0.034, 0.380 ± 0.035, and 0.345 ± 0.081, respectively (n = 6 tissues). Because the photoinitiator LAP does not have any green autofluorescence, the action potentials of ECTs were monitored using an hiPSC line with a GEVI. Recordings of spontaneous action potentials were acquired using a high-speed camera attached to a fluorescence microscope (Figure 5.6D–E). A custom MATLAB code was used for analyzing the fluorescent recordings to quantify the action potential duration (APD) and conduction velocity. The

APD at 50 and 80% repolarization was 314 ± 42.0 and 452 ± 57.4 for LAP 365; similarly, the APD at 50 and 80% repolarization was 296 ± 40.7 and 397 ± 42.5 for LAP 405. The speed at which the propagation traveled across the tissue, or conduction velocity, was 1.54 ± 0.46 and 1.43 ± 0.93 for LAP 365 and LAP 405, respectively (n = 3 recordings).

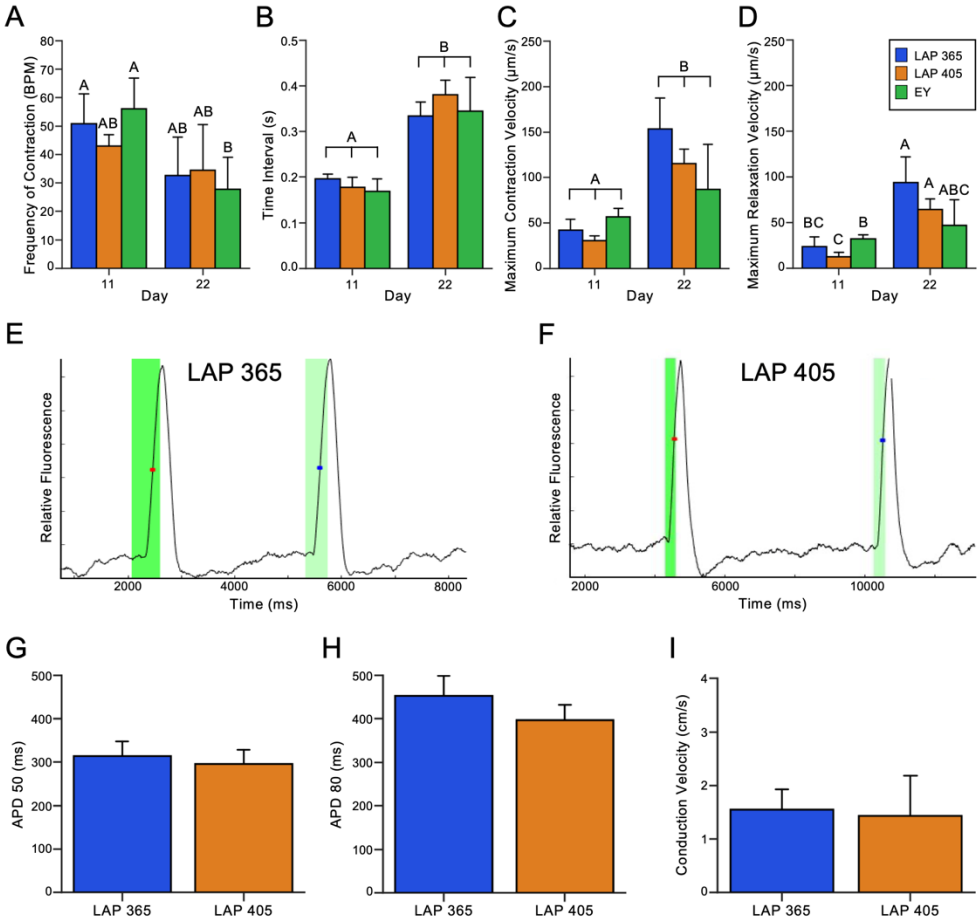

Figure 5.6 Photocrosslinking of LAP allows for non-destructive recording of action potentials using a GEVI.

(A) The ECTs began to spontaneously contract by day 10 of differentiation, and the spontaneous contraction frequency on day 11 and 22 was 50.9 ± 11.5, 43.0 ± 4.33, and 56.1 ± 12.5 and 32.5 ± 14.8, 34.4 ± 17.7, and 27.7 ± 12.3 beats per minute (BPM) for LAP 365, LAP 405, and Eosin Y (EY), respectively. (B) ECTs for LAP 365, LAP 405, and EY had

time intervals of 0.196 ± 0.011, 0.178 ± 0.023, and 0.168 ± 0.032 s on day 11 and 0.334 ± 0.034, 0.380 ± 0.035, and 0.345 ± 0.081 s on day 22. (C) The maximum contraction velocities were 42.1 ± 12.9, 30.3 ± 6.19, and 56.5 ± 10.9 μm/s and 153 ± 37.7, 115 ± 17.7, and 86.6 ± 54.5 μm/s in ECTs photocrosslinked with LAP 365, LAP 405, and EY on days 11 and 22, respectively. (D) ECTs had a maximum relaxation velocity of 23.6 ± 11.9, 12.2 ± 5.51, and 32.0 ± 5.40 on day 11 and 93.8 ± 30.5, 64.0 ± 12.8, and 46.6 ± 30.7 μm/s on day 22 for LAP 365, LAP 405, and EY. (E–I) An optical mapping system was used for acquiring electrophysiological recordings of the action potentials using a fluorescent microscope, and a custom MATLAB code was used for data processing and analysis, with example traces shown in (E–F). (G) The action potential duration (APD) at 50% repolarization was 314 ± 42 and 296 ± 41 ms for LAP 365 and LAP 405, respectively. (H) Similarly, the APD at 80% repolarization was 452 ± 57.4 and 397 ± 42.5 ms for LAP 365 and LAP 405. (I) The conduction velocity for LAP 365 and LAP 405 ECTs was 1.54 ± 0.46 and 1.43 ± 0.93 cm/s. A value of $p < 0.05$ was used for significance; samples that do not share a letter are significantly different.

Discussion

There is great potential for clinical applications employing ECT; for advancement of ECT utilization in downstream applications, the ability to non-destructively monitor CM functionality could provide substantial cost and time savings. Here, it is demonstrated that LAP-initiated photocrosslinking can be employed to encapsulate hiPSCs with a GEVI in PEG-fibrinogen for direct differentiation to produce 3D-ECTs and monitor the action potentials non-destructively over time. The photoinitiator LAP has absorbance from 340–

400 nm; therefore, two light sources were used for photocrosslinking of PEG-fibrinogen for hiPSC encapsulation. The PEG-fibrinogen was photocrosslinked using a UV lamp with a wavelength of 365 nm for 1 min and with a handheld low-cost blue flashlight with wavelength 390–410 nm for 2 minutes. LAP-initiated photocrosslinking of PEG-fibrinogen for encapsulation and subsequent direct cardiac differentiation was compared to our previous method using Eosin Y with visible light photoinitiation for photocrosslinking. Hydrogels produced with LAP 365 and Eosin Y had similar mechanical properties, while hydrogels produced with LAP 405 were significantly softer. Following encapsulation with LAP, the hiPSCs maintained high viability and appropriate proliferative and pluripotent phenotypes. Three days after encapsulation, cardiac differentiation was initiated through small molecule control of the Wnt pathway. During differentiation, the cells remodeled the provided PEG-fibrinogen matrix, and the overall tissue area increased. In all three conditions, cardiac differentiation occurred similarly both in terms of differentiation efficiency and the resulting number of cells. Furthermore, spontaneous contractions initiated by day 7 and the maximum contraction and relaxation velocities increased with time, a feature of maturing CMs. Photocrosslinking with LAP overcame the autofluorescence encountered with Eosin Y, allowing for monitoring of the action potentials using the GEVI. Taken together, these results indicate that photocrosslinking with LAP overcomes the autofluorescence issues of Eosin Y and can be used for encapsulation of hiPSCs and direct differentiation for the production of ECT.

Photocrosslinking is beneficial for cell encapsulation for the creation of 3D tissues due to its rapid polymerization times and ability for crosslinking at physiological conditions, such as temperature and pH. Photocrosslinking occurs through a two-step

process; first, light is absorbed, causing excitation, followed by the chain reaction of polymerization. This polymerization occurs through free-radical or ionic chain polymerization. Commonly used photoinitiators include compounds with peroxides, ketones, quinones, and azo groups due to their ability to form radicals for free-radical polymerization (Fisher et al. 2001). Some of the commonly used photoinitiators require lengthy crosslinking times and exposure to UV light; however, Eosin Y can be crosslinked rapidly (< 40 s) using visible light (Petra Kerscher, Kaczmarek, et al. 2016; P. Kerscher, Turnbull, et al. 2016). Eosin Y has autofluorescence in the green channel, limiting its use in some cell imaging assays, and this study demonstrates the ability to utilize the photoinitiator LAP for photocrosslinking of PEG-fibrinogen with no autofluorescence.

LAP is a type I photoinitiator established by Fairbanks et al., with absorbance between 340 and 400 nm with the maximum occurring at 375 nm; this photoinitiator demonstrated success in neonatal fibroblast encapsulation when crosslinked for 5 minutes at a LAP concentration of 2.2 mM with a 405 nm light source with an intensity of 10 mW/cm^2 (Fairbanks et al. 2009). Furthermore, LAP has previously been used for photocrosslinking of PEG or gelatin-based hydrogels for hepatocyte differentiation (Greene et al. 2017), 3D printing a chambered cardiac organoid (Kupfer et al. 2020), and for studying breast cancer dormancy (Pradhan and Slater 2019). In these studies, the concentration of LAP ranged from 4 mM to 17 mM with a minimum crosslinking time of 1 min. Furthermore, LAP has been used for photocrosslinking of synthetic ECM composed of PEG and biomimetic peptides with cancer cell lines at a concentration of 2 mM with a 365 nm light source (10 mW/cm^2). Preliminary studies showed that PEGDA hydrogels were successfully crosslinked using a 365 nm UV-light with an intensity of 3 mW/cm^2

with a minimum crosslinking time of 30 s at a LAP concentration of 5 mM and 60s for LAP concentrations of 1.5, 2.0, and 2.5 mM. The final concentration of 2.5 mM LAP was chosen to keep the volume of precursor solutions similar between the LAP and Eosin Y initiated photocrosslinking. Furthermore, using the 365 nm light source for crosslinking 1 min produced hydrogels with the same stiffness as crosslinking with Eosin Y; this is similar to previously published results showing that 4 mM LAP and 0.1 mM Eosin Y had similar shear moduli when photocrosslinked with a halogen cold light lamp (400–700 nm, equivalent to 10 mW/cm^2) for 5 minutes (Greene et al. 2017). This was chosen to directly compare the effect of the light source and photoinitiator only without introducing other variables. The time for crosslinking with the 405 nm light source was chosen based on the desire to find the minimum amount of time for crosslinking since the hiPSCs are without media during the crosslinking process.

It has previously been shown that a stiff microenvironment is beneficial for promoting maturation of CMs (Young and Engler 2011; Hazeltine et al. 2014); however, in previous work, it is demonstrated that an initial soft microenvironment is suitable for production of 3D-ECT with high efficiency of differentiation and features of CM maturity over time. Similar to previous results from our lab with GelMA (Petra Kerscher, Kaczmarek, et al. 2016) and with ECT microspheres, there is a decrease in elastic modulus after incorporation of the cells on day -2. The role of stiffness during *in vitro* 3D cardiac differentiation has yet to be studied; although there were no significant differences from day -2 to day 8 of cardiac differentiation in LAP 365 and LAP 405 ECTs, this platform provides the opportunity for a more in-depth investigation of the effect of stiffness on resulting ECTs because of the different photoinitiators and light sources established in this

study. Further experiments are needed to fully elucidate the effect of 3D microenvironment stiffness on resulting ECT properties.

For utilization of ECTs in regenerative medicine applications, the resulting CMs will need to have the appropriate phenotype and maturity for engraftment, electrical coupling, and enhanced function. Typically, PSC-CMs have an immature phenotype compared to adults CMs, particularly in terms of morphology, metabolism, and functional properties, including electrophysiology and calcium handling (Feric and Radisic 2016a), and recent efforts have been made in improving the maturity of PSC-CMs through mechanical and/or electrical stimulation (Ronaldson-Bouchard et al. 2018; Nunes et al. 2013), maturation media (Feyen et al. 2020), T3 growth hormone supplementation (C. Jackman, Li, and Bursac 2018; Yang et al. 2014), pulsatile flow, cyclic strain, extended culture time (Shen et al. 2017), and addition of miRNAs (White, Pang, and Yang 2016). Furthermore, the differentiation process is costly, both in terms of time and materials, and taken together with the potential need to enhance cardiac maturation following differentiation, there is a great opportunity for assay development that can measure ECT properties, specifically electrophysiology, non-destructively over time. One important parameter for assessing maturity and function of ECT is through electrophysiological recordings of the action potential, or change in voltage, that occurs as a result of calcium, sodium, and potassium ion transport through the CMs, resulting in the contractile motion of the cardiac tissue. Typically, voltage or calcium indicator dyes are used for analyzing action potentials, which can only be used at one time point, and are costly and easily photobleached. Previously, the Gepstein lab created a hiPSC line containing a genetically encoded voltage indicator (GEVI) with a green fluorescent protein (Shinnawi et al. 2015),

and the use of a GEVI overcomes these challenges and provides substantial improvements for non-destructive analysis of action potentials over time. Here, that established hiPSC line was utilized for the formation of ECTs photocrosslinked with LAP and Eosin Y, and a high-speed camera attached to a fluorescent microscope was employed for non-destructive analysis of ECTs photocrosslinked with Eosin Y. The APD and conduction velocity of the ECTs was determined, and the conduction velocities were 1.54 and 1.43 cm/s for LAP 365 and LAP 405, respectively. Although these are considerably lower than mature adult cardiac tissue (Feric and Radisic 2016a), they are within the range of PSC-CMs, and there are indications of CM maturity including increasing contraction and relaxation velocities over time. Full characterization of the resulting CM maturity and ECT properties will be needed prior to clinical translation; however, this initial proof-of-concept study demonstrates the ability to produce 3D-ECT without autofluorescence for non-destructive monitoring of a GEVI.

This study demonstrates the ability to rapidly fabricate and produce 3D-ECT through LAP initiated photocrosslinking of PEG-fibrinogen. Successful photocrosslinking of PEG-fibrinogen hydrogels using the photoinitiator LAP occurred with two different light sources. A UV-lamp and low-cost handheld blue light were successfully employed to encapsulate hiPSCs with high viability and appropriate phenotype following encapsulation. ECTs could be directly differentiated from PEG-fibrinogen encapsulated hiPSCs, and this platform was used for non-destructive monitoring of action potentials using a genetically encoded voltage indicator cell line. This study shows the ability to overcome the autofluorescence of Eosin Y using LAP with similar mechanical properties. Importantly, this work provides the foundation for future studies with other fluorescent indicator cell

lines. This 3D direct differentiation platform employing LAP initiated photocrosslinking demonstrates potential for future use in a 3D bioprinter and for use in our custom microfluidic encapsulation system for scalable production of ECT microspheroids.

Chapter 6: Thalidomide-Induced Changes to 3D Human Pluripotent Stem Cell Derived Cardiac Tissue Formation

Introduction

Congenital heart defects (CHDs) are the most common type of birth defect worldwide (Gelb et al. 2013), with occurrences between 2.4 and 13.7 per 1000 live births (Virani et al. 2020). Moreover, CHDs are the leading cause of infant deaths (Dean, Udelsman, and Breuer 2012). However, the underlying causes are only partially understood, particularly those caused by drug-induced mutations during organ development. Although great progress has been shown, many cardiac defects, like ventricular septal defects (VSDs), must be repaired by open heart surgery (Limperopoulos et al. 1999), or in severe cases, with pediatric heart transplantation. Even when treated, CHDs can cause developmental delays, long-term cardiac complications, shortened life expectancy, and increased risk for certain cancers (Mandalenakis et al. 2019; Mussatto et al. 2015).

In 1957, Thalidomide ((±)2-(2,6-Dioxo-3-piperidinyl)-1H-isoindole-1,3(2H)-dione) (Kumar et al. 2012), a sedative drug prescribed for morning sickness in pregnant women, was launched in many European countries. Originally, thalidomide was considered a "wonder drug" due to its non-lethal effects when overdosing in mice and was publicized immediately after small animal experimentations (Smithells and Newman 1992). Insufficient testing of thalidomide prior to its release led to formation of birth defects in more than 10,000 children (Smithells and Newman 1992). Although thalidomide exposure caused a variety of birth defects, this drug is primarily affiliated with symmetrical limb deformation (Therapontos et al. 2009). Approximately 6% of affected infants had

CHDs including VSDs and atrial septic defects (ASDs). 30–40% of those affected died due to severe defects (Smithells and Newman 1992), and an unknown number of miscarriages occurred in the aftermath of thalidomide treatment (Ito, Ando, and Handa 2011). Studies now show that thalidomide's interactions during organogenesis are species-dependent, bringing awareness to obstacles for effectively screening candidate drugs (Parman, Wiley, and Wells 1999; Stephens 1988).

The thalidomide incident revealed the need for more thorough testing of candidate pharmaceuticals and led to significant changes in the testing required for the regulatory approval process, particularly for drugs prescribed during pregnancy. However, current methods for developmental toxicity studies primarily focus on small animal models, which do not fully recapitulate human heart development and can result in false information on the safety and efficacy of potential, new pharmaceuticals on the developing organ. Attempts have been made to incorporate *in vitro* assays with *in vivo* animal models for pharmaceutical testing, but current state-of-the-art drug-screening platforms for identification of teratogenic compounds continue to primarily employ animal subjects, which are expensive and time-consuming, and can result in misleading outcomes due to interspecies variability (T.W. Kim, Che, and Yun 2019; Grimm et al. 2018; Caspi et al. 2009; Meseguer-Ripolles et al. 2018). Furthermore, due to the fact that adult cardiomyocytes (CMs) cannot be cultured long-term *in vitro*, these studies are carried out using other cell types. The preclinical assays for determining cardiac side-effects typically only involve the use of immortalized cell lines with an overexpression of a particular ion channel. However, recent advances in stem cell differentiation provide the ability to mimic human developmental processes *in vitro* to better understand heart development and

enhance drug discovery and toxicology (Caspi et al. 2009; Grimm et al. 2018). *In vitro* specification and differentiation of cardiac cells from human induced pluripotent stem cells (hiPSCs) follow pathways analogous to those seen in *in vivo* heart development (van den Heuvel et al. 2014). Stem cell biologists have drawn upon developmental biology to establish high-efficiency protocols for cardiac differentiation of hiPSCs (Lian et al. 2013a; Burridge et al. 2014; Burridge et al. 2011; Kuo et al. 2020), which can now be employed to mimic development and better predict cardiac toxicity of pharmaceuticals. Small molecule-based differentiation using Wnt/β-catenin signaling has proven efficient, resulting in mesoderm formation and cardiogenesis (Lian et al. 2012)**.** Human induced pluripotent stem cell-derived CMs (hiPSC-CMs) provide a powerful option to enhance preclinical testing and developmental toxicity screening by providing a CM cell source, while simultaneously overcoming the interspecies variations (Adler et al. 2008).

Currently, there are no established *in vitro* assays to assess the effect of compounds on human 3D developing heart tissues; *in vitro* cardiac toxicity screening with PSCs has been focused on the use of pre-differentiated hiPSC-derived CMs, which has limitations for use in mechanistic studies and in screening of potential cardiac teratogens. Although existing 2D differentiation systems are highly effective for CM production, they provide limited ability to study mechanical, structural, and functional properties of cardiac tissue development; previously published work suggests 3D biomaterial encapsulation and subsequent differentiation is advantageous for mesoderm teratogen screening (Belair et al. 2020). Mechanical and structural cues, provided primarily by the 3D microenvironment of surrounding cells and matrix material, are important in guiding embryogenesis. Without recapitulation of the 3D microenvironment present during development, even basic

questions concerning the impact of teratogen exposure or genetic variants on developing human cardiac tissue properties, particularly extracellular matrix (ECM) composition and tissue function, cannot be investigated.

Previously, our group established the first 3D platform for direct cardiac differentiation of hiPSCs encapsulated within a biomaterial matrix (Petra Kerscher, Kaczmarek, et al. 2016; P. Kerscher, Turnbull, et al. 2016), and the objective of this study was to determine if these 3D developing engineered cardiac tissues (3D-dECT) could be used to identify drug-induced congenital heart defects with thalidomide treatment during and after cardiac differentiation. Starting directly with human induced pluripotent stem cells (hiPSCs), rather than pre-differentiated cardiomyocytes, a 3D-dECT model enables investigation of cardiac tissue properties both in the early stages of cardiac specification and in later stages of cardiac differentiation. Here, hiPSCs were encapsulated in hybrid biomaterial PEG-fibrinogen on day -3 and were allowed to adjust to their new microenvironment prior to initiation of cardiac differentiation on day 0. Prior to drug treatment, we first verified that there were no changes to short term hiPSC viability, proliferation, and mitochondria distribution after thalidomide exposure. Beginning on day 1 of cardiac differentiation, thalidomide was administered to 3D-dECTs at 0 μM (drug solvent), 10 μM, and 70 μM. In our 3D-dECT model, we detected changes in tissue architecture and efficiency of cardiac differentiation. Differences in mitochondria distribution and sarcomere alignment were visualized in thalidomide-treated CMs compared to control CMs. Importantly, we studied functional properties of the 3D-dECT and saw thalidomide induced changes in ECM composition and gene expression. Overall,

our findings show that our 3D-dECT model of the developing heart is a robust 3D model that can be used to detect drug-induced changes during development.

Materials and Methods

HiPSC culture

Human induced pluripotent stem cells (hiPSCs, IMR-90 Clone 1, WiCell) were cultured on hESC qualified Matrigel (Corning) using mTeSR-1 medium (Stem Cell Technologies). HiPSCs were passaged using Versene (Life Technologies) and cultured in mTeSR-1 medium supplemented with 5 μM rock inhibitor (Y-27632, Stem Cell Technologies) for 24 h after passaging.

Cell viability and immunofluorescence staining

HiPSC viability and proliferation were assessed 24 h after thalidomide addition using a LIVE/DEAD viability kit (Molecular Probes) and immunofluorescence staining with proliferating cell nuclear antigen (PCNA, Millipore) and 4',6-diamidino-2-phenylindole (DAPI, Molecular Probes) (n = 3 per condition). The percentages of viable and proliferating cells were calculated as the number of viable and PCNA positive cells divided by total cell number.

2D monolayer formation

For 2D monolayer differentiations, hiPSCs were dissociated using Accutase (Innovative Cell Technologies) and seeded on Matrigel coated PDMS coverslips in a 12-well plate (0.5×10^6 hiPSCs per well). Cells were cultured in mTeSR-1 medium supplemented with

5 μM rock inhibitor for 24 h (day -4), followed by a daily mTeSR-1 medium exchange until the initiation of cardiac differentiation on day 0.

3D developing engineered cardiac tissue (3D-dECT) formation process

All chemicals were purchased from Sigma-Aldrich unless reported otherwise. PEG-fibrinogen was synthesized as previously described (Almany and Seliktar 2005). In short, tris (2-carboxyethyl) phosphine (TCEP, Acros Organics) was mixed with 7 mg/ml fibrinogen in 8 M urea-PBS. Next, PEGDA was reacted with fibrinogen for 3 h, precipitated in acetone, and dissolved in 8M urea-PBS. The reacted PEG-fibrinogen was dialyzed in PBS for 24 h at 4 °C.

For 3D encapsulation, hiPSCs were dissociated with Versene, and the cell pellet was combined with liquid PEG-fibrinogen precursor solution containing 1.5% (v/v) triethanolamine (TEOA), 0.39% (v/v) N-vinyl pyrrolidone (NVP), and 0.1 mM Eosin Y (Fisher Scientific) at a cell density of $55 \pm 8.5 \times 10^6$ hiPSCs/ml of PEG-fibrinogen. 8 μl of this mixture was transferred into a circular PDMS mold on acrylated glass (P. Kerscher, Turnbull, et al. 2015) and photocrosslinked with visible light for 30 s. Following photocrosslinking, the PDMS mold was removed, and cell-laden hydrogels attached to the acrylated glass were cultured in mTeSR-1 medium supplemented with 5 μM rock inhibitor for 24 h. On day -2 and day -1, mTeSR-1 medium was changed daily.

Cardiac differentiation and thalidomide treatment

Media components and timeline of cardiac differentiation followed the previously published protocol (Lian et al. 2013a). Briefly, on day 0 of differentiation, media of 2D

monolayers and 3D-dECTs was changed to RPMI/B27 without insulin (Life Technologies) + 12 μM CHIR99021 (Stem Cell Technologies) for 24 h. Media was exchanged with RPMI/B27 without insulin for an additional 48 h. On day 3 of differentiation, an equal volume of old media was combined with RPMI/B27 without insulin and supplemented with 5 μM IWP2 (Stem Cell Technologies) for 48 h. On day 5, the media was exchanged with fresh RPMI/B27 without insulin. On day 7, media was replaced with RPMI/B27 (Life Technologies); the media was changed every three to four days with RPMI/B27.

Thalidomide (MP Biomedicals) was dissolved in dimethyl sulfoxide (DMSO) and stored at 4 ºC. To determine the effect of thalidomide on cardiac differentiation, the drug vehicle (0 μM), 10 μM, and 70 μM thalidomide were added to the media beginning on day 1 of differentiation (Figure 6.1A).

Early growth progression of differentiating 3D-dECTs

Low magnification images of whole tissues from day -2 to day 7 were acquired using an Andor Luca S camera attached to a phase contrast microscope (Ti Eclipse, Nikon). The lateral surface area of control, 10 μM, and 70 μM thalidomide treated 3D-dECTs were analyzed using ImageJ software with standard analysis plugins (n = 9 tissues per condition). Each tissue was normalized to its area on day 1 of differentiation (the first day of thalidomide treatment).

Enzymatic cardiac tissue dissociation

Tissues were dissociated with collagenase Type 2 (1 mg/mL, Worthington) in dissociation solution supplemented with 30 μM $CaCl_2$ and 5 μM rock inhibitor at 37 ºC for 2 h.

Dissociation solution was composed of 120 mM NaCl, 5.4 mM KCl, 5 mM $MgSO_4$, 5 mM Na-pyruvate, 20 mM glucose, 20 mM taurine, and 10 mM HEPES in PBS (pH 6.9). Cells were further dissociated with 0.25% Trypsin EDTA (Corning) at 37ºC for 5 min. All cells were resuspended in RPMI20 medium (RPMI 1640 medium (Gibco) with 20% fetal bovine serum (FBS, Atlanta Biologics)) supplemented with 5 μM rock inhibitor and plated onto fibronectin coated PDMS glass coverslips.

Flow Cytometry

On day 15 of differentiation, control (0 μM), 10 μM, and 70 μM 3D-dECTs were dissociated into single cells as described above. Singularized cells were transferred to RPMI20 media (RPMI + 20% FBS) and centrifuged at 200 g for 5 min. Cells were prepared for cell counting using flow cytometry, using previously described methods (P. Kerscher, Turnbull, et al. 2015).

Immunocytochemistry and sarcomere length quantification

Following dissociation and seeding on coverslips, hiPSCs and dissociated tissues were fixed using 4% paraformaldehyde (Electron Microscopy Sciences), permeabilized using PBS-T (PBS with 1% bovine serum albumin (BSA) and 0.2% Triton X-100) and blocked in 3% FBS in PBS (blocking buffer). Primary antibody α-sarcomeric actinin (αSA) and secondary antibody Alexa Fluor 488 (Invitrogen) were then added consecutively. All samples were counterstained with DAPI and visualized using a Nikon A1R laser-scanning confocal microscope.

On day 38 of differentiation, dissociated 3D-dECTs were labeled with αSA for quantification of sarcomere length. Images were acquired using a 60X plan apochromat oil-immersion objective on the confocal microscope. All images were imported to Image J, where fast Fourier transform and intensity profiles of drawn paths along well-defined, in-plane sarcomeres were collected. Data from intensity profiles were used to perform fast Fourier transform. A minimum of ten sarcomeres per treatment group were selected based on continuity of sarcomeres in the field of view.

Mitochondria localization and analysis of thalidomide-treated hiPSCs and 3D-dECT CMs

The mitochondria in HiPSCs and dissociated 3D-dECT cells for all treatment groups were visualized using MitoTracker Red (Invitrogen) diluted to a final concentration of 1 nM in cell culture media. The MitoTracker Red working solution was added to all wells and incubated at 37 °C for 30 min. Cells were rinsed with PBS, fixed, permeabilized, and blocked with blocking buffer. 3D-dECT cells were also stained with αSA to identify mitochondria of CMs, and samples were counterstained with DAPI. The number and area of mitochondria per CM were quantified using Mitochondrial Quantification using MATLAB (MQM), a custom MATLAB script (P. Kerscher, Bussie, et al. 2015), from three images per well with areas of similar confluency.

Contraction Analysis and Optical Mapping

Videos of spontaneously contracting tissues were acquired on days 11, 14, 17, and 42 using a phase contrast microscope with Andor Luca S camera. The videos were converted to tiff

files and imported into an open-source motion tracking software for quantification of frequency (Hz), time interval (s), maximum contraction velocity (μm/s), and maximum relaxation velocity (μm/s) (Huebsch et al. 2015).

Day 17 cardiac monolayers were incubated in the calcium sensitive dye Rhod-2 (Invitrogen) for 30 min followed by thorough rinsing with Tyrode's solution (1.8 mM $CaCl_2$, 5 mM glucose, 5 mM HEPES, 1.0 mM $MgCl_2$, 5.4 mM KCl, 135 mM NaCl, and 0.33 mM NaH_2PO_4, pH 7.4) before experimentation. To study calcium transient durations, 2D monolayers were optically mapped; duplicate recordings were taken in multiple tissue regions per sample using an Andor iXon+ 860 EMCCD camera and results were analyzed in a custom MATLAB code.

Gene expression

Two-step RT-qPCR was performed on control, 10 μM, and 70μM 3D-dECTs on days 0, 10, and 30 of differentiation. RNA was isolated from each tissue using a NucleoSpin RNA kit (Machery-Nagel). cDNA was synthesized using a SuperScript™ IV First-Strand Synthesis System (Thermo Fisher Scientific).

RT-qPCR was conducted on a QuantStudio™ using SYBR™ Green PCR Master Mix (Thermo Fisher Scientific) with KiCqStart® SYBR® Green Primers (Sigma Aldrich) or TaqMan™ Fast Advanced Master Mix with previously designed primers. SYBR Green reactions contained 5 ng of cDNA and 500 nM of forward and reverse primer. Taqman reactions were run in duplex with 5 ng cDNA, 200 nM forward and reverse primer (GAPDH and gene of interest), and 100 nM probe (HEX and FAM). Primers were annealed

at 58 and 55 °C for SYBR green and Taqman, respectively. Gene expression values were normalized to GAPDH, and the fold change was quantified using the $2^{(-\Delta\Delta Ct)}$ method.

Enrichment for ECM proteins in microtissues

Proteomics analysis was performed by Bre Duffy and Dr. Lauren Black at Tufts University. Three tissue samples from each treatment group were used for proteomics analysis. Half of each microtissue was used for proteomics analysis. Tissues were decellularized using 0.05% sodium dodecyl sulfate (SDS), 2 mL per tissue, on an inverter at room temperature for 30 minutes. Samples were then washed with deionized water with gentle agitation on an inverter at room temperature for 30 minutes, repeated once. Decellularized tissues were dried by lyophilization and frozen at -20°C until digestion.

Dried samples were precipitated using 2 mL cold acetone for 60 minutes at -20 °C, centrifuged at 13,000 g for 10 min, and the supernatant removed. Acetone precipitation was repeated once to remove any remaining SDS and PEG.

Microtissue sample digestion into peptides

Microtissue samples were solubilized and disulfide bonds were reduced in 8M urea, 50 mM DTT, 50 mM TrisHCL (pH 8.5). Samples were minced with microscissors to aid in solubilization of the matrix and incubated at 37°C on an orbital shaker for 30 min. Free cystines were alkylated by adding iodoacetamine at a final concentration of 100 mM for 15 min in the dark at room temperature. Samples were diluted to 2M urea with 50 mM TrisHCL with 1 mM calcium chloride (pH 8.5) and digested with trypsin (Sigma) at 1:50 protease:protein (wt:wt) for 13 hours at 37°C with agitation. Digestion was stopped by

decreasing the pH to 2–3 using formic acid. Any particulates were removed with centrifugation at 10,000 rpm for 10 min, and the supernatant was removed and stored at -20 °C until liquid chromatography-mass spectrometry (LC-MS) analysis.

Liquid Chromatography-Tandem Mass Spectrometry (LC-MS/MS)

Untargeted LC-MS/MS analysis was performed using a TripleTOF 5600 System (SCIEX, Framingham, MA) coupled to a 1260 Infinity liquid chromatography system (Agilent, Santa Clara, CA). 100 µL of peptide solution was injected with an aqueous solvent of LCMS grade water with 0.1% LCMS grade formic acid (Sigma-Aldrich) and separated on Ascentis Express Peptide ES-C18 column (MilliporeSigma, St. Louis, MO) of 15 cm length, 2.1 mm inner diameter, and 2.7 µm particle size. Peptides were eluted with a 65 min gradient from 2–45% acetonitrile with 0.1% formic acid. Information Dependent Acquisition was performed from 300–1250 Da with charge states from 2–5. Up to 50 candidate ions exceeding 100 cps were selected per cycle, with a 15 second exclusion after 1 count, for fragmentation with rolling collision energy.

Protein identification and data analysis for microtissue samples

Raw files were searched against a UniProt KB protein database for *homo sapiens* updated February 10, 2016 using ProteinPilot software's Paragon algorithm (AB SCIEX). Search settings included trypsin specificity, urea denaturation, thorough ID search effort, and 0.05 (10.0%) detected protein threshold. Proteins matching the reversed database or contaminants were removed.

Relative quantification was obtained by spectral counts of peptides with at least 95% confidence normalized by total ECM spectral counts. Relative quantification across samples was obtained by spectral counts using a custom MATLAB script. Peptides identified with ≤ 95% confidence and proteins not associated with the extracellular matrix were removed. Peptides associated with each protein were counted and normalized to the total ECM spectral counts from the sample.

The results were analyzed with Prism (GraphPad, San Diego, CA) and the mean ± SD normalized to control tissues was reported. In order to perform statistical analysis, proteins which were not identified in at least 2 biological replicates of 2 conditions were removed. Within each protein, data was analyzed by one-way ANOVA with Tukey's multiple comparisons test. A value of $p < 0.05$ was considered statistically significant for all tests.

Statistics

Data are presented as mean ± SD, and statistical analysis was performed using Minitab 19 unless otherwise specified. The assumptions for normality and equal variances were confirmed, and one-way analysis of variance (ANOVA) was performed with Tukey's test for post-hoc analysis. A value of $p < 0.05$ was considered statistically significant.

Results

Thalidomide influenced the cardiac tissue formation process

In this proof-of-concept study, we investigated if our 3D developing engineered cardiac tissues (3D-dECTs) directly differentiated from PEG-fibrinogen encapsulated hiPSCs

could be used for identification and quantification of changes in tissue properties in response to drug exposure. Thalidomide, a known teratogen, whose mechanisms for defect formation are largely unknown (Ito, Ando, and Handa 2011), was used as a drug candidate to determine if 3D-dECTs uncover information about disease manifestation and progression, compared to standard 2D monolayer cardiac differentiation. Before evaluating the effect of thalidomide on cardiac differentiation from hiPSCs in a 3D microenvironment, short term effects of the drug-carrier, DMSO, and the highest thalidomide concentration (70 μM) were tested to verify that the drug and its carrier did not cause abnormal changes in cell viability and proliferation at the selected concentrations (X. Gao, Sprando, and Yourick 2015). Monolayer hiPSCs were treated with the drug-carrier control (0 μM) and 70 μM thalidomide for 24 h; the hiPSCs maintained high viability and proliferation capacity after treatment. (Figure 6.1B–C). Furthermore, the mitochondria area and location, with respect to the nuclear membrane, of control and thalidomide-treated hiPSCs were evaluated using our custom developed MQM code (P. Kerscher, Bussie, et al. 2015). No significant differences in mitochondria distribution were detected between treatment groups.

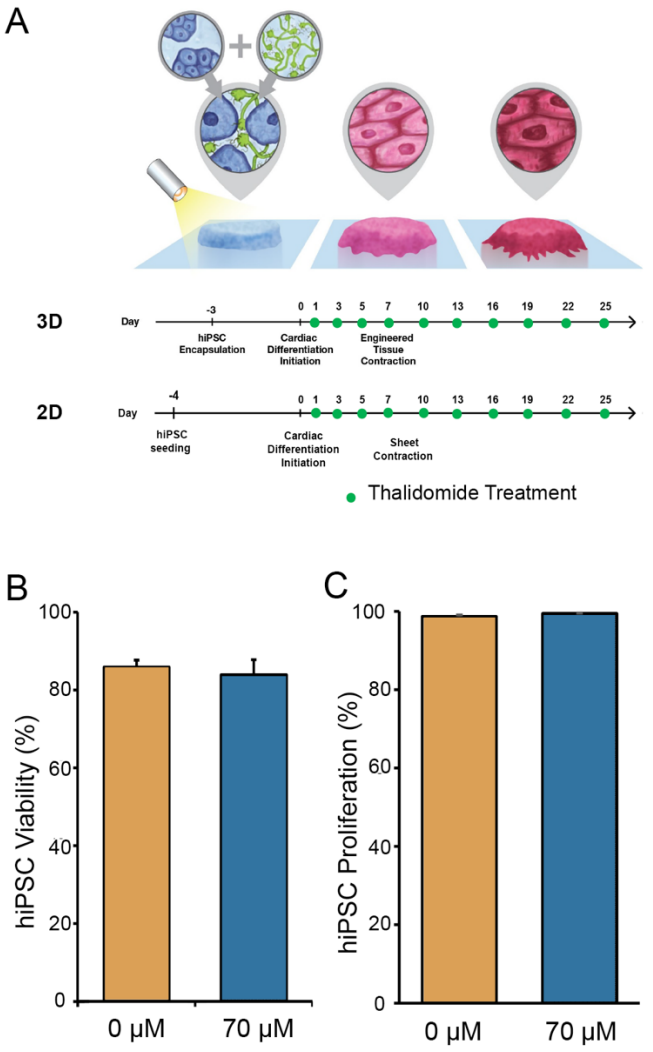

Figure 6.1 HiPSC differentiation timeline to form 3D developing engineered cardiac tissues (3D-dECTs) and 2D monolayers for thalidomide drug-testing.

(A) HiPSCs were combined with aqueous PEG-fibrinogen precursor solution, photocrosslinked to form 3D-dhECTs, and cultured for three days before initiation of cardiac differentiation. For 2D monolayer differentiation, hiPSCs were seeded onto a Matrigel coated 12-well plate and cultured for four days prior to initiation of cardiac differentiation on day 0. 3D and 2D differentiations were assigned to thalidomide treatment groups, consisting of control (0 μM drug carrier), 10 μM, and 70 μM thalidomide, on days

1, 3, 5, 7, and every three days after that. Figure reprinted with permission from (P. Kerscher, Turnbull, et al. 2016). Thalidomide treatment for 24 h did not influence hiPSC (B) viability or (C) proliferation, determined by percentage of PCNA+ cells (n = 3).

To produce the 3D-dECTs, hiPSCs were encapsulated within a hybrid biomaterial, PEG-fibrinogen on day -3. For encapsulation, hiPSCs were collected in a cell pellet and combined with the polymer precursor solution, pipetted into PDMS molds on acrylated glass, and photocrosslinked using visible light. Cardiac differentiation was initiated three days later (day 0) through activation subsequent inhibition of Wnt signaling using previously established protocols (P. Kerscher, Turnbull, et al. 2016; Petra Kerscher, Kaczmarek, et al. 2016; Lian et al. 2013a). For drug-treatment, thalidomide was administered at 0, 10, and 70 μM in the culture media on days 1, 3, 5, 7, and every 3 days thereafter with media changes (Figure 6.1A). These concentrations were chosen for this study because thalidomide doses of 10 and 70 μM previously showed significant changes during 2D hESC differentiation in transcriptomic and proteomic profiles (Meganathan et al. 2012). During cardiac differentiation, changes in tissue formation progression were observed in thalidomide treated samples. In all treatment concentrations, an increase in lateral surface area was observed from day 1 to day 5 (Figure 6.2). On day 5, control tissues displayed a significant increase in size compared to treatment groups at 1.33 ± 0.03, 1.23 ± 0.04, and 1.17 ± 0.02 times the day 1 tissue size for 0, 10, and 70 μM thalidomide treated tissue, respectively (Figure 6.2B, n = 9 tissues per group, *$p < 0.05$); this change in tissue growth was accompanied by the presence of an increased amount of cell debris surrounding the 10 and 70 μM thalidomide-treated tissues (Figure 6.2A). In comparison, control 3D-

dECTs (0 µM) exhibited more defined edges throughout differentiation (Figure 6.2A). A 2D monolayer differentiation approach was attempted to study thalidomide-induced effects for comparison to the 3D microenvironment in the 3D-dECTs. However, 2D differentiation in the presence of 70 µM thalidomide did not result in contracting monolayers and had substantial cell loss and insufficient cardiac differentiation. This was expected due to the direct drug exposure in the 2D environment, and limited samples were able to be used for assessment of CM properties.

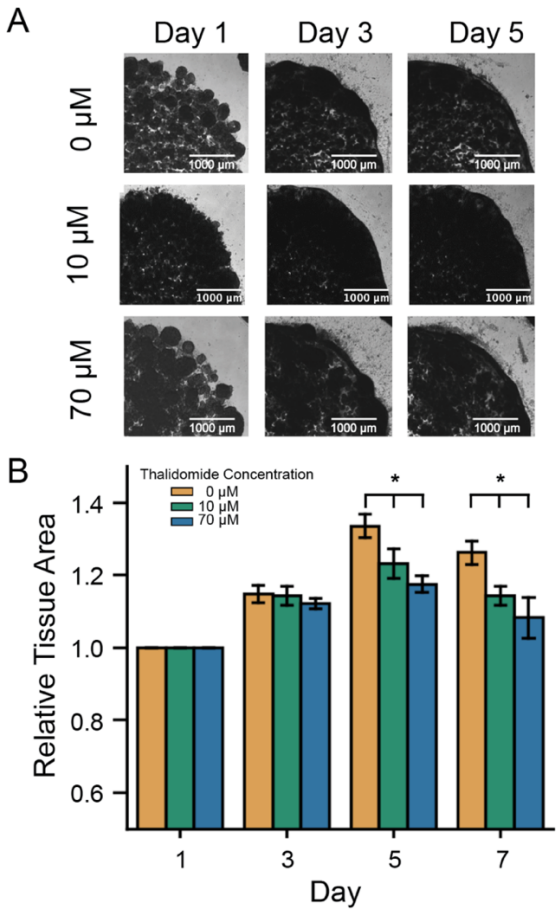

Figure 6.2 Thalidomide influenced the early tissue formation process and growth.

(A) After PEG-fibrinogen encapsulation, hiPSCs grew within the hydrogel. Edges of 0 µM (control), 10µM, and 70 µM thalidomide tissues started to differ on day 3 of differentiation,

with more cell debris and less dense tissue formation in 70 μM thalidomide treated tissues. (B) Relative tissue area increased from day 1 to day 5 for all groups. Control tissues showed a greater in increase in tissue area compared to thalidomide treated tissues on days 5 and 7 ($n = 9$ tissues per group, $*p < 0.05$).

Thalidomide influenced cardiac differentiation and resulting CM phenotype

Following cardiac differentiation, the efficiency of cardiac differentiation was assessed by positive expression of cTnT and quantified with flow cytometry. Cardiac differentiation efficiency showed a dose dependent response with control 3D-dECTs having the highest percentage of CMs followed by 10 and 70 μM thalidomide-treated 3D-dECTs (Figure 6.3D); the percentage of cTnT+ cells on day 10 was 41.2 ± 2.57, 30.9 ± 1.91, and 25.1 ± 1.29 for 0, 10, and 70 μM, respectively, and 36.8 ± 2.57, 38.1 ± 11.2, and 33.0 ± 3.34 percentage on day 20 ($n = 3$ tissues per treatment group, $*p < 0.05$). On day 17, the total cell number in control and thalidomide-treated 3D-dECTs was similar compared to control samples (0 μM: 1.00 ± 0.072, 70 μM: 0.896 ± 0.061 cells, Figure 6.3C).

To further investigate the CM population, cell size and sarcomere length were used as indicators of initial CM structural development and maturity. On day 38 of differentiation, 3D-dECTs from all three treatment groups were dissociated into single cells and replated to observe CM size and sarcomere length using positive expression of αSA. The area of CMs from 3D-dECTs treated with 10 μm thalidomide was 2150 ± 991 μm^2, which is significantly smaller in size compared to control CMs (3450 ± 898 μm^2) ($n \geq 11$ tissues per treatment group, Figure 6.3A). Sarcomere length was 2.02 ± 0.16 and 1.88 ± 0.21 μm in control and 70 μM thalidomide-treated CMs, respectively (Figure 6.3B), which

is within the range for native adult CM sarcomere length (2.0–2.2 µm) for the control CMs (Feric and Radisic 2016a). Furthermore, the sarcomeres of control 3D-dECT CMs appeared to be more defined and organized compared to thalidomide treated CMs; sarcomere organization is an indicator of CM structural maturity (Figure 6.3E). In the 70 µM thalidomide treated samples, a high number of cells did not express αSA, a cardiomyocyte antibody, indicating a presence of non-CM cell types.

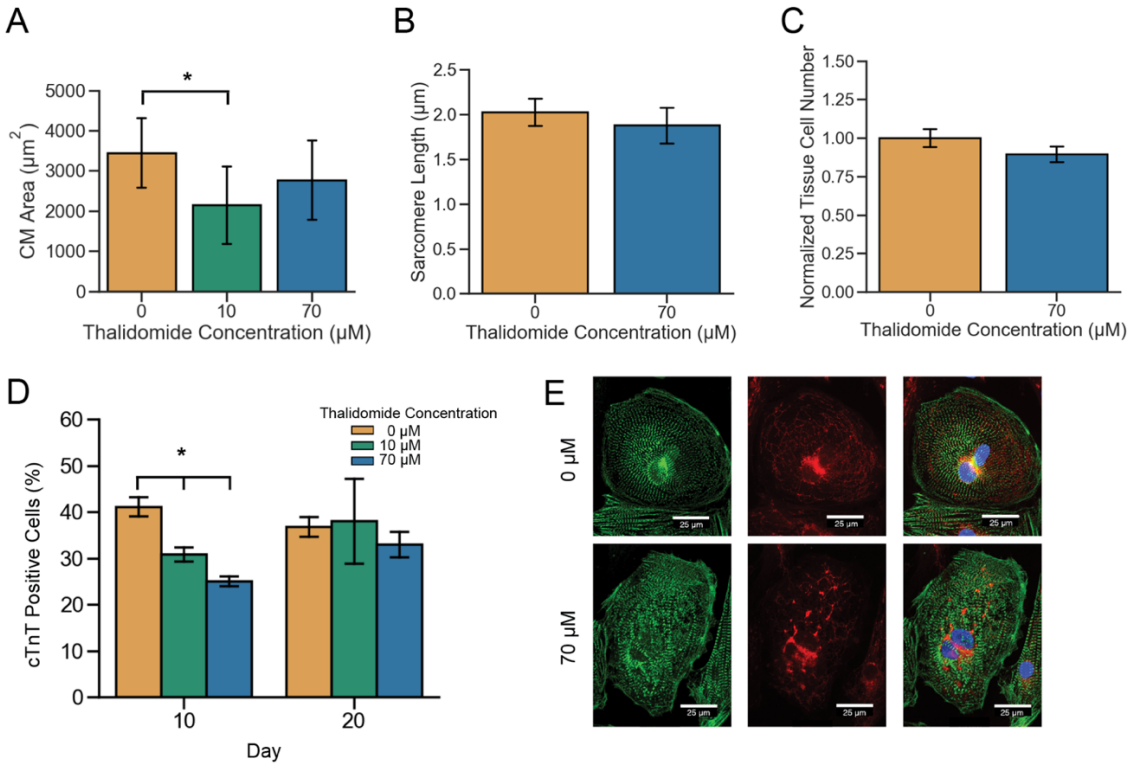

Figure 6.3 Thalidomide influenced cardiac differentiation and CM phenotype.

(A) On day 38, the 3D-dECTs were dissociated, and CMs treated with 10 µM thalidomide were significantly smaller compared to control CMs; 70 µM thalidomide-treated CMs also showed a trend in smaller cell size compared to control ($n \geq 11$ cells per condition, *$p < 0.05$). (B) Sarcomere spacing was similar in 70 µM thalidomide treated tissues compared to age-matched controls ($n \geq 10$ cells per condition). (C) On day 17, quantification of total

cell number per tissue showed a similar number of cells in thalidomide-treated tissues (n = 3 tissues per condition). (D) A lower percentage of CMs were detected in thalidomide-treated tissues compared to control, suggesting less efficient CM differentiation in the presence of thalidomide (n = 3 tissues per condition, *$p < 0.05$). (E) Sarcomeres (green) were more defined and organized in control CMs when compared to thalidomide-treated CMs; furthermore, the mitochondria (red) evenly distributed throughout the cytoplasm of control CMs but were clustered in thalidomide-treated CMs.

Following thalidomide treatment during cardiac differentiation, there were differences in mitochondria structure and distribution in thalidomide treated CMs compared to controls. Mitochondria are the primary organelle responsible for energy production within the cell and are an important component influencing normal heart development and contractile function. During early stages of CM development, mitochondria are only a small portion within the cytoplasm of the cell and are structurally visible in a reticular arrangement, while in adult CMs, mitochondria occupy approximately 20–40% of the total CM volume because of the high energy requirements needed for contraction; at this stage, mitochondria exhibit a regular distribution with a "crystal-like lattice pattern" (Schaper, Meiser, and Stammler 1985). To visualize mitochondria distribution, control and 70 μM thalidomide treated CMs were stained with MitoRed (Figure 6.3E). In control CMs (0 μM), mitochondria were evenly distributed throughout the entire cell, including overlapping with areas with well-defined sarcomeres. The mitochondria structure, morphology, and location in the cytoplasm were visually different in thalidomide-treated cells, showing a clustered pattern (Figure 6.3E). In immature CMs,

a large quantity of mitochondria is normally located close to the nucleus, which was seen in both treatment-group cells (0 and 70 μM).

Thalidomide-treated 3D-dECTs showed slower spontaneous contraction than age-matched controls

Here, our control 3D-dECTs also showed first areas of spontaneous contraction on day 7, similar to our previously published results (P. Kerscher, Turnbull, et al. 2016); however, thalidomide-treated 3D-dECTs started to contract one or two days later (day 8 or day 9). Although contractions started later for thalidomide treated 3D-dECTs, there were no significant differences in the frequency of spontaneous contraction between control and thalidomide-treated 3D-dECTs. On day 11, the time interval between contraction and relaxation was significantly longer in 70 μM tissue compared to control *(n* = 3 tissues per condition. *$p < 0.05$). This trend continued on day 14 where both 10 and 70 μM tissues showed prolonged time intervals compared to control (Figure 6.4A). From day 17 to 42, control and 10 μM thalidomide-treated 3D-dECTs showed significant increases in contraction and relaxation velocity, whereas 70 μM thalidomide-treated tissues did not (Figure 6.4B, C, n = 3 tissues per condition. $p < 0.05$).

To evaluate the influence of thalidomide on calcium transient duration and conduction velocity, optical mapping of day 17 2D cardiac monolayers was performed (Figure 6.4D–E). Both control and 70 μM thalidomide monolayers displayed spontaneous calcium propagation. Calcium transient durations in thalidomide-treated 2D monolayers were significantly longer for both 50 and 80% repolarization at 546 ± 176 ms and 874 ± 321 ms for control compared to 1212 ± 61 ms and 2162 ± 158 ms for 70 μM tissues (Figure

6.4D, n = 3 tissues per condition. *$p < 0.05$). Additionally, the calcium conduction velocity was slower when compared to age-matched controls at 1.58 ± 0.07 and 1.05 ± 0.199 cm/s for control and 70 μM tissues, respectively (Figure 6.4E, F, G). Calcium transient duration is important in the function and maturation of CMs. Our lab previously showed that nitric oxide-treated SC-CMs had a positive effect on CM differentiation; treated CMs also exhibited faster calcium transient durations compared to untreated controls (A. J. Hodge, Zhong, and Lipke 2016). Here, thalidomide, which negatively impacts CM function, had a detrimental impact on calcium transient duration.

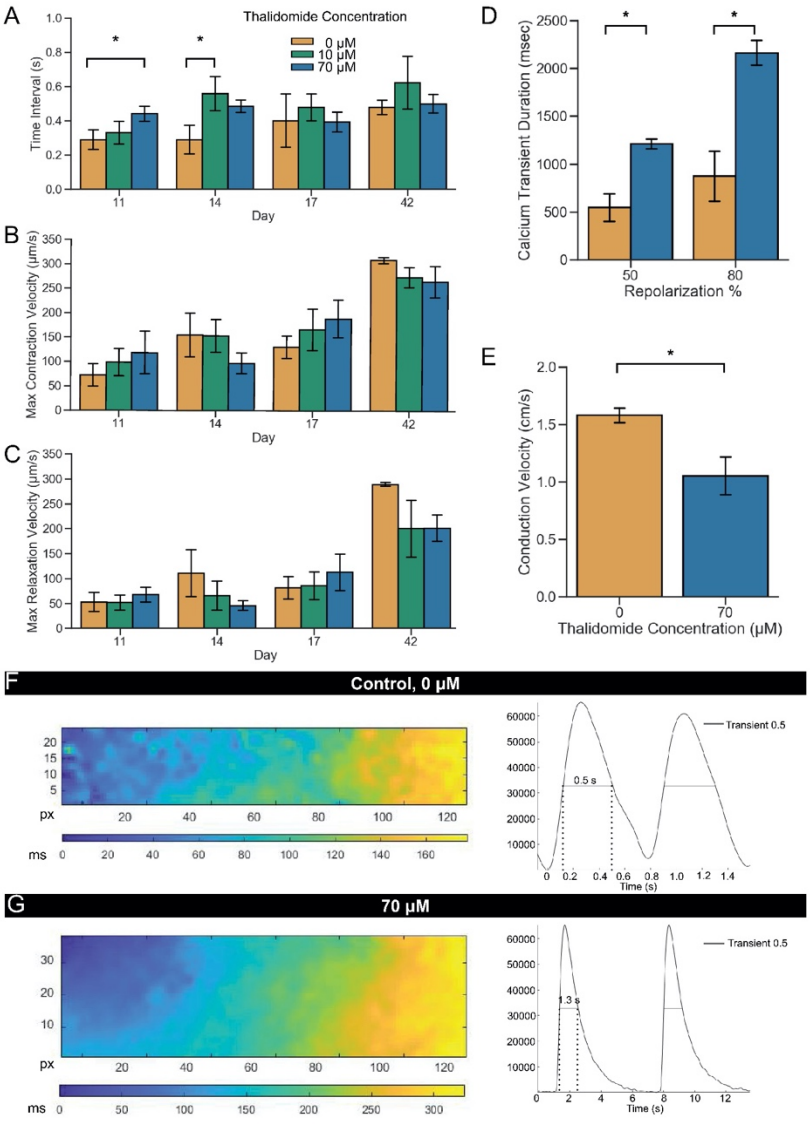

Figure 6.4 Thalidomide treatment induced differences in contractility and calcium handling.

(A) Significant differences in time interval between contraction and relaxation for control and 70 µM thalidomide-treated tissues were observed on days 11 and 14 ($n \geq 3$ tissues per condition). (B, C) Control and 10 µM tissues significantly increased contraction and relaxation velocity from day 17 to day 42 compared to 70 µM thalidomide treatment groups (n ≥ 3 tissues per condition). Representative isochrone maps and traces of (F) Control and

(G) 70 μM calcium wave propagation showed significantly longer (D) CTD at both 50 and 80% repolarization and (E) slower conduction velocity in thalidomide treated samples compared to control (n = 3 monolayers per condition, *p < 0.05).

Thalidomide treatment induces changes in gene expression and ECM production

The direct mechanism by which thalidomide damages cardiac tissue is not fully and clearly established. Previous studies have indicated a potential target of thalidomide on genes that regulate ECM production (Choe et al. 2010). Several cardiac and ECM related genes were explored in this study using RT-qPCR to further elucidate differences in gene expression following treatment with the known teratogen. Expression of cardiac specific genes GJA5, MYH6, and MYH7 were similar in all treatment groups and changed appropriately over time (Figure 6.5A). MYH7 expression increased significantly between each timepoint in all groups, as expected. ECM related gene expression including FN1, COL1A1, and POSTN increased over time in all groups as the cells began to produce their own ECM proteins. On day 10, POSTN expression was significantly higher in both thalidomide-treated samples compared to control (Figure 6.5D, n = 3 tissues per condition, *p < 0.05). The impact of thalidomide exposure on SALL4 and TBX20 expression has been explored in previous studies (Donovan et al. 2018; Khalil et al. 2017; Papaioannou 2014); here, SALL4 expression was downregulated over time and TBX20 expression was upregulated after differentiation with no significant differences between treatment groups (Figure 6.5A).

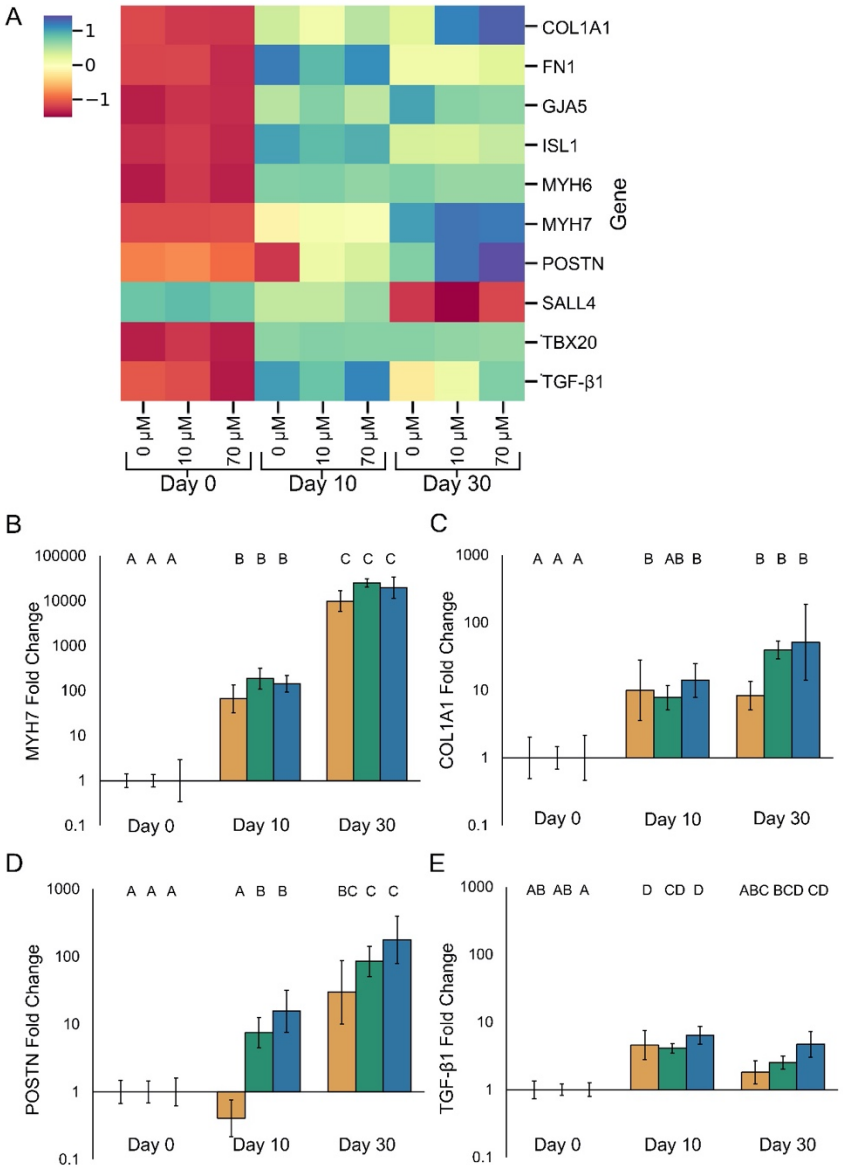

Figure 6.5 Thalidomide treatment impacts gene expression.

(A) A heat map comparing gene expression of various cardiac and ECM-related genes for each treatment group on days 0, 10, and 30 was produced. (B) Expression of cardiac gene MYH7 showed temporally appropriate upregulation in all groups over time. (C) Gene expression of COL1A1 increased in all groups from day 0 to day 10. (D) Periostin expression was higher in thalidomide treated samples on day 10. (E) From day 10 to day

30, TGF-β expression was maintained in 70 μM tissues compared and downregulated in control tissues (n = 3 samples per treatment group per timepoint, data is normalized to GAPDH and day 0 using $2^{(-\Delta\Delta Ct)}$ method, *$p < 0.05$).

The ECM composition was characterized on day 20 by decellularization of the 3D-dECT, digestion of the protein into peptides, and quantification using untargeted LC-MS; protein identification occurred using a UniProt KB database. Relative quantification was obtained by spectral counts of peptides with at least 95% confidence normalized by total ECM spectral counts. To examine the deposited ECM proteins, the fibrinogens were removed from the analysis, as these were provided by the biomaterial, PEG-fibrinogen. Deposited ECM components included fibrillin, fibronectin, perlecan, collagen, vitronectin, EMILIN-2, laminin, and periostin (POSTN) (Figure 6.6A), with significant differences in collagen alpha-1(I) chain (COL1A1), collagen alpha-1(II) chain (COL2A1), and fibrillin-1 deposition (Figure 6.6B). COL2A1 was significantly higher in control samples compared to 10 and 70 μM thalidomide treated 3D-dECTs. The ECM characterization showed increased levels of COL1A1 in 70 μM thalidomide treated samples compared to control (Figure 6.6B), but there was not a significant increase in COL1A1 gene expression in 70 μM day 30 3D-dECTs (Figure 6.5C). The increase in COL1A1 can potentially be explained by changes in TGF-β expression over time. From day 10 to day 30, TGF-β expression remained upregulated in 70 μM samples compared to control tissues, where TGF-β expression was downregulated to pre-differentiation levels. Previous studies have shown an increase in TGF-β stimulates ECM protein production (Hanna and Frangogiannis 2019) and inhibits collagenase secretions resulting in a buildup of ECM proteins over time

(Bowers, Banerjee, and Baudino 2010). Through utilization of a 3D-dECT model, thalidomide induced changes to ECM composition and gene expression changes from the pluripotent state through cardiac tissue formation and differentiation could be quantified.

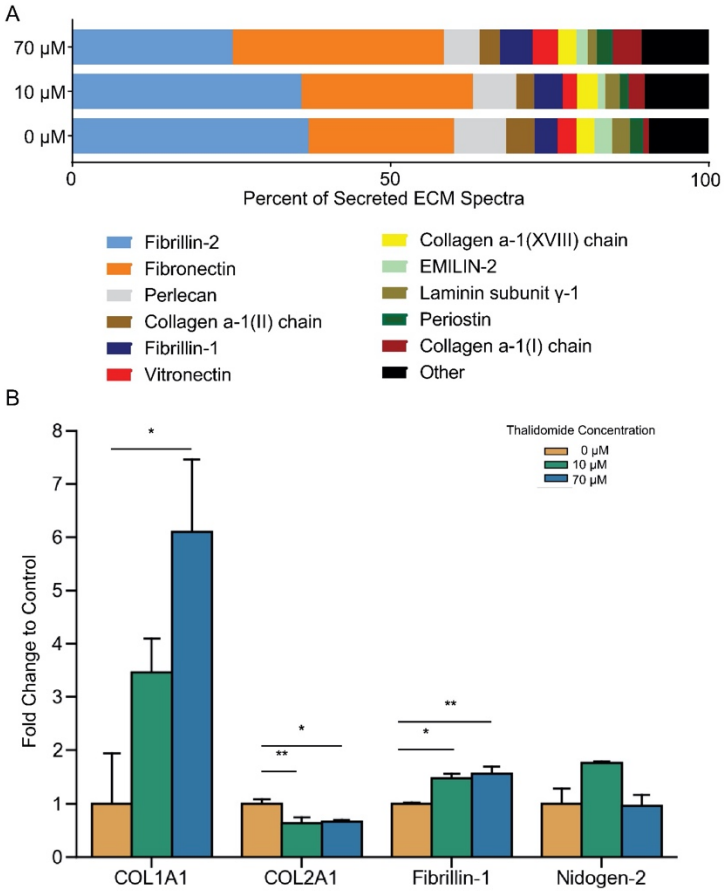

Figure 6.6 Thalidomide treatment impacts ECM composition.

(A) The ECM composition was characterized using LC-MS. The percent of secreted ECM spectra are shown for 0, 10, and 70 µM samples on day 20, with over 50% of the secreted ECM coming from fibrillin-2 and fibronectin in all treatment groups. The total ECM composition includes fibrillin, fibronectin, perlecan, collagen, vitronectin, periostin and others. (B) 70 µM ECM had significantly higher presence of collagen alpha-1(I) chain. Additionally, control ECM had significantly higher collagen alpha-1(II) chain compared to thalidomide treated groups (n=3 tissues, fold change is percent compared to control, (A)

one-way ANOVA, * = $p < 0.05$, ** = $p < 0.01$. (B) Tukey's multiple comparisons test within each protein, * = $p < 0.05$, ** = $p < 0.01$).

Discussion

In this proof-of-concept study, we show that our 3D developing engineered cardiac tissues (3D-dECTs) can be used to study drug-induced changes to cardiac tissue properties caused by thalidomide treatment during and after 3D cardiac differentiation. These developing cardiac tissues are directly differentiated from hiPSCs, allowing for examination of the cumulative effect of teratogen exposure on the cardiac tissue properties as well as during differentiation as the cells progress from pluripotent cells to cardiac tissue. Although thalidomide is a widely studied pharmaceutical, less is known about its interactions during development, particularly with differentiating hiPSCs. We first verified that thalidomide did not change short term hiPSC viability, proliferation, and mitochondria distribution compared to control groups. Thalidomide-treatment groups were administered to 3D-dECTs starting from day 1 of cardiac differentiation and showed effects after initial dosage administration. Tissue growth in thalidomide-treated 3D-dECTs was significantly less on days 5 and 7 when compared to control 3D-dECTs. In our 3D-dECT model we detected changes in tissue architecture and efficiency of cardiac differentiation on day 10 between the three treatment groups. Tissues began to spontaneously contract in all treatment groups; however, in the 70 μM thalidomide treated 3D-dECTs, contractions initiated later than age-matched controls. Initial contraction time intervals of thalidomide-treated 3D-dECTs were significantly longer and tissue formation was not as apparent as controls. When dissociated, thalidomide treated CMs contained localized and clustered

mitochondria while control CMs developed more evenly distributed mitochondria throughout the cytoplasm. Although most 2D monolayers did not result in contracting sheets when treated with thalidomide, some electrophysiological results could be obtained with this 2D approach. During optical mapping of control and thalidomide-treated 2D cardiac monolayers, calcium transient durations were longer and there was a slower conduction velocity in the thalidomide-treated samples compared to the control. By providing a 3D microenvironment throughout the timeline of stem cell differentiation, developmental changes and abnormalities that cannot be studied in 2D were identified in 3D-dECTs. Changes in ECM deposition were detected between the treatment groups; notably, thalidomide treated samples had a larger amount of collagen alpha-1(I) chain and fibrillin-1, and smaller amount of collagen alpha-1(II) chain; additionally, there were significant differences in nidogen-2 production. Appropriate changes in cardiac gene expression were detected in all three treatment groups, and there were significant differences in periostin and TGF-β1 expression between the treatment groups. Here we show that thalidomide negatively influences cardiac tissue formation, contractile function, mitochondria development, ECM composition, gene expression, and electrophysiology.

Historically for studying the formation of human CHDs, animal models (Ho et al. 1991), culture of explanted developing myocardium (Rivera-Feliciano and Tabin 2006), and 2D cell culture models with control and diseased cell lines have been employed. Animal models provide the ability to study the systemic development *in vivo*; however, because of the high cost and recommendations to minimize animal testing, they are not conducive for use in high-throughput screening assays; furthermore, they do not always accurately detect human-specific developmental defects, such as with the drug thalidomide

(Giacomotto and Segalat 2010). Explanted myocardium can provide relevant biological insights such as structural changes in tissue formation and changes in gene expression; however, there are a limited number of samples available and cannot be maintained long-term *in vitro.* Although *in vitro* models will always be an imperfect representation of the *in vivo* reality, reduction in the number of variables in the system can provide insights that would otherwise be clouded by systemic complexity. Previously, gene expression profiles of differentiating hPSCs treated with thalidomide significantly downregulated a variety of genes, including genes important for cell differentiation and organ development (Mayshar, Yanuka, and Benvenisty 2011; Meganathan et al. 2012), indicating that an *in vitro* hPSC-derived model may successfully recapitulate key aspects of development and provide insight in thalidomide-induced cardiac defect formation.

Utilizing temporal addition of small molecules has resulted in recent improvements in cardiac differentiation efficiency in 2D monolayer differentiation systems, which provides better reproducibility between experiments and allows for more accurate drug-testing; however, to achieve high yields of CMs and reproducible results, a critical component for success is the initial cell seeding density and cell proliferation (Lian et al. 2012; Lian et al. 2013a). Drug exposure impacts adherent cell concentration, making 2D differentiation challenging for systematically assessing the effects of teratogens. Previous work has been done using hPSCs as model systems to detect thalidomide induced changes, but these still rely on platforms that are only based on cells (Mayshar, Yanuka, and Benvenisty 2011; Xing et al. 2015; Z. Ma, Wang, et al. 2015). Alternatively, the approach of assembling of ECTs after CM differentiation does not allow for investigation of teratogen-induced changes that can occur during heart development**.** Particularly with

thalidomide-induced genetic mutations, an *in vitro* 3D direct differentiation tissue model is advantageous to study the impact of the drug-treatment throughout the process of cardiac tissue differentiation and formation. Because cardiac development is a 3D process, creating a reproducible and straight-forward 3D developing engineered cardiac tissue (3D-dECT) platform for developmental pharmacology provides the opportunity to be able to detect changes that will influence the developing 3D tissue that cannot be detected in 2D.

Thalidomide, which was tested in high concentrations on mice and rats, did not show any teratogenicity; years later researchers discovered that the teratogenic effects of thalidomide are species specific. This species specificity emphasizes the importance of human based *in vitro* studies (Parman, Wiley, and Wells 1999). Previous research has suggested that thalidomide is anti-angiogenic (Therapontos et al. 2009), with effects on chondrogenesis, DNA intercalation, and cell survival and proliferation (Stephens, Bunde, and Fillmore 2000). Thalidomide is known to bind to CRBN, potentially explaining the limb deformities because of the resulting inhibition of E3 ubiquitin ligase function (Ito, Ando, and Handa 2011); more recently, it has been shown that thalidomide can bind to Tbx5 (Khalil et al. 2017) and promote degradation of SALL4 (Donovan et al. 2018), potentially explaining the resulting cardiac phenotype. Additionally, thalidomide was previously shown to induce oxidative stress due to free radical production; in rabbits, thalidomide generates reactive oxygen species (ROS) that carry out DNA oxidation and inhibits fibroblast growth factor expression (Parman, Wiley, and Wells 1999; Hansen and Harris 2004). Knobloch *et al.* showed that thalidomide induced oxidative stress enhances Bmp signaling (i.e. up-regulation of Bmp) and inhibition of Wnt/β-catenin signaling pathways (Knobloch, Shaughnessy, and Ruther 2007). The upregulation of Bmp

downregulates Akt signaling; the Akt1 gene is essential for angiogenesis in the heart (Shiojima and Walsh 2006). Both Bmp and Wnt signaling pathways are important in cardiac development, particularly in small molecule guided stem cell differentiation (Lian et al. 2013a; Lian et al. 2012); furthermore, these pathways play a critical role in cell survival, proliferation, and death (Vargesson 2015). This perturbation in these developmental signaling pathways could therefore lead to thalidomide-induced CHDs and potentially explain the reason for lower efficiency of differentiation and resulting size of CMs in thalidomide treated samples in this study along with the noticeable differences in tissue growth and architecture.

The ECM composition of the resulting 3D-dECTs were quantified, and deposited ECM included fibrillin, fibronectin, perlecan, collagen, vitronectin, EMILIN-2, laminin, and periostin, with significant differences in COL1A1, COL2A1, fibrillin-1, and nidogen-2 deposition between thalidomide-treated 3D-dECTs and the control. Thalidomide has been previously investigated for improving the inflammatory response after heart failure; in these studies, thalidomide was found to decrease the collagen content (Yndestad et al. 2006). In addition, type I collagen production was significantly inhibited in cultured human lung fibroblasts exposed to thalidomide (Tseng et al. 2013). Interestingly, the effects of thalidomide on (ECM) production during heart development in our 3D-dECT platform showed opposite effects of type 1 collagen, with significantly more COL1A1 ECM deposition in thalidomide treated samples, which can potentially be explained by increased TGF-β production. Furthermore, there was a significant decrease in COL2A1 ECM production in thalidomide treated samples.

Mitochondria are complex organelles that are important in ATP production and cell signaling (Dorn, Vega, and Kelly 2015), and differences in mitochondria distribution and structure could were observed following thalidomide administration. The thalidomide-treated 3D-dECTs contained CMs with clustered mitochondria that were not distributed evenly throughout the cytoplasm of cells. In comparison, control CMs contained mitochondria close to the cell nuclei, throughout the cytoplasm, and close to and between sarcomeres, which is common in healthy muscle cells (Hom and Sheu 2009). Differences in mitochondria morphology and volume are often associated with increased reactive oxygen species (ROS) production and apoptosis (Parra et al. 2008), a proposed mechanism of thalidomide treatment; however more experiments are needed to fully elucidate the mechanism for the clustering of mitochondria in thalidomide treated CMs.

Thalidomide forever changed the field of drug testing procedures and regulations, especially for those who are pregnant; however, thalidomide was eventually approved by the FDA in 1998 for treating multiple myeloma and leprosy, although major warnings and routine screenings are a requirement to ensure that patients do not become pregnant while taking this drug (Rehman, Arfons, and Lazarus 2011). Here, we used this known teratogen as a proof-of-concept to demonstrate that the 3D-dECT model can be used to detect differences in tissue properties caused by drug administration during cardiac development. Because the successful production of contracting 3D-dECTs is not closely dependent on the initial seeding density and cell proliferation, all of our thalidomide-treated 3D-dECTs showed some degree of spontaneous contraction, which potentially would not have resulted in contracting CMs in other cell-based studies, particularly those carried out in 2D. Overall, this platform can be used to identify important differences between control and thalidomide

treatment groups, including differences in tissue formation and architecture, cardiac differentiation, contractile function, mitochondrial distribution, ECM deposition, and gene expression profiles. This study revealed that the 3D-dECT platform can be used to study drug induced changes to tissue properties during cardiac development and has the potential to be used in high-throughput drug screening applications and disease modeling.

Chapter 7: Overall Summary and Conclusions

Engineered cardiac tissues that can be directly produced from human induced pluripotent stem cells (hiPSCs) in scalable, suspension culture systems are needed to meet the demands of cardiac regenerative medicine. In the first project (Chapter 2), successful production of functional cardiac tissue microspheres through direct differentiation of hydrogel encapsulated hiPSCs is demonstrated. To form the microspheres, hiPSCs were suspended within the photocrosslinkable biomaterial, PEG-fibrinogen, and were encapsulated at a rate of 420,000 cells/minute using a novel microfluidic system. Even at this high cell density and rapid production rate, high intra-batch and batch-to-batch reproducibility were achieved. Following microsphere formation, hiPSCs maintained high cell viability and continued to grow within and beyond the original PEG-fibrinogen matrix. These initially soft microspheres (< 250 Pa) supported efficient cardiac differentiation using the established RPMI/B27 protocol; spontaneous contractions initiated by differentiation day 8, and the microspheres contained > 70% cardiomyocytes (CMs). CMs responded appropriately to pharmacological stimuli and exhibited 1:1 capture up to 6.0 Hz when electrically paced. Over time, cells formed cell-cell junctions and aligned myofibril fibers; engineered cardiac microspheres were maintained in culture over 3 years. The capability to rapidly generate uniform cardiac microsphere tissues is critical for advancing downstream applications including biomanufacturing, multi-well plate drug screening, and injection-based regenerative therapies.

A key component for clinical translation of ECTs is the need for production to occur using clinically relevant culture conditions. In Chapter 3, ECT microsphere production

using chemically defined conditions, including stem cell media (E8) and cardiac differentiation media (CDM3), is established. The custom microfluidic cell encapsulation system was used to encapsulate hiPSCs in PEG-fibrinogen microspheres ranging from 400–1000 μm in diameter. High cell viability and phenotype were maintained following microfluidic encapsulation. Microspheres were highly spherical and were uniform within a batch. Three days after encapsulation, cardiac differentiation was initiated through continuous control of the Wnt signaling through supplementation with small molecules. Efficient cardiac differentiation occurred, and this differentiation protocol could be used to achieve CM contents greater than with the RPMI/B27 differentiation protocol; however, there was larger variability in differentiation outcomes. ECT microspheres spontaneously contracted between day 7 and day 10 of differentiation and responded to electrical pacing up to 1.5 Hz. Resulting CMs had the presence of well-defined sarcomeres, and the expression of gap junction protein, Cx43, increased with culture time. Current biomanufacturing of CMs in large scale bioreactors involves the formation and differentiation of self-aggregated EBs; therefore, the resulting CM content and cell yield of microspheres were compared to self-aggregated EBs. Three different platforms for EB formation and differentiation were utilized: formation and differentiation in a shaker flask and well plate, and formation in a shaker flask and differentiation in a well plate. CM differentiation efficiency and resulting number of CMs were similar between the ECT microspheres and EBs; however, there were indications that a higher number of CMs could be obtained with the microspheres. Future studies will include a more in-depth investigation of the differences between the microspheres and the EBs, particularly with regard to CM formation and maturation.

Building on this work, the production of ECT microspheroids from encapsulated hiPSCs with varying size and shape is presented in Chapter 4. Through microfluidic system parameter modulation, such as PDMS device design and flow fraction, microspheroids with sizes ranging from 400–1000 μm in diameter with axial ratios (ARs) of 1–9 could be achieved. An initial design of experiments was produced to systematically investigate the impact of initial cell concentration, PEG-fibrinogen concentration, microspheroid size, and AR on cardiac differentiation and maturity. Encapsulated hiPSCs maintained high cell viability at each of the geometries and continued to proliferate and grow, forming a continuous tissue following chemically defined cardiac differentiation. ECT microspheroids began to spontaneously contract between days 7 and 10 of differentiation. The CM content was assessed on day 10 and there was large variability in cardiac differentiation efficiencies. Single analysis investigation did not reveal any significant differences between these features and CM content or cell yield, the number of CMs per input hiPSC; therefore, feature engineering and data-driven modeling were performed to investigate these features in combination. A classification model using support vector machines was developed that could predict CM content with an accuracy of 68% and Matthew's correlation coefficient of 0.31. Resulting CMs had the presence of well-defined sarcomeres by day 30, with indications that microspheroids with higher AR (> 2) resulted in increased CM elongation and sarcomere organization. Initial scale-up studies demonstrated the ability to culture and differentiate the microspheroids in shaker flasks, and over 40 million cells per batch were obtained with high reproducibility in efficiency of differentiation between batches. Future work will involve further characterization of CM functionality and maturity by quantification of sarcomere length, sarcomere organization,

cell size, and cell circularity throughout long-term culture; furthermore, future characterization will include gene expression of structural and maturity genes and optical mapping for electrophysiological characterization of action potentials and quantification of conduction velocity. These results will be used to continue to build and improve the data-driven models for predicting cardiac differentiation and functionality.

The ability to non-destructively monitor CM differentiation and function in ECTs would provide advancements in biomanufacturing. One way to monitor CM function is through electrophysiological recordings of action potentials, and Dr. Gepstein's research group previously established an hiPSC line with a genetically encoded voltage indicator (Shinnawi et al. 2015). Previous research in the Lipke Lab involved the direct differentiation of ECTs from PEG-fibrinogen encapsulated hiPSC photocrosslinking with Eosin Y (P. Kerscher, Turnbull, et al. 2016; Petra Kerscher, Kaczmarek, et al. 2016). Although Eosin Y is water soluble, biocompatible, and can be photocrosslinked with visible light, it exhibits green autofluorescence that overlaps with common fluorophores used in cell-imaging assays and the genetically voltage indicator. In Chapter 5, the ability of the photoinitiator lithium phenyl-2,4,6-trimethlybenzoylphosphinate (LAP) to support crosslinking of PEG-fibrinogen hydrogels and generate ECTs without autofluorescence was demonstrated. Two light sources were used for photocrosslinking with LAP, a 365 nm UV lamp (LAP 365) and a 405 nm hand-held blue light (LAP 405); these were compared to the previously established crosslinking method using a visible light source for crosslinking with Eosin Y. Hydrogels crosslinked with LAP 405 were significantly softer than those photocrosslinked with LAP 365 and EY. A microisland and rectangular geometry were used for hiPSCs encapsulation in PEG-fibrinogen; encapsulated hiPSCs

maintained high cell viability and appropriate proliferative and pluripotency phenotype following LAP-initiated photocrosslinking. Encapsulated hiPSCs could be differentiated to form a dense, continuous ECT. These ECTs spontaneously contracted with increasing contraction velocities over time, a feature of maturing CMs. There were no significant differences in the CM differentiation efficiency or cell number on day 10 between samples crosslinked with LAP 365, LAP 405, or EY. ECTs photocrosslinked with LAP could be used for non-destructive monitoring of the action potentials. This study shows the ability to overcome the autofluorescence of Eosin Y using LAP, and this platform can be used for monitoring of hiPSCs with a genetically encoded voltage indicator (GEVI) and shows potential for the use of the direct differentiation system in a 3D bioprinter.

In the last study (Chapter 6), the ability to use the previously established 3D developing ECT (3D-dECT) model to detect drug-induced changes to cardiac tissue and formation was demonstrated using the known teratogen, thalidomide. HiPSCs were encapsulated in PEG-fibrinogen microislands and were cultured for three days prior to initiation of cardiac differentiation. On day 0, cardiac differentiation was initiated; the media was supplemented with thalidomide in three concentrations 0 μM (drug carrier), 10 μM, and 70 μM, beginning on day 1 and continued throughout the time course of differentiation and 3D-dECT culture. Thalidomide treatment impacted tissue formation and growth in a dose-dependent matter, with statistical differences in tissue area by day 5. This significant decrease in tissue area in thalidomide treated samples was accompanied by a subsequent increase in cell debris. On day 10, the percentage of CMs was significantly lower in thalidomide treated samples compared to the control. Furthermore, there were differences in function and electrophysiology between the thalidomide treated samples and

the control. 3D-dECTs from all treatment groups demonstrated appropriate temporal change in cardiac gene expression. The secreted ECM was quantified using LC-MS, and thalidomide treatment impacted the composition of secreted ECM, most notably collagen I, which may be due in part to the upregulation of TGF-β gene expression. These results indicate that the direct differentiation platform can be used for drug-testing, particularly studying the cumulative effect of drugs throughout cardiac differentiation.

Taken together, these results indicate that the 3D direct differentiation platform can be used to produce functional ECT microspheres from encapsulated hiPSCs using a custom microfluidic system; furthermore, the flexibility of this system can be utilized to produce ECT microspheroids with a range of geometries, initial cell concentrations, and PEG-fibrinogen concentrations using a chemically defined differentiation protocol. This direct cardiac differentiation platform was extended to be used in LAP-initiated photocrosslinking of PEG-fibrinogen for non-destructive monitoring of action potentials using a genetically encoded voltage indicator. Finally, the ability for this direct differentiation platform to detect drug-induced changes during development was demonstrated. These results demonstrate the potential for the use of the 3D direct differentiation microspheroid platform for scalable production, 3D printing, and high-throughput drug-screening.

References

Abecasis, B., T. Aguiar, E. Arnault, R. Costa, P. Gomes-Alves, A. Aspegren, M. Serra, and P. M. Alves. 2017. "Expansion of 3D human induced pluripotent stem cell aggregates in bioreactors: Bioprocess intensification and scaling-up approaches." *J Biotechnol* 246: 81-93. https://doi.org/10.1016/j.jbiotec.2017.01.004. https://www.ncbi.nlm.nih.gov/pubmed/28131858.

Adler, S., C. Pellizzer, L. Hareng, T. Hartung, and S. Bremer. 2008. "First steps in establishing a developmental toxicity test method based on human embryonic stem cells." *Toxicol In Vitro* 22 (1): 200-11. https://doi.org/10.1016/j.tiv.2007.07.013. http://www.ncbi.nlm.nih.gov/pubmed/17961973.

Almany, L., and D. Seliktar. 2005. "Biosynthetic hydrogel scaffolds made from fibrinogen and polyethylene glycol for 3D cell cultures." *Biomaterials* 26 (15): 2467-77. https://doi.org/10.1016/j.biomaterials.2004.06.047. https://www.ncbi.nlm.nih.gov/pubmed/15585249.

Anna, Shelley L., Nathalie Bontoux, and Howard A. Stone. 2003. "Formation of dispersions using “flow focusing” in microchannels." *Applied Physics Letters* 82 (3): 364-366. https://doi.org/10.1063/1.1537519.

Badrossamay, M. R., K. Balachandran, A. K. Capulli, H. M. Golecki, A. Agarwal, J. A. Goss, H. Kim, K. Shin, and K. K. Parker. 2014. "Engineering hybrid polymer-protein super-aligned nanofibers via rotary jet spinning." *Biomaterials* 35 (10): 3188-97. https://doi.org/10.1016/j.biomaterials.2013.12.072. https://www.ncbi.nlm.nih.gov/pubmed/24456606.

Bajaj, P., R. M. Schweller, A. Khademhosseini, J. L. West, and R. Bashir. 2014. "3D biofabrication strategies for tissue engineering and regenerative medicine." *Annu Rev Biomed Eng* 16: 247-76. https://doi.org/10.1146/annurev-bioeng-071813-105155. https://www.ncbi.nlm.nih.gov/pubmed/24905875.

Beauchamp, P., W. Moritz, J. M. Kelm, N. D. Ullrich, I. Agarkova, B. D. Anson, T. M. Suter, and C. Zuppinger. 2015. "Development and Characterization of a Scaffold-Free 3D Spheroid Model of Induced Pluripotent Stem Cell-Derived Human Cardiomyocytes." *Tissue Eng Part C Methods* 21 (8): 852-61. https://doi.org/10.1089/ten.TEC.2014.0376. https://www.ncbi.nlm.nih.gov/pubmed/25654582.

Belair, D. G., G. Lu, L. E. Waller, J. A. Gustin, N. D. Collins, and K. L. Kolaja. 2020. "Thalidomide Inhibits Human iPSC Mesendoderm Differentiation by Modulating CRBN-dependent Degradation of SALL4." *Sci Rep* 10 (1): 2864. https://doi.org/10.1038/s41598-020-59542-x. https://www.ncbi.nlm.nih.gov/pubmed/32071327.

Bellamy, V., V. Vanneaux, A. Bel, H. Nemetalla, S. Emmanuelle Boitard, Y. Farouz, P. Joanne, M. C. Perier, E. Robidel, C. Mandet, A. Hagege, P. Bruneval, J. Larghero, O. Agbulut, and P. Menasche. 2015. "Long-term functional benefits of human embryonic stem cell-derived cardiac progenitors embedded into a fibrin scaffold."

J Heart Lung Transplant 34 (9): 1198-207. https://doi.org/10.1016/j.healun.2014.10.008. https://www.ncbi.nlm.nih.gov/pubmed/25534019.

Blin, G., D. Nury, S. Stefanovic, T. Neri, O. Guillevic, B. Brinon, V. Bellamy, C. Rucker-Martin, P. Barbry, A. Bel, P. Bruneval, C. Cowan, J. Pouly, S. Mitalipov, E. Gouadon, P. Binder, A. Hagege, M. Desnos, J. F. Renaud, P. Menasche, and M. Puceat. 2010. "A purified population of multipotent cardiovascular progenitors derived from primate pluripotent stem cells engrafts in postmyocardial infarcted nonhuman primates." *J Clin Invest* 120 (4): 1125-39. https://doi.org/10.1172/JCI40120. https://www.ncbi.nlm.nih.gov/pubmed/20335662.

Boffito, Monica, Susanna Sartori, and Gianluca Ciardelli. 2014. "Polymeric scaffolds for cardiac tissue engineering: requirements and fabrication technologies." *Polymer International* 63 (1): 2-11. https://doi.org/10.1002/pi.4608.

Boheler, K. R. 2002. "Differentiation of Pluripotent Embryonic Stem Cells Into Cardiomyocytes." *Circulation Research* 91 (3): 189-201. https://doi.org/10.1161/01.res.0000027865.61704.32.

Bowers, S. L., I. Banerjee, and T. A. Baudino. 2010. "The extracellular matrix: at the center of it all." *J Mol Cell Cardiol* 48 (3): 474-82. https://doi.org/10.1016/j.yjmcc.2009.08.024. https://www.ncbi.nlm.nih.gov/pubmed/19729019.

Branco, M. A., J. P. Cotovio, C. A. V. Rodrigues, S. H. Vaz, T. G. Fernandes, L. M. Moreira, J. M. S. Cabral, and M. M. Diogo. 2019. "Transcriptomic analysis of 3D Cardiac Differentiation of Human Induced Pluripotent Stem Cells Reveals Faster Cardiomyocyte Maturation Compared to 2D Culture." *Sci Rep* 9 (1): 9229. https://doi.org/10.1038/s41598-019-45047-9. https://www.ncbi.nlm.nih.gov/pubmed/31239450.

Bratt-Leal, A. M., R. L. Carpenedo, and T. C. McDevitt. 2009. "Engineering the embryoid body microenvironment to direct embryonic stem cell differentiation." *Biotechnol Prog* 25 (1): 43-51. https://doi.org/10.1002/btpr.139. https://www.ncbi.nlm.nih.gov/pubmed/19198003.

Bratt-Leal, A. M., R. L. Carpenedo, M. D. Ungrin, P. W. Zandstra, and T. C. McDevitt. 2011. "Incorporation of biomaterials in multicellular aggregates modulates pluripotent stem cell differentiation." *Biomaterials* 32 (1): 48-56. https://doi.org/10.1016/j.biomaterials.2010.08.113. https://www.ncbi.nlm.nih.gov/pubmed/20864164.

Brooks, Elizabeth A., Lauren E. Jansen, Maria F. Gencoglu, Annali M. Yurkevicz, and Shelly R. Peyton. 2018. "Complementary, Semiautomated Methods for Creating Multidimensional PEG-Based Biomaterials." *ACS Biomaterials Science & Engineering* 4 (2): 707-718. https://doi.org/10.1021/acsbiomaterials.7b00737.

Burridge, P. W., D. Anderson, H. Priddle, M. D. Barbadillo Munoz, S. Chamberlain, C. Allegrucci, L. E. Young, and C. Denning. 2007. "Improved human embryonic stem cell embryoid body homogeneity and cardiomyocyte differentiation from a novel V-96 plate aggregation system highlights interline variability." *Stem Cells* 25 (4): 929-38. https://doi.org/10.1634/stemcells.2006-0598. http://www.ncbi.nlm.nih.gov/pubmed/17185609.

Burridge, P. W., E. Matsa, P. Shukla, Z. C. Lin, J. M. Churko, A. D. Ebert, F. Lan, S. Diecke, B. Huber, N. M. Mordwinkin, J. R. Plews, O. J. Abilez, B. Cui, J. D. Gold, and J. C. Wu. 2014. "Chemically defined generation of human cardiomyocytes." *Nat Methods* 11 (8): 855-60. https://doi.org/10.1038/nmeth.2999. https://www.ncbi.nlm.nih.gov/pubmed/24930130.

Burridge, P. W., S. Thompson, M. A. Millrod, S. Weinberg, X. Yuan, A. Peters, V. Mahairaki, V. E. Koliatsos, L. Tung, and E. T. Zambidis. 2011. "A universal system for highly efficient cardiac differentiation of human induced pluripotent stem cells that eliminates interline variability." *PLoS One* 6 (4): e18293. https://doi.org/10.1371/journal.pone.0018293. http://www.ncbi.nlm.nih.gov/pubmed/21494607.

Carpenter, L., C. Carr, C. T. Yang, D. J. Stuckey, K. Clarke, and S. M. Watt. 2012. "Efficient differentiation of human induced pluripotent stem cells generates cardiac cells that provide protection following myocardial infarction in the rat." *Stem Cells Dev* 21 (6): 977-86. https://doi.org/10.1089/scd.2011.0075. https://www.ncbi.nlm.nih.gov/pubmed/22182484.

Caspi, O., I. Itzhaki, I. Kehat, A. Gepstein, G. Arbel, I. Huber, J. Satin, and L. Gepstein. 2009. "In vitro electrophysiological drug testing using human embryonic stem cell derived cardiomyocytes." *Stem Cells Dev* 18 (1): 161-72. https://doi.org/10.1089/scd.2007.0280. http://www.ncbi.nlm.nih.gov/pubmed/18510453.

Chan, H. F., Y. Zhang, and K. W. Leong. 2016. "Efficient One-Step Production of Microencapsulated Hepatocyte Spheroids with Enhanced Functions." *Small*. https://doi.org/10.1002/smll.201502932. http://www.ncbi.nlm.nih.gov/pubmed/27038291.

Chang, S., F. Finklea, B. Williams, H. Hammons, A. Hodge, S. Scott, and E. Lipke. 2020a. "Emulsion-based encapsulation of pluripotent stem cells in hydrogel microspheres for cardiac differentiation." *Biotechnol Prog* 36 (4): e2986. https://doi.org/10.1002/btpr.2986. https://www.ncbi.nlm.nih.gov/pubmed/32108999.

Chen, V. C., J. Ye, P. Shukla, G. Hua, D. Chen, Z. Lin, J. C. Liu, J. Chai, J. Gold, J. Wu, D. Hsu, and L. A. Couture. 2015. "Development of a scalable suspension culture for cardiac differentiation from human pluripotent stem cells." *Stem Cell Res* 15 (2): 365-75. https://doi.org/10.1016/j.scr.2015.08.002. http://www.ncbi.nlm.nih.gov/pubmed/26318718.

Choe, J. Y., H. J. Jung, K. Y. Park, Y. S. Kum, G. G. Song, D. S. Hyun, S. H. Park, and S. K. Kim. 2010. "Anti-fibrotic effect of thalidomide through inhibiting TGF-beta-induced ERK1/2 pathways in bleomycin-induced lung fibrosis in mice." *Inflamm Res* 59 (3): 177-88. https://doi.org/10.1007/s00011-009-0084-9. https://www.ncbi.nlm.nih.gov/pubmed/19757088.

Choi, C. H., J. H. Jung, Y. W. Rhee, D. P. Kim, S. E. Shim, and C. S. Lee. 2007. "Generation of monodisperse alginate microbeads and in situ encapsulation of cell in microfluidic device." *Biomed Microdevices* 9 (6): 855-62. https://doi.org/10.1007/s10544-007-9098-7. https://www.ncbi.nlm.nih.gov/pubmed/17578667.

Chong, J. J., X. Yang, C. W. Don, E. Minami, Y. W. Liu, J. J. Weyers, W. M. Mahoney, B. Van Biber, S. M. Cook, N. J. Palpant, J. A. Gantz, J. A. Fugate, V. Muskheli, G. M. Gough, K. W. Vogel, C. A. Astley, C. E. Hotchkiss, A. Baldessari, L. Pabon, H. Reinecke, E. A. Gill, V. Nelson, H. P. Kiem, M. A. Laflamme, and C. E. Murry. 2014. "Human embryonic-stem-cell-derived cardiomyocytes regenerate non-human primate hearts." *Nature* 510 (7504): 273-7. https://doi.org/10.1038/nature13233. http://www.ncbi.nlm.nih.gov/pubmed/24776797.

Chow, A., D. J. Stuckey, E. Kidher, M. Rocco, R. J. Jabbour, C. A. Mansfield, A. Darzi, S. E. Harding, M. M. Stevens, and T. Athanasiou. 2017. "Human Induced Pluripotent Stem Cell-Derived Cardiomyocyte Encapsulating Bioactive Hydrogels Improve Rat Heart Function Post Myocardial Infarction." *Stem Cell Reports* 9 (5): 1415-1422. https://doi.org/10.1016/j.stemcr.2017.09.003. https://www.ncbi.nlm.nih.gov/pubmed/28988988.

Chu, Lily, and David K. Robinson. 2001. "Industrial choices for protein production by large-scale cell culture." *Current Opinion in Biotechnology* 12 (2): 180-187. https://doi.org/http://dx.doi.org/10.1016/S0958-1669(00)00197-X. http://www.sciencedirect.com/science/article/pii/S095816690000197X.

Cruise, G. M., O. D. Hegre, D. S. Scharp, and J. A. Hubbell. 1998. "A sensitivity study of the key parameters in the interfacial photopolymerization of poly(ethylene glycol) diacrylate upon porcine islets." *Biotechnol Bioeng* 57 (6): 655-65. https://doi.org/10.1002/(sici)1097-0290(19980320)57:6<655::aid-bit3>3.0.co;2-k. https://www.ncbi.nlm.nih.gov/pubmed/10099245.

Davidson, Lance, and Ray Keller. 2007. "Measuring Mechanical Properties of Embryos and Embryonic Tissues." 83: 425-439. https://doi.org/10.1016/s0091-679x(07)83018-4.

Dean, E. W., B. Udelsman, and C. K. Breuer. 2012. "Current advances in the translation of vascular tissue engineering to the treatment of pediatric congenital heart disease." *Yale J Biol Med* 85 (2): 229-38. http://www.ncbi.nlm.nih.gov/pubmed/22737051.

Del Alamo, J. C., D. Lemons, R. Serrano, A. Savchenko, F. Cerignoli, R. Bodmer, and M. Mercola. 2016. "High throughput physiological screening of iPSC-derived cardiomyocytes for drug development." *Biochim Biophys Acta* 1863 (7 Pt B): 1717-27. https://doi.org/10.1016/j.bbamcr.2016.03.003. http://www.ncbi.nlm.nih.gov/pubmed/26952934.

DeLong, S. A., J. J. Moon, and J. L. West. 2005. "Covalently immobilized gradients of bFGF on hydrogel scaffolds for directed cell migration." *Biomaterials* 26 (16): 3227-34. https://doi.org/10.1016/j.biomaterials.2004.09.021. http://www.ncbi.nlm.nih.gov/pubmed/15603817.

Dikovsky, D., H. Bianco-Peled, and D. Seliktar. 2006. "The effect of structural alterations of PEG-fibrinogen hydrogel scaffolds on 3-D cellular morphology and cellular migration." *Biomaterials* 27 (8): 1496-506. https://doi.org/10.1016/j.biomaterials.2005.09.038. http://www.ncbi.nlm.nih.gov/pubmed/16243393.

Ding, M., H. Andersson, S. Martinsson, A. Sabirsh, A. Jonebring, Q. D. Wang, A. T. Plowright, and L. Drowley. 2020. "Aligned nanofiber scaffolds improve functionality of cardiomyocytes differentiated from human induced pluripotent

stem cell-derived cardiac progenitor cells." *Sci Rep* 10 (1): 13575. https://doi.org/10.1038/s41598-020-70547-4. https://www.ncbi.nlm.nih.gov/pubmed/32782331.

Domenech, M., L. Polo-Corrales, J. E. Ramirez-Vick, and D. O. Freytes. 2016. "Tissue Engineering Strategies for Myocardial Regeneration: Acellular Versus Cellular Scaffolds?" *Tissue Eng Part B Rev* 22 (6): 438-458. https://doi.org/10.1089/ten.TEB.2015.0523. https://www.ncbi.nlm.nih.gov/pubmed/27269388.

Don, C. W., and C. E. Murry. 2013. "Improving survival and efficacy of pluripotent stem cell-derived cardiac grafts." *J Cell Mol Med* 17 (11): 1355-62. https://doi.org/10.1111/jcmm.12147. https://www.ncbi.nlm.nih.gov/pubmed/24118766.

Donovan, K. A., J. An, R. P. Nowak, J. C. Yuan, E. C. Fink, B. C. Berry, B. L. Ebert, and E. S. Fischer. 2018. "Thalidomide promotes degradation of SALL4, a transcription factor implicated in Duane Radial Ray Syndrome." *Elife* 7. https://doi.org/10.7554/eLife.38430. https://www.ncbi.nlm.nih.gov/pubmed/30067223.

Dorn, G. W., 2nd, R. B. Vega, and D. P. Kelly. 2015. "Mitochondrial biogenesis and dynamics in the developing and diseased heart." *Genes Dev* 29 (19): 1981-91. https://doi.org/10.1101/gad.269894.115. http://www.ncbi.nlm.nih.gov/pubmed/26443844.

dos Santos, F. F., P. Z. Andrade, C. L. da Silva, and J. M. Cabral. 2013. "Bioreactor design for clinical-grade expansion of stem cells." *Biotechnol J* 8 (6): 644-54. https://doi.org/10.1002/biot.201200373. https://www.ncbi.nlm.nih.gov/pubmed/23625834.

Dunn, D. A., A. J. Hodge, and E. A. Lipke. 2014. "Biomimetic materials design for cardiac tissue regeneration." *Wiley Interdiscip Rev Nanomed Nanobiotechnol* 6 (1): 15-39. https://doi.org/10.1002/wnan.1241. https://www.ncbi.nlm.nih.gov/pubmed/24123919.

Dunn, K. K., I. M. Reichardt, A. D. Simmons, G. Jin, M. E. Floy, K. M. Hoon, and S. P. Palecek. 2019. "Coculture of Endothelial Cells with Human Pluripotent Stem Cell-Derived Cardiac Progenitors Reveals a Differentiation Stage-Specific Enhancement of Cardiomyocyte Maturation." *Biotechnol J* 14 (8): e1800725. https://doi.org/10.1002/biot.201800725. https://www.ncbi.nlm.nih.gov/pubmed/30927511.

Dunn, Kaitlin K., and Sean P. Palecek. 2018. "Engineering Scalable Manufacturing of High-Quality Stem Cell-Derived Cardiomyocytes for Cardiac Tissue Repair." *Frontiers in Medicine* 5. https://doi.org/10.3389/fmed.2018.00110.

El-Kirat-Chatel, S., A. Beaussart, S. P. Vincent, M. Abellan Flos, P. Hols, P. N. Lipke, and Y. F. Dufrene. 2015. "Forces in yeast flocculation." *Nanoscale* 7 (5): 1760-7. https://doi.org/10.1039/c4nr06315e. http://www.ncbi.nlm.nih.gov/pubmed/25515338.

Elbert, D. L., and J. A. Hubbell. 2001. "Conjugate addition reactions combined with free-radical cross-linking for the design of materials for tissue engineering." *Biomacromolecules* 2 (2): 430-41. https://doi.org/10.1021/bm0056299. https://www.ncbi.nlm.nih.gov/pubmed/11749203.

Ellis, Morgan E., and Elizabeth A. Lipke. 2018. "Direct Production of Engineered Cardiac Tissue within Hybrid Biomaterials." *CEP*: 73-79.

Fairbanks, B. D., M. P. Schwartz, C. N. Bowman, and K. S. Anseth. 2009. "Photoinitiated polymerization of PEG-diacrylate with lithium phenyl-2,4,6-trimethylbenzoylphosphinate: polymerization rate and cytocompatibility." *Biomaterials* 30 (35): 6702-7. https://doi.org/10.1016/j.biomaterials.2009.08.055. https://www.ncbi.nlm.nih.gov/pubmed/19783300.

Fedorovich, N. E., M. H. Oudshoorn, D. van Geemen, W. E. Hennink, J. Alblas, and W. J. Dhert. 2009. "The effect of photopolymerization on stem cells embedded in hydrogels." *Biomaterials* 30 (3): 344-53. https://doi.org/10.1016/j.biomaterials.2008.09.037. https://www.ncbi.nlm.nih.gov/pubmed/18930540.

Fennema, E., N. Rivron, J. Rouwkema, C. van Blitterswijk, and J. de Boer. 2013. "Spheroid culture as a tool for creating 3D complex tissues." *Trends Biotechnol* 31 (2): 108-15. https://doi.org/10.1016/j.tibtech.2012.12.003. https://www.ncbi.nlm.nih.gov/pubmed/23336996.

Feric, N. T., and M. Radisic. 2016a. "Maturing human pluripotent stem cell-derived cardiomyocytes in human engineered cardiac tissues." *Adv Drug Deliv Rev* 96: 110-34. https://doi.org/10.1016/j.addr.2015.04.019. https://www.ncbi.nlm.nih.gov/pubmed/25956564.

---. 2016b. "Strategies and Challenges to Myocardial Replacement Therapy." *Stem Cells Transl Med* 5 (4): 410-6. https://doi.org/10.5966/sctm.2015-0288. https://www.ncbi.nlm.nih.gov/pubmed/26933042.

Fermini, B., S. T. Coyne, and K. P. Coyne. 2018. "Clinical Trials in a Dish: A Perspective on the Coming Revolution in Drug Development." *SLAS Discov* 23 (8): 765-776. https://doi.org/10.1177/2472555218775028. https://www.ncbi.nlm.nih.gov/pubmed/29862873.

Ferri, N., P. Siegl, A. Corsini, J. Herrmann, A. Lerman, and R. Benghozi. 2013. "Drug attrition during pre-clinical and clinical development: understanding and managing drug-induced cardiotoxicity." *Pharmacol Ther* 138 (3): 470-84. https://doi.org/10.1016/j.pharmthera.2013.03.005. https://www.ncbi.nlm.nih.gov/pubmed/23507039.

Feyen, D. A. M., W. L. McKeithan, A. A. N. Bruyneel, S. Spiering, L. Hormann, B. Ulmer, H. Zhang, F. Briganti, M. Schweizer, B. Hegyi, Z. Liao, R. P. Polonen, K. S. Ginsburg, C. K. Lam, R. Serrano, C. Wahlquist, A. Kreymerman, M. Vu, P. L. Amatya, C. S. Behrens, S. Ranjbarvaziri, R. G. C. Maas, M. Greenhaw, D. Bernstein, J. C. Wu, D. M. Bers, T. Eschenhagen, C. M. Metallo, and M. Mercola. 2020. "Metabolic Maturation Media Improve Physiological Function of Human iPSC-Derived Cardiomyocytes." *Cell Rep* 32 (3): 107925. https://doi.org/10.1016/j.celrep.2020.107925. https://www.ncbi.nlm.nih.gov/pubmed/32697997.

Fisher, J. P., D. Dean, P. S. Engel, and A. G. Mikos. 2001. "Photoinitiated polymerization of biomaterials." *Annual Review of Materials Research* 31: 171-181. https://doi.org/DOI 10.1146/annurev.matsci.31.1.171. <Go to ISI>://WOS:000171808700008.

Fonoudi, H., H. Ansari, S. Abbasalizadeh, M. R. Larijani, S. Kiani, S. Hashemizadeh, A. S. Zarchi, A. Bosman, G. M. Blue, S. Pahlavan, M. Perry, Y. Orr, Y. Mayorchak, J. Vandenberg, M. Talkhabi, D. S. Winlaw, R. P. Harvey, N. Aghdami, and H. Baharvand. 2015. "A Universal and Robust Integrated Platform for the Scalable Production of Human Cardiomyocytes From Pluripotent Stem Cells." *Stem Cells Transl Med* 4 (12): 1482-94. https://doi.org/10.5966/sctm.2014-0275. http://www.ncbi.nlm.nih.gov/pubmed/26511653.

Gao, L., Z. R. Gregorich, W. Zhu, S. Mattapally, Y. Oduk, X. Lou, R. Kannappan, A. V. Borovjagin, G. P. Walcott, A. E. Pollard, V. G. Fast, X. Hu, S. G. Lloyd, Y. Ge, and J. Zhang. 2018. "Large Cardiac Muscle Patches Engineered From Human Induced-Pluripotent Stem Cell-Derived Cardiac Cells Improve Recovery From Myocardial Infarction in Swine." *Circulation* 137 (16): 1712-1730. https://doi.org/10.1161/CIRCULATIONAHA.117.030785. https://www.ncbi.nlm.nih.gov/pubmed/29233823.

Gao, X., R. L. Sprando, and J. J. Yourick. 2015. "Thalidomide induced early gene expression perturbations indicative of human embryopathy in mouse embryonic stem cells." *Toxicol Appl Pharmacol* 287 (1): 43-51. https://doi.org/10.1016/j.taap.2015.05.009. http://www.ncbi.nlm.nih.gov/pubmed/26006729.

Garbern, J. C., A. Helman, R. Sereda, M. Sarikhani, A. Ahmed, G. O. Escalante, R. Ogurlu, S. L. Kim, J. F. Zimmerman, A. Cho, L. MacQueen, V. J. Bezzerides, K. K. Parker, D. A. Melton, and R. T. Lee. 2020. "Inhibition of mTOR Signaling Enhances Maturation of Cardiomyocytes Derived From Human-Induced Pluripotent Stem Cells via p53-Induced Quiescence." *Circulation* 141 (4): 285-300. https://doi.org/10.1161/CIRCULATIONAHA.119.044205. https://www.ncbi.nlm.nih.gov/pubmed/31707831.

Gelb, B., M. Brueckner, W. Chung, E. Goldmuntz, J. Kaltman, J. P. Kaski, R. Kim, J. Kline, L. Mercer-Rosa, G. Porter, A. Roberts, E. Rosenberg, H. Seiden, C. Seidman, L. Sleeper, S. Tennstedt, J. Kaltman, C. Schramm, K. Burns, G. Pearson, and E. Rosenberg. 2013. "The Congenital Heart Disease Genetic Network Study: rationale, design, and early results." *Circ Res* 112 (4): 698-706. https://doi.org/10.1161/CIRCRESAHA.111.300297. http://www.ncbi.nlm.nih.gov/pubmed/23410879.

Gerbin, K. A., X. Yang, C. E. Murry, and K. L. Coulombe. 2015. "Enhanced Electrical Integration of Engineered Human Myocardium via Intramyocardial versus Epicardial Delivery in Infarcted Rat Hearts." *PLoS One* 10 (7): e0131446. https://doi.org/10.1371/journal.pone.0131446. https://www.ncbi.nlm.nih.gov/pubmed/26161513.

Giacomelli, E., V. Meraviglia, G. Campostrini, A. Cochrane, X. Cao, R. W. J. van Helden, A. Krotenberg Garcia, M. Mircea, S. Kostidis, R. P. Davis, B. J. van Meer, C. R. Jost, A. J. Koster, H. Mei, D. G. Miguez, A. A. Mulder, M. Ledesma-Terron, G. Pompilio, L. Sala, D. C. F. Salvatori, R. C. Slieker, E. Sommariva, A. A. F. de Vries, M. Giera, S. Semrau, L. G. J. Tertoolen, V. V. Orlova, M. Bellin, and C. L. Mummery. 2020. "Human-iPSC-Derived Cardiac Stromal Cells Enhance Maturation in 3D Cardiac Microtissues and Reveal Non-cardiomyocyte Contributions to Heart Disease." *Cell Stem Cell* 26 (6): 862-879 e11.

https://doi.org/10.1016/j.stem.2020.05.004.
https://www.ncbi.nlm.nih.gov/pubmed/32459996.

Giacomotto, J., and L. Segalat. 2010. "High-throughput screening and small animal models, where are we?" *Br J Pharmacol* 160 (2): 204-16. https://doi.org/10.1111/j.1476-5381.2010.00725.x.
http://www.ncbi.nlm.nih.gov/pubmed/20423335.

Giusti, Paolo, Luigi Lazzeri, Niccoletta Barbani, Letizia Lelli, Silvano De Petris, and Maria G. Cascone. 1994. "Blends of natural and synthetic polymers: A new route to novel biomaterials." *Macromolecular Symposia* 78 (1): 285-297. https://doi.org/10.1002/masy.19940780124.
http://dx.doi.org/10.1002/masy.19940780124.

Greene, Tanja, Tsai-Yu Lin, Ourania M. Andrisani, and Chien-Chi Lin. 2017. "Comparative study of visible light polymerized gelatin hydrogels for 3D culture of hepatic progenitor cells." *Journal of Applied Polymer Science* 134 (11). https://doi.org/10.1002/app.44585.

Grimm, F. A., A. Blanchette, J. S. House, K. Ferguson, N. H. Hsieh, C. Dalaijamts, A. A. Wright, B. Anson, F. A. Wright, W. A. Chiu, and I. Rusyn. 2018. "A Human Population-Based Organotypic In Vitro Model for Cardiotoxicity Screening." *Altex-Alternatives to Animal Experimentation* 35 (4): 441-452. https://doi.org/10.14573/altex.1805301. <Go to ISI>://WOS:000450970600003.

Guyette, J. P., J. M. Charest, R. W. Mills, B. J. Jank, P. T. Moser, S. E. Gilpin, J. R. Gershlak, T. Okamoto, G. Gonzalez, D. J. Milan, G. R. Gaudette, and H. C. Ott. 2016. "Bioengineering Human Myocardium on Native Extracellular Matrix." *Circ Res* 118 (1): 56-72. https://doi.org/10.1161/CIRCRESAHA.115.306874. http://www.ncbi.nlm.nih.gov/pubmed/26503464.

Gwathmey, J. K., K. Tsaioun, and R. J. Hajjar. 2009. "Cardionomics: a new integrative approach for screening cardiotoxicity of drug candidates." *Expert Opin Drug Metab Toxicol* 5 (6): 647-60. https://doi.org/10.1517/17425250902932915. http://www.ncbi.nlm.nih.gov/pubmed/19442031.

Habib, M., K. Shapira-Schweitzer, O. Caspi, A. Gepstein, G. Arbel, D. Aronson, D. Seliktar, and L. Gepstein. 2011. "A combined cell therapy and in-situ tissue-engineering approach for myocardial repair." *Biomaterials* 32 (30): 7514-23. https://doi.org/10.1016/j.biomaterials.2011.06.049.
https://www.ncbi.nlm.nih.gov/pubmed/21783246.

Halloin, C., K. Schwanke, W. Lobel, A. Franke, M. Szepes, S. Biswanath, S. Wunderlich, S. Merkert, N. Weber, F. Osten, J. de la Roche, F. Polten, K. Wollert, T. Kraft, M. Fischer, U. Martin, I. Gruh, H. Kempf, and R. Zweigerdt. 2019. "Continuous WNT Control Enables Advanced hPSC Cardiac Processing and Prognostic Surface Marker Identification in Chemically Defined Suspension Culture." *Stem Cell Reports*. https://doi.org/10.1016/j.stemcr.2019.06.004.
https://www.ncbi.nlm.nih.gov/pubmed/31353227.

Hanna, A., and N. G. Frangogiannis. 2019. "The Role of the TGF-beta Superfamily in Myocardial Infarction." *Front Cardiovasc Med* 6: 140. https://doi.org/10.3389/fcvm.2019.00140.
https://www.ncbi.nlm.nih.gov/pubmed/31620450.

Hansen, J. M., and C. Harris. 2004. "A novel hypothesis for thalidomide-induced limb teratogenesis: redox misregulation of the NF-kappaB pathway." *Antioxid Redox Signal* 6 (1): 1-14. https://doi.org/10.1089/152308604771978291. https://www.ncbi.nlm.nih.gov/pubmed/14713331.

Hazeltine, L. B., M. G. Badur, X. Lian, A. Das, W. Han, and S. P. Palecek. 2014. "Temporal impact of substrate mechanics on differentiation of human embryonic stem cells to cardiomyocytes." *Acta Biomater* 10 (2): 604-12. https://doi.org/10.1016/j.actbio.2013.10.033. http://www.ncbi.nlm.nih.gov/pubmed/24200714.

Hinderer, S., E. Brauchle, and K. Schenke-Layland. 2015. "Generation and Assessment of Functional Biomaterial Scaffolds for Applications in Cardiovascular Tissue Engineering and Regenerative Medicine." *Adv Healthc Mater* 4 (16): 2326-41. https://doi.org/10.1002/adhm.201400762. https://www.ncbi.nlm.nih.gov/pubmed/25778713.

Hirt, M. N., J. Boeddinghaus, A. Mitchell, S. Schaaf, C. Bornchen, C. Muller, H. Schulz, N. Hubner, J. Stenzig, A. Stoehr, C. Neuber, A. Eder, P. K. Luther, A. Hansen, and T. Eschenhagen. 2014. "Functional improvement and maturation of rat and human engineered heart tissue by chronic electrical stimulation." *J Mol Cell Cardiol* 74: 151-61. https://doi.org/10.1016/j.yjmcc.2014.05.009. https://www.ncbi.nlm.nih.gov/pubmed/24852842.

Ho, S. Y., R. P. Thompson, S. R. Gibbs, M. M. Swindle, and R. H. Anderson. 1991. "Ventricular septal defects in a family of Yucatan miniature pigs." *Int J Cardiol* 33 (3): 419-25. http://www.ncbi.nlm.nih.gov/pubmed/1761337.

Hodge, A. J., J. Zhong, and E. A. Lipke. 2016. "Enhanced stem cell-derived cardiomyocyte differentiation in suspension culture by delivery of nitric oxide using S-nitrosocysteine." *Biotechnol Bioeng* 113 (4): 882-94. https://doi.org/10.1002/bit.25849. https://www.ncbi.nlm.nih.gov/pubmed/26444682.

Hodge, A.J. , P. Kerscher, D. A. Dunn, and E.A. Lipke. 2013. "Biomimetic Materials for Cardiac Regeneration." In *Handbook of Biomimetics and Bioinspiration*, edited by E. Jabbari, D. H. Kim, L.P. Lee, A. Ghaemmaghami and A. Khademhosseini, 1057-1088. Biologically-Driven Engineering of Materials, Processes, Devices, and Systems: World Scientific.

Hodgkinson, C. P., A. Bareja, J. A. Gomez, and V. J. Dzau. 2016. "Emerging Concepts in Paracrine Mechanisms in Regenerative Cardiovascular Medicine and Biology." *Circ Res* 118 (1): 95-107. https://doi.org/10.1161/CIRCRESAHA.115.305373. https://www.ncbi.nlm.nih.gov/pubmed/26837742.

Hom, J., and S. S. Sheu. 2009. "Morphological dynamics of mitochondria--a special emphasis on cardiac muscle cells." *J Mol Cell Cardiol* 46 (6): 811-20. https://doi.org/10.1016/j.yjmcc.2009.02.023. http://www.ncbi.nlm.nih.gov/pubmed/19281816.

Huebsch, N., P. Loskill, M. A. Mandegar, N. C. Marks, A. S. Sheehan, Z. Ma, A. Mathur, T. N. Nguyen, J. C. Yoo, L. M. Judge, C. I. Spencer, A. C. Chukka, C. R. Russell, P. L. So, B. R. Conklin, and K. E. Healy. 2015. "Automated Video-Based Analysis of Contractility and Calcium Flux in Human-Induced Pluripotent Stem Cell-

Derived Cardiomyocytes Cultured over Different Spatial Scales." *Tissue Eng Part C Methods* 21 (5): 467-79. https://doi.org/10.1089/ten.TEC.2014.0283.

Huyer, L. D., M. Montgomery, Y. Zhao, Y. Xiao, G. Conant, A. Korolj, and M. Radisic. 2015. "Biomaterial based cardiac tissue engineering and its applications." *Biomed Mater* 10 (3): 034004. https://doi.org/10.1088/1748-6041/10/3/034004. https://www.ncbi.nlm.nih.gov/pubmed/25989939.

Ito, T., H. Ando, and H. Handa. 2011. "Teratogenic effects of thalidomide: molecular mechanisms." *Cell Mol Life Sci* 68 (9): 1569-79. https://doi.org/10.1007/s00018-010-0619-9. https://www.ncbi.nlm.nih.gov/pubmed/21207098.

Jackman, C., H. Li, and N. Bursac. 2018. "Long-term contractile activity and thyroid hormone supplementation produce engineered rat myocardium with adult-like structure and function." *Acta Biomater* 78: 98-110. https://doi.org/10.1016/j.actbio.2018.08.003. https://www.ncbi.nlm.nih.gov/pubmed/30086384.

Jackman, C. P., I. Y. Shadrin, A. L. Carlson, and N. Bursac. 2015. "Human Cardiac Tissue Engineering: From Pluripotent Stem Cells to Heart Repair." *Curr Opin Chem Eng* 7: 57-64. https://doi.org/10.1016/j.coche.2014.11.004. https://www.ncbi.nlm.nih.gov/pubmed/25599018.

Jenkins, M. J., and S. S. Farid. 2015. "Human pluripotent stem cell-derived products: advances towards robust, scalable and cost-effective manufacturing strategies." *Biotechnol J* 10 (1): 83-95. https://doi.org/10.1002/biot.201400348. http://www.ncbi.nlm.nih.gov/pubmed/25524780.

Jiang, Z., B. Xia, R. McBride, and J. Oakey. 2017. "A microfluidic-based cell encapsulation platform to achieve high long-term cell viability in photopolymerized PEGNB hydrogel microspheres." *J Mater Chem B Mater Biol Med* 5 (1): 173-180. https://doi.org/10.1039/C6TB02551J. https://www.ncbi.nlm.nih.gov/pubmed/28066550.

Jing, D., A. Parikh, and E. S. Tzanakakis. 2010. "Cardiac cell generation from encapsulated embryonic stem cells in static and scalable culture systems." *Cell Transplant* 19 (11): 1397-412. https://doi.org/10.3727/096368910X513955. https://www.ncbi.nlm.nih.gov/pubmed/20587137.

Joanne, P., M. Kitsara, S. E. Boitard, H. Naemetalla, V. Vanneaux, M. Pernot, J. Larghero, P. Forest, Y. Chen, P. Menasche, and O. Agbulut. 2016. "Nanofibrous clinical-grade collagen scaffolds seeded with human cardiomyocytes induces cardiac remodeling in dilated cardiomyopathy." *Biomaterials* 80: 157-68. https://doi.org/10.1016/j.biomaterials.2015.11.035. http://www.ncbi.nlm.nih.gov/pubmed/26708641.

Kang, H. W., S. J. Lee, I. K. Ko, C. Kengla, J. J. Yoo, and A. Atala. 2016. "A 3D bioprinting system to produce human-scale tissue constructs with structural integrity." *Nat Biotechnol* 34 (3): 312-9. https://doi.org/10.1038/nbt.3413. http://www.ncbi.nlm.nih.gov/pubmed/26878319.

Karbassi, E., A. Fenix, S. Marchiano, N. Muraoka, K. Nakamura, X. Yang, and C. E. Murry. 2020. "Cardiomyocyte maturation: advances in knowledge and implications for regenerative medicine." *Nat Rev Cardiol* 17 (6): 341-359. https://doi.org/10.1038/s41569-019-0331-x. https://www.ncbi.nlm.nih.gov/pubmed/32015528.

Kehat, Izhak, Dorit Kenyagin-Karsenti, Mirit Snir, Hana Segev, Michal Amit, Amira Gepstein, Erella Livne, Ofer Binah, Joseph Itskovitz-Eldor, and Lior Gepstein. 2001. "Human embryonic stem cells can differentiate into myocytes with structural and functional properties of cardiomyocytes." *Journal of Clinical Investigation* 108 (3): 407-414. https://doi.org/10.1172/jci200112131.

Kempf, H., C. Kropp, R. Olmer, U. Martin, and R. Zweigerdt. 2015. "Cardiac differentiation of human pluripotent stem cells in scalable suspension culture." *Nat Protoc* 10 (9): 1345-61. https://doi.org/10.1038/nprot.2015.089. http://www.ncbi.nlm.nih.gov/pubmed/26270394.

Kempf, H., R. Olmer, A. Haase, A. Franke, E. Bolesani, K. Schwanke, D. Robles-Diaz, M. Coffee, G. Gohring, G. Drager, O. Potz, T. Joos, E. Martinez-Hackert, A. Haverich, F. F. Buettner, U. Martin, and R. Zweigerdt. 2016. "Bulk cell density and Wnt/TGFbeta signalling regulate mesendodermal patterning of human pluripotent stem cells." *Nat Commun* 7: 13602. https://doi.org/10.1038/ncomms13602. https://www.ncbi.nlm.nih.gov/pubmed/27934856.

Kempf, H., R. Olmer, C. Kropp, M. Ruckert, M. Jara-Avaca, D. Robles-Diaz, A. Franke, D. A. Elliott, D. Wojciechowski, M. Fischer, A. Roa Lara, G. Kensah, I. Gruh, A. Haverich, U. Martin, and R. Zweigerdt. 2014. "Controlling expansion and cardiomyogenic differentiation of human pluripotent stem cells in scalable suspension culture." *Stem Cell Reports* 3 (6): 1132-46. https://doi.org/10.1016/j.stemcr.2014.09.017. http://www.ncbi.nlm.nih.gov/pubmed/25454631.

Kempf, Henning, Birgit Andree, and Robert Zweigerdt. 2016. "Large-scale production of human pluripotent stem cell derived cardiomyocytes." *Advanced Drug Delivery Reviews* 96: 18-30. https://doi.org/http://dx.doi.org/10.1016/j.addr.2015.11.016. http://www.sciencedirect.com/science/article/pii/S0169409X1500280X.

Kerscher, P., B. S. Bussie, K. M. DeSimone, D. A. Dunn, and E. A. Lipke. 2015. "Characterization of mitochondrial populations during stem cell differentiation." *Methods Mol Biol* 1264: 453-63. https://doi.org/10.1007/978-1-4939-2257-4_37. http://www.ncbi.nlm.nih.gov/pubmed/25631034.

Kerscher, P., I. C. Turnbull, A. J. Hodge, J. Kim, D. Seliktar, C. J. Easley, K. D. Costa, and E. A. Lipke. 2015. "Direct hydrogel encapsulation of pluripotent stem cells enables ontomimetic differentiation and growth of engineered human heart tissues." *Biomaterials* 83: 383-395. https://doi.org/10.1016/j.biomaterials.2015.12.011. http://www.ncbi.nlm.nih.gov/pubmed/26826618.

Kerscher, Petra, Jennifer A. Kaczmarek, Sara E. Head, Morgan E. Ellis, Wen J. Seeto, Joonyul Kim, Subhrajit Bhattacharya, Vishnu Suppiramaniam, and Elizabeth A. Lipke. 2016. "Direct Production of Human Cardiac Tissues by Pluripotent Stem Cell Encapsulation in Gelatin Methacryloyl." *ACS Biomaterials Science & Engineering* 3 (8): 1499-1509. https://doi.org/10.1021/acsbiomaterials.6b00226. http://dx.doi.org/10.1021/acsbiomaterials.6b00226.

Khalil, A., R. Tanos, N. El-Hachem, M. Kurban, P. Bouvagnet, F. Bitar, and G. Nemer. 2017. "A HAND to TBX5 Explains the Link Between Thalidomide and Cardiac Diseases." *Sci Rep* 7 (1): 1416. https://doi.org/10.1038/s41598-017-01641-3. https://www.ncbi.nlm.nih.gov/pubmed/28469241.

Khan, M., Y. Xu, S. Hua, J. Johnson, A. Belevych, P. M. Janssen, S. Gyorke, J. Guan, and M. G. Angelos. 2015. "Evaluation of Changes in Morphology and Function of Human Induced Pluripotent Stem Cell Derived Cardiomyocytes (HiPSC-CMs) Cultured on an Aligned-Nanofiber Cardiac Patch." *PLoS One* 10 (5): e0126338. https://doi.org/10.1371/journal.pone.0126338. https://www.ncbi.nlm.nih.gov/pubmed/25993466.

Kim, D. H., E. A. Lipke, P. Kim, R. Cheong, S. Thompson, M. Delannoy, K. Y. Suh, L. Tung, and A. Levchenko. 2010. "Nanoscale cues regulate the structure and function of macroscopic cardiac tissue constructs." *Proc Natl Acad Sci U S A* 107 (2): 565-70. https://doi.org/10.1073/pnas.0906504107. https://www.ncbi.nlm.nih.gov/pubmed/20018748.

Kim, K., J. Cheng, Q. Liu, X. Y. Wu, and Y. Sun. 2010. "Investigation of mechanical properties of soft hydrogel microcapsules in relation to protein delivery using a MEMS force sensor." *J Biomed Mater Res A* 92 (1): 103-13. https://doi.org/10.1002/jbm.a.32338. https://www.ncbi.nlm.nih.gov/pubmed/19165782.

Kim, T. W., J. H. Che, and J. W. Yun. 2019. "Use of stem cells as alternative methods to animal experimentation in predictive toxicology." *Regulatory Toxicology and Pharmacology* 105: 15-29. https://doi.org/10.1016/j.yrtph.2019.03.016. <Go to ISI>://WOS:000476683800002.

Kinney, M. A., T. A. Hookway, Y. Wang, and T. C. McDevitt. 2014. "Engineering three-dimensional stem cell morphogenesis for the development of tissue models and scalable regenerative therapeutics." *Ann Biomed Eng* 42 (2): 352-67. https://doi.org/10.1007/s10439-013-0953-9. http://www.ncbi.nlm.nih.gov/pubmed/24297495.

Knobloch, J., J. D. Shaughnessy, Jr., and U. Ruther. 2007. "Thalidomide induces limb deformities by perturbing the Bmp/Dkk1/Wnt signaling pathway." *FASEB J* 21 (7): 1410-21. https://doi.org/10.1096/fj.06-7603com. http://www.ncbi.nlm.nih.gov/pubmed/17283219.

Kodo, K., S. G. Ong, F. Jahanbani, V. Termglinchan, K. Hirono, K. InanlooRahatloo, A. D. Ebert, P. Shukla, O. J. Abilez, J. M. Churko, I. Karakikes, G. Jung, F. Ichida, S. M. Wu, M. P. Snyder, D. Bernstein, and J. C. Wu. 2016. "iPSC-derived cardiomyocytes reveal abnormal TGF-beta signalling in left ventricular non-compaction cardiomyopathy." *Nat Cell Biol* 18 (10): 1031-42. https://doi.org/10.1038/ncb3411. https://www.ncbi.nlm.nih.gov/pubmed/27642787.

Kumar, N., U. Sharma, C. Singh, and B. Singh. 2012. "Thalidomide: chemistry, therapeutic potential and oxidative stress induced teratogenicity." *Curr Top Med Chem* 12 (13): 1436-55. http://www.ncbi.nlm.nih.gov/pubmed/22650376.

Kuo, H. H., X. Gao, J. M. DeKeyser, K. A. Fetterman, E. A. Pinheiro, C. J. Weddle, H. Fonoudi, M. V. Orman, M. Romero-Tejeda, M. Jouni, M. Blancard, T. Magdy, C. L. Epting, A. L. George, Jr., and P. W. Burridge. 2020. "Negligible-Cost and Weekend-Free Chemically Defined Human iPSC Culture." *Stem Cell Reports*. https://doi.org/10.1016/j.stemcr.2019.12.007. https://www.ncbi.nlm.nih.gov/pubmed/31928950.

Kupfer, M. E., W. H. Lin, V. Ravikumar, K. Qiu, L. Wang, L. Gao, D. Bhuiyan, M. Lenz, J. Ai, R. R. Mahutga, D. Townsend, J. Zhang, M. C. McAlpine, E. G. Tolkacheva, and B. M. Ogle. 2020. "In Situ Expansion, Differentiation and Electromechanical Coupling of Human Cardiac Muscle in a 3D Bioprinted, Chambered Organoid." *Circ Res*. https://doi.org/10.1161/CIRCRESAHA.119.316155. https://www.ncbi.nlm.nih.gov/pubmed/32228120.

Laco, F., A. T. Lam, T. L. Woo, G. Tong, V. Ho, P. L. Soong, E. Grishina, K. H. Lin, S. Reuveny, and S. K. Oh. 2020. "Selection of human induced pluripotent stem cells lines optimization of cardiomyocytes differentiation in an integrated suspension microcarrier bioreactor." *Stem Cell Res Ther* 11 (1): 118. https://doi.org/10.1186/s13287-020-01618-6. https://www.ncbi.nlm.nih.gov/pubmed/32183888.

Laco, F., T. L. Woo, Q. Zhong, R. Szmyd, S. Ting, F. J. Khan, C. L. L. Chai, S. Reuveny, A. Chen, and S. Oh. 2018. "Unraveling the Inconsistencies of Cardiac Differentiation Efficiency Induced by the GSK3beta Inhibitor CHIR99021 in Human Pluripotent Stem Cells." *Stem Cell Reports* 10 (6): 1851-1866. https://doi.org/10.1016/j.stemcr.2018.03.023. https://www.ncbi.nlm.nih.gov/pubmed/29706502.

Laflamme, M. A., K. Y. Chen, A. V. Naumova, V. Muskheli, J. A. Fugate, S. K. Dupras, H. Reinecke, C. Xu, M. Hassanipour, S. Police, C. O'Sullivan, L. Collins, Y. Chen, E. Minami, E. A. Gill, S. Ueno, C. Yuan, J. Gold, and C. E. Murry. 2007. "Cardiomyocytes derived from human embryonic stem cells in pro-survival factors enhance function of infarcted rat hearts." *Nat Biotechnol* 25 (9): 1015-24. https://doi.org/10.1038/nbt1327. https://www.ncbi.nlm.nih.gov/pubmed/17721512.

Landa, N., L. Miller, M. S. Feinberg, R. Holbova, M. Shachar, I. Freeman, S. Cohen, and J. Leor. 2008. "Effect of injectable alginate implant on cardiac remodeling and function after recent and old infarcts in rat." *Circulation* 117 (11): 1388-96. https://doi.org/10.1161/CIRCULATIONAHA.107.727420. https://www.ncbi.nlm.nih.gov/pubmed/18316487.

Lee, Jia Min, Swee Leong Sing, Edgar Yong Sheng Tan, and Wai Yee Yeong. 2016. "Bioprinting in cardiovascular tissue engineering: a review." *International Journal of Bioprinting* 2 (2). https://doi.org/10.18063/ijb.2016.02.006.

Li, F., V. X. Truong, H. Thissen, J. E. Frith, and J. S. Forsythe. 2017. "Microfluidic Encapsulation of Human Mesenchymal Stem Cells for Articular Cartilage Tissue Regeneration." *ACS Appl Mater Interfaces* 9 (10): 8589-8601. https://doi.org/10.1021/acsami.7b00728. https://www.ncbi.nlm.nih.gov/pubmed/28225583.

Li, Zhenqing, and Jianjun Guan. 2011. "Hydrogels for Cardiac Tissue Engineering." *Polymers* 3 (4): 740-761. https://doi.org/10.3390/polym3020740.

Lian, X., C. Hsiao, G. Wilson, K. Zhu, L. B. Hazeltine, S. M. Azarin, K. K. Raval, J. Zhang, T. J. Kamp, and S. P. Palecek. 2012. "Robust cardiomyocyte differentiation from human pluripotent stem cells via temporal modulation of canonical Wnt signaling." *Proc Natl Acad Sci U S A* 109 (27): E1848-57. https://doi.org/10.1073/pnas.1200250109. https://www.ncbi.nlm.nih.gov/pubmed/22645348.

Lian, X., J. Zhang, S. M. Azarin, K. Zhu, L. B. Hazeltine, X. Bao, C. Hsiao, T. J. Kamp, and S. P. Palecek. 2013a. "Directed cardiomyocyte differentiation from human pluripotent stem cells by modulating Wnt/beta-catenin signaling under fully defined conditions." *Nat Protoc* 8 (1): 162-75. https://doi.org/10.1038/nprot.2012.150. http://www.ncbi.nlm.nih.gov/pubmed/23257984.

Liau, B., N. Christoforou, K. W. Leong, and N. Bursac. 2011. "Pluripotent stem cell-derived cardiac tissue patch with advanced structure and function." *Biomaterials* 32 (35): 9180-7. https://doi.org/10.1016/j.biomaterials.2011.08.050. https://www.ncbi.nlm.nih.gov/pubmed/21906802.

Limperopoulos, C., A. Majnemer, M. I. Shevell, B. Rosenblatt, C. Rohlicek, and C. Tchervenkov. 1999. "Neurologic status of newborns with congenital heart defects before open heart surgery." *Pediatrics* 103 (2): 402-8. http://www.ncbi.nlm.nih.gov/pubmed/9925832.

Lopaschuk, G. D., and J. S. Jaswal. 2010. "Energy metabolic phenotype of the cardiomyocyte during development, differentiation, and postnatal maturation." *J Cardiovasc Pharmacol* 56 (2): 130-40. https://doi.org/10.1097/FJC.0b013e3181e74a14. https://www.ncbi.nlm.nih.gov/pubmed/20505524.

Lu, H. F., M. F. Leong, T. C. Lim, Y. P. Chua, J. K. Lim, C. Du, and A. C. A. Wan. 2017. "Engineering a functional three-dimensional human cardiac tissue model for drug toxicity screening." *Biofabrication* 9 (2): 025011. https://doi.org/10.1088/1758-5090/aa6c3a. https://www.ncbi.nlm.nih.gov/pubmed/28393762.

Lu, W. N., S. H. Lu, H. B. Wang, D. X. Li, C. M. Duan, Z. Q. Liu, T. Hao, W. J. He, B. Xu, Q. Fu, Y. C. Song, X. H. Xie, and C. Y. Wang. 2009. "Functional improvement of infarcted heart by co-injection of embryonic stem cells with temperature-responsive chitosan hydrogel." *Tissue Eng Part A* 15 (6): 1437-47. https://doi.org/10.1089/ten.tea.2008.0143. https://www.ncbi.nlm.nih.gov/pubmed/19061432.

Lundy, S. D., J. A. Gantz, C. M. Pagan, D. Filice, and M. A. Laflamme. 2014. "Pluripotent stem cell derived cardiomyocytes for cardiac repair." *Curr Treat Options Cardiovasc Med* 16 (7): 319. https://doi.org/10.1007/s11936-014-0319-0. https://www.ncbi.nlm.nih.gov/pubmed/24838687.

Ma, X., S. Dewan, J. Liu, M. Tang, K. L. Miller, C. Yu, N. Lawrence, A. D. McCulloch, and S. Chen. 2018. "3D printed micro-scale force gauge arrays to improve human cardiac tissue maturation and enable high throughput drug testing." *Acta Biomater*. https://doi.org/10.1016/j.actbio.2018.12.026. https://www.ncbi.nlm.nih.gov/pubmed/30576862.

Ma, Y., Y. Ji, G. Huang, K. Ling, X. Zhang, and F. Xu. 2015. "Bioprinting 3D cell-laden hydrogel microarray for screening human periodontal ligament stem cell response to extracellular matrix." *Biofabrication* 7 (4): 044105. https://doi.org/10.1088/1758-5090/7/4/044105. http://www.ncbi.nlm.nih.gov/pubmed/26696269.

Ma, Z., J. Wang, P. Loskill, N. Huebsch, S. Koo, F. L. Svedlund, N. C. Marks, E. W. Hua, C. P. Grigoropoulos, B. R. Conklin, and K. E. Healy. 2015. "Self-organizing human cardiac microchambers mediated by geometric confinement." *Nat Commun* 6:

7413. https://doi.org/10.1038/ncomms8413. https://www.ncbi.nlm.nih.gov/pubmed/26172574.

Madden, L. R., D. J. Mortisen, E. M. Sussman, S. K. Dupras, J. A. Fugate, J. L. Cuy, K. D. Hauch, M. A. Laflamme, C. E. Murry, and B. D. Ratner. 2010. "Proangiogenic scaffolds as functional templates for cardiac tissue engineering." *Proc Natl Acad Sci U S A* 107 (34): 15211-6. https://doi.org/10.1073/pnas.1006442107. https://www.ncbi.nlm.nih.gov/pubmed/20696917.

Mandalenakis, Z., C. Karazisi, K. Skoglund, A. Rosengren, G. Lappas, P. Eriksson, and M. Dellborg. 2019. "Risk of Cancer Among Children and Young Adults With Congenital Heart Disease Compared With Healthy Controls." *Jama Network Open* 2 (7). https://doi.org/ARTN e196762

10.1001/jamanetworkopen.2019.6762. <Go to ISI>://WOS:000477895900019.

Marchiano, S., A. Bertero, and C. E. Murry. 2019. "Learn from Your Elders: Developmental Biology Lessons to Guide Maturation of Stem Cell-Derived Cardiomyocytes." *Pediatr Cardiol*. https://doi.org/10.1007/s00246-019-02165-5. https://www.ncbi.nlm.nih.gov/pubmed/31388700.

Mathur, A., P. Loskill, K. Shao, N. Huebsch, S. Hong, S. G. Marcus, N. Marks, M. Mandegar, B. R. Conklin, L. P. Lee, and K. E. Healy. 2015. "Human iPSC-based cardiac microphysiological system for drug screening applications." *Sci Rep* 5: 8883. https://doi.org/10.1038/srep08883. https://www.ncbi.nlm.nih.gov/pubmed/25748532.

Mathur, A., Z. Ma, P. Loskill, S. Jeeawoody, and K. E. Healy. 2016. "In vitro cardiac tissue models: Current status and future prospects." *Adv Drug Deliv Rev* 96: 203-13. https://doi.org/10.1016/j.addr.2015.09.011. https://www.ncbi.nlm.nih.gov/pubmed/26428618.

Matthews, B. W. 1975. "Comparison of Predicted and Observed Secondary Structure of T4 Phage Lysozyme." *Biochimica Et Biophysica Acta* 405 (2): 442-451. https://doi.org/Doi 10.1016/0005-2795(75)90109-9. <Go to ISI>://WOS:A1975AU09000022.

Mayshar, Y., O. Yanuka, and N. Benvenisty. 2011. "Teratogen screening using transcriptome profiling of differentiating human embryonic stem cells." *J Cell Mol Med* 15 (6): 1393-401. https://doi.org/10.1111/j.1582-4934.2010.01105.x. http://www.ncbi.nlm.nih.gov/pubmed/20561110.

Meganathan, K., S. Jagtap, V. Wagh, J. Winkler, J. A. Gaspar, D. Hildebrand, M. Trusch, K. Lehmann, J. Hescheler, H. Schluter, and A. Sachinidis. 2012. "Identification of thalidomide-specific transcriptomics and proteomics signatures during differentiation of human embryonic stem cells." *PLoS One* 7 (8): e44228. https://doi.org/10.1371/journal.pone.0044228. http://www.ncbi.nlm.nih.gov/pubmed/22952932.

Menasche, P. 2018. "Cell therapy trials for heart regeneration - lessons learned and future directions." *Nat Rev Cardiol* 15 (11): 659-671. https://doi.org/10.1038/s41569-018-0013-0. https://www.ncbi.nlm.nih.gov/pubmed/29743563.

Menasche, P., V. Vanneaux, A. Hagege, A. Bel, B. Cholley, A. Parouchev, I. Cacciapuoti, R. Al-Daccak, N. Benhamouda, H. Blons, O. Agbulut, L. Tosca, J. H. Trouvin, J. R. Fabreguettes, V. Bellamy, D. Charron, E. Tartour, G. Tachdjian, M. Desnos, and J. Larghero. 2018. "Transplantation of Human Embryonic Stem Cell-Derived

Cardiovascular Progenitors for Severe Ischemic Left Ventricular Dysfunction." *J Am Coll Cardiol* 71 (4): 429-438. https://doi.org/10.1016/j.jacc.2017.11.047. https://www.ncbi.nlm.nih.gov/pubmed/29389360.

Meseguer-Ripolles, J., S. R. Khetani, J. G. Blanco, M. Iredale, and D. C. Hay. 2018. "Pluripotent Stem Cell-Derived Human Tissue: Platforms to Evaluate Drug Metabolism and Safety (vol 20, 2017)." *Aaps Journal* 20 (2). https://doi.org/UNSP 30
10.1208/s12248-018-0191-z. <Go to ISI>://WOS:000427539900011.

Mihic, A., J. Li, Y. Miyagi, M. Gagliardi, S. H. Li, J. Zu, R. D. Weisel, G. Keller, and R. K. Li. 2014. "The effect of cyclic stretch on maturation and 3D tissue formation of human embryonic stem cell-derived cardiomyocytes." *Biomaterials* 35 (9): 2798-808. https://doi.org/10.1016/j.biomaterials.2013.12.052. https://www.ncbi.nlm.nih.gov/pubmed/24424206.

Miki, K., H. Uenaka, A. Saito, S. Miyagawa, T. Sakaguchi, T. Higuchi, T. Shimizu, T. Okano, S. Yamanaka, and Y. Sawa. 2012. "Bioengineered myocardium derived from induced pluripotent stem cells improves cardiac function and attenuates cardiac remodeling following chronic myocardial infarction in rats." *Stem Cells Transl Med* 1 (5): 430-7. https://doi.org/10.5966/sctm.2011-0038. https://www.ncbi.nlm.nih.gov/pubmed/23197822.

Mironi-Harpaz, I., D. Y. Wang, S. Venkatraman, and D. Seliktar. 2012. "Photopolymerization of cell-encapsulating hydrogels: crosslinking efficiency versus cytotoxicity." *Acta Biomater* 8 (5): 1838-48. https://doi.org/10.1016/j.actbio.2011.12.034. https://www.ncbi.nlm.nih.gov/pubmed/22285429.

Mirotsou, Maria, Tilanthi M. Jayawardena, Jeffrey Schmeckpeper, Massimiliano Gnecchi, and Victor J. Dzau. 2011. "Paracrine mechanisms of stem cell reparative and regenerative actions in the heart." *Journal of Molecular and Cellular Cardiology* 50 (2): 280-289. https://doi.org/https://doi.org/10.1016/j.yjmcc.2010.08.005. http://www.sciencedirect.com/science/article/pii/S0022282810002920.

Mordwinkin, N. M., P. W. Burridge, and J. C. Wu. 2013. "A review of human pluripotent stem cell-derived cardiomyocytes for high-throughput drug discovery, cardiotoxicity screening, and publication standards." *J Cardiovasc Transl Res* 6 (1): 22-30. https://doi.org/10.1007/s12265-012-9423-2. https://www.ncbi.nlm.nih.gov/pubmed/23229562.

Mozaffarian, D., E. J. Benjamin, A. S. Go, D. K. Arnett, M. J. Blaha, M. Cushman, S. R. Das, S. de Ferranti, J. P. Despres, H. J. Fullerton, V. J. Howard, M. D. Huffman, C. R. Isasi, M. C. Jimenez, S. E. Judd, B. M. Kissela, J. H. Lichtman, L. D. Lisabeth, S. Liu, R. H. Mackey, D. J. Magid, D. K. McGuire, E. R. Mohler, 3rd, C. S. Moy, P. Muntner, M. E. Mussolino, K. Nasir, R. W. Neumar, G. Nichol, L. Palaniappan, D. K. Pandey, M. J. Reeves, C. J. Rodriguez, W. Rosamond, P. D. Sorlie, J. Stein, A. Towfighi, T. N. Turan, S. S. Virani, D. Woo, R. W. Yeh, M. B. Turner, Committee American Heart Association Statistics, and Subcommittee Stroke Statistics. 2016. "Heart Disease and Stroke Statistics-2016 Update: A Report From the American Heart Association." *Circulation* 133 (4): e38-360. https://doi.org/10.1161/CIR.0000000000000350. https://www.ncbi.nlm.nih.gov/pubmed/26673558.

Mummery, C. L., J. Zhang, E. S. Ng, D. A. Elliott, A. G. Elefanty, and T. J. Kamp. 2012. "Differentiation of human embryonic stem cells and induced pluripotent stem cells to cardiomyocytes: a methods overview." *Circ Res* 111 (3): 344-58. https://doi.org/10.1161/CIRCRESAHA.110.227512. https://www.ncbi.nlm.nih.gov/pubmed/22821908.

Mussatto, K. A., R. Hoffmann, G. Hoffman, J. S. Tweddell, L. Bear, Y. M. Cao, J. Tanem, and C. Brosig. 2015. "Risk Factors for Abnormal Developmental Trajectories in Young Children With Congenital Heart Disease." *Circulation* 132 (8): 755-761. https://doi.org/10.1161/Circulationaha.114.014521. <Go to ISI>://WOS:000360204800013.

Ng, E. S., R. P. Davis, L. Azzola, E. G. Stanley, and A. G. Elefanty. 2005. "Forced aggregation of defined numbers of human embryonic stem cells into embryoid bodies fosters robust, reproducible hematopoietic differentiation." *Blood* 106 (5): 1601-3. https://doi.org/10.1182/blood-2005-03-0987. https://www.ncbi.nlm.nih.gov/pubmed/15914555.

Ng, S. Y., C. K. Wong, and S. Y. Tsang. 2010. "Differential gene expressions in atrial and ventricular myocytes: insights into the road of applying embryonic stem cell-derived cardiomyocytes for future therapies." *Am J Physiol Cell Physiol* 299 (6): C1234-49. https://doi.org/10.1152/ajpcell.00402.2009. https://www.ncbi.nlm.nih.gov/pubmed/20844252.

Nguyen, K. T., and J. L. West. 2002. "Photopolymerizable hydrogels for tissue engineering applications." *Biomaterials* 23 (22): 4307-14. https://www.ncbi.nlm.nih.gov/pubmed/12219820.

Nunes, S. S., J. W. Miklas, J. Liu, R. Aschar-Sobbi, Y. Xiao, B. Zhang, J. Jiang, S. Masse, M. Gagliardi, A. Hsieh, N. Thavandiran, M. A. Laflamme, K. Nanthakumar, G. J. Gross, P. H. Backx, G. Keller, and M. Radisic. 2013. "Biowire: a platform for maturation of human pluripotent stem cell-derived cardiomyocytes." *Nat Methods* 10 (8): 781-7. https://doi.org/10.1038/nmeth.2524. https://www.ncbi.nlm.nih.gov/pubmed/23793239.

Olivetti, G., E. Cigola, R. Maestri, D. Corradi, C. Lagrasta, S. R. Gambert, and P. Anversa. 1996. "Aging, cardiac hypertrophy and ischemic cardiomyopathy do not affect the proportion of mononucleated and multinucleated myocytes in the human heart." *J Mol Cell Cardiol* 28 (7): 1463-77. https://doi.org/10.1006/jmcc.1996.0137. https://www.ncbi.nlm.nih.gov/pubmed/8841934.

Onakpoya, I. J., C. J. Heneghan, and J. K. Aronson. 2016. "Post-marketing withdrawal of 462 medicinal products because of adverse drug reactions: a systematic review of the world literature." *BMC Med* 14: 10. https://doi.org/10.1186/s12916-016-0553-2. https://www.ncbi.nlm.nih.gov/pubmed/26843061.

Osafune, K., L. Caron, M. Borowiak, R. J. Martinez, C. S. Fitz-Gerald, Y. Sato, C. A. Cowan, K. R. Chien, and D. A. Melton. 2008. "Marked differences in differentiation propensity among human embryonic stem cell lines." *Nat Biotechnol* 26 (3): 313-5. https://doi.org/10.1038/nbt1383. https://www.ncbi.nlm.nih.gov/pubmed/18278034.

Ou, D. B., Y. He, R. Chen, J. W. Teng, H. T. Wang, D. Zeng, X. T. Liu, L. Ding, J. Y. Huang, and Q. S. Zheng. 2011. "Three-dimensional co-culture facilitates the differentiation of embryonic stem cells into mature cardiomyocytes." *J Cell*

Biochem 112 (12): 3555-62. https://doi.org/10.1002/jcb.23283. https://www.ncbi.nlm.nih.gov/pubmed/21780160.

Ouyang, L., R. Yao, S. Mao, X. Chen, J. Na, and W. Sun. 2015. "Three-dimensional bioprinting of embryonic stem cells directs highly uniform embryoid body formation." *Biofabrication* 7 (4): 044101. https://doi.org/10.1088/1758-5090/7/4/044101. http://www.ncbi.nlm.nih.gov/pubmed/26531008.

Papaioannou, V. E. 2014. "The T-box gene family: emerging roles in development, stem cells and cancer." *Development* 141 (20): 3819-33. https://doi.org/10.1242/dev.104471. https://www.ncbi.nlm.nih.gov/pubmed/25294936.

Parman, T., M. J. Wiley, and P. G. Wells. 1999. "Free radical-mediated oxidative DNA damage in the mechanism of thalidomide teratogenicity." *Nat Med* 5 (5): 582-5. https://doi.org/10.1038/8466. http://www.ncbi.nlm.nih.gov/pubmed/10229238.

Parra, V., V. Eisner, M. Chiong, A. Criollo, F. Moraga, A. Garcia, S. Hartel, E. Jaimovich, A. Zorzano, C. Hidalgo, and S. Lavandero. 2008. "Changes in mitochondrial dynamics during ceramide-induced cardiomyocyte early apoptosis." *Cardiovasc Res* 77 (2): 387-97. https://doi.org/10.1093/cvr/cvm029. http://www.ncbi.nlm.nih.gov/pubmed/18006463.

Pasquier, J., R. Gupta, D. Rioult, J. Hoarau-Vechot, R. Courjaret, K. Machaca, J. Al Suwaidi, E. G. Stanley, S. Rafii, D. A. Elliott, C. Abi Khalil, and A. Rafii. 2017. "Coculturing with endothelial cells promotes in vitro maturation and electrical coupling of human embryonic stem cell-derived cardiomyocytes." *J Heart Lung Transplant* 36 (6): 684-693. https://doi.org/10.1016/j.healun.2017.01.001. https://www.ncbi.nlm.nih.gov/pubmed/28169114.

Paul, A., A. Hasan, H. A. Kindi, A. K. Gaharwar, V. T. Rao, M. Nikkhah, S. R. Shin, D. Krafft, M. R. Dokmeci, D. Shum-Tim, and A. Khademhosseini. 2014. "Injectable graphene oxide/hydrogel-based angiogenic gene delivery system for vasculogenesis and cardiac repair." *ACS Nano* 8 (8): 8050-62. https://doi.org/10.1021/nn5020787. https://www.ncbi.nlm.nih.gov/pubmed/24988275.

Pereira, Rúben F., and Paulo J. Bártolo. 2015. "3D bioprinting of photocrosslinkable hydrogel constructs." *Journal of Applied Polymer Science* 132 (48): n/a-n/a. https://doi.org/10.1002/app.42458. http://dx.doi.org/10.1002/app.42458.

Pettinato, G., X. Wen, and N. Zhang. 2014. "Formation of well-defined embryoid bodies from dissociated human induced pluripotent stem cells using microfabricated cell-repellent microwell arrays." *Sci Rep* 4: 7402. https://doi.org/10.1038/srep07402. https://www.ncbi.nlm.nih.gov/pubmed/25492588.

Pioner, J. M., L. Santini, C. Palandri, D. Martella, F. Lupi, M. Langione, S. Querceto, B. Grandinetti, V. Balducci, P. Benzoni, S. Landi, A. Barbuti, F. Ferrarese Lupi, L. Boarino, L. Sartiani, C. Tesi, D. L. Mack, M. Regnier, E. Cerbai, C. Parmeggiani, C. Poggesi, C. Ferrantini, and R. Coppini. 2019. "Optical Investigation of Action Potential and Calcium Handling Maturation of hiPSC-Cardiomyocytes on Biomimetic Substrates." *Int J Mol Sci* 20 (15). https://doi.org/10.3390/ijms20153799. https://www.ncbi.nlm.nih.gov/pubmed/31382622.

Politi, Pierluigi, Marco Piccinelli, Paolo Fusar Poli, Catherine Klersy, Carlo Campana, Claudio Goggi, Mario Viganò, and Francesco Barale. 2004. "Ten Years of "Extended" Life: Quality of Life Among Heart Transplantation Survivors." *Transplantation Journal* 78 (2): 257-263. https://doi.org/10.1097/01.tp.0000133537.87951.f2.

Portner, R., S. Nagel-Heyer, C. Goepfert, P. Adamietz, and N. M. Meenen. 2005. "Bioreactor design for tissue engineering." *J Biosci Bioeng* 100 (3): 235-45. https://doi.org/10.1263/jbb.100.235. https://www.ncbi.nlm.nih.gov/pubmed/16243271.

Pradhan, S., J. M. Clary, D. Seliktar, and E. A. Lipke. 2017. "A three-dimensional spheroidal cancer model based on PEG-fibrinogen hydrogel microspheres." *Biomaterials* 115: 141-154. https://doi.org/10.1016/j.biomaterials.2016.10.052. https://www.ncbi.nlm.nih.gov/pubmed/27889665.

Pradhan, S., and J. H. Slater. 2019. "Tunable hydrogels for controlling phenotypic cancer cell states to model breast cancer dormancy and reactivation." *Biomaterials* 215: 119177. https://doi.org/10.1016/j.biomaterials.2019.04.022. https://www.ncbi.nlm.nih.gov/pubmed/31176804.

Radisic, M., and K. L. Christman. 2013. "Materials science and tissue engineering: repairing the heart." *Mayo Clin Proc* 88 (8): 884-98. https://doi.org/10.1016/j.mayocp.2013.05.003. https://www.ncbi.nlm.nih.gov/pubmed/23910415.

Rajala, K., M. Pekkanen-Mattila, and K. Aalto-Setala. 2011. "Cardiac differentiation of pluripotent stem cells." *Stem Cells Int* 2011: 383709. https://doi.org/10.4061/2011/383709. http://www.ncbi.nlm.nih.gov/pubmed/21603143.

Rajamohan, D., S. Kalra, M. Duc Hoang, V. George, A. Staniforth, H. Russell, X. Yang, and C. Denning. 2016. "Automated Electrophysiological and Pharmacological Evaluation of Human Pluripotent Stem Cell-Derived Cardiomyocytes." *Stem Cells Dev* 25 (6): 439-52. https://doi.org/10.1089/scd.2015.0253. https://www.ncbi.nlm.nih.gov/pubmed/26906236.

Rajamohan, D., E. Matsa, S. Kalra, J. Crutchley, A. Patel, V. George, and C. Denning. 2013. "Current status of drug screening and disease modelling in human pluripotent stem cells." *Bioessays* 35 (3): 281-98. https://doi.org/10.1002/bies.201200053. http://www.ncbi.nlm.nih.gov/pubmed/22886688.

Rehman, W., L. M. Arfons, and H. M. Lazarus. 2011. "The rise, fall and subsequent triumph of thalidomide: lessons learned in drug development." *Ther Adv Hematol* 2 (5): 291-308. https://doi.org/10.1177/2040620711413165. https://www.ncbi.nlm.nih.gov/pubmed/23556097.

Reis, L. A., L. L. Chiu, N. Feric, L. Fu, and M. Radisic. 2016. "Biomaterials in myocardial tissue engineering." *J Tissue Eng Regen Med* 10 (1): 11-28. https://doi.org/10.1002/term.1944. https://www.ncbi.nlm.nih.gov/pubmed/25066525.

Rivera-Feliciano, J., and C. J. Tabin. 2006. "Bmp2 instructs cardiac progenitors to form the heart-valve-inducing field." *Dev Biol* 295 (2): 580-8. https://doi.org/10.1016/j.ydbio.2006.03.043. http://www.ncbi.nlm.nih.gov/pubmed/16730346.

Roh, K. H., R. M. Nerem, and K. Roy. 2016. "Biomanufacturing of Therapeutic Cells: State of the Art, Current Challenges, and Future Perspectives." *Annu Rev Chem Biomol Eng* 7: 455-78. https://doi.org/10.1146/annurev-chembioeng-080615-033559. https://www.ncbi.nlm.nih.gov/pubmed/27276552.

Ronaldson-Bouchard, K., S. P. Ma, K. Yeager, T. Chen, L. Song, D. Sirabella, K. Morikawa, D. Teles, M. Yazawa, and G. Vunjak-Novakovic. 2018. "Advanced maturation of human cardiac tissue grown from pluripotent stem cells." *Nature* 556 (7700): 239-243. https://doi.org/10.1038/s41586-018-0016-3. https://www.ncbi.nlm.nih.gov/pubmed/29618819.

Rossow, Torsten, Philipp S. Lienemann, and David J. Mooney. 2017. "Cell Microencapsulation by Droplet Microfluidic Templating." *Macromolecular Chemistry and Physics* 218 (2): 1600380. https://doi.org/10.1002/macp.201600380.

Sackmann, E. K., A. L. Fulton, and D. J. Beebe. 2014. "The present and future role of microfluidics in biomedical research." *Nature* 507 (7491): 181-9. https://doi.org/10.1038/nature13118. https://www.ncbi.nlm.nih.gov/pubmed/24622198.

Santoro, R., G. L. Perrucci, A. Gowran, and G. Pompilio. 2019. "Unchain My Heart: Integrins at the Basis of iPSC Cardiomyocyte Differentiation." *Stem Cells Int* 2019: 8203950. https://doi.org/10.1155/2019/8203950. https://www.ncbi.nlm.nih.gov/pubmed/30906328.

Saunders, R., and M. Amoroso. 2010. "SEM investigation of heart tissue samples." *Journal of Physics: Conference Series* 241: 012023. https://doi.org/10.1088/1742-6596/241/1/012023.

Scadden, D. T. 2006. "The stem-cell niche as an entity of action." *Nature* 441 (7097): 1075-9. https://doi.org/10.1038/nature04957. https://www.ncbi.nlm.nih.gov/pubmed/16810242.

Schaper, J., E. Meiser, and G. Stammler. 1985. "Ultrastructural morphometric analysis of myocardium from dogs, rats, hamsters, mice, and from human hearts." *Circ Res* 56 (3): 377-91. http://www.ncbi.nlm.nih.gov/pubmed/3882260.

Scuderi, G. J., and J. Butcher. 2017. "Naturally Engineered Maturation of Cardiomyocytes." *Front Cell Dev Biol* 5: 50. https://doi.org/10.3389/fcell.2017.00050. https://www.ncbi.nlm.nih.gov/pubmed/28529939.

Seeto, W. J., Y. Tian, S. Pradhan, P. Kerscher, and E. A. Lipke. 2019. "Rapid Production of Cell-Laden Microspheres Using a Flexible Microfluidic Encapsulation Platform." *Small* 15 (47): e1902058. https://doi.org/10.1002/smll.201902058. https://www.ncbi.nlm.nih.gov/pubmed/31468632.

Seeto, W. J., Y. Tian, R. L. Winter, F. J. Caldwell, A. A. Wooldridge, and E. A. Lipke. 2017. "Encapsulation of Equine Endothelial Colony Forming Cells in Highly Uniform, Injectable Hydrogel Microspheres for Local Cell Delivery." *Tissue Eng Part C Methods* 23 (11): 815-825. https://doi.org/10.1089/ten.TEC.2017.0233. https://www.ncbi.nlm.nih.gov/pubmed/28762895.

Shadrin, I. Y., B. W. Allen, Y. Qian, C. P. Jackman, A. L. Carlson, M. E. Juhas, and N. Bursac. 2017. "Cardiopatch platform enables maturation and scale-up of human pluripotent stem cell-derived engineered heart tissues." *Nat Commun* 8 (1): 1825.

https://doi.org/10.1038/s41467-017-01946-x.
https://www.ncbi.nlm.nih.gov/pubmed/29184059.

Shao, Y., J. Sang, and J. Fu. 2015. "On human pluripotent stem cell control: The rise of 3D bioengineering and mechanobiology." *Biomaterials* 52: 26-43. https://doi.org/10.1016/j.biomaterials.2015.01.078.
http://www.ncbi.nlm.nih.gov/pubmed/25818411.

Shen, N., A. Knopf, C. Westendorf, U. Kraushaar, J. Riedl, H. Bauer, S. Poschel, S. L. Layland, M. Holeiter, S. Knolle, E. Brauchle, A. Nsair, S. Hinderer, and K. Schenke-Layland. 2017. "Steps toward Maturation of Embryonic Stem Cell-Derived Cardiomyocytes by Defined Physical Signals." *Stem Cell Reports*. https://doi.org/10.1016/j.stemcr.2017.04.021.
https://www.ncbi.nlm.nih.gov/pubmed/28528699.

Shiba, Y., T. Gomibuchi, T. Seto, Y. Wada, H. Ichimura, Y. Tanaka, T. Ogasawara, K. Okada, N. Shiba, K. Sakamoto, D. Ido, T. Shiina, M. Ohkura, J. Nakai, N. Uno, Y. Kazuki, M. Oshimura, I. Minami, and U. Ikeda. 2016. "Allogeneic transplantation of iPS cell-derived cardiomyocytes regenerates primate hearts." *Nature* 538 (7625): 388-391. https://doi.org/10.1038/nature19815.
https://www.ncbi.nlm.nih.gov/pubmed/27723741.

Shih, H., and C. C. Lin. 2013. "Visible-light-mediated thiol-ene hydrogelation using eosin-Y as the only photoinitiator." *Macromol Rapid Commun* 34 (3): 269-73. https://doi.org/10.1002/marc.201200605.
https://www.ncbi.nlm.nih.gov/pubmed/23386583.

Shin, S. R., S. M. Jung, M. Zalabany, K. Kim, P. Zorlutuna, S. B. Kim, M. Nikkhah, M. Khabiry, M. Azize, J. Kong, K. T. Wan, T. Palacios, M. R. Dokmeci, H. Bae, X. S. Tang, and A. Khademhosseini. 2013. "Carbon-nanotube-embedded hydrogel sheets for engineering cardiac constructs and bioactuators." *ACS Nano* 7 (3): 2369-80. https://doi.org/10.1021/nn305559j.
https://www.ncbi.nlm.nih.gov/pubmed/23363247.

Shinnawi, R., I. Huber, L. Maizels, N. Shaheen, A. Gepstein, G. Arbel, A. J. Tijsen, and L. Gepstein. 2015. "Monitoring Human-Induced Pluripotent Stem Cell-Derived Cardiomyocytes with Genetically Encoded Calcium and Voltage Fluorescent Reporters." *Stem Cell Reports* 5 (4): 582-96. https://doi.org/10.1016/j.stemcr.2015.08.009.
https://www.ncbi.nlm.nih.gov/pubmed/26372632.

Shiojima, I., and K. Walsh. 2006. "Regulation of cardiac growth and coronary angiogenesis by the Akt/PKB signaling pathway." *Genes Dev* 20 (24): 3347-65. https://doi.org/10.1101/gad.1492806.
http://www.ncbi.nlm.nih.gov/pubmed/17182864.

Singelyn, J. M., and K. L. Christman. 2010. "Injectable materials for the treatment of myocardial infarction and heart failure: the promise of decellularized matrices." *J Cardiovasc Transl Res* 3 (5): 478-86. https://doi.org/10.1007/s12265-010-9202-x.
https://www.ncbi.nlm.nih.gov/pubmed/20632221.

Smith, A. S., J. Macadangdang, W. Leung, M. A. Laflamme, and D. H. Kim. 2017. "Human iPSC-derived cardiomyocytes and tissue engineering strategies for disease modeling and drug screening." *Biotechnol Adv* 35 (1): 77-94.

https://doi.org/10.1016/j.biotechadv.2016.12.002.
https://www.ncbi.nlm.nih.gov/pubmed/28007615.

Smithells, R. W., and C. G. Newman. 1992. "Recognition of thalidomide defects." *J Med Genet* 29 (10): 716-23. http://www.ncbi.nlm.nih.gov/pubmed/1433232.

Sokolova, M., and G. Lapalme. 2009. "A systematic analysis of performance measures for classification tasks." *Information Processing & Management* 45 (4): 427-437. https://doi.org/10.1016/j.ipm.2009.03.002. <Go to ISI>://WOS:000267170100003.

Sommer, C. A., A. G. Sommer, T. A. Longmire, C. Christodoulou, D. D. Thomas, M. Gostissa, F. W. Alt, G. J. Murphy, D. N. Kotton, and G. Mostoslavsky. 2010. "Excision of reprogramming transgenes improves the differentiation potential of iPS cells generated with a single excisable vector." *Stem Cells* 28 (1): 64-74. https://doi.org/10.1002/stem.255.
https://www.ncbi.nlm.nih.gov/pubmed/19904830.

Spearman, B. S., A. J. Hodge, J. L. Porter, J. G. Hardy, Z. D. Davis, T. Xu, X. Zhang, C. E. Schmidt, M. C. Hamilton, and E. A. Lipke. 2015. "Conductive interpenetrating networks of polypyrrole and polycaprolactone encourage electrophysiological development of cardiac cells." *Acta Biomater* 28: 109-120. https://doi.org/10.1016/j.actbio.2015.09.025.
https://www.ncbi.nlm.nih.gov/pubmed/26407651.

Stephens, T. D. 1988. "Proposed mechanisms of action in thalidomide embryopathy." *Teratology* 38 (3): 229-39. https://doi.org/10.1002/tera.1420380307. https://www.ncbi.nlm.nih.gov/pubmed/3067416.

Stephens, T. D., C. J. Bunde, and B. J. Fillmore. 2000. "Mechanism of action in thalidomide teratogenesis." *Biochem Pharmacol* 59 (12): 1489-99. http://www.ncbi.nlm.nih.gov/pubmed/10799645.

Stevens, K. R., and C. E. Murry. 2018. "Human Pluripotent Stem Cell-Derived Engineered Tissues: Clinical Considerations." *Cell Stem Cell* 22 (3): 294-297. https://doi.org/10.1016/j.stem.2018.01.015.
https://www.ncbi.nlm.nih.gov/pubmed/29499147.

Sugiura, S., J. M. Cha, F. Yanagawa, P. Zorlutuna, H. Bae, and A. Khademhosseini. 2016. "Dynamic three-dimensional micropatterned cell co-cultures within photocurable and chemically degradable hydrogels." *J Tissue Eng Regen Med* 10 (8): 690-9. https://doi.org/10.1002/term.1843.
https://www.ncbi.nlm.nih.gov/pubmed/24170301.

Sun, X., and S. S. Nunes. 2015. "Overview of hydrogel-based strategies for application in cardiac tissue regeneration." *Biomed Mater* 10 (3): 034005. https://doi.org/10.1088/1748-6041/10/3/034005.
https://www.ncbi.nlm.nih.gov/pubmed/26040708.

---. 2017. "Bioengineering Approaches to Mature Human Pluripotent Stem Cell-Derived Cardiomyocytes." *Front Cell Dev Biol* 5: 19. https://doi.org/10.3389/fcell.2017.00019.
https://www.ncbi.nlm.nih.gov/pubmed/28337437.

Takahashi, K., K. Tanabe, M. Ohnuki, M. Narita, T. Ichisaka, K. Tomoda, and S. Yamanaka. 2007. "Induction of pluripotent stem cells from adult human fibroblasts by defined factors." *Cell* 131 (5): 861-72.

https://doi.org/10.1016/j.cell.2007.11.019.
https://www.ncbi.nlm.nih.gov/pubmed/18035408.

Takahashi, K., and S. Yamanaka. 2006. "Induction of pluripotent stem cells from mouse embryonic and adult fibroblast cultures by defined factors." *Cell* 126 (4): 663-76. https://doi.org/10.1016/j.cell.2006.07.024.
https://www.ncbi.nlm.nih.gov/pubmed/16904174.

Teh, S. Y., R. Lin, L. H. Hung, and A. P. Lee. 2008. "Droplet microfluidics." *Lab Chip* 8 (2): 198-220. https://doi.org/10.1039/b715524g.
https://www.ncbi.nlm.nih.gov/pubmed/18231657.

Therapontos, C., L. Erskine, E. R. Gardner, W. D. Figg, and N. Vargesson. 2009. "Thalidomide induces limb defects by preventing angiogenic outgrowth during early limb formation." *Proc Natl Acad Sci U S A* 106 (21): 8573-8. https://doi.org/10.1073/pnas.0901505106.
https://www.ncbi.nlm.nih.gov/pubmed/19433787.

Thomson, J. A., J. Itskovitz-Eldor, S. S. Shapiro, M. A. Waknitz, J. J. Swiergiel, V. S. Marshall, and J. M. Jones. 1998. "Embryonic stem cell lines derived from human blastocysts." *Science* 282 (5391): 1145-7. https://www.ncbi.nlm.nih.gov/pubmed/9804556.

Thomson, J. A., and V. S. Marshall. 1998. "Primate embryonic stem cells." *Curr Top Dev Biol* 38: 133-65. https://www.ncbi.nlm.nih.gov/pubmed/9399078.

Tian, Yuan, and Elizabeth A. Lipke. 2020. "Microfluidic Production of Cell-Laden Microspheroidal Hydrogels with Different Geometric Shapes." *ACS Biomaterials Science & Engineering*. https://doi.org/10.1021/acsbiomaterials.0c00980.

Ting, S., A. Chen, S. Reuveny, and S. Oh. 2014. "An intermittent rocking platform for integrated expansion and differentiation of human pluripotent stem cells to cardiomyocytes in suspended microcarrier cultures." *Stem Cell Res* 13 (2): 202-13. https://doi.org/10.1016/j.scr.2014.06.002.
https://www.ncbi.nlm.nih.gov/pubmed/25043964.

Torisawa, Y. S., B. H. Chueh, D. Huh, P. Ramamurthy, T. M. Roth, K. F. Barald, and S. Takayama. 2007. "Efficient formation of uniform-sized embryoid bodies using a compartmentalized microchannel device." *Lab Chip* 7 (6): 770-6. https://doi.org/10.1039/b618439a.
https://www.ncbi.nlm.nih.gov/pubmed/17538720.

Trattnig, S., K. Ohel, V. Mlynarik, V. Juras, S. Zbyn, and A. Korner. 2015. "Morphological and compositional monitoring of a new cell-free cartilage repair hydrogel technology - GelrinC by MR using semi-quantitative MOCART scoring and quantitative T2 index and new zonal T2 index calculation." *Osteoarthritis Cartilage* 23 (12): 2224-2232. https://doi.org/10.1016/j.joca.2015.07.007.
https://www.ncbi.nlm.nih.gov/pubmed/26187572.

Tseng, C. M., Y. H. Hsiao, V. Y. Su, K. C. Su, Y. C. Wu, K. T. Chang, and D. W. Perng. 2013. "The suppression effects of thalidomide on human lung fibroblasts: cell proliferation, vascular endothelial growth factor release, and collagen production." *Lung* 191 (4): 361-8. https://doi.org/10.1007/s00408-013-9477-1.
http://www.ncbi.nlm.nih.gov/pubmed/23722461.

Tulloch, N. L., V. Muskheli, M. V. Razumova, F. S. Korte, M. Regnier, K. D. Hauch, L. Pabon, H. Reinecke, and C. E. Murry. 2011. "Growth of engineered human

myocardium with mechanical loading and vascular coculture." *Circ Res* 109 (1): 47-59. https://doi.org/10.1161/CIRCRESAHA.110.237206. https://www.ncbi.nlm.nih.gov/pubmed/21597009.

Tung, Y. C., A. Y. Hsiao, S. G. Allen, Y. S. Torisawa, M. Ho, and S. Takayama. 2011. "High-throughput 3D spheroid culture and drug testing using a 384 hanging drop array." *Analyst* 136 (3): 473-8. https://doi.org/10.1039/c0an00609b. https://www.ncbi.nlm.nih.gov/pubmed/20967331.

Ullah, I., R. B. Subbarao, and G. J. Rho. 2015. "Human mesenchymal stem cells - current trends and future prospective." *Biosci Rep* 35 (2). https://doi.org/10.1042/BSR20150025. https://www.ncbi.nlm.nih.gov/pubmed/25797907.

Ungrin, M. D., C. Joshi, A. Nica, C. Bauwens, and P. W. Zandstra. 2008. "Reproducible, ultra high-throughput formation of multicellular organization from single cell suspension-derived human embryonic stem cell aggregates." *PLoS One* 3 (2): e1565. https://doi.org/10.1371/journal.pone.0001565. https://www.ncbi.nlm.nih.gov/pubmed/18270562.

van den Heuvel, N. H., T. A. van Veen, B. Lim, and M. K. Jonsson. 2014. "Lessons from the heart: mirroring electrophysiological characteristics during cardiac development to in vitro differentiation of stem cell derived cardiomyocytes." *J Mol Cell Cardiol* 67: 12-25. https://doi.org/10.1016/j.yjmcc.2013.12.011. http://www.ncbi.nlm.nih.gov/pubmed/24370890.

Vargesson, N. 2015. "Thalidomide-induced teratogenesis: history and mechanisms." *Birth Defects Res C Embryo Today* 105 (2): 140-56. https://doi.org/10.1002/bdrc.21096.

Virani, S. S., A. Alonso, E. J. Benjamin, M. S. Bittencourt, C. W. Callaway, A. P. Carson, A. M. Chamberlain, A. R. Chang, S. Cheng, F. N. Delling, L. Djousse, M. S. V. Elkind, J. F. Ferguson, M. Fornage, S. S. Khan, B. M. Kissela, K. L. Knutson, T. W. Kwan, D. T. Lackland, T. T. Lewis, J. H. Lichtman, C. T. Longenecker, M. S. Loop, P. L. Lutsey, S. S. Martin, K. Matsushita, A. E. Moran, M. E. Mussolino, A. M. Perak, W. D. Rosamond, G. A. Roth, U. K. A. Sampson, G. M. Satou, E. B. Schroeder, S. H. Shah, C. M. Shay, N. L. Spartano, A. Stokes, D. L. Tirschwell, L. B. VanWagner, C. W. Tsao, Epidemiology American Heart Association Council on, Committee Prevention Statistics, and Subcommittee Stroke Statistics. 2020. "Heart Disease and Stroke Statistics-2020 Update: A Report From the American Heart Association." *Circulation* 141 (9): e139-e596. https://doi.org/10.1161/CIR.0000000000000757. https://www.ncbi.nlm.nih.gov/pubmed/31992061.

Wang, Q., H. Yang, A. Bai, W. Jiang, X. Li, X. Wang, Y. Mao, C. Lu, R. Qian, F. Guo, T. Ding, H. Chen, S. Chen, J. Zhang, C. Liu, and N. Sun. 2016. "Functional engineered human cardiac patches prepared from nature's platform improve heart function after acute myocardial infarction." *Biomaterials* 105: 52-65. https://doi.org/10.1016/j.biomaterials.2016.07.035. https://www.ncbi.nlm.nih.gov/pubmed/27509303.

Wendel, J. S., L. Ye, P. Zhang, R. T. Tranquillo, and J. J. Zhang. 2014. "Functional consequences of a tissue-engineered myocardial patch for cardiac repair in a rat infarct model." *Tissue Eng Part A* 20 (7-8): 1325-35.

https://doi.org/10.1089/ten.TEA.2013.0312.
https://www.ncbi.nlm.nih.gov/pubmed/24295499.

White, M. C., L. Pang, and X. Yang. 2016. "MicroRNA-mediated maturation of human pluripotent stem cell-derived cardiomyocytes: Towards a better model for cardiotoxicity?" *Food Chem Toxicol*. https://doi.org/10.1016/j.fct.2016.05.025. https://www.ncbi.nlm.nih.gov/pubmed/27265266.

Williams, Bianca, Wiebke Löbel, Ferdous Finklea, Caroline Halloin, Katharina Ritzenhoff, Felix Manstein, Samira Mohammadi, Mohammadjafar Hashemi, Robert Zweigerdt, Elizabeth Lipke, and Selen Cremaschi. 2020. "Prediction of Human Induced Pluripotent Stem Cell Cardiac Differentiation Outcome by Multifactorial Process Modeling." *Frontiers in Bioengineering and Biotechnology* 8 (851). https://doi.org/10.3389/fbioe.2020.00851.
https://www.frontiersin.org/article/10.3389/fbioe.2020.00851.

Wilson, K. D., and J. C. Wu. 2015. "Induced pluripotent stem cells." *JAMA* 313 (16): 1613-4. https://doi.org/10.1001/jama.2015.1846. https://www.ncbi.nlm.nih.gov/pubmed/25919522.

Xing, J., Y. C. Toh, S. Xu, and H. Yu. 2015. "A method for human teratogen detection by geometrically confined cell differentiation and migration." *Sci Rep* 5: 10038. https://doi.org/10.1038/srep10038.
http://www.ncbi.nlm.nih.gov/pubmed/25966467.

Yang, X., L. Pabon, and C. E. Murry. 2014. "Engineering adolescence: maturation of human pluripotent stem cell-derived cardiomyocytes." *Circ Res* 114 (3): 511-23. https://doi.org/10.1161/CIRCRESAHA.114.300558.
https://www.ncbi.nlm.nih.gov/pubmed/24481842.

Yang, X., M. Rodriguez, L. Pabon, K. A. Fischer, H. Reinecke, M. Regnier, N. J. Sniadecki, H. Ruohola-Baker, and C. E. Murry. 2014. "Tri-iodo-l-thyronine promotes the maturation of human cardiomyocytes-derived from induced pluripotent stem cells." *J Mol Cell Cardiol* 72: 296-304. https://doi.org/10.1016/j.yjmcc.2014.04.005.
https://www.ncbi.nlm.nih.gov/pubmed/24735830.

Yndestad, A., L. E. Vinge, R. Bjornerheim, T. Ueland, J. E. Wang, S. S. Froland, H. Attramadal, P. Aukrust, and E. Oie. 2006. "Thalidomide attenuates the development of fibrosis during post-infarction myocardial remodelling in rats." *Eur J Heart Fail* 8 (8): 790-6. https://doi.org/10.1016/j.ejheart.2006.02.007. http://www.ncbi.nlm.nih.gov/pubmed/16549389.

Yoon, S. J., Y. H. Fang, C. H. Lim, B. S. Kim, H. S. Son, Y. Park, and K. Sun. 2009. "Regeneration of ischemic heart using hyaluronic acid-based injectable hydrogel." *J Biomed Mater Res B Appl Biomater* 91 (1): 163-71. https://doi.org/10.1002/jbm.b.31386.
https://www.ncbi.nlm.nih.gov/pubmed/19399850.

Young, J. L., and A. J. Engler. 2011. "Hydrogels with time-dependent material properties enhance cardiomyocyte differentiation in vitro." *Biomaterials* 32 (4): 1002-9. https://doi.org/10.1016/j.biomaterials.2010.10.020.
http://www.ncbi.nlm.nih.gov/pubmed/21071078.

Yu, L., M. C. Chen, and K. C. Cheung. 2010. "Droplet-based microfluidic system for multicellular tumor spheroid formation and anticancer drug testing." *Lab Chip* 10

(18): 2424-32. https://doi.org/10.1039/c004590j. https://www.ncbi.nlm.nih.gov/pubmed/20694216.

Yu, L., and J. Ding. 2008. "Injectable hydrogels as unique biomedical materials." *Chem Soc Rev* 37 (8): 1473-81. https://doi.org/10.1039/b713009k. https://www.ncbi.nlm.nih.gov/pubmed/18648673.

Yuhas, John M., Albert P. Li, Andrew O. Martinez, and Aaron J. Ladman. 1977. "A Simplified Method for Production and Growth of Multicellular Tumor Spheroids." *Cancer Research* 37 (10): 3639-3643.

Zhang, D., I. Y. Shadrin, J. Lam, H. Q. Xian, H. R. Snodgrass, and N. Bursac. 2013. "Tissue-engineered cardiac patch for advanced functional maturation of human ESC-derived cardiomyocytes." *Biomaterials* 34 (23): 5813-20. https://doi.org/10.1016/j.biomaterials.2013.04.026. https://www.ncbi.nlm.nih.gov/pubmed/23642535.

Zhang, Y., J. Mignone, and W. R. MacLellan. 2015. "Cardiac Regeneration and Stem Cells." *Physiol Rev* 95 (4): 1189-204. https://doi.org/10.1152/physrev.00021.2014. http://www.ncbi.nlm.nih.gov/pubmed/26269526.

Zhao, Guoxu, Xiaohui Zhang, Tian Jian Lu, and Feng Xu. 2015. "Recent Advances in Electrospun Nanofibrous Scaffolds for Cardiac Tissue Engineering." *Advanced Functional Materials* 25 (36): 5726-5738. https://doi.org/10.1002/adfm.201502142.

Zhao, M., Y. Tang, Y. Zhou, and J. Zhang. 2019. "Deciphering Role of Wnt Signalling in Cardiac Mesoderm and Cardiomyocyte Differentiation from Human iPSCs: Four-dimensional control of Wnt pathway for hiPSC-CMs differentiation." *Sci Rep* 9 (1): 19389. https://doi.org/10.1038/s41598-019-55620-x. https://www.ncbi.nlm.nih.gov/pubmed/31852937.

Zhao, Xin, Shen Liu, Lara Yildirimer, Hong Zhao, Ruihua Ding, Huanan Wang, Wenguo Cui, and David Weitz. 2016. "Injectable Stem Cell-Laden Photocrosslinkable Microspheres Fabricated Using Microfluidics for Rapid Generation of Osteogenic Tissue Constructs." *Advanced Functional Materials*: n/a-n/a. https://doi.org/10.1002/adfm.201504943. http://dx.doi.org/10.1002/adfm.201504943.

Zweigerdt, R. 2009. "Large scale production of stem cells and their derivatives." *Adv Biochem Eng Biotechnol* 114: 201-35. https://doi.org/10.1007/10_2008_27. https://www.ncbi.nlm.nih.gov/pubmed/19513633.

Zweigerdt, Robert, Ruth Olmer, Harmeet Singh, Axel Haverich, and Ulrich Martin. 2011. "Scalable expansion of human pluripotent stem cells in suspension culture." *Nat. Protocols* 6 (5): 689-700. http://dx.doi.org/10.1038/nprot.2011.318.